The Graduate University for Advanced Studies,
SOKENDAI

Department of Accelerator Science

Beam-Beam Effects and Optics Aberrations at IP of SuperKEKB

Kouki Hirosawa

Supervisor:

Tetsuya Kobayashi

March 2020

Abstract

Optics Aberrations of colliding beam dymanics at the interaction point (IP) is one of most important topics for recent colliders. There is no alternative component for complicated beam–beam effects due to the beam collision. In addition, especially for the circular type collider, cumulative effects of the beam–beam collision is developed in turn by turn. The objective of this research is the X–Y betatron coupling of the second order aberration at the IP for KEK SuperB–Factory (SuperKEKB). SuperKEKB is an asymmetric energy electron–positron circular collider. It is the luminosity upgrade accelerator from KEK B–Factory (KEKB) of the worldrecord holder inthe highest luminosity for the lepton collider. The achievement target of design SuperKEKB is 40 times of the achieved luminosity of KEKB by using new collision method called nano–beam scheme and high beam current upgrade. The nano–beam scheme consists of large crossing-angle and extremely low beta function and low emittance. The final focusing superconducting magnets system (QCS) is newly designed and installed for the nano–beam scheme. Phase-2 of SuperKEKB beam commissioning was tested after BELLE-II detector installed, and then it was ovserved that the first collision and the paircreation, after that IP collision tuning was traind with beta squeezing step by step. Studying for the effects of the QCS on the IP beam dynamics is also so important since the final focusing system optimized for nano–beam scheme is first operation in the world. Beam optics for global XY coupling and dispersion is corrected by newly installed Non–interleaved sextupoels system, which can be fine tunable system for them separately. The Non-Interleaved sextupole system consists of a pair of sextupole magnets and dispersion or X–Y coupling can be selectively applied globally by exciting two magnetic fields symmetrically or antisymmetrically. The skew quadrupole field is adjusted effectively by exciting the skew quadrupole auxiliary coil provided in each sextupole magnet. During repetition of collision tuning in the beam commissioning, the global X–Y coupling correction could not effectively optimize the effect on the beam property with a low beta function at the IP. Therefore I proposed local coupling correction near the IP in interaction region (IR). The global coupling values of the entire ring were measured by beam position monitors (BPM) and they were sufficiently corrected. It was possible that the symmetric error of the

magnet in the IR is the error source of the IP optics aberration. The effect of the magnetic field on both sides of the IP was calculated by the transfer matrix using accelerator calculation code called SAD, in order to perform the correction by locally confining the X–Y coupling in the IR. By determining the specific value of the optics aberration at the IP as a relationship with the skew qadrupole component of the QCS, the possibility of actual adjustment was examined. The IP coupling parameters was determined by a peak detecting method using a luminosity monitor. Global XY coupling by skew quadrupoles out of IR could be corrected r_1, r_3, and r_4 parameters enough. However globally tunable range did not reach r_2 error value, I proposed the IP locally correction method for r_2 correction by using QCS skew quadrupoles adding to traditional global correction method. As the result of new correcting method, all linear XY coupling parameters were well corrected and luminosity was much improved as twice. Following three items are suggested as new results of this study. First, It is shown that the X-Y coupling at the IP is a very important adjustment task in the extremely low beta function and the focusing magnet system to achieve thier target. Second, X–Y coupling adjustment for the nanobeam scheme cannot be completely adjusted only by a globally correcting the coupling coefficient over the entire ring, and it is critically important to use the skew corrector coils of the final focusing magnet. Third, we obtained results that greatly contributed to the future progress of the collider, as the first work to study the IP coupling in the collider from both theoretical and experimental aspects.

Contents

List of Figures

Chapter 1

Introduction

1.1 Circular Lepton Accelerators

Historically, the particle accelerator has been closely related to many of the achievements of modern science[1, 2, 3, 4]. The x-rays that are generated by accelerators have attracted the attention of researchers working in various fields since the first paper regarding X-rays was submitted by Wilhelm Röntgen in 1895. A report concerning an experiment involving a certain type of x-ray had already been presented by William Morgan in 1785, but this was only concerned with the physical phenomena. However, it is conceivable to consider that the race to build modern particle accelerators began in 1911, when Rutherford discovered the nucleus by scattering α-particles. Modern scientists continue to use accelerators regardless of their field, as accelerators are used in many applications such as nuclear and particle physics, industrial applications such as ion implantation and lithography, biological and medical research that uses synchrotron light sources, and the material and medical sciences using neutron sources, among others. Our accelerator, “SuperKEKB", is contributing to the field of particle physics by producing mainly B-mesons.

Technological improvements to accelerators have involved many branches of science, including electromagnetism, solid-state physics, atomic physics, superconductivity, nonlinear dynamics, plasma physics, and quantum physics. These advances in technology have induced a significant increase in the energy and luminosity that is available for the study of fundamental physics. In terms of high energy, the progress made was measured in MeVs in the 1930s and in TeVs by the 1990s. Similar progress has been made in terms of high luminosity, which is sometimes called high intensity in pulse-operated colliders, with 10^9 particles per pulse in the 1950s and 10^14 particles per pulse in the 1990s. Since 1970, high energy and high luminosity colliders have become basic tools that are commonly used in nuclear and particle physics re-

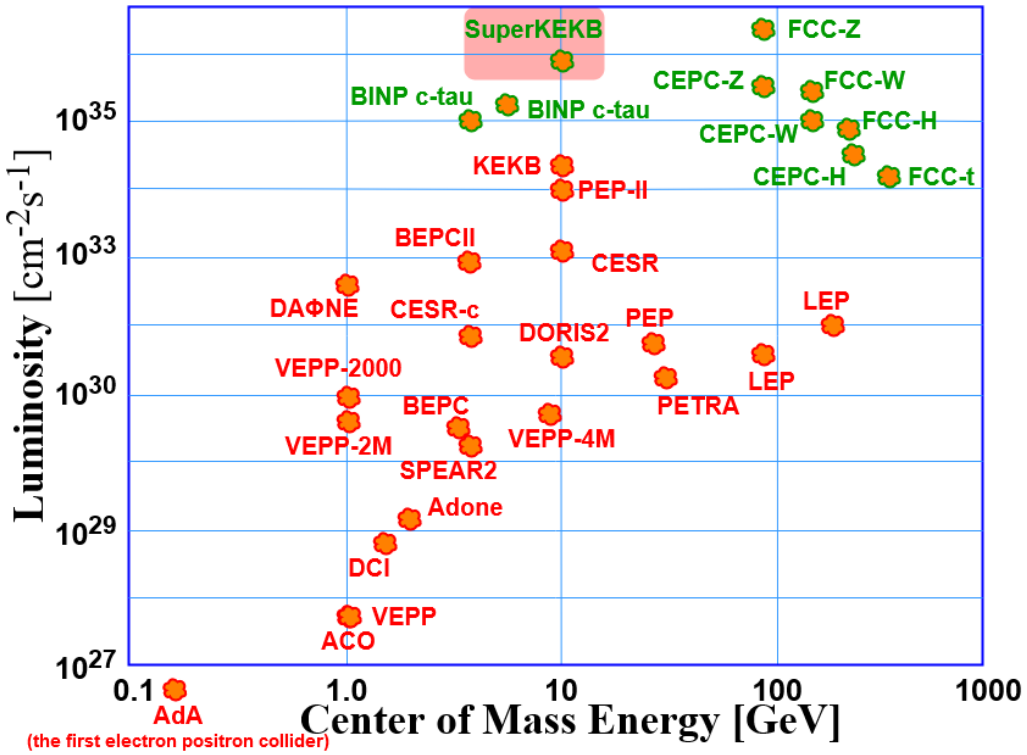

Figure 1.1: Summary of the historical development of the lepton collider. Red and green markers denote the achievements and design of individual colliders, respectively.

search. The developments made in the lepton collider are summarized in the chart in Figure 1.1.

1.2 An Overview of SuperKEKB

1.2.1 The Upgrade from KEKB to SuperKEKB

Experimental Motivation

The KEKB B-Factory has been in operation since 1999, carrying out a collision experiment (known as the Belle experiment), mainly with a $\Upsilon(4S)$ resonance. KEKB consists of two rings; an 8-GeV electron ring (HER) and a 3.5-GeV positron ring (LER), both with a circumference of 3016 m and located in a tunnel 11 m below ground level. The highest luminosity recorded as a result of the collision of these two beams was $\mathcal{L} = 2.1 \times 10^{34}\text{cm}^{-2}\text{s}^{-1}$, which was recorded in 2009. The peak luminosity was realized by the smaller β_y^* (6 mm vs. 10 mm) horizontal betatron, which was tuned closer to a half integer (LER: 0.505/ HER: 0.511) with crab crossing. This experiment produced important results for B-Physics and CP-violation, among others. The Belle

experiment was designed and optimized for the observation of CP-violation in the B-meson system. In 2001, Belle was used to observe large CP-asymmetries in B-decays, which were expected and consistent with the theoretical proposals of Kobayashi and Maskawa.

Scientists are currently hoping to use such systems in order to find new physics (NP). There are two conceivable approaches to finding NP with particle colliders; reaching the energy frontier and the luminosity frontier, which are the direct results of improvements to the precision. To find deviations from the predictions made using the Standard Model, it is necessary to precisely measure the reactions of known particles close to the luminosity frontier. The Belle II detector aims to search for the charged Higgs particle by using $B \to \tau\nu$ and $B \to D^{(*)}\tau\nu$ decays, radiative and electroweak penguin decays, and to measure ϕ_1 and ϕ_2 [5]. To conduct these types of experiments, SuperKEKB is required to provide extremely high luminosity. A comparison of the parameters used in KEKB and SuperKEKB is given in Table 1.1[6]. Improvements that have been made as a result of the development of SuperKEKB include the nano beam scheme, which provides a new collision method and higher beam current that is nearly 1.5 times higher than that of KEKB.

Hardware Upgrades

The main objective of the new collider is increasing the luminosity, for which two major approaches are conceivable; improving the collision method and operating at a high current. These two methods are generally independent of each other; thus improvements can be made in both methods simultaneously in order to achieve the luminosity required[7].

In the injector linac, it is necessary that the beam satisfies all steps of the commissioning plan. To reduce the emittance and reshape the bunches, a positron damping ring (DR) is installed in the positron injector linac[8]. The whole DR system, including the infra-structure, was newly constructed for the SuperKEKB upgrade; thus, the commissioning of the DR was carried out during operation of the SuperKEKB Phase-2 testing[9]. Most of the specifications for the DR were satisfied via the request values used for injection, and the further improvement of beam conditions such as emittance have continued, even during SuperKEKB Phase-3 and the physics run. The photocathode RF electron gun was newly developed for SuperKEKB in order to produce electron and positron beams with high charge and low emittance. The beam parameters required are 4 nC with 20 mm mrad and 4 nC with 6 mm mrad for the electron and positron beams, respectively. A thermal cathode DC gun was used in KEKB; however, the DC gun cannot produce beams with such low emittance[10].

		KEKB		SuperKEKB		
		LER	HER	LER	HER	Units
Beam energy	E	3.5	8.0	4.0	7.007	GeV
Circumference	C	3016.262		3016.315		m
Half crossing angle	θ_x	0(crab)		41.5		mrad
Piwinski angle	ϕ_{Pwi}	0	0	24.6	19.3	rad
Horizontal emittance	ε_x	18	24	1.9	4.4	nm
Vertical emittance	ε_y	150	150	8.64	12.9	pm
Coupling	$\varepsilon_y/\varepsilon_x$	0.83	0.62	0.27	0.28	%
Beta function at IP	$\beta_x^*\|\beta_y^*$	1200|5.9	1200|5.9	32|0.27	25|0.30	mm
Horizontal beam size at IP	σ_x^*	147	170	10.1	10.7	μm
Vertical beam size at IP	σ_y^*	940	940	48	62	nm
Horizontal betatron tune	ν_x	45.506	44.511	44.530	45.530	
Vertical betatron tune	ν_y	43.561	41.585	46.570	43.570	
Momentum compaction	α_{c}	3.3	3.4	3.2	4.55	10^{-4}
Energy spread	σ_δ	7.3	6.7	7.53	6.3	10^{-4}
Beam current	I	1.64	1.19	3.6	2.6	A
Number of bunches	n_{b}	1584		2500		
Particles/bunch	N	6.47	4.72	9.04	6.53	10^{10}
Energy loss/turn	U_0	1.64	3.48	1.76	2.43	MeV
Long. damping time	τ_s	21.5	23.2	22.8	29.0	msec
RF frequency	f_{RF}	508.9		508.9		MHz
Total cavity voltage	V_{c}	8.0	13.0	9.4	15.0	MV
Total beam power	P_{b}	3	4	8.3	7.5	MW
Synchrotron tune	ν_s	-0.0246	-0.0209	-0.0245	-0.0280	
Bunch length	σ_z	7	7	4.7	4.9	mm
Horizontal B-B param.	ξ_x	0.127	0.102	0.0028	0.0012	
Vertical B-B param.	ξ_y	0.129	0.090	0.088	0.081	

Table 1.1: Machine Parameters of KEKB and SuperKEKB without intrabeam scattering.

Research and development is currently being carried out using this system in order to produce beams with the quality required by the design. The components in the storage ring have also been improved in order to produce beams with the SuperKEKB design parameters. Many sub-systems of the SuperKEKB accelerator need to be upgraded in order to achieve the required luminosity that is 40 times higher than that of KEKB. The most important part is the vertical beam size, which is significantly narrowed as shown in Figure 1.2.

- The existing tunnel, infrastructure, and accelerator components from KEKB were reused wherever possible and were also improved and modified when necessary[7].

- For the design of the new optics, many of the magnets and the power supplies for the magnets needed to be replaced, re-arranged, and added, although the original cell structures in the arc sections have basically been retained in both rings[11, 12].

- The power supplies for the new QCS main magnets (2 kA, 10 V of DC) and corrector magnets ($\pm$60 A, $\pm$5 V of DC) were newly developed to meet requirements[13].

- Some of the power supplies were improved to satisfy the requirements of the optical design, and some were replaced with new power supplies. For example, the arrangement of the wiggler magnets in SuperKEKB is different from that of KEKB, meaning that the new power supplies for the wiggler magnets had to be newly manufactured[14].

- The requirements for upgrading the vacuum system comes from the higher beam currents in both rings. The synchrotron radiation and photon density are both high, especially in the wiggler sections. The beam impedance of various vacuum components also had to be minimized in order to suppress the excitation of HOM. Effective countermeasures are required to reduce the electron density in the beam pipes[15].

- Antechamber beam pipes have been adopted to reduce both the SR power density at the beam pipe walls and the beam impedance[16].

- The RF systems used with the ARES cavities and SCCs in KEKB are reused as much as possible, with necessary reinforcements. One ARES cavity is powered by one klystron.

- A new low-level RF (LLRF) control system, which is composed of μTCA-platform FPGA boards with embedded experimental physics and industrial control system input-output controllers, was developed for higher accuracy and flexibility. The new LLRF system was installed in 9 of the 22 RF stations for the ARES cavities, replacing the existing system[17].

1.2.2 Advantages of New Collision Scheme and Upgrades

To achieve the target luminosity of 8×10^{35} cm^{-2}s^{-1}, which is 40 times as high as the peak luminosity of KEKB, the vertical beta function at the interaction point (IP) needs to be decreased to 1/20 and the beam current needs to be increased to twice

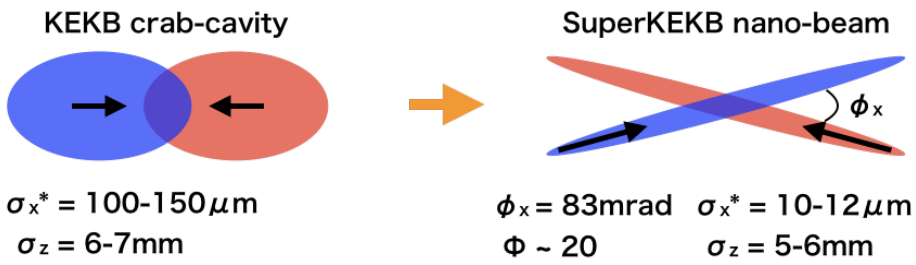

Figure 1.2: The beam size comparison between crab cavity collision of KEKB(left) and nano-beam shceme collision of SuperKEKB (right).

that of KEKB, while maintaining the same beam–beam parameters in the vertical direction. Prediction of the beambeam limit is difficult because the phenomenon has nonlinear effects and involves the interaction of many particles.

The vertical beta function at the IP is reduced to $270 - 300$ μm, while the bunch length is $5 - 6$ mm long. In order to avoid degradation in the luminosity from the hourglass effect, the “nano-beam scheme" that was proposed by P. Raimondi was adopted for use in SuperKEKB. New final focusing quadrupole magnets (QCS) were developed and located nearer to the IP than in KEKB; this is because the collision scheme was changed from a crab crossing scheme to a nano-beam scheme[18].

In first proposing the idea for the nano-beam scheme, a luminosity of $= \ 0.8 \times 10^{36}$ is given for the multi turn, with crab focusing on the vertical plane that is close to the SuperKEKB design parameters[19]. It was suggested that the advantages of the new crab waist collision scheme are the reduced ‘hourglass’ effect, the higher geometrical luminosity, and the greatly reduced beam-beam effect. The crab waist collision scheme consists of a large crossing angle collision and the crab waist in vertical beta. However, the original idea includes two powerful key methods, and handling the beam becomes extremely complicated with either method. When crab sextupoles were installed in the SuperKEKB rings, severe dynamic aperture degradation that was due to strong nonlinearity at the interaction region (IR) was confirmed by the lattice calculation of SAD. Therefore, the crab waist is not used in SuperKEKB[20].

The nano–beam scheme consists of a large crossing angle, low emittance, and a low beta. The important point of this scheme is that the beams collide at a large crossing angle. Figure **??** is a schematic comparison of the standard bunch, the crab crossing (KEKB), and the large crossing angle (SuperKEKB). As can be seen from Figure **??**, the large crossing angle has a much smaller region of overlap than the other methods used for collision. The detailed calculation of the nano–beam scheme with a large crossing angle is discussed in Section 2.2.2.

1.2.3 The Final Focusing System

The collider is provided with a final focusing magnet system so that the beam is only squeezed at the interaction point (IP). The beam size in 6-dimensional space is given by:

$$\sigma_{x,y,z} = \sqrt{\beta_{x,y,z}\varepsilon_{x,y,z}}, \tag{1.1}$$

$$\sigma_{p_x,p_y,p_z} = \sqrt{\frac{\varepsilon_{x,y,z}}{\beta_{x,y,z}}}, \tag{1.2}$$

where β is the β-function of the Courant-Snyder twiss parameter and ε is the emittance. The emittance $\varepsilon_{x,y,z}$ is normally constant within the storage ring, meaning that the β has to be squeezed in order to achieve a small beam size.

The role of the quadrupole magnet is to focus the charged particles, in the same manner as a lens focuses light, acting on the β-function. As the collision scheme of SuperKEKB is based on the crab waist collision scheme, the original idea of final focusing using the quadrupoles is only a minor change from the design of the SuperB interaction region.

In order to correct the X-Y coupling at the IP, new sextupole magnets with variable tilting angle are installed on the tilting tables in the LER ring, which can be remotely controlled from the central operation room[**?**].

1.3 Beam-Beam Effects

1.3.1 The General Overview of the beam–beam effect

The effect of the beam–beam interaction is one of the most important issues concerning particle colliders and can lead to significant limits to the performance in terms of luminosity. Beam–beam interaction has therefore attracted interest at both the design and the operational stages of a colliding beam facility. A particle beam is a collection of a large number of charged particles that represents an electromagnetic potential to other particles, therefore exerting forces both on itself and on other beams. These forces are most important when high-density beams with high intensities and small beam sizes are produced, and are the key to producing high luminosity.

1.4 Perspective of this thesis

This thesis consists of three main chapters. In Chapter 2, beam–beam interactions and luminosity formulae are discussed, together with several boundary conditions. In Chapter 3, the effect of optical aberrations on the interaction point is discussed. This study is an evaluation of the luminosity produced by a machine with imperfections in the beam properties at the crossing region of colliding bunches. This thesis is therefore mainly concerned with the theoretical degradation in luminosity that is caused by linear optical aberrations at the IP. Details of the studies conducted for this paper are given in Chapter 4; in addition to the correction of linear optical aberrations at the IP, an evaluation of the methods used for the analysis of the data describing the beam-position for IP coupling, and a newly proposed method for identifying errors are described. The data analyzed in these studies were measured during the Phase-2 and Phase-3 commissioning of SuperKEKB.

Chapter 2

Beam-beam effects

2.1 Introduction of the Beam–Beam Effect

2.1.1 Toy Model of the Bunch–Bunch Collision

Luminosity is the most important parameter affecting the performance of a collider in terms of producing the required number of interactions. The luminosity is defined as the proportionality factor between the number of collisions per second dR/dt and the reaction cross-section σ_{p}:

$$\frac{dR}{dt} = \mathcal{L} \cdot \sigma_{\mathrm{p}}, \tag{2.1}$$

From the dimensional analysis, the unit used to describe luminosity is $[\mathrm{cm}^{-2}\mathrm{s}^{-1}]$.

In this section, a toy model is used to discuss the concept of the luminosity. In this step, a rectangular cross sectional area is used to represent the colliding bunches. The schematic of this idea is shown in Fig. 2.1. In the case illustrated in the figure, the probability of a collision dR/dt between a particle and a bunch containing N particle is $dR/dt = N\sigma_{\mathrm{p}}/S$, where the bunch has a cross sectional area of $S = \sigma_x \cdot \sigma_y$. When such bunches collide in a circular collider with a revolution frequency of f and the number of particles within the target bunch and the colliding bunch are denoted by N_+ and N_-, respectively, Eq. (2.1) can be modified to:

$$\frac{dR}{dt} = \frac{N_+ N_-}{\sigma_x \sigma_y} f \cdot \sigma_{\mathrm{p}}, \tag{2.2}$$

$$= \mathcal{L}\sigma_{\mathrm{p}}. \tag{2.3}$$

The cross–sectional area S is therefore generally the integral of the transverse particle distributions. If the transverse beam sizes of both beams are the same, the luminosity is written as

$$\mathcal{L} = \iint dxdy\{\Delta\mathcal{L}\} = \frac{N_+ N_-}{4\pi\sigma_x^*\sigma_y^*} f, \tag{2.4}$$

where σ_x^* and σ_y^* are the horizontal and vertical beam sizes at the interaction point and the standard deviations of the Gaussian distribution in each direction.

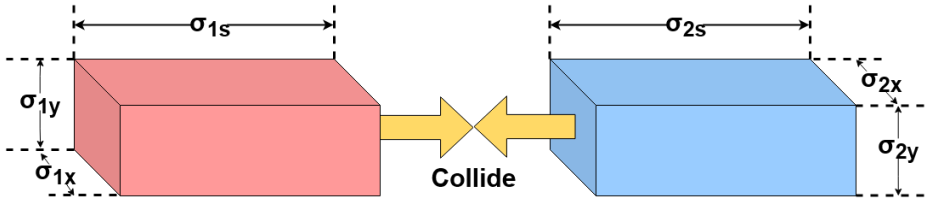

Figure 2.1: Schematic of rectangular bunches that are colliding head-on

2.1.2 Beam–beam effects

Beam-Beam Force

The interaction between two particles is described using the Lorentz force equation. The Lorentz force in a Lorentz boosted frame $\vec{F}$ is given by

$$\vec{F} = q(\vec{E} + \vec{c} \times \vec{B}), \tag{2.5}$$

which satisfies

$$E_\parallel = E'_\parallel, \quad E_\perp = \gamma E'_\perp, \quad \vec{B} = \vec{\beta} \times \frac{\vec{E}}{c}. \tag{2.6}$$

It is generally assumed that bunches are Gaussian in distribution, which is described in Cartesian coordinates as

$$\rho(x, y) = \frac{Nq}{(2\pi)^{\frac{3}{2}}\sigma_x\sigma_y} \exp\left(-\frac{x^2}{2\sigma_x^2} - \frac{y^2}{2\sigma_y^2}\right). \tag{2.7}$$

In a transverse plane, the electrostatic potential for an electric charge distribution

$U(x, y)$ is the solution of the Poisson equation:

$$U(x,y) = \frac{1}{\epsilon_0}\int dx'dy' \left\{ \frac{\rho(x',y')}{4\pi|x-x'|\cdot|y-y'|} \right\} \tag{2.8}$$

$$= \frac{Nq}{4\pi\epsilon_0}\int_o^\infty dt \left\{ \frac{\exp\left(\frac{x^2}{2\sigma_x^2+t}+\frac{y^2}{2\sigma_y^2+t}\right)-1}{\sqrt{2\sigma_x^2+t}\sqrt{2\sigma_y^2+t}} \right\}. \tag{2.9}$$

Equation (2.8) can be derived using the Green function method. A detailed procedure performed with these equations is provided in the Appendix **??**. The kick forces can be calculated from the electrostatic potential with the effective temporal region $-\frac{\Delta t}{2} \leq t \leq \frac{\Delta t}{2}$ as follows:

$$\Delta x' = \int_{-\frac{\Delta t}{2}}^{\frac{\Delta t}{2}} dt\,\{F_x\} = q\int_{-\frac{\Delta t}{2}}^{\frac{\Delta t}{2}} dt\,\{E_x\} = e\frac{\partial U}{\partial x}, \tag{2.10}$$

$$\Delta y' = \int_{-\frac{\Delta t}{2}}^{\frac{\Delta t}{2}} dt\,\{F_y\} = q\int_{-\frac{\Delta t}{2}}^{\frac{\Delta t}{2}} dt\,\{E_y\} = e\frac{\partial U}{\partial y}. \tag{2.11}$$

In the case of a flat beam where $\sigma_x \ll \sigma_y$, the formulae for the kick force is provided by M. Basseti and G. A. Erskin using the complex error function (Faddeeva function) : $w(x) = e^{-x^2}\mathrm{erfc}(-ix)$[21] leading to:

$$\Delta x' = -i\frac{Nr_e}{\gamma}\sqrt{\frac{2\pi}{\sigma_x^2-\sigma_y^2}}\,\mathrm{Im}(\mathcal{W}), \tag{2.12}$$

$$\Delta y' = \frac{Nr_e}{\gamma}\sqrt{\frac{2\pi}{\sigma_x^2-\sigma_y^2}}\,\mathrm{Re}(\mathcal{W}), \tag{2.13}$$

$$\tag{2.14}$$

where $\mathcal{W}$ is the term of error function:

$$\mathcal{W} = \left[w\left(\frac{x+iy}{\sqrt{2(\sigma_x^2-\sigma_y^2)}}\right) - \exp\left(-\frac{x^2}{2\sigma_x^2}-\frac{y^2}{2\sigma_y^2}\right) w\left(\frac{\frac{\sigma_y}{\sigma_x}x+i\frac{\sigma_x}{\sigma_y}y}{\sqrt{2(\sigma_x^2-\sigma_y^2)}}\right)\right]. \tag{2.15}$$

In the vicinity of the bunch center $x \ll \sigma_x$, $y \ll \sigma_y$, these formulae become very

simple form:

$$\Delta x' = \frac{Nr_e}{\gamma}\frac{x}{2\pi\sigma_x(\sigma_x+\sigma_y)}, \tag{2.16}$$

$$\Delta y' = \frac{Nr_e}{\gamma}\frac{y}{2\pi\sigma_y(\sigma_x+\sigma_y)}, \tag{2.17}$$

using a linear approximation for x and y.

In a cylindrical (axisymmetrical) coordinate system with round Gaussian beams, the beam–beam force is given by

$$F_r(r,s,t) = -\frac{Ne^2(1+\beta^2)}{\sqrt{8\pi^3}\varepsilon_0 r\sigma_s}\{1-\exp(-\frac{r^2}{2\sigma^2})\}\{\exp(-\frac{(s+vt)^2}{2\sigma_2^2})\}. \tag{2.18}$$

In a similar manner to Cartesian coordinates, the beam–beam kick in cylindrical coordinates is given by

$$\Delta r' = \frac{1}{mc\beta\gamma}\int_{-\frac{\Delta t}{2}}^{\frac{\Delta t}{2}} dt\{F_r(r,s,t)\}. \tag{2.19}$$

Figure 2.2 shows the 1D beam–beam kick force as a function of x. The effect of the beam–beam kick can work as a thin quadrupole linear kick in the range of $1 \gg /x\sigma_x$, outside of which it behaves in a nonlinear manner. This linear approximation is a critical factor for discussing the beam–beam tune shift.

The Linear Beam–Beam Tune Shift

The matrix describing one turn matrix of the storage ring with betatron tune : ν is given by

$$M = \begin{pmatrix} \cos 2\pi\nu + \alpha\sin 2\pi\nu & \beta\sin 2\pi\nu \\ -\gamma\sin 2\pi\nu & \cos 2\pi\nu - \alpha\sin 2\pi\nu \end{pmatrix} = \mathrm{I}\cos 2\pi\nu + \mathrm{J}\sin 2\pi\nu$$

where I is the unit matrix and

$$\mathrm{J} = \begin{pmatrix} \alpha & \beta \\ -\gamma & -\alpha \end{pmatrix}, \quad \mathrm{J}^2 = -\mathrm{I}$$

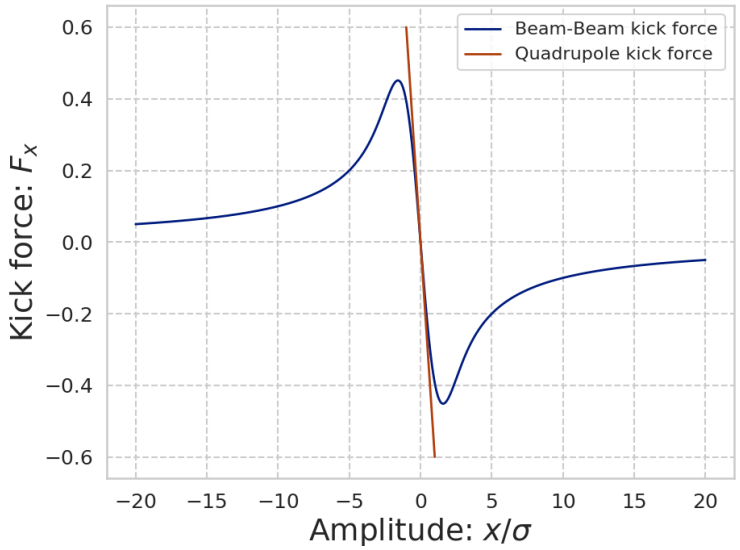

Figure 2.2: Beam–beam force as a function of the amplitude of round beams which are normalized using the beam size σ.

is a matrix with zero trace and a unit determinant, and these (α, β, and γ) are Courant-Snyder Twiss parameters[22]. It was discussed in Section 2.1.2 that the beam–beam kick works as if it were a quadrupole field with a small amplitude of x/σ. Therefore, we can assume that the effect of a beam–beam collision can be approximated as a linear thin focus lens , forming a a simple collision model that can be used to describe collision.

The Courant-Snyder Twiss parameters at the IP are $\alpha(0) = 0$ and $\beta(0) = \beta^*$, thus the one turn matrix becomes:

$$\mathrm{M}_0 = \begin{pmatrix} \cos 2\pi\nu_0 & \beta_0^* \sin 2\pi\nu_0 \\ -\frac{1}{\beta_0^*} \sin 2\pi\nu_0 & \cos 2\pi\nu_0. \end{pmatrix}$$

. As the thin lens model of a quadrupole is given as

$$\mathrm{K_q}(k) = \begin{pmatrix} 1 & 0 \\ -k & 1 \end{pmatrix},$$

where k is the strength of a quadrupole, the new one turn matrix with the center of

the thin lens of the beam–beam kick force can be obtained by

$$\mathrm{M_{bb}} = \mathrm{K_q}(\Delta r')\mathrm{M_0}\mathrm{K_q}(\Delta r') \tag{2.20}$$

$$= \begin{pmatrix} 1 & 0 \\ -\Delta r' & 1 \end{pmatrix} \begin{pmatrix} \cos 2\pi\nu_0 & \beta_0^* \sin 2\pi\nu_0 \\ -\frac{1}{\beta_0^*}\sin 2\pi\nu_0 & \cos 2\pi\nu_0 \end{pmatrix} \begin{pmatrix} 1 & 0 \\ -\Delta r' & 1 \end{pmatrix} \tag{2.21}$$

$$= \begin{pmatrix} \cos 2\pi\nu_0 - \Delta r'\beta_0^* \sin 2\pi\nu_0 & \beta_0^* \sin 2\pi\nu_0 \\ \left((\Delta r')^2\beta_0^* - \frac{1}{\beta_0^*}\right)\sin 2\pi\nu_0 - 2\Delta r' \cos 2\pi\nu_0 & -\Delta r'\beta_0^* \cos 2\pi\nu_0. \end{pmatrix} \tag{2.22}$$

On the other hand, the new one turn matrix can also be written as the same Courant–Snyder Twiss matrix, thus the one turn matrix with beam–beam effect approximated to a quadrupole field is written as

$$\mathrm{M_{bb}} = \begin{pmatrix} \cos 2\pi\nu_{\mathrm{bb}} & \beta_{\mathrm{bb}}^* \sin 2\pi\nu_{\mathrm{bb}} \\ -\frac{1}{\beta_{\mathrm{bb}}^*}\sin 2\pi\nu_{\mathrm{bb}} & \cos 2\pi\nu_{\mathrm{bb}} \end{pmatrix}, \tag{2.23}$$

where $2\pi\nu_{\mathrm{bb}}$ is the new betatron tune with beam–beam effect. When $1 \gg \Delta r\beta_0^*$ is assumed, this can result in the eigenvalue problem seen in Eq. (2.20) and Eq. (2.23).

From the relationship between components (1,1) and (1,2), factors of the betatron function with beam–beam effect are represented by

$$\begin{cases} \cos 2\pi\nu_{\mathrm{bb}} & = \cos 2\pi\nu_0 - \Delta r'\beta_0^* \sin 2\pi\nu_0, \\ \frac{\beta_{\mathrm{bb}}^*}{\beta_0^*} & = \frac{\sin 2\pi\nu_0}{\sin 2\pi\nu_{\mathrm{bb}}}. \end{cases} \tag{2.24}$$

The upper part of Eq. (2.24) yields the value of beam–beam tune shift. The detailed

transformation of Eq. (2.24) in form of the tune shift is given by

$$\cos 2\pi\nu_{\rm bb} = \sqrt{1+(\Delta r'\beta_0^*)^2}\cos\{2\pi(\nu_0+\Delta\nu)\} \tag{2.25}$$

$$\simeq \cos\{2\pi(\nu_0+\Delta\nu)\},$$

$$\Delta\nu = \frac{\tan^{-1}(\Delta r'\beta_0^*)}{2\pi} \simeq \frac{\Delta r'\beta_0^*}{2\pi}, \tag{2.26}$$

from the linear approximation of $\Delta r\beta_0^*$. The lower part of Eq. (2.24) describes the change in the β-function, which is known as *Dynamic-β* and is associated with phenomena called *β-beats*. The strength of the linear quadrupole effect of the beam–beam force are sometimes expressed in terms of the beam–beam parameter. The beam–beam parameter is defined by

$$\xi = -\frac{\beta_0^*}{4\pi}\Delta p'|_0 = \frac{\beta_0^*}{4\pi}\frac{\Delta r'}{2}. \tag{2.27}$$

This parameter is defined to each direction of x and y. Then the tune shift is given simply by

$$\Delta\nu \approx \xi, \tag{2.28}$$

for tunes far from an integer or half–integer resonance. Substituting $\Delta r'$ for ξ of y direction, ξ_y can be expressed by

$$\xi_{y\pm} = \frac{r_e}{2\pi\gamma_\pm}\frac{\beta_{y\pm}^* N_\mp}{\sigma_{y\mp}^*(\sigma_{x\mp}^*+\sigma_{y\mp}^*)}. \tag{2.29}$$

This beam–beam parameter is the important parameter to discuss the luminosity and the beam–beam effect for the beam physics in the collider.

The Hourglass Effect

The β-function, when focused to β^* in the drift space, is given by

$$\beta_{x,y}(s) = \beta_{x,y}^* + \frac{s^2}{\beta_{x,y}^*} \tag{2.30}$$

as a function of the position at point of β^*. This relationship can be adopted at the point of collision. As bunched beams are of finite bunch lengths, the transverse beam

size behaves as the β-distribution in Eq. (2.30) even in both are in the same bunch. If the cross section includes an effective part of the β-distribution, bunches that are within large beams collide at different points to the IP.

$$\mathcal{L} = \frac{N_+ N_-}{4\pi\sigma_x^*\sigma_y^*} f\mathcal{R}_\mathcal{L} \tag{2.31}$$

$$\xi_{y\pm} = \frac{r_e}{2\pi\gamma_\pm} \frac{\beta_{y\pm}^* N_\mp}{\sigma_{y\mp}^*(\sigma_{x\mp}^* + \sigma_{y\mp}^*)} r_{\xi\mp} \tag{2.32}$$

where r_ξ is the geometrical factor of the beam-beam parameter.

Combining Eq. (2.31) and (2.32), the luminosity can be represented by

$$\mathcal{L} = (1 + \frac{\sigma_{y\pm}^*}{\sigma_{x\pm}^*}) \frac{\gamma_\pm}{2er_e} \frac{\xi_{y\pm} I_\pm}{\beta_{y\pm}^*} \frac{\mathcal{R}_\mathcal{L}}{r_\xi}. \tag{2.33}$$

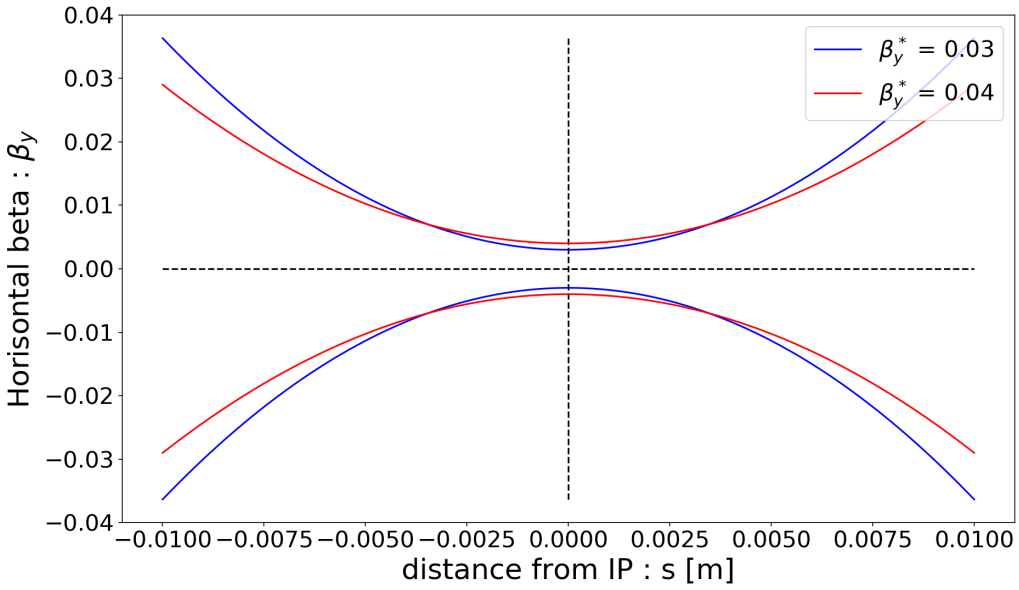

Figure 2.3: An example of the beam size distribution as a function of distance from the IP s.

2.2 Luminosity of the Circular Collider

In the case where two beams collide, both beams act as the collision target and the IP simultaneously. As we discussed in Section 2.1, the spatial 3-D distribution and the relation of the distance between the IP and the bunches are the most important factors affecting collision[23, 24, 25]. Figure 2.4 is a schematic view of two colliding beams, demonstrating several parameters. The distance from the two beams to the central collision point $s_0 = ct$ acts as a time variable; thus, the luminosity is given by the 4-D integral. The general Luminosity formula describing luminosity is therefore represented by[26]

$$\mathcal{L} = \frac{N_1 N_2}{S_\mathrm{b}} \mathcal{K} \iiiint_{-\infty}^{\infty} dxdydsds_0 \{\rho_1(x, y, s, -s_0)\rho_2(x, y, s, -s_0)\}, \tag{2.34}$$

$$\tag{2.35}$$

where K is a kinetic factor defined by:

$$\mathcal{K} = \sqrt{(\vec{v}_1 - \vec{v}_2)^2 - \left(\frac{\vec{v}_1 \times \vec{v}_2}{c}\right)^2}. \tag{2.36}$$

In Eq. (2.34), ρ_1 and ρ_2 are the time-dependent beam density distribution functions, and N_1 and N_2 are the number of particles in a bunch within beam #1 and beam #2, respectively. As the beams are moving towards each other, Eq. (2.36) has to be multiplied by the luminosity formula, producing a kinetic factor.

In the case of head-on collisions ($\vec{v}_1 = -\vec{v}_2$), where there is no correlations between the planes, the density distribution can be separated into each direction. Then, the luminosity is written by:

$$\mathcal{L} = 2N_1 N_2 f N_\mathrm{b} \iiiint_{-\infty}^{\infty} dxdydsds_0 \{\rho_{1x}(x)\rho_{1y}(y)\rho_{1s}(s - s_0)\rho_{2x}(x)\rho_{2y}(y)\rho_{2s}(s + s_0)\}, \tag{2.37}$$

where N_b is the number of bunches in each ring, f is the revolution frequency, and the relationship $v/S_\mathrm{b} = vN_\mathrm{b}/c = fN_\mathrm{b}$ is satisfied. In the following sections, the luminosity model is used only in the head-on region, and not for long-range collisions, because the calculation of long-range effect are significantly more complicated.

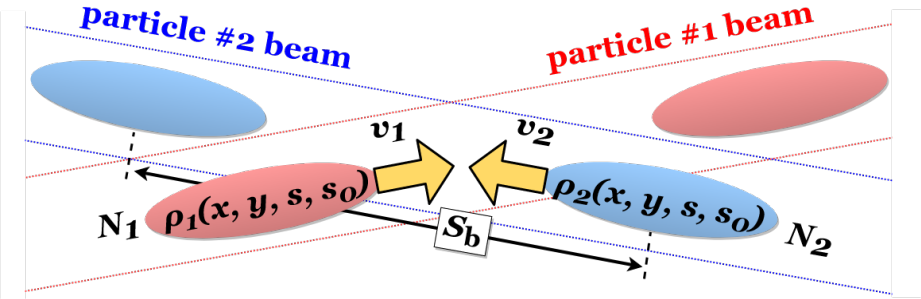

Figure 2.4: Schematic of head-on colliding bunches of rectangular shape

2.2.1 No Angle Collision Model

The most simplified model that can be used to describe beam collision is Gaussian Head-on Collision. An example of the this is given in Figure 2.5. The bunches can be described as Gaussian ellipsoids with:

$$\rho \propto \exp\left(-\left(\frac{x^2}{2\sigma_x^2}+\frac{y^2}{2\sigma_y^2}+\frac{z^2}{2\sigma_z^2}\right)\right), \tag{2.38}$$

where $\sigma_{\{x,y,z\}}$ is the beam size for several of the axes. The actual expression describing the Gaussian profiles in all dimensions is denoted by

$$\rho_{ik}(l) = \frac{1}{\sigma_k\sqrt{2\pi}}\exp\left(-\frac{l^2}{2\sigma_k^2}\right), \tag{2.39}$$

$$\rho_s(s \pm s_0) = \frac{1}{\sigma_s\sqrt{\pi}}\exp\left(-\frac{(s \pm s_0)^2}{2\sigma_s^2}\right), \tag{2.40}$$

where subscriptions are $i = \{1, 2\}$, $k = \{x, y, s\}$, and $l = \{x, y, s \pm s_0\}$, respectively. Using Eq. (2.37) and (2.39), the luminosity formula is obtained as the first integral:

$$\mathcal{L} = \frac{2N_1N_2fN_\mathrm{b}}{8\pi^3\sigma_s^2\sigma_x^2\sigma_y^2}\iiiint dxdydsds_0\left\{e^{-\frac{x^2}{\sigma_x^2}}e^{-\frac{y^2}{\sigma_y^2}}e^{-\frac{s^2}{\sigma_s^2}}e^{-\frac{s_0^2}{\sigma_s^2}}\right\}. \tag{2.41}$$

By using the Gaussian integral for each direction, the simple formula for the luminosity is obtained as:

$$\mathcal{L} = \frac{2N_1N_2fN_\mathrm{b}}{8\pi^2\sigma_x^2\sigma_y^2}\iint dxdy\{e^{-\frac{x^2}{\sigma_x^2}}e^{-\frac{y^2}{\sigma_y^2}}\} \tag{2.42}$$

$$= \frac{N_1N_2fN_\mathrm{b}}{4\pi\sigma_x\sigma_y}. \tag{2.43}$$

Equation (2.43) is the standard expression for the luminosity of two Gaussian beams colliding head-on.

However, it is more likely that the two beams will be of different sizes. In the case where: $\sigma_{1x} \neq \sigma_{2x}, \sigma_{1y} \neq \sigma_{2y}, \sigma_{1s} \approx \sigma_{2s}$, the luminosity formula is modified to

$$\mathcal{L} = \frac{N_1N_2fN_\mathrm{b}}{2\pi\sqrt{(\sigma_{1x}^2+\sigma_{2x}^2)(\sigma_{1y}^2+\sigma_{2y}^2)}}. \tag{2.44}$$

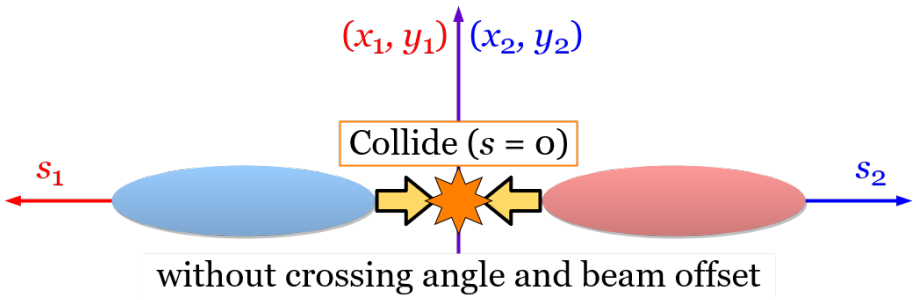

Figure 2.5: Schematic of a head-on collision with no crossing angle or beam offset, meaning that both trajectories have same coordinates in the IR ($x_1 = x_2, y_1 = y_2, s_1 = -s_2$).

2.2.2 No Angle Collision with Hourglass effect Model

More details concerning the information in Section 2.1.2 are discussed in this section. The relationship between the β, beam sizes σ, and the emittance ε follows

$$\beta_{x,y} = \beta^*_{x,y} + \frac{s^2}{\beta^*_{x,y}} = \beta^*_{x,y}\left\{1 + \frac{s^2}{\beta^{*2}_{x,y}}\right\}, \tag{2.45}$$

$$\sigma_{x,y}(s) = \sqrt{\varepsilon_{x,y}\beta_{x,y}(s)}. \tag{2.46}$$

where the β-function vicinity of the IP is changed as in Eq. (2.45). This is an important relationship for calculating the luminosity with the hourglass effect as the model includes long–range and the head-on interactions.

In addition, the Gaussian distribution in Eq. (2.39) is modified by the hourglass effect near the IP:

$$\rho_{il}(s) = \frac{1}{\sigma^*_{il}\sqrt{2\pi\left(1+\frac{s^2}{\beta^{*2}_{il}}\right)}} \exp\left(-\frac{l^2}{2\sigma^{*2}_{il}(1+\frac{s^2}{\beta^{*2}_{il}})}\right), \tag{2.47}$$

where subscriptions are $i = \{1, 2\}$ and $k = \{x, y\}$.

The luminosity formula is also changed by following the modified distribution Eq. (2.47), and the substitution and integrals are calculated step by step:

$$\mathcal{L} = \frac{N_1 N_2 f N_\mathrm{b}}{2\pi} \frac{1}{\pi\sigma_{1s}\sigma_{2s}} \iint_{-\infty}^{\infty} ds ds_0 \left\{ \frac{\exp\left(-\{\frac{(s-s_0)^2}{2\sigma^2_{1s}} + \frac{(s-s_0)^2}{2\sigma^2_{2s}}\}\right)}{\sqrt{(\sigma^2_{1x}+\sigma^2_{2x})(\sigma^2_{1y}+\sigma^2_{2y})}} \right\} \tag{2.48}$$

$$= \frac{N_1 N_2 f N_\mathrm{b}}{2\pi} \frac{1}{\pi\sigma_{1s}\sigma_{2s}} \iint_{-\infty}^{\infty} ds ds_0 \left\{ \frac{\exp\left(-\{\frac{(s-s_0)^2}{2\sigma^2_{1s}} + \frac{(s-s_0)^2}{2\sigma^2_{2s}}\}\right)}{\Sigma} \right\} \tag{2.49}$$

$$= \frac{N_1 N_2 f N_\mathrm{b}}{2\pi} \frac{1}{\pi\sigma_{1s}\sigma_{2s}} \int_{-\infty}^{\infty} ds \left\{ \sqrt{\frac{2}{\pi(\sigma^2_{1s}+\sigma^2_{2s})}} \frac{\exp\left(-\frac{s^2}{\sigma^2_{1s}+\sigma^2_{2s}}\right)}{\Sigma} \right\} \tag{2.50}$$

$$= \frac{N_1 N_2 f N_\mathrm{b}}{2\pi\sqrt{(\sigma^{*2}_{1x}+\sigma^{*2}_{2x})(\sigma^{*2}_{1y}+\sigma^{*2}_{2y})}} \frac{1}{\sqrt{\pi}} \int_{-\infty}^{\infty} dt \left\{ \frac{e^{-t^2}}{\sqrt{(1+\frac{t^2}{t^2_x})(1+\frac{t^2}{t^2_y})}} \right\} \tag{2.51}$$

$$\approx \frac{N_1 N_2 f N_\mathrm{b} t_y e^{\frac{1}{2}t^2_y}}{\sqrt{4\pi^3(\sigma^{*2}_{1x}+\sigma^{*2}_{2x})(\sigma^{*2}_{1y}+\sigma^{*2}_{2y})}} \cdot K_0\left(\frac{1}{2}t^2_y\right), \tag{2.52}$$

where K_0 is the modified Bessel function of the second kind. Between Eq. (2.48)

and (2.49), the Σ is defined by:

$$\Sigma = \sqrt{\left\{\sigma_{1x}^{*2}\left(1+\frac{s^2}{\beta_{1x}^{*2}}\right)+\sigma_{2x}^{*2}\left(1+\frac{s^2}{\beta_{2x}^{*2}}\right)\right\}\left\{\sigma_{1y}^{*2}\left(1+\frac{s^2}{\beta_{1y}^{*2}}\right)+\sigma_{2y}^{*2}\left(1+\frac{s^2}{\beta_{2y}^{*2}}\right)\right\}}.s \tag{2.53}$$

Between Eq. (2.49) and (2.50), Gaussian integral is applied to the equation as:

$$\frac{1}{\pi\sigma_{1s}\sigma_{2s}}\int_{-\infty}^{\infty} ds_0 \left\{\exp\left(-\left[\frac{(s-s_0)^2}{2\sigma_{1s}^2}+\frac{(s-s_0)^2}{2\sigma_{2s}^2}\right]\right)\right\} \tag{2.54}$$

$$= \frac{1}{\pi\sigma_{1s}\sigma_{2s}}\sqrt{\frac{\pi}{(2\sigma_{1s})^{-2}+(2\sigma_{2s})^{-2}}}\exp\left(\frac{(\sigma_{1s}^{-2}-\sigma_{2s}^{-2})^2 s^2 - 2(\sigma_{1s}^{-2}+\sigma_{2s}^{-2})^2 s^2}{2(\sigma_{1s}^{-2}+\sigma_{2s}^{-2})}\right) \tag{2.55}$$

$$= \sqrt{\frac{2}{\pi(\sigma_{1s}^2+\sigma_{2s}^2)}}\exp\left(-\frac{2s^2}{\sigma_{1s}^2+\sigma_{2s}^2}\right). \tag{2.56}$$

Between Eq. (2.50) and (2.51), following relations are used for each nonation of t, t_x, and t_y:

$$t \equiv \sqrt{\frac{2}{\sigma_{1s}^2+\sigma_{2s}^2}}\cdot s, \tag{2.57}$$

$$t_x^2 = \frac{2(\sigma_{1x}^{*2}+\sigma_{2x}^{*2})}{(\sigma_{1s}^{*2}+\sigma_{2s}^{*2})(\frac{\sigma_{1x}^{*2}}{\beta_{1x}^{*2}}+\frac{\sigma_{2x}^{*2}}{\beta_{2x}^{*2}})}, \tag{2.58}$$

$$t_y^2 = \frac{2(\sigma_{1y}^{*2}+\sigma_{2y}^{*2})}{(\sigma_{1s}^{*2}+\sigma_{2s}^{*2})(\frac{\sigma_{1y}^{*2}}{\beta_{1y}^{*2}}+\frac{\sigma_{2y}^{*2}}{\beta_{2y}^{*2}})}. \tag{2.59}$$

Between Eq. (2.51) and (2.52), assuming $t_x \leq t_y$, the integral for t is approximated

as:

$$\frac{1}{\sqrt{\pi}}\int_{-\infty}^{\infty} dt \left\{ \frac{e^{-t^2}}{\sqrt{(1+\frac{t^2}{t_x^2})(1+\frac{t^2}{t_y^2})}} \right\} \approx \frac{1}{\sqrt{\pi}}\int_{-\infty}^{\infty} dt \left\{ \frac{e^{-t^2}}{\sqrt{1+\frac{t^2}{t_y^2}}} \right\} \tag{2.60}$$

$$= \frac{1}{\sqrt{\pi}} t_y e^{\frac{1}{2}t_y^2} K_0(\frac{1}{2}t_y^2), \tag{2.61}$$

by linear approximation of Taylor series for t where $1 \gg t_y/t_x$, and then the K_0 is the integral of the cosine expressed by:

$$K_0(x) = \int_0^{\infty} dt\{\cos(x\sinh(t))\} = \int_0^{\infty} dt \left\{ \frac{\cos(xt)}{\sqrt{t^2+1}} \right\}. \tag{2.62}$$

2.2.3 Crossing Angle Collision with the Hourglass effect Model

As discussed in Section 2.1.2, crossing angle collision is one of approaches that can be used to avoid the beam–beam limit caused by the hourglass effect. In the case of the crossing angle collision, the coordinates in the equation of motion are also the difference between the two beams[27]. Figure 2.6 shows a schematic illustration of the coordinate relationship between the two beams. As the beam axis is tilted in the $x-s$ plane by the rotation matrix of angle $\theta/2$, the coordinates of both beams satisfy

$$\begin{cases} x_1 &= x_0\cos\frac{\theta}{2} - s_0\sin\frac{\theta}{2} \\ \\ s_1 &= s_0\cos\frac{\theta}{2} + x_0\sin\frac{\theta}{2} \end{cases}, \tag{2.63}$$

$$\begin{cases} x_2 &= x_0\cos\frac{\theta}{2} + s_0\sin\frac{\theta}{2} \\ \\ s_2 &= s_0\cos\frac{\theta}{2} - x_0\sin\frac{\theta}{2} \end{cases}, \tag{2.64}$$

where $(x,\ s)$ is the reference coordinates of collision center.

The relative velocities are different from cases where there is no crossing angle

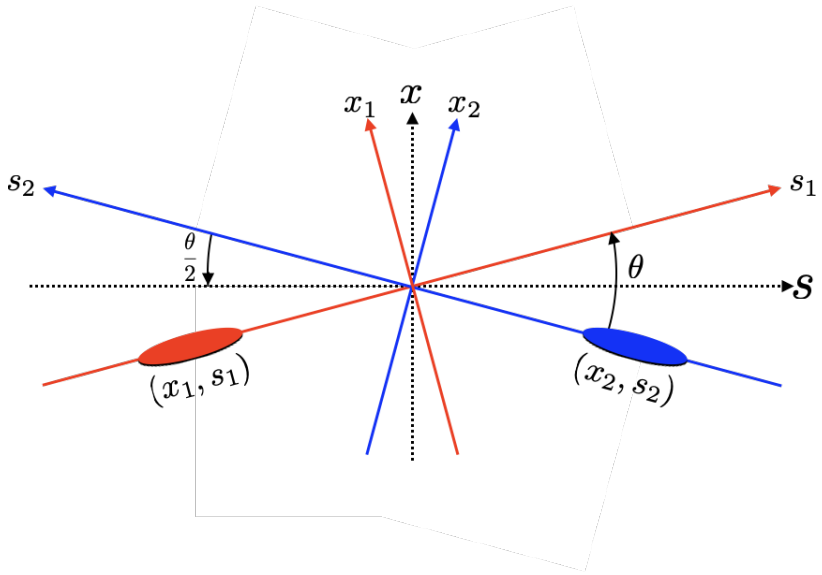

Figure 2.6: Coordinates with crossing angle θ (red and blue lines) and reference coordinates(dotted lines)

case: $|\vec{v}_1| = |\vec{v}_2| = v$, and the kinematic factor Eq. (2.36) is modified to

$$\mathcal{K} = \sqrt{(\vec{v}_1 - \vec{v}_2)^2 - \frac{(\vec{v}_1 \times \vec{v}_2)^2}{c^2}} \tag{2.65}$$

$$= \sqrt{(2v\cos\frac{\theta}{2})^2 \frac{v^4}{c^2}\sin^2\theta} \tag{2.66}$$

$$= 2v\cos\frac{\theta}{2}\sqrt{1 - \frac{v^2}{c^2}\sin^2\frac{\theta}{2}} \tag{2.67}$$

$$\approx 2v\cos^2\frac{\theta}{2}, \tag{2.68}$$

where the approximation between Eq. (2.66) and (2.68) can occur under conditions where $v/c \simeq 1$, as seen in lepton colliders. Using Eq. (2.66) and (2.68), the luminosity

formula can be applied to the crossing angle collision:

$$\mathcal{L} = \frac{8\pi^3\mathcal{A}}{\cos\frac{\theta}{2}}\sqrt{1-\frac{v^2}{c^2}\sin^2\frac{\theta}{2}}\iiiint_{-\infty}^{\infty} dxdydsds_0\left\{\prod_{i,k}\rho_{ik}(k_i)\rho_{is}(s_i \mp s_0)\right\} \tag{2.69}$$

$$\approx 8\pi^3\mathcal{A}\iiiint_{-\infty}^{\infty} dxdydsds_0\left\{\prod_{i,k}\rho_{ik}(k_i)\rho_{is}(s_i \mp s_0)\right\} \tag{2.70}$$

$$= \mathcal{A}\iiiint_{-\infty}^{\infty} dxdydsds_0\left\{\prod_{i,k}\frac{\exp\left(-\frac{k_i^2}{2\sigma_{ik}^2(s_i)}\right)}{\sigma_{ik}(s_i)}\frac{\exp\left(-\frac{(s_i\mp s_0)^2}{2\sigma_{is}^2}\right)}{\sigma_{is}}\right\} \tag{2.71}$$

$$= \mathcal{A}\iiint_{-\infty}^{\infty} dxdsds_0\left\{\sqrt{\frac{2\pi}{\sum_i\sigma_{iy}^2(s_i)}}\prod_i\frac{\exp\left(-\frac{x_i^2}{2\sigma_{ix}^2(s_i)}\right)}{\sigma_{ix}(s_i)}\frac{\exp\left(-\frac{(s_i\mp s_0)^2}{2\sigma_{is}^2}\right)}{\sigma_{is}}\right\} \tag{2.72}$$

$$= \mathcal{A}\iint_{-\infty}^{\infty} dxds\left\{\frac{2\pi\exp\left(-\frac{(\sum_i s_i)^2}{2(\sum_i\sigma_{is}^2)}\right)}{\sqrt{(\sum_i\sigma_{iy}^2(s_i))(\sum_i\sigma_{is}^2)}}\prod_i\frac{\exp\left(-\frac{x_i^2}{2\sigma_{ix}^2(s_i)}\right)}{\sigma_{ix}(s_i)}\right\} \tag{2.73}$$

$$= \mathcal{A}\iint_{-\infty}^{\infty} dxds\left\{\frac{2\pi\exp\left(-\frac{(\sum_i s_i)^2}{2(\sum_i\sigma_{is}^2)}\right)}{\sqrt{\left(\sum_i\sigma_{iy}^{*2}(1+\frac{s_i^2}{\beta_{iy}^{*2}})\right)(\sum_i\sigma_{is}^2)}}\prod_i\frac{\exp\left(-\frac{x_i^2}{2\sigma_{ix}^{*2}(1+\frac{s_i^2}{\beta_{ix}^{*2}})}\right)}{\sigma_{ix}^*\sqrt{1+\frac{s_i^2}{\beta_{ix}^{*2}}}}\right\}, \tag{2.74}$$

where $\{i = 1, 2\}$ and $\{k = x, y\}$, then the sign $\mp = \{-, +\}$ of s_0 corresponds to $\{i = 1, 2\}$, respectively. The coefficient $\mathcal{A} \equiv 2N_1N_2fN_{\rm b}\cos^2\frac{\theta}{2}/8\pi^3$. Furthermore, Eq. (2.74) can be separated into an IP constant factor and a collision condition factor, which is also known as the geometric factor. Now we define the parameter $\mathcal{R}$

as a collision condition factor. Then Eq. (2.74) can be rewritten as

$$\mathcal{L} = \frac{N_1 N_2 f N_{\rm b}}{2\pi\sqrt{\sigma_{1x}^{*2}+\sigma_{2x}^{*2}}\sqrt{\sigma_{1y}^{*2}+\sigma_{2y}^{*2}}} \cdot \mathcal{R}_{\rm H\theta}, \tag{2.75}$$

$$\begin{aligned}\mathcal{R}_{\rm H\theta} = {} & \frac{\cos^2\frac{\theta}{2}\prod_k \sqrt{\sum_i \sigma_{ik}^{*2}}}{\pi\sqrt{\sum_i \sigma_{is}^{*2}}} \\ & \times \iint_{-\infty}^{\infty} dxds \left\{ \frac{\exp\left(-\frac{(\sum_i s_i)^2}{2(\sum_i \sigma_{is}^2)}\right)}{\sqrt{\sum_i \sigma_{iy}^{*2}\left(1+\frac{s_i^2}{\beta_{iy}^{*2}}\right)}} \cdot \prod_{i=\{1,2\}} \frac{\exp\left(-\frac{x_i^2}{2\sigma_{ix}^{*2}\left(1+\frac{s_i^2}{\beta_{ix}^{*2}}\right)}\right)}{\sigma_{ix}^{*}\sqrt{1+\frac{s_i^2}{\beta_{ix}^{*2}}}} \right\},\end{aligned} \tag{2.76}$$

where Hθ of $\mathcal{R}_{\rm H\theta}$ is equal to the geometric factor of the luminosity for the Gaussian crossing angle collision with the hourglass effect.

Equation (3.78) is the standard formula used for crossing angles with the hourglass effect. The estimated luminosity of design parameter is calculated on the basis of this formulae as the geometric luminosity, which is the ideal luminosity. In the actual situation, several type of the luminosity degradation is affected by the linear optics aberration, the nonlinear effect , and the beam–beam effect caused by collisions. In the next subsection, the influence of beam–beam effect on parameters of the single beam motion will be discussed. In the next section, the degradation model under existence of linear optics aberration is discussed.

2.3 The Beam–Beam Tune Shift

The source of beam-beam tune shift is a result of the electromagnetic interaction between two particles[28, 29]. As discussed in Sec. 2.1.2, one approach used for evaluating the effect of a beam–beam kick is calculating the kick force under several assumptions. The general conditions underlying the relationship between the two coordinates of the incoming beams are given in Fig. 2.7. The coulomb force of the reference bunch affects the test particle at the IR. Typically, in the case of a lepton collider, the coordinates are transformed via a Lorentz boost from the perspective of the laboratory system. The transformation of these coordinates is as follows:

$$\begin{cases} x_1 = x_2 \cos\theta + s_2 \sin\theta \\ \\ s_1 = s_2 \cos\theta - x_2 \sin\theta \end{cases} \tag{2.77}$$

$$\begin{cases} x_2 = x_1 \cos\theta - s_1 \sin\theta \\ \\ s_2 = s_1 \cos\theta + x_1 \sin\theta \end{cases} \tag{2.78}$$

Assuming a Gaussian distribution for a bunch in three-dimensional space and no hourglass effect, the electrostatic potential at the beam coordinates is described by

$$U(\vec{r}_1) = \frac{1}{4\pi\varepsilon_0} \int d\vec{r}_1' \left\{ \frac{\rho_1(\vec{r}_1')}{|\vec{r}_1 - \vec{r}_1'|} \right\} \tag{2.79}$$

$$\rho_1(\tilde{x}_1, \tilde{y}_1, \tilde{s}_1) = \frac{N_1 e_1}{\sqrt{2\pi}^3 \sigma_{1\tilde{x}} \sigma_{1\tilde{y}} \sigma_{1\tilde{s}}} \exp\left(-\frac{\tilde{x}_1^2}{2\sigma_{1\tilde{x}}^2} - \frac{\tilde{y}_1^2}{2\sigma_{1\tilde{y}}^2} - \frac{\tilde{s}_1^2}{2\sigma_{1\tilde{s}}^2} \right) \tag{2.80}$$

where $\vec{\tilde{r}}_1 = (\tilde{x}_1, \tilde{y}_1, \tilde{s}_1)$ is the position vector of the reference bunch from the crossing point and the tilde indicates the same quantity at the normal beam coordinates.

The integral function of Eq. (2.79) can be represented as a type of definite integral. Following the Green function method in Appendix **??**, which is equal to Eq. (2.8),

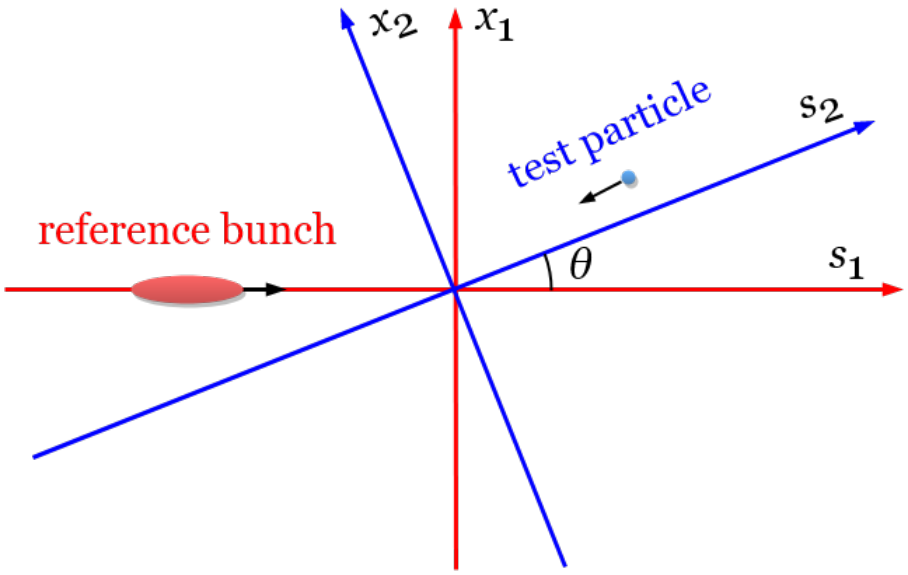

Figure 2.7: Relationship of coordinated between reference bunch and an incoming particle with crossing angle θ.

Eq. (2.79) can be rewritten:

$$U(\tilde{x}_1,\tilde{y}_1,\tilde{s}_1) = \frac{1}{4\sqrt{\pi}^3\varepsilon_0}\int_0^\infty dt\left\{\frac{1}{\sqrt{t}^3}\int d\vec{\tilde{r}}_1'\left\{\rho_1(\vec{\tilde{r}}_1')\exp\left(-\frac{|\vec{\tilde{r}}_1-\vec{\tilde{r}}_1'|^2}{t}\right)\right\}\right\} \tag{2.81}$$

$$= \frac{N_1 e_1}{8\sqrt{2}\pi^3\varepsilon_0\sigma_{1\tilde{x}}\sigma_{1\tilde{y}}\sigma_{1\tilde{s}}} \tag{2.82}$$
$$\times\int_0^\infty dt\left\{\frac{1}{\sqrt{t}^3}\prod_{k=\{x,y,s\}}\left[\int_{-\infty}^\infty d\tilde{k}_1'\left\{\exp\left(-\frac{\tilde{k}_1'^2}{2\sigma_{1\tilde{k}}^2}-\frac{(\tilde{k}_1-\tilde{k}_1')^2}{t}\right)\right\}\right]\right\}$$

$$= \frac{N_1 e_1}{4\sqrt{\pi}^3\varepsilon_0}\int_0^\infty dt\left\{\prod_{k=\{x,y,s\}}\left[\frac{\exp\left(-\frac{\tilde{k}_1^2}{2\sigma_{1\tilde{k}}^2+t}\right)}{\sqrt{2\sigma_{1\tilde{k}}^2+t}}\right]\right\} \tag{2.83}$$

The Lorentz Transformation

The relationship between non-relativistic coordinates and relativistic coordinates is described by

$$\begin{cases} \bar{x} = & x,\ \bar{\sigma_x} = \sigma_x \\ \bar{y} = & y,\ \bar{\sigma_y} = \sigma_y \\ \bar{s} = & \gamma(s - c\tau),\ \bar{\sigma_s} = \gamma\sigma_s \end{cases} \tag{2.84}$$

, which is known as the Lorentz transformation. For relativistic particles, the beam–beam kick potential in Eq. (2.83) is transformed to

$$U(\tilde{x}_1, \tilde{y}_1, \tilde{s}_1) = \frac{N_1 e_1}{4\sqrt{\pi}^3 \varepsilon_0} \int_0^\infty dt \left\{ \frac{\exp\left(-\frac{\gamma_1^2(\tilde{k}_1 - c\tau)^2}{2\gamma_1^2\sigma_{1\tilde{s}}^2 + t}\right)}{\sqrt{2\gamma_1^2\sigma_{1\tilde{s}}^2 + t}} \prod_{k=\{x,y\}} \left[\frac{\exp\left(-\frac{\tilde{k}_1^2}{2\sigma_{1\tilde{k}}^2 + t}\right)}{\sqrt{2\sigma_{1\tilde{k}}^2 + t}} \right] \right\} \tag{2.85}$$

by using Eq. (2.84). The electromagnetic fields of the beam–beam kick can thus be derived as

$$E_{1x} = -\gamma_1 \frac{\partial U}{\partial x_1} \tag{2.86}$$

$$= \frac{\gamma_1 N_1 e_1 x_1}{2\pi\varepsilon_0\sqrt{\pi}} \int_0^\infty dt \left\{ \frac{\exp\left(-\frac{\gamma_1^2(\tilde{k}_1 - c\tau)^2}{2\gamma_1^2\sigma_{1\tilde{s}}^2 + t}\right)}{(2\sigma_{1\tilde{s}}^2 + t)\sqrt{2\gamma_1^2\sigma_{1\tilde{s}}^2 + t}} \prod_{k=\{x,y\}} \left[\frac{\exp\left(-\frac{\tilde{k}_1^2}{2\sigma_{1\tilde{k}}^2 + t}\right)}{\sqrt{2\sigma_{1\tilde{k}}^2 + t}} \right] \right\} \tag{2.87}$$

$$E_{1y} = -\gamma_1 \frac{\partial U}{\partial y_1} \tag{2.88}$$

$$= \frac{\gamma_1 N_1 e_1 y_1}{2\pi\varepsilon_0\sqrt{\pi}} \int_0^\infty dt \left\{ \frac{\exp\left(-\frac{\gamma_1^2(\tilde{k}_1 - c\tau)^2}{2\gamma_1^2\sigma_{1\tilde{s}}^2 + t}\right)}{(2\sigma_{1\tilde{s}}^2 + t)\sqrt{2\gamma_1^2\sigma_{1\tilde{s}}^2 + t}} \prod_{k=\{x,y\}} \left[\frac{\exp\left(-\frac{\tilde{k}_1^2}{2\sigma_{1\tilde{k}}^2 + t}\right)}{\sqrt{2\sigma_{1\tilde{k}}^2 + t}} \right] \right\} \tag{2.89}$$

and

$$B_{1x} = -\frac{1}{c}E_{1y} \tag{2.90}$$

$$B_{1y} = \frac{1}{c}E_{1x} \tag{2.91}$$

.

Transformation of the coordinates of a test particle to the reference bunch

Generally, the coordinates of a test particle and a reference bunch are different, as seen in Fig. 2.7, meaning that the coordinates of the test particle require transformation. The relationship is

$$\begin{cases} x_1(t) = & x_2 cos\theta + (s_1 - c\tau)\sin\theta \\ y_1(t) = & y_2 \\ s_1(t) = & (s_2 - c\tau)\cos\theta - x_-\sin\theta \end{cases} \tag{2.92}$$

from which the relationship with velocity is found via:

$$\begin{cases} v_{1x} = & -c\sin\theta \\ v_{1y} = & 0 \\ v_{1s} = & -c\cos\theta \end{cases} \tag{2.93}$$

where $v_2 \sim c$ because relativistic conditions are assumed. The transformation of the test particle is then considered, as transforming the kick force is easier than transforming relativistic fields; thus, this transformation is used because it yields the same result as the transformation of a reference bunch. The Lorentz force $\vec{F}_1 =$

(F_{1x}, F_{1y}, F_{1s}) of the transformed system is described by

$$\begin{cases} F_{1x} = & e_2(E_{1x} - v_{1s}B_{1y}) = e_2E_{1x}(1+\cos\theta) \\ F_{1y} = & e_2(E_{1y} + v_{1s}B_{1x}) = e_2E_{1y}(1+\cos\theta) \\ F_{1s} = & e_2v_{1x}B_{1y}) = -e_2E_{1x}\sin\theta \end{cases} \tag{2.94}$$

. The impact of a beam–beam kick force on a test particle is equal to the kick force that is projected back towards the coordinates of the test particle:

$$\begin{cases} F_{2x} = & F_{1x}\cos\theta - F_{1s}\sin\theta \\ F_{2y} = & F_{1y} \\ F_{2s} = & F_{1x}\sin\theta + F_{1s}\cos\theta \end{cases} \tag{2.95}$$

. The deviation in the momentum of the test particle in each direction is obtained from the integral of the kick force on τ:

$$\Delta p_{2x} = \frac{\Delta p_{2x}}{p_2} = \frac{1}{p_{2x0}}\int_{-\infty}^{\infty} d\tau\{F_{2x}\} \tag{2.96}$$

$$\Delta p_{2y} = \frac{\Delta p_{2x}}{p_2} = \frac{1}{p_{2x0}}\int_{-\infty}^{\infty} d\tau\{F_{2y}\} \tag{2.97}$$

By using Eq. (2.96) and (2.97), the tune shift formula from the perturbation theory is expressed as

$$\xi_{2x} = -\frac{\beta_{2x}}{4\pi p_{2x0}}\int_{-\infty}^{\infty} d\tau\{\frac{\partial F_{2x}}{\partial x_2}\} \tag{2.98}$$

$$\xi_{2y} = -\frac{\beta_{2y}}{4\pi p_{2y0}}\int_{-\infty}^{\infty} d\tau\{\frac{\partial F_{2y}}{\partial y_2}\} \tag{2.99}$$

To substitute (F_{2x}, F_{2y}) as the actual form, we transform Eq. (2.94) into

$$F_{2x} = F_{1x} = e_2(1+\cos\theta)\frac{\gamma_1 N_1 e_1[x_2\cos\theta + (s_2 - c\tau)\sin\theta]}{2\pi\varepsilon_0\sqrt{\pi}} \times \int_0^\infty dt \left\{ \frac{\exp\left(\frac{[x_2\cos\theta+(s_2-c\tau)\sin\theta]^2}{2\sigma_{1x}^2+t} - \frac{y_2^2}{2\sigma_{1y}^2+t} - \frac{\gamma_1^2[(s_2-c\tau)\cos\theta - x_2\sin\theta - c\tau]^2}{2\gamma_1^2\sigma_{1s}+t}\right)}{(2\sigma_{1x}+t)\sqrt{(2\sigma_{1x}^2+t)(2\sigma_{1y}^2+t)(2\gamma_1\sigma_{1s}^2+t)}} \right\} \tag{2.100}$$

$$F_{2y} = F_{1y} = e_2(1+\cos\theta)\frac{\gamma_1 N_1 e_1 y_2}{2\pi\varepsilon_0\sqrt{\pi}} \times \int_0^\infty dt \left\{ \frac{\exp\left(\frac{[x_2\cos\theta+(s_2-c\tau)\sin\theta]^2}{2\sigma_{1x}^2+t} - \frac{y_2^2}{2\sigma_{1y}^2+t} - \frac{\gamma_1^2[(s_2-c\tau)\cos\theta - x_2\sin\theta - c\tau]^2}{2\gamma_1^2\sigma_{1s}+t}\right)}{(2\sigma_{1y}+t)\sqrt{(2\sigma_{1x}^2+t)(2\sigma_{1y}^2+t)(2\gamma_1\sigma_{1s}^2+t)}} \right\} \tag{2.101}$$

with the derivatives

$$\frac{\partial F_{2x}}{\partial x_2} = e_2(1+\cos\theta)\frac{\gamma_1 N_1 e_1}{2\pi\varepsilon_0\sqrt{\pi}} \times \int_0^\infty dt \left\{ \left\{ \cos\theta + [x_2\cos\theta + (s_2-c\tau)\sin\theta]\frac{-2\cos\theta[x_2\cos\theta + (s_2-c\tau)\sin\theta]}{2\sigma_{1x}^2+t} + [x_2\cos\theta + (s_2-c\tau)\sin\theta]\frac{2\gamma_1^2\sin\theta[(s_12-c\tau)\cos\theta - x_2\sin\theta - c\tau]}{2\gamma_1^2\sigma_{1s}^2+t} \right\} \times \frac{\exp\left(\frac{[x_2\cos\theta+(s_2-c\tau)\sin\theta]^2}{2\sigma_{1x}^2+t} - \frac{y_2^2}{2\sigma_{1y}^2+t} - \frac{\gamma_1^2[(s_2-c\tau)\cos\theta - x_2\sin\theta - c\tau]^2}{2\gamma_1^2\sigma_{1s}+t}\right)}{(2\sigma_{1x}+t)\sqrt{(2\sigma_{1x}^2+t)(2\sigma_{1y}^2+t)(2\gamma_1\sigma_{1s}^2+t)}} \right\} \tag{2.102}$$

$$\frac{\partial F_{2y}}{\partial y_2} = e_2(1+\cos\theta)\frac{\gamma_1 N_1 e_1}{2\pi\varepsilon_0\sqrt{\pi}}\left(1 - \frac{2y_2^2}{2\sigma_{1y}^2+t}\right) \times \int_0^\infty dt \left\{ \frac{\exp\left(\frac{[x_2\cos\theta+(s_2-c\tau)\sin\theta]^2}{2\sigma_{1x}^2+t} - \frac{y_2^2}{2\sigma_{1y}^2+t} - \frac{\gamma_1^2[(s_2-c\tau)\cos\theta - x_2\sin\theta - c\tau]^2}{2\gamma_1^2\sigma_{1s}+t}\right)}{(2\sigma_{1y}^2+t)\sqrt{(2\sigma_{1x}^2+t)(2\sigma_{1y}^2+t)(2\gamma_1\sigma_{1s}^2+t)}} \right\} \tag{2.103}$$

The case of $\beta_{2x} = \beta_{2y} = const.$

if it is assumed that $\beta_{2x} = \beta_{2y} = const.$, a different parametrization can be used to improve clarity. The horizontal beam–beam parameter of a constant beta-function

at the collision point is represented by

$$\begin{aligned}\xi_{2x} =& \frac{N_1 r_e \beta_{2x}}{2\pi} \int_0^\infty dt \left\{ \frac{e^{-\frac{y_2^2}{2\sigma_{1y}^2+t}}}{\sqrt{2\sigma_{1y}^2+t}} \right. \\ & \times \frac{1}{(2\sigma_{1s}^2 \tan^2\frac{\theta}{2} + 2\sigma_{1x} + t + \frac{t}{\gamma_1^2}\tan^2\frac{\theta}{2})^{3/2}} \\ & \times \exp\left(-\frac{(s_2 \sin\theta + (1+\cos\theta x_2))^2}{(1+\cos\theta)^2(2\sigma_{1s}^2\tan^2\frac{\theta}{2} + 2\sigma_{1x}^2 + t + \frac{t}{\gamma_1^2}\tan^2\frac{\theta}{2})} \right) \\ & \left. \times \left\{ 1 - \frac{2(s_2\sin\theta + (1+\cos\theta)x_2)^2}{(1+\cos\theta)^2(2\sigma_{1s}^2\tan^2\frac{\theta}{2} + 2\sigma_{1x}^2 + t + \frac{t}{\gamma_1^2}\tan^2\frac{\theta}{2})} \right\} \right\}, \end{aligned} \tag{2.104}$$

where $p_0 = \gamma_2 m_0 c$, $r_e = e^2/(4\pi\varepsilon_0 m_0 c^2)$, and $e_1 = e_2 = e$ for each parameter. On the other hand, the vertical beam–beam parameter is

$$\begin{aligned}\int_{-\infty}^{\infty} dt \left\{ \frac{\partial F_{2y}}{\partial y_2} \right\} =& e_2(1+\cos\theta)\frac{\gamma_1 N_1 e_1}{2\pi^{3/2}\varepsilon_0 c} \\ & \times \int_{-\infty}^{\infty} dt \left\{ \left(1 - \frac{2y_2^2}{2\sigma_{1y}^2+t} \right) \right. \\ & \left. \times \frac{\exp\left(-\frac{y_2^2}{2\sigma_{1y}^2+t}\right)}{(2\sigma_{1y}^2+t)\sqrt{(2\sigma_{1x}^2+t)(2\sigma_{1y}^2+t)(2\gamma_1^2\sigma_{1s}^2+t)}} \right\} \\ & \times \int_{-\infty}^{\infty} d(c\tau) \left\{ \exp\left(-\frac{(C+Dc\tau)^2}{H} - \frac{\gamma_1^2(F+G+c\tau)^2}{I} \right) \right\}. \end{aligned} \tag{2.105}$$

The complete integral for $c\tau$ in Eq. (2.105) can thus be written as

$$\begin{aligned}\int_{-\infty}^{\infty} d(c\tau) \left\{ \exp\left(-\frac{(C+Dc\tau)^2}{H} - \frac{\gamma_1^2(F+G+c\tau)^2}{I} \right) \right\} &= \frac{\exp\left(-\frac{\gamma_1^2(DF-CG)^2}{D^2I+G^2H\gamma_1} HI\sqrt{\pi} \right)}{\sqrt{HI(D^2I+G^2H\gamma_1^2)}} \\ =& \frac{\sqrt{\pi}}{\gamma_1(1+\cos\theta)} \frac{\sqrt{(2\sigma_{1y}^2+t)(2\gamma_1^2\sigma_{1s}^2+t)}}{\sqrt{2\sigma_{1s}^2\tan^2\frac{\theta}{2} + 2\sigma_{1x}^2 + t + \frac{t}{\gamma_1^2}\tan^2\frac{\theta}{2}}} \\ & \times \exp - \frac{(s_2\sin\theta + (1+\cos\theta)x_2)^2}{(1+\cos\theta)^2(2\sigma_{1s}^2\tan^2\frac{\theta}{2} + 2\sigma_{1x}^2 + t + \frac{t}{\gamma_1^2}\tan^2\frac{\theta}{2})}. \end{aligned} \tag{2.106}$$

As a result, the vertical beam-beam parameter is represented by

$$\xi_{2y} = \frac{N_1 r_e \beta_{2y}}{2\pi\gamma_2} \int_{-\infty}^{\infty} dt \left\{ \frac{\exp -\frac{y_2^2}{2\sigma_{1y}^2+t}}{(2\sigma_{1y}^2+t)^{3/2}} \right. \\ \left. \times \frac{\exp\left(-\frac{[s_2\sin\theta+(1+\cos\theta)x_2]^2}{(1+\cos\theta)^2(2\sigma_{1s}^2\tan^2\frac{\theta}{2}+2\sigma_{1x}^2+t+\frac{t}{\gamma_1^2}\tan^2\frac{\theta}{2})} \right)}{\sqrt{2\sigma_{1s}^2\tan^2\frac{\theta}{2}+2\sigma_{1x}^2+t+\frac{t}{\gamma_1^2}\tan^2\frac{\theta}{2}}} \right\}. \quad (2.107)$$

These two beam-beam parameters from Eq. (2.104) and (2.107) are formulae without any approximation. Under the assumptions of several conditions, Eq. (2.104) and (2.107) can be simplified, as seen in the following subsections.

2.3.1 Beam–Beam Tune Shift with x=y=s=0

The condition $x = y = s = 0$ points to means the situation in which there is zero offset, which corresponds to the exact of the IP. Thus, Eq. (2.104) and (2.107) becomes

$$\xi_{2x} = \frac{N_1 r_e \beta_{2x}}{2\pi\gamma_2} \int_0^{\infty} dt \left\{ \frac{1}{\sqrt{2\sigma_{1y}^2+t}(2\sigma_{1s}^2\tan^2\frac{\theta}{2}+2\sigma_{1x}^2+t+\frac{t}{\gamma_1^2}\tan^2\frac{\theta}{2})^{3/2}} \right\}, \quad (2.108)$$

$$\xi_{2y} = \frac{N_1 r_e \beta_{2y}}{2\pi\gamma_2} \int_0^{\infty} dt \left\{ \frac{1}{(2\sigma_{1y}^2+t)^{3/2}\sqrt{2\sigma_{1s}^2\tan^2\frac{\theta}{2}+2\sigma_{1x}^2+t+\frac{t}{\gamma_1^2}\tan^2\frac{\theta}{2}}} \right\}, \quad (2.109)$$

as $x_1 = x_2 = 0$ and $y_1 = y_2 = 0$ in each of the equations.

This tune shift representation is considered for only ideal situation. In the actual operation, beam trajectory can be disturbed by several error source in the ring. In that error case, independent discussion for each situation should be required.

2.4 Numerical Simulations of Beam–Beam Interaction

2.4.1 Introduction of the Beam–Beam Simulation

With the simple formulae used for the beam dynamics in the storage ring, beam–beam interactions are not considered useful for understanding global properties. However, many of the issues that surround circular colliders are caused by beam–beam interactions, including the growth of emittance and a reduction in the lifetime of the beams. These problems are critical sources of the limitations in the luminosity of particle colliders; it is therefore critical that the effects that beam–beam interaction have on IP beam dynamics are calculated. To study the effects of machine imperfections and beam–beam interactions, several simulations have been developed [30, 31, 30, 32].

In collider simulations, two beams that are moving in opposite directions are represented by macroparticles, as shown in Fig 3.1. The macroparticles consist of the same charge to mass ratio as the particles in the accelerator. Simulations of collisions usually only deal with colliding bunches, so two important parameters that are used to describe beam intensity are the number of particles within a bunch and the revolution frequency. According to these two parameters and the assumed bunch distribution, the charge ratio of a macroparticle can be estimated.

A six-dimensional bunch distribution is used to simulate the long-term evolution of a beam. The transverse and longitudinal motions of the beam are simulated using linear and nonlinear transfer maps. When the Hamiltonian can be written as the sum of two terms, the transfer maps constructed by the splitting method are generally represented as an action of the Hamiltonian on which the Lie transformation is applied, as follows:

$$e^{-L:\mathcal{H}:} = e^{-L:\mathcal{H}_1+\mathcal{H}_2:} \tag{2.110}$$

$$\approx e^{-L:\mathcal{H}_1:}e^{-L:\mathcal{H}_2:}, \tag{2.111}$$

where L is the length of the component and $\mathcal{H}$ is the Hamiltonian of the component, which can be represented by the sum of two terms; $\mathcal{H} = \mathcal{H}_1 + \mathcal{H}_2$. As an example, for a sextupole magnet with one-degree of freedom, the Hamiltonian with a relativistic limit $\gamma_0 \longrightarrow \infty$ is given by

$$\mathcal{H} = -\sqrt{1 - p_x^2} + \frac{1}{6}k_2 x^3. \tag{2.112}$$

Because this Hamiltonian can be written by splitting the representation into two

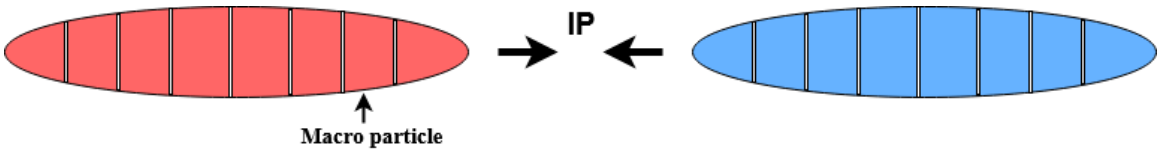

Figure 2.8: An image of bunches that consist of macro particles moving in opposite directions.

separate Hamiltonians:

$$\mathcal{H}_1 \equiv -\sqrt{1-p_x^2} \tag{2.113}$$

$$\mathcal{H}_2 \equiv \frac{1}{6}k_2 x^3, \tag{2.114}$$

the Lie transformation $e^{-L:\mathcal{H}:}$, when applied to the physical variables of horizontal motion, can be written as:

$$e^{-L:\mathcal{H}:}\begin{pmatrix} x \\ p_x \end{pmatrix} \approx e^{-L:\mathcal{H}_1:}e^{-L:\mathcal{H}_2:}\begin{pmatrix} x \\ p_x \end{pmatrix} \tag{2.115}$$

$$= e^{-L:\mathcal{H}_1:}\begin{pmatrix} x \\ p_x - \frac{1}{2}k_2 L x^2 \end{pmatrix} \tag{2.116}$$

$$= \begin{pmatrix} x + \frac{Lp_x}{\sqrt{1-p_x^2}} \\ p_x - \frac{1}{2}k_2 L x^2 - \frac{k_2 L^2 x p_x}{\sqrt{1-p_x^2}} - \frac{k_2 L^3 p_x^2}{2(1-p_x^2)} \end{pmatrix}. \tag{2.117}$$

Within the linear transfer maps, the dynamic action of a particle can be represented using a six-dimensional matrix. When nonlinear effects are considered in deriving the result from a simulation of colliding beam, the representation of the Lie transformation produced by the splitting method is used as a substitute for the linear transfer matrices.

2.4.2 Formulations in the Weak-Strong Simulation

The weak-strong model assumes that the “weak" beam is affected by both the head–on collision and the long–range interactions of the beam–beam kick. On the other hand, the “strong" beam is not affected by these factors. In other words, a bunch distribution using only the “weak" beam effects is modified by beam–beam effects in every collision.

If the weak bunch conditions can be preserved during the iteration of a weak–strong model, the result can be considered as a simulation of a collision that is affected by only the beam-optical design of the accelerator. Beam dynamics can be

explained completely in six–dimensional phase space variables, so the situation at the collision point is also determined by only the six–dimensional vector of each particle. If the difference between the laboratory and the beam coordinates is taken into consideration, it is necessary to rotate the coordinates at the collision point, but the basic model is the same as single particle dynamics in a fixed frame. The method of dividing the bunch distribution into several macro particles and integrating the action of each beam kick is used. If the distribution of the charge within a bunch is Gaussian, the charge and shape of a macroparticle used for the calculation of the actions of the electromagnetic field can be defined using the sliced Gaussian. The interaction of each macroparticle at the collision point is obtained by integrating the kick force received from the opposite beam. In the collision simulation, this calculation is performed for each revolution, meaning that all the actions that occur within one revolution should be integrated around the collision point. In other words, the core part of the simulation requires only the performance of an integral describing the kick force from each direction as a function of time s.

The actual calculation process used in this study executes a loop of items 2-5 in the following list:

1. Initialization
2. Calculation of the beam–beam kick
3. Produce a map illustrating one revolution of the ring
4. Calculate the radiation damping and quantum excitation
5. Calculate the transverse wake force and chromaticity

Initialization describes the generation of macroparticles with a Gaussian distribution in six-dimensional phase space. The initial emittances of the beam are set to the nominal values. The other effects are the same as above. The luminosity is then calculated using:

$$\mathcal{L} = f_0 \int dsdzdz' \{ \int dxdy \{ \rho^+(x,y,s(z)) \rho^-(x,y,-s(z')) \times \delta(s-(z-z')/2) \} \} \tag{2.118}$$

where $\rho^{\pm}(x,y,s)$ is the charge distribution density of the $e^{\pm}$ beam. The integration is evaluated by summing the macroparticle density at each of the mesh points.

Generally, the charge distribution of a bunch within the strong beam is fixed and assumed to be Gaussian:

$$\rho = \frac{Ne}{(2\pi)^{3/2}\sigma_x\sigma_y\sigma_s}\exp\left(-\frac{x^2}{2\sigma_x^2}-\frac{y^2}{2\sigma_y^2}-\frac{s^2}{2\sigma_s^2}\right), \tag{2.119}$$

where the notation of each parameter is the same as that used in the previous sections. In this distribution, the coordinates (x, y, and s) are the physical coordinates of the rest frame in the strong beam. When only transverse beam dynamics are required, the distribution of the particles in the bunch should be integrated along the longitudinal direction, as $\rho(x,y) = \int ds\{\rho(x,y,s)\}$.

Only the longitudinal distribution is important for slicing a Gaussian bunch, which is replaced with a summation of the weighted delta functions from N_s times as

$$\rho(x,y,s) \propto \rho(s) = \frac{\exp\left(-s^2/2\sigma_s^2\right)}{\sqrt{2\pi}\sigma_s} \tag{2.120}$$

$$\rightarrow \hat{\rho}(z) = \sum_{k=-L}^{L} w_k\delta(z-z_k), \tag{2.121}$$

where $N_s \equiv 2L+1$ is the slice number within the bunch and $\sum_{k=-L}^{L} w_k = 1$. There are several slicing algorithms that may be used to produce macroparticles[33].

The first factor for consideration is the equal spacing of the slices. The location of the beam–beam kicks is equally spaced with weights that are proportional to the Gaussian density at s_k:

$$\frac{s_k}{\sigma_s} = \frac{2k}{N_s-1}\left(1+\frac{N_s-3}{12}\right) \tag{2.122}$$

$$w_k = \frac{\hat{\rho}(s_k)}{\sum_{m=-L}^{L}\hat{\rho}(s_m)}, \tag{2.123}$$

where $k = 0, \pm1, \cdots, \pm L$, $N_s \geq 3$.

The second factor for consideration is the use of slices of equal area. If the Gaussian distribution is divided into N_s slices of equal area, the macroparticles will have equal charge. The kicks are located at the center of the charge of each slice, which is the same as the center of mass. The weight function is uniform, at $w_k = 1/N_s$. The

formula for the Gaussian slice is therefore described using the error function, as

$$\frac{s_k}{\sigma_s} = \sqrt{2}\mathrm{erf}^{-1}\left(\frac{2k}{N_s}\right), \tag{2.124}$$

where k is the same as that in Eq. (3.14).

Slicing the Gaussian distribution uses the same principles as the first and second considerations mentioned above, but the kick locations are changed from the center of the slice to the edge of the slice. The formula giving the kick location is

$$\frac{s_k}{\sigma_s} = N_s[\hat{\rho}(l_k) - \hat{\rho}(l_{K+1})],(k = 1, \cdots, L), \tag{2.125}$$

$$\tag{2.126}$$

where l_k is the k–th position on the edge of the slice. Two slicing algorithms can thus be combined:

$$\frac{s_k}{\sigma_k} = \frac{1}{w_k}[\hat{\rho}(l_k) - \hat{\rho}(l_{k+1})] \tag{2.127}$$

The final consideration used in the production of a slicing algorithm is to select values for s_k and w_k such that the area enclosed by the two functions $\int_0^s ds'\{\rho(s')\}$ and $\int_0^s ds'\{\hat{\rho}(s')\}$ is minimal. These requirements lead to a set of nonlinear values for s_k and w_k in the algorithm "Combination method", which is most easily solved by iteration. Table 3.1 lists the values of z_k and w_k for five slicing patterns when $N_s = 5$.

	# 1	# 2	# 3	# 4	# 5
z_1	-1.167	-1.282	-1.400	-1.599	-1.442
z_2	-0.584	-0.524	-0.532	-0.679	-0.676
z_3	0.0	0.0	0.0	0.0	0.0
z_4	0.583	0.524	0.532	0.679	0.636
z_5	1.167	1.282	1.400	1.599	1.442
w_1	0.137	0.2	0.2	0.174	0.149
w_2	0.228	0.2	0.2	0.232	0.226
w_3	0.270	0.2	0.2	0.261	0.247
w_4	0.228	0.2	0.2	0.232	0.226
w_5	0.137	0.2	0.2	0.174	0.149

Table 2.1: Comparison of the patterns produced by different Gaussian bunch slicing methods

Next, the collision point is determined as a consequence of the assumptions listed

in Table 3.1. Thus, it is assumed that the bunches move towards each other according to $s_{\pm} = \pm ct$, so that $t = 0$ corresponds to the instant at which the central collision occurs. If z_+ and z_- are the longitudinal position of a positron and an electron bunch, respectively, then the s–coordinates of the colliding position in the positron beam (s_+) and the opposing electron beam (s_-) at time t are $s_+ = ct + z_+$ and $s_- = -ct - z_-$, respectively. The point at which the positron and electron macroparticle collide is determined by setting $s_+ = s_- = s_c$, which implies that the collision point is $s_c = \frac{1}{2}(z_+ + z_-)$. Transverse coordinates should also be defined for the center of the macroparticle, as this is necessary for calculating the integrals of the beam–beam kick force on the transverse plane. The transformation from the bunch center to the actual collision point is a simple drift, as the detector solenoid field is well compensated for by the solenoid canceler coils in the colliding beam.

The process used for calculating the beam–beam kick force has already been discussed in Sec. 2.1.2. The formula for the beam–beam kick is the same as that described. The charge of the particle should then replace the macroparticle', which is discussed in this section. In the following, factors that are important for calculating the beam–beam interaction are introduced as the physical meaning and the associated formula. A bunch collision is depicted in Fig. 3.2.

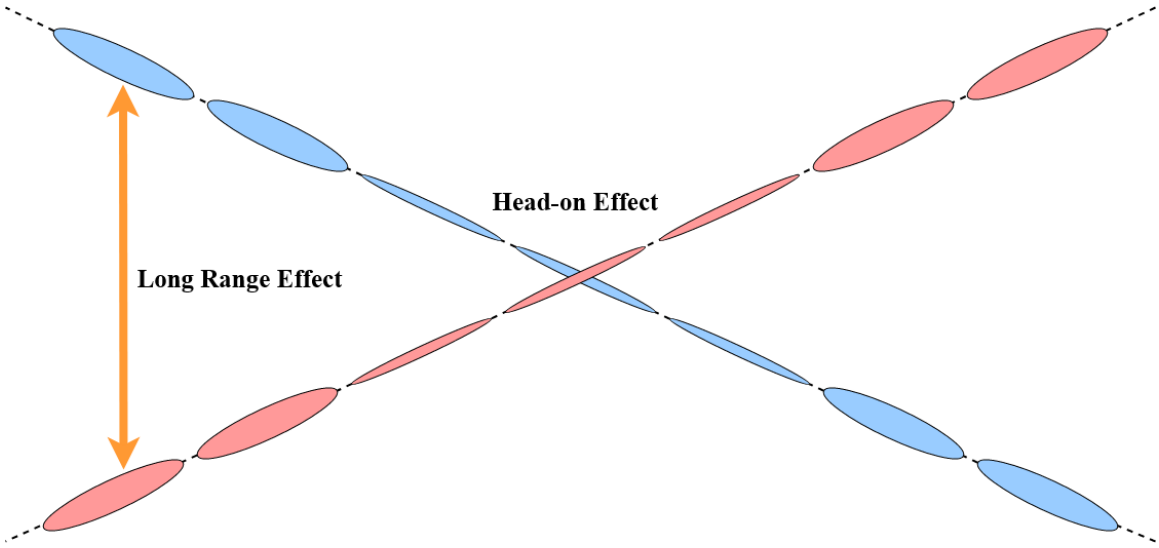

Figure 2.9: Image showing the for Head-on and Long-range effects of a collision.

Some of the factors required for calculating the beam–beam effect are introduced in this section. The required effects are selected according to the model used.

Head-on collision

For beam–beam interaction, a rounded Gaussian distribution is assumed for the charge distribution in the bunch. The effect of a head-on collision is given by

$$\Delta p_x = \frac{2r_e N_b}{\gamma}\frac{x}{r^2}\left(1 - e^{-\frac{r^2}{2\sigma^2}}\right), \tag{2.128}$$

$$\Delta p_y = \frac{2r_e N_b}{\gamma}\frac{y}{r^2}\left(1 - e^{-\frac{r^2}{2\sigma^2}}\right), \tag{2.129}$$

where $\sigma \equiv \sigma_x = \sigma_y$ is the rms beam size at the IP. These equations will be replaced with other formulae for other conditions, as discussed in Sec. 2.3.

Long range interaction

For the calculation of the long–range interaction, the effect of all parasitic collisions that overlap each other around the IP during the time range under investigation are integrated[**?**, **?**]. The long–range interactions can be approximately expressed as a beam–beam kick with a displacement from the IP coordinates, while the trajectory slope at the IP remains unchanged. In the case of a horizontal crossing, the displacements can be written as

$$\Delta x = -\, n_{\mathrm{par}}\frac{2r_e N_b}{\gamma}\left[\frac{p_x + \theta_c}{\theta_t^2}\left(1 - e^{-\frac{\theta_t^2}{2\theta_{x,y}^2}}\right) - \frac{1}{\theta_c}\left(1 - e^{-\frac{\theta_c^2}{2\theta_{x,y}^2}}\right)\right] \tag{2.130}$$

$$\Delta y = -\, n_{\mathrm{par}}\frac{2r_e N_b}{\gamma}\frac{p_y}{\theta_t^2}\left(1 - e^{-\frac{\theta_t^2}{2\theta_{x,y}^2}}\right) \tag{2.131}$$

for the horizontal and vertical axis, respectively ,where $\theta_t \equiv [(p_x + \theta_c)^2 + p_y^2]^{1/2}$ and $\theta_{x,y}$ is the rms beam divergence at the IP.

Triplet Nonlinearities

The integrated effect of the higher-order multipoles in the low-β quadrupoles can be written in complex form. The nonlinear kick on the incoming side of the IP with

horizontal crossing is given by

$$\Delta x = -K\mathrm{Re}\left\{\sum_{n=3}^{nmax} \times \mathcal{G}_n \left(-\frac{1}{r_0}\right)^{n-1} \left[\left(x' + \frac{\theta_c}{2} + iy'\right)^{n-1} - (n-1)\left(\frac{\theta_c}{2}\right)^{n-2}(x' + iy') - \left(\frac{\theta_c}{2}\right)^{n-1}\right]\right\}, \tag{2.132}$$

$$\Delta y = K\mathrm{Im}\left\{\sum_{n=3}^{nmax} \times \mathcal{G}_n \left(-\frac{1}{r_0}\right)^{n-1} \left[\left(x' + \frac{\theta_c}{2} + iy'\right)^{n-1} - (n-1)\left(\frac{\theta_c}{2}\right)^{n-2}(x' + iy') - \left(\frac{\theta_c}{2}\right)^{n-1}\right]\right\}, \tag{2.133}$$

$Irwin_b b_1 989, Her$

where the complex coefficient $\mathcal{G}_n$ is the effective strength of an nth order multipole kick.

Tune modulation

Tune modulation is described using a linear transport matrix in the form

$$\mathcal{M}_{tune} = \begin{pmatrix} \cos\Delta\phi_x & \beta_x^* \sin\Delta\phi_x & 0 & 0 \\ \frac{-1}{\beta_x^*}\sin\Delta\phi_x & \cos\Delta\phi_x & 0 & 0 \\ 0 & 0 & \cos\Delta\phi_y & \beta_y^*\sin\Delta\phi_y \\ 0 & 0 & \frac{-1}{\beta_y^*}\sin\Delta\phi_y & \cos\Delta\phi_y \end{pmatrix}, \tag{2.135}$$

where

$$\Delta\phi_x = 2\pi\Delta\mathrm{Q}_x \sin 2\pi f_x t, \tag{2.136}$$

$$\Delta\phi_y = 2\pi\Delta\mathrm{Q}_y \sin 2\pi f_y t. \tag{2.137}$$

where, $\Delta\mathrm{Q}_{x,y}$ and $f_{x,y}$ are the amplitude and frequency of the modulation, respectively.

Möbius insertion

A möbius transformation can be used in order to investigate the stabilization[34]. The Möbius twist is written in the simple form:

$$\begin{pmatrix} x \\ p_x \\ y \\ p_y \end{pmatrix}_i = \begin{pmatrix} 0 & 0 & -1 & 0 \\ 0 & 0 & 0 & -1 \\ -1 & 0 & 0 & 0 \\ 0 & -1 & 0 & 0 \end{pmatrix} \begin{pmatrix} x \\ p_x \\ y \\ p_y \end{pmatrix}_j , \tag{2.138}$$

where the indices labelled i and j denote the time before and after the application of the twist. Because of the additional symmetry of a Möbius lattice, an independent tune value is used.

Chapter 3

IP optics aberrations

3.1 Numerical Simulations of Beam–Beam Interaction

3.1.1 Introduction of the Beam–Beam Simulation

With the simple formulae used for the beam dynamics in the storage ring, beam–beam interactions are not considered useful for understanding global properties. However, many of the issues that surround circular colliders are caused by beam–beam interactions, including the growth of emittance and a reduction in the lifetime of the beams. These problems are critical sources of the limitations in the luminosity of particle colliders; it is therefore critical that the effects that beam–beam interaction have on IP beam dynamics are calculated. To study the effects of machine imperfections and beam–beam interactions, several simulations have been developed [30, 31, 30, 32].

In collider simulations, two beams that are moving in opposite directions are represented by macroparticles, as shown in Fig 3.1. The macroparticles consist of the same charge to mass ratio as the particles in the accelerator. Simulations of collisions usually only deal with colliding bunches, so two important parameters that are used to describe beam intensity are the number of particles within a bunch and the revolution frequency. According to these two parameters and the assumed bunch distribution, the charge ratio of a macroparticle can be estimated.

A six-dimensional bunch distribution is used to simulate the long-term evolution of a beam. The transverse and longitudinal motions of the beam are simulated using linear and nonlinear transfer maps. When the Hamiltonian can be written as the sum of two terms, the transfer maps constructed by the splitting method are generally represented as an action of the Hamiltonian on which the Lie transformation is

applied, as follows:

$$e^{-L:\mathcal{H}:} = e^{-L:\mathcal{H}_1+\mathcal{H}_2:} \tag{3.1}$$

$$\approx e^{-L:\mathcal{H}_1:}e^{-L:\mathcal{H}_2:}, \tag{3.2}$$

where L is the length of the component and $\mathcal{H}$ is the Hamiltonian of the component, which can be represented by the sum of two terms; $\mathcal{H} = \mathcal{H}_1 + \mathcal{H}_2$. As an example, for a sextupole magnet with one-degree of freedom, the Hamiltonian with a relativistic limit $\gamma_0 \longrightarrow \infty$ is given by

$$\mathcal{H} = -\sqrt{1-p_x^2} + \frac{1}{6}k_2x^3. \tag{3.3}$$

Because this Hamiltonian can be written by splitting the representation into two separate Hamiltonians:

$$\mathcal{H}_1 \equiv -\sqrt{1-p_x^2} \tag{3.4}$$

$$\mathcal{H}_2 \equiv \frac{1}{6}k_2x^3, \tag{3.5}$$

the Lie transformation $e^{-L:\mathcal{H}:}$, when applied to the physical variables of horizontal motion, can be written as:

$$e^{-L:\mathcal{H}:}\begin{pmatrix} x \\ p_x \end{pmatrix} \approx e^{-L:\mathcal{H}_1:}e^{-L:\mathcal{H}_2:}\begin{pmatrix} x \\ p_x \end{pmatrix} \tag{3.6}$$

$$= e^{-L:\mathcal{H}_1:}\begin{pmatrix} x \\ p_x - \frac{1}{2}k_2Lx^2 \end{pmatrix} \tag{3.7}$$

$$= \begin{pmatrix} x + \frac{Lp_x}{\sqrt{1-p_x^2}} \\ p_x - \frac{1}{2}k_2Lx^2 - \frac{k_2L^2xp_x}{\sqrt{1-p_x^2}} - \frac{k_2L^3p_x^2}{2(1-p_x^2)} \end{pmatrix}. \tag{3.8}$$

Within the linear transfer maps, the dynamic action of a particle can be represented using a six-dimensional matrix. When nonlinear effects are considered in deriving the result from a simulation of colliding beam, the representation of the Lie transformation produced by the splitting method is used as a substitute for the linear transfer matrices.

3.1.2 Formulations in the Weak-Strong Simulation

The weak-strong model assumes that the “weak" beam is affected by both the head–on collision and the long–range interactions of the beam–beam kick. On the other

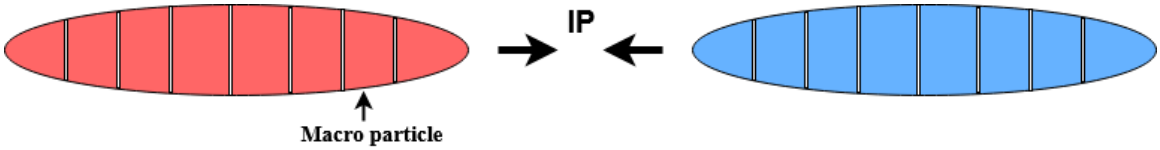

Figure 3.1: An image of bunches that consist of macro particles moving in opposite directions.

hand, the “strong" beam is not affected by these factors. In other words, a bunch distribution using only the “weak" beam effects is modified by beam–beam effects in every collision.

If the weak bunch conditions can be preserved during the iteration of a weak–strong model, the result can be considered as a simulation of a collision that is affected by only the beam–optical design of the accelerator. Beam dynamics can be explained completely in six–dimensional phase space variables, so the situation at the collision point is also determined by only the six–dimensional vector of each particle. If the difference between the laboratory and the beam coordinates is taken into consideration, it is necessary to rotate the coordinates at the collision point, but the basic model is the same as single particle dynamics in a fixed frame. The method of dividing the bunch distribution into several macro particles and integrating the action of each beam kick is used. If the distribution of the charge within a bunch is Gaussian, the charge and shape of a macroparticle used for the calculation of the actions of the electromagnetic field can be defined using the sliced Gaussian. The interaction of each macroparticle at the collision point is obtained by integrating the kick force received from the opposite beam. In the collision simulation, this calculation is performed for each revolution, meaning that all the actions that occur within one revolution should be integrated around the collision point. In other words, the core part of the simulation requires only the performance of an integral describing the kick force from each direction as a function of time s.

The actual calculation process used in this study executes a loop of items 2-5 in the following list:

1. Initialization
2. Calculation of the beam–beam kick
3. Produce a map illustrating one revolution of the ring
4. Calculate the radiation damping and quantum excitation
5. Calculate the transverse wake force and chromaticity

Initialization describes the generation of macroparticles with a Gaussian distribution in six-dimensional phase space. The initial emittances of the beam are set to the nominal values. The other effects are the same as above. The luminosity is then calculated using:

$$\mathcal{L} = f_0 \int dsdzdz' \{ \int dxdy \{ \rho^+(x,y,s(z)) \rho^-(x,y,-s(z')) \times \delta(s-(z-z')/2) \} \} \quad (3.9)$$

where $\rho^{\pm}(x,y,s)$ is the charge distribution density of the $e^{\pm}$ beam. The integration is evaluated by summing the macroparticle density at each of the mesh points.

Generally, the charge distribution of a bunch within the strong beam is fixed and assumed to be Gaussian:

$$\rho = \frac{Ne}{(2\pi)^{3/2}\sigma_x\sigma_y\sigma_s} \exp\left(-\frac{x^2}{2\sigma_x^2} - \frac{y^2}{2\sigma_y^2} - \frac{s^2}{2\sigma_s^2}\right), \quad (3.10)$$

where the notation of each parameter is the same as that used in the previous sections. In this distribution, the coordinates (x, y, and s) are the physical coordinates of the rest frame in the strong beam. When only transverse beam dynamics are required, the distribution of the particles in the bunch should be integrated along the longitudinal direction, as $\rho(x,y) = \int ds\{\rho(x,y,s)\}$.

Only the longitudinal distribution is important for slicing a Gaussian bunch, which is replaced with a summation of the weighted delta functions from N_s times as

$$\rho(x,y,s) \propto \rho(s) = \frac{\exp\left(-s^2/2\sigma_s^2\right)}{\sqrt{2\pi}\sigma_s} \quad (3.11)$$

$$\rightarrow \hat{\rho}(z) = \sum_{k=-L}^{L} w_k \delta(z - z_k), \quad (3.12)$$

where $N_s \equiv 2L+1$ is the slice number within the bunch and $\sum_{k=-L}^{L} w_k = 1$. There are several slicing algorithms that may be used to produce macroparticles[33].

The first factor for consideration is the equal spacing of the slices. The location of the beam–beam kicks is equally spaced with weights that are proportional to the

Gaussian density at s_k:

$$\frac{s_k}{\sigma_s} = \frac{2k}{N_s - 1}\left(1 + \frac{N_s - 3}{12}\right) \tag{3.13}$$

$$w_k = \frac{\hat{\rho}(s_k)}{\sum_{m=-L}^{L} \hat{\rho}(s_m)}, \tag{3.14}$$

where $k = 0, \pm 1, \cdots, \pm L$, $N_s \geq 3$.

The second factor for consideration is the use of slices of equal area. If the Gaussian distribution is divided into N_s slices of equal area, the macroparticles will have equal charge. The kicks are located at the center of the charge of each slice, which is the same as the center of mass. The weight function is uniform, at $w_k = 1/N_s$. The formula for the Gaussian slice is therefore described using the error function, as:

$$\frac{s_k}{\sigma_s} = \sqrt{2}\mathrm{erf}^{-1}\left(\frac{2k}{N_s}\right), \tag{3.15}$$

where k is the same as that in Eq. (3.14).

Slicing the Gaussian distribution uses the same principles as the first and second considerations mentioned above, but the kick locations are changed from the center of the slice to the edge of the slice. The formula giving the kick location is

$$\frac{s_k}{\sigma_s} = N_s[\hat{\rho}(l_k) - \hat{\rho}(l_{K+1})], (k = 1, \cdots, L), \tag{3.16}$$

$$\tag{3.17}$$

where l_k is the k–th position on the edge of the slice. Two slicing algorithms can thus be combined:

$$\frac{s_k}{\sigma_k} = \frac{1}{w_k}[\hat{\rho}(l_k) - \hat{\rho}(l_{k+1})] \tag{3.18}$$

The final consideration used in the production of a slicing algorithm is to select values for s_k and w_k such that the area enclosed by the two functions $\int_0^s ds'\{\rho(s')\}$ and $\int_0^s ds'\{\hat{\rho}(s')\}$ is minimal. These requirements lead to a set of nonlinear values for s_k and w_k in the algorithm "Combination method", which is most easily solved by iteration. Table 3.1 shows the value of z_k and w_k for five slicing patterns when $N_s = 5$.

Next, the collision point is determined as a consequence of the assumptions listed in Table 3.1. Thus, it is assumed that the bunches move towards each other according

	# 1	# 2	# 3	# 4	# 5
z_1	-1.167	-1.282	-1.400	-1.599	-1.442
z_2	-0.584	-0.524	-0.532	-0.679	-0.676
z_3	0.0	0.0	0.0	0.0	0.0
z_4	0.583	0.524	0.532	0.679	0.636
z_5	1.167	1.282	1.400	1.599	1.442
w_1	0.137	0.2	0.2	0.174	0.149
w_2	0.228	0.2	0.2	0.232	0.226
w_3	0.270	0.2	0.2	0.261	0.247
w_4	0.228	0.2	0.2	0.232	0.226
w_5	0.137	0.2	0.2	0.174	0.149

Table 3.1: Comparison of the patterns produced by different Gaussian bunch slicing methods

to $s_\pm = \pm ct$, so that $t = 0$ corresponds to the instant at which the central collision occurs. If z_+ and z_- are the longitudinal position of a positron and an electron bunch, respectively, then the s–coordinates of the colliding position in the positron beam (s_+) and the opposing electron beam (s_-) at time t are $s_+ = ct + z_+$ and $s_- = -ct - z_-$, respectively. The point at which the positron and the electron macroparticle collide is determined by setting $s_+ = s_- = s_c$, which implies that the collision point is $s_c = \frac{1}{2}(z_+ + z_-)$. Transverse coordinates should also be defined for the center of the macroparticle, as this is necessary for calculating the integrals of the beam–beam kick force on the transverse plane. The transformation from the bunch center to the actual collision point is a simple drift, as the detector solenoid field is well compensated for by the solenoid canceler coils in the colliding beam.

The process used for calculating the beam–beam kick force have already been discussed in Sec. 2.1.2. The formula for the beam–beam kick is the same as that described. The charge of the particle should then replace the Śmacroparticle', which is discussed in this section. In the following, factors that are important in calculating the beam–beam interaction are introduced as the physical meaning and the associated formula. A bunch collision is shown in Fig. 3.2.

Some of the factors required for calculating the beam–beam effect are introduced in this section. The required effects are selected according to the model used.

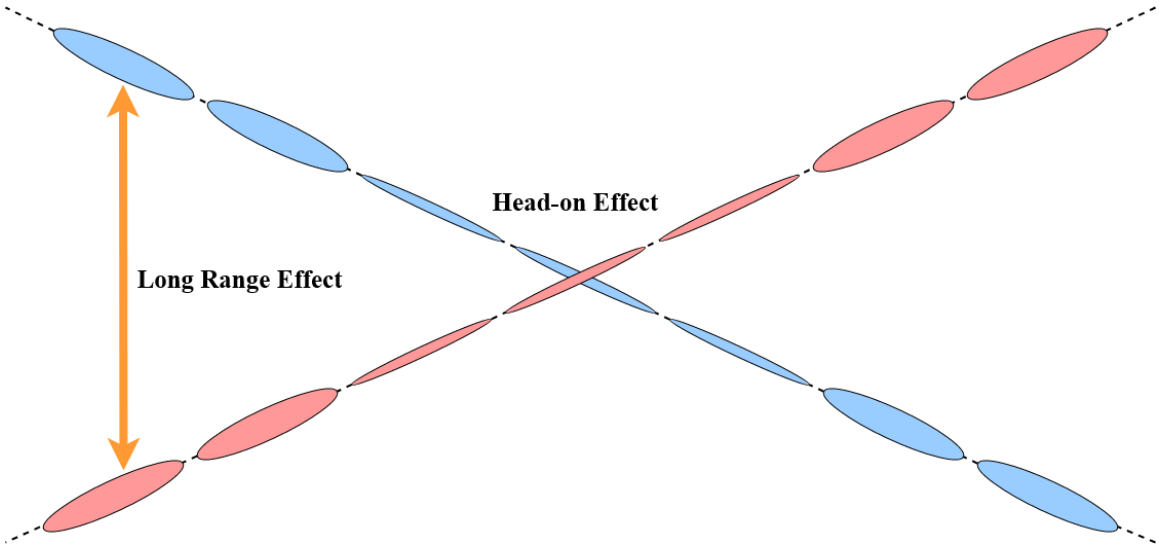

Figure 3.2: Image showing the for Head-on and Long-range effects of a collision.

Head-on collision

For beam–beam interaction, a rounded Gaussian distribution is assumed for the charge distribution in the bunch. The effect of a head-on collision is given by

$$\Delta p_x = \frac{2 r_e N_b}{\gamma} \frac{x}{r^2} \left(1 - e^{-\frac{r^2}{2\sigma^2}} \right), \tag{3.19}$$

$$\Delta p_y = \frac{2 r_e N_b}{\gamma} \frac{y}{r^2} \left(1 - e^{-\frac{r^2}{2\sigma^2}} \right), \tag{3.20}$$

where $\sigma \equiv \sigma_x = \sigma_y$ is the rms beam size at the IP. These equations will be replaced with other formulae for other conditions, as discussed in Sec. 2.3.

As several type of application for the beam–beam simulation, following items introduced in below sub–subsections can be considered.

Long range interaction

For the calculation of the long–range interaction, the effect of all parasitic collisions that overlap each other around the IP during the time range under investigation are integrated. The long–range interactions can be approximately expressed as a beam–beam kick with a displacement from the IP coordinates, while the trajectory slope at the IP remains unchanged. In the case of a horizontal crossing, the displacements

can be written as:

$$\Delta x = - n_{\rm par}\frac{2r_{\rm e}N_{\rm b}}{\gamma}\left[\frac{p_x+\theta_c}{\theta_t^2}\left(1-e^{-\frac{\theta_t^2}{2\theta_{x,y}^2}}\right)-\frac{1}{\theta_c}\left(1-e^{-\frac{\theta_c^2}{2\theta_{x,y}^2}}\right)\right] \tag{3.21}$$

$$\Delta y = - n_{\rm par}\frac{2r_{\rm e}N_{\rm b}}{\gamma}\frac{p_y}{\theta_t^2}\left(1-e^{-\frac{\theta_t^2}{2\theta_{x,y}^2}}\right) \tag{3.22}$$

for the horizontal and vertical axis, respectively ,where $\theta_t \equiv [(p_x+\theta_c)^2+p_y^2]^{1/2}$ and $\theta_{x,y}$ is the rms beam divergence at the IP.

Triplet Nonlinearities

The integrated effect of the higher-order multipoles in the low-β quadrupoles can be written in complex form. The nonlinear kick on the incoming side of the IP with horizontal crossing is given by

$$\Delta x = - K{\rm Re}\left\{\sum_{n=3}^{nmax} \times \mathcal{G}_n\left(-\frac{1}{r_0}\right)^{n-1}\left[\left(x'+\frac{\theta_c}{2}+iy'\right)^{n-1}-(n-1)\left(\frac{\theta_c}{2}\right)^{n-2}(x'+iy')-\left(\frac{\theta_c}{2}\right)^{n-1}\right]\right\}, \tag{3.23}$$

$$\Delta y = K{\rm Im}\left\{\sum_{n=3}^{nmax} \times \mathcal{G}_n\left(-\frac{1}{r_0}\right)^{n-1}\left[\left(x'+\frac{\theta_c}{2}+iy'\right)^{n-1}-(n-1)\left(\frac{\theta_c}{2}\right)^{n-2}(x'+iy')-\left(\frac{\theta_c}{2}\right)^{n-1}\right]\right\}, \tag{3.24}$$

$$MF - AZ_B BSin($$

where the complex coefficient $\mathcal{G}_n$ is the effective strength of a nth order multipole kick.

Tune modulation

Tune modulation is described using a linear transport matrix in the form

$$\mathcal{M}_{tune} = \begin{pmatrix} \cos\Delta\phi_x & \beta_x^* \sin\Delta\phi_x & 0 & 0 \\ \frac{-1}{\beta_x^*}\sin\Delta\phi_x & \cos\Delta\phi_x & 0 & 0 \\ 0 & 0 & \cos\Delta\phi_y & \beta_y^*\sin\Delta\phi_y \\ 0 & 0 & \frac{-1}{\beta_y^*}\sin\Delta\phi_y & \cos\Delta\phi_y \end{pmatrix}, \tag{3.26}$$

where

$$\Delta\phi_x = 2\pi\Delta\mathrm{Q}_x \sin 2\pi f_x t, \tag{3.27}$$

$$\Delta\phi_y = 2\pi\Delta\mathrm{Q}_y \sin 2\pi f_y t. \tag{3.28}$$

where, $\Delta\mathrm{Q}_{x,y}$ and $f_{x,y}$ are the amplitude and frequency of the modulation, respectively.

Möbius insertion

A möbius transformation can be used in order to investigate the stabilization[34]. The Möbius twist is written in the simple form:

$$\begin{pmatrix} x \\ p_x \\ y \\ p_y \end{pmatrix}_i = \begin{pmatrix} 0 & 0 & -1 & 0 \\ 0 & 0 & 0 & -1 \\ -1 & 0 & 0 & 0 \\ 0 & -1 & 0 & 0 \end{pmatrix} \begin{pmatrix} x \\ p_x \\ y \\ p_y \end{pmatrix}_j, \tag{3.29}$$

where the indices labelled i and j denote the time before and after the application of the twist. Because of the additional symmetry of a Möbius lattice, an independent tune value is used.

3.2 Different types of Optical Error

3.2.1 1st order: Closed Orbit Distortions

The COD and dispersion functions determine the central trajectory, and the focusing-defocusing force causes oscillations in the betatron. The small vibration around the central orbit is known as the betatron oscillation, which has the β-function of an envelope. The COD of a section is equivalent to the installation error of the components in that section.

The effects that magnet imperfections have on the beam dynamics in a strong focusing lattice has been an important field of investigation. The COD is caused by dipole field error. Horizontal and vertical dipole errors cause perturbations in the vertical and horizontal motion of a particle, respectively. The Hamiltonian for vertical particle motion can be written as

$$\mathcal{H} = \frac{\mathcal{J}_y}{\beta_y(s)} - \frac{q}{P_0}\Delta B_x(s)y, \tag{3.30}$$

where q is the particle charge, P_0 is the reference momentum, and ΔB_x is the horizontal error of the dipole field as a function of its position along the ideal trajectory. The coordinate y of a betatron oscillation in terms of the action–angle variables $\mathcal{J}_y$ and ϕ_y is

$$y = \sqrt{2\beta_y\mathcal{J}_y}\cos\phi_y, \tag{3.31}$$

thus, the Hamiltonian becomes

$$\mathcal{H} = \frac{\mathcal{J}_y}{\beta_y(s)} - \sqrt{2\beta_y\mathcal{J}_y}\frac{q}{P_0}\Delta B_x(s)(e^{-i\phi_y} + e^{i\phi_y}). \tag{3.32}$$

A particle motion that is affected by dipole error follows the canonical equation for the Hamiltonian (Eq. (3.32)).

For uncorrelated misalignment of quadrupoles in a periodic lattice, the RMS closed orbit distortion $\sigma_{\mathrm{COD}}(s)$ at position (s) has been shown to be

$$\sigma_{\mathrm{COD}}(s) = \frac{\sqrt{\beta(s)}\sqrt{\langle\beta\rangle}}{2\sin(\pi\nu_\beta)}\frac{\sigma_q}{|L_f|}\frac{\sqrt{N}}{2}, \tag{3.33}$$

where σ_q is the transverse RMS quadrupole misalignment, L_f is the focal length of the quadrupoles, and N is the number of quadrupoles. Generally, $N/2$ corresponds to the number of identical FODO sections.

Bending magnets are usually used to correct COD. These corrector magnets can undertake both horizontal and vertical bend, and are therefore generally known as "steering magnets". A steering magnet kicks the beam and changes the orbit of a beam by a specific angle. Its COD is represented by

$$x_{\mathrm{COD}}(s_2) = \frac{\sqrt{\beta(s_2)}\beta(s_1)}{2\sin(\pi\nu)}\cos(\pi\nu - |\mu(s_2) - \mu(s_1)|)\delta\theta(s_1) \tag{3.34}$$

where s_2 is the monitor position and s_1 is the kick position. COD should therefore be eliminated by using steering magnets at monitoring positions:

$$\begin{pmatrix} x_{\mathrm{COD}}(s_1) \\ x_{\mathrm{COD}}(s_2) \\ \vdots \\ x_{\mathrm{COD}}(s_n) \end{pmatrix} + \begin{pmatrix} f_{11} & f12 & \cdots & f_{1n} \\ f_{21} & f22 & \cdots & f_{2n} \\ \vdots & \vdots & & \vdots \\ f_{n1} & fn2 & \cdots & f_{nn} \end{pmatrix} \begin{pmatrix} \delta\theta_1 \\ \delta\theta_2 \\ \vdots \\ \delta\theta_n \end{pmatrix} = 0 \tag{3.35}$$

The f_{mn} parameters correspond to Eq. (3.34) for several different combinations of kick and monitor positions.

3.2.2 2nd order: Linear Optics Aberrations

Coupling Errors on unexpected skew quadrupoles

Coupling errors arise from unexpectedly skewed quadrupoles and solenoid fields, which are discussed from the perspective of the thin lens approximation[35, 36, 37, 38, 39]. The components of a magnetic field in which the quadrupoles are skewed are

$$B_x = -(B\rho)k_1 x \tag{3.36}$$
$$B_y = (B\rho)k_1 y \tag{3.37}$$
$$B_z = 0 \tag{3.38}$$

where $B\rho = P_0/q$ is the magnetic rigidity (P_0 is the reference momentum and q is the charge of a particle) and k_1 is the normalized gradient of the skewed quadrupole. In the thin lens approximation, a skew quadrupole field is described using a six–

dimensional transfer matrix:

$$R_{sq} = \begin{pmatrix} 1 & 0 & 0 & 0 & 0 & 0 \\ 0 & 1 & -K & 0 & 0 & 0 \\ 0 & 0 & 1 & 0 & 0 & 0 \\ -K & 0 & 0 & 1 & 0 & 0 \\ 0 & 0 & 0 & 0 & 1 & 0 \\ 0 & 0 & 0 & 0 & 0 & 1 \end{pmatrix} \tag{3.39}$$

where $K = k_1 L$ and L is the length of the skew quadrupole[40]. The physical meaning of this action is very simple; the skew kick strength proportional to the coefficient K. As block matrices, the first diagonal 4×4 block matrix denotes the transfer on the transverse plane and the other diagonal 2×2 block matrix denotes the transfer on the longitudinal axis. Other off–diagonal 2×4 and 4×2 block matrices correspond to the coupling effect between the transverse and longitudinal motion. In linear beam transportation, every property of the beam can be described using matrices and vectors.

The transverse statistical property of a beam is described using a 4×4 sigma covariance matrix. This transverse four–dimensional matrix can be separated to form 2×2 of 2×2 block matrices.

$$\sigma = \begin{pmatrix} \langle x \rangle & \langle x p_x \rangle & \langle xy \rangle & \langle x p_y \rangle \\ \langle p_x x \rangle & \langle p_x \rangle & \langle p_x y \rangle & \langle p_x p_y \rangle \\ \langle yx \rangle & \langle y p_x \rangle & \langle y \rangle & \langle y p_y \rangle \\ \langle p_y x \rangle & \langle p_y p_x \rangle & \langle p_y y \rangle & \langle p_y \rangle \end{pmatrix} \tag{3.40}$$

This beam matrix can also be written as a block matrix in order to simplify the

representation and verify the role of each component. The block matrix is

$$\sigma = \begin{pmatrix} \sigma_x & \sigma_{xy} \\ \sigma_{yx} & \sigma_y \end{pmatrix} \tag{3.41}$$

$$\begin{cases} \sigma_x = \begin{pmatrix} \langle x \rangle & \langle x p_x \rangle \\ \langle p_x x \rangle & \langle p_x \rangle \end{pmatrix} & \begin{cases} \sigma_{xy} = \begin{pmatrix} \langle xy \rangle & \langle x p_y \rangle \\ \langle p_x y \rangle & \langle p_x p_y \rangle \end{pmatrix} = {}^t\sigma_{yx}, \\ \sigma_{yx} = \begin{pmatrix} \langle yx \rangle & \langle y p_x \rangle \\ \langle p_y x \rangle & \langle p_y p_x \rangle \end{pmatrix} \end{cases} \\ \sigma_y = \begin{pmatrix} \langle y \rangle & \langle y p_y \rangle \\ \langle p_y y \rangle & \langle p_y \rangle \end{pmatrix} & \end{cases}$$

where x and y are the horizontal and vertical coordinates of the BPMs and the magnets, respectively, and p_x and p_y are the derivatives with respect to the longitudinal coordinates. The matrixes σ_x and σ_y represent the pure U-mode and V-mode projected beam sizes, respectively. The variables $\sigma_{xy} = {}^t\sigma_{yx}$ describe the coupling correlation between the U-mode and the V-mode. If no x-y coupling occurs, or the conditions are decoupled, $\sigma_{xy} = 0$.

The transformation from the normalized coordinates for individual eigenmodes to betatron oscillation coordinates at s is described by

$$\begin{pmatrix} u(s) \\ p_u(s) \\ v(s) \\ p_v(s) \end{pmatrix} = \begin{pmatrix} \sqrt{\beta_u(s)} & 0 & 0 & 0 \\ -\frac{\alpha_u(s)}{\sqrt{\beta_u(s)}} & \frac{1}{\sqrt{\beta_u(s)}} & 0 & 0 \\ 0 & 0 & \sqrt{\beta_v(s)} & 0 \\ 0 & 0 & -\frac{\alpha_v(s)}{\sqrt{\beta_v(s)}} & \frac{1}{\sqrt{\beta_v(s)}} \end{pmatrix} \begin{pmatrix} u_{\mathrm{N}}(s) \\ p_{u\mathrm{N}}(s) \\ v_{\mathrm{N}}(s) \\ p_{v\mathrm{N}}(s) \end{pmatrix} \tag{3.42}$$

$$= \begin{pmatrix} \sqrt{2\mathcal{J}_u \beta_u(s)} \cos(\phi_u + \phi_{u0}) \\ -\alpha_u(s)\sqrt{\frac{2\mathcal{J}_u}{\beta_u(s)}} \cos(\phi_u + \phi_{u0}) - \sqrt{\frac{2\mathcal{J}_u}{\beta_u(s)}} sin(\phi_u + \phi_{u0}) \\ \sqrt{2\mathcal{J}_v \beta_v(s)} \cos(\phi_v + \phi_{v0}) \\ -\alpha_v(s)\sqrt{\frac{2\mathcal{J}_v}{\beta_v(s)}} \cos(\phi_v + \phi_{v0}) - \sqrt{\frac{2\mathcal{J}_v}{\beta_v(s)}} \sin(\phi_v + \phi_{v0}) \end{pmatrix} \tag{3.43}$$

where β and α are the Courant-Snyder twiss parameters of the orthogonal betatron os-

cillation, ϕ is the phase of the betatron oscillation, and $2\mathcal{J} = \varepsilon$ is the Courant-Snyder invariant, which is also an action variable. Most of these parameters are a function of the longitudinal position s (without invariants). The normalized coordinates for the individual betatron modes are

$$\vec{u}_{\mathrm{N}}(s) = \begin{pmatrix} u_{\mathrm{N}}(s) \\ p_{u\mathrm{N}}(s) \\ 0 \\ 0 \end{pmatrix} = \begin{pmatrix} \sqrt{2\mathcal{J}_u}\cos\left(\phi_u(s)\right) \\ -\sqrt{2\mathcal{J}_u}\sin\left(\phi_u(s)\right) \\ 0 \\ 0 \end{pmatrix} \tag{3.44}$$

$$\vec{v}_{\mathrm{N}}(s) = \begin{pmatrix} 0 \\ 0 \\ v_{\mathrm{N}}(s) \\ p_{v\mathrm{N}}(s) \end{pmatrix} = \begin{pmatrix} 0 \\ 0 \\ \sqrt{2\mathcal{J}_v}\cos\left(\phi_v(s)\right) \\ -\sqrt{2\mathcal{J}_v}\sin\left(\phi_v(s)\right) \end{pmatrix} \tag{3.45}$$

The normalized coordinates describe the circular motion with a radius of $= \sqrt{2\mathcal{J}}$ in both U-mode and V-mode phase space.

The transformation from normalized coordinates to the coordinates of the is

$$\mathcal{RB} = \begin{pmatrix} r_0 & 0 & r_4 & -r_2 \\ 0 & r_0 & -r_3 & r_1 \\ -r_1 & -r_2 & r_0 & 0 \\ -r_3 & -r_4 & 0 & r_0 \end{pmatrix} \begin{pmatrix} \sqrt{\beta_u} & 0 & 0 & 0 \\ -\frac{\alpha_u}{\sqrt{\beta_u}} & \frac{1}{\sqrt{\beta_u}} & 0 & 0 \\ 0 & 0 & \sqrt{\beta_v} & 0 \\ 0 & 0 & -\frac{\alpha_v}{\sqrt{\beta_v}} & \frac{1}{\sqrt{\beta_v}} \end{pmatrix} \tag{3.46}$$

$$= \begin{pmatrix} r_0\sqrt{\beta_u} & 0 & r_2\frac{\alpha_v}{\sqrt{\beta_v}} + r_4\sqrt{\beta_v} & -r_2\frac{1}{\sqrt{\beta_v}} \\ -r_0\frac{\alpha_u}{\sqrt{\beta_u}} & r_0\frac{1}{\sqrt{\beta_u}} & -\left(r_1\frac{\alpha_v}{\sqrt{\beta_v}} + r_3\sqrt{\beta_v}\right) & r_1\frac{1}{\sqrt{\beta_v}} \\ -r_1\sqrt{\beta_u} + r_2\frac{\alpha_u}{\sqrt{\beta_u}} & -r_2\frac{1}{\sqrt{\beta_u}} & r_0\sqrt{\beta_v} & 0 \\ -r_3\sqrt{\beta_u} + r_4\frac{\alpha_u}{\sqrt{\beta_u}} & -r_4\frac{1}{\sqrt{\beta_u}} & -r_0\frac{\alpha_v}{\sqrt{\beta_v}} & r_0\frac{1}{\sqrt{\beta_v}} \end{pmatrix} \tag{3.47}$$

and the total expression describing the transverse motion of the physical coordinates

is

$$\vec{x} = \mathcal{RB}(\vec{u}_{\mathcal{N}} + \vec{v}_{\mathcal{N}}) \tag{3.48}$$

$$\mathcal{RB}\vec{u}_{\mathcal{N}} = \begin{pmatrix} r_0\sqrt{2\mathcal{J}_u\beta_u}\cos(\phi_u) \\ -r_0\left(\alpha_u\sqrt{\frac{2\mathcal{J}_u}{\beta u}}\cos(\phi_u(s)) + \sqrt{\frac{2\mathcal{J}_u}{\beta_u}}\sin(\phi_u(s))\right) \\ (-r_1\sqrt{2\mathcal{J}_u\beta_u} + r_2\alpha_u\sqrt{\frac{2\mathcal{J}_u}{\beta_u}})\cos(\phi_u(s)) - r_2\sqrt{\frac{2\mathcal{J}_u}{\beta_u}}\sin(\phi_u(s)) \\ (-r_3\sqrt{2\mathcal{J}_u\beta_u} + r_4\alpha_u\sqrt{\frac{2\mathcal{J}_u}{\beta_u}})\cos(\phi_u(s)) - r_4\sqrt{\frac{2\mathcal{J}_u}{\beta_u}}\sin(\phi_u(s)) \end{pmatrix} \tag{3.49}$$

$$\mathcal{RB}\vec{v}_{\mathcal{N}} = \begin{pmatrix} \left(r_2\alpha_v\sqrt{\frac{2\mathcal{J}_v}{\beta_v}} + r_4\sqrt{2\mathcal{J}_v\beta_v}\right)\cos(\phi_v(s)) + r_2\sqrt{\frac{2\mathcal{J}_v}{\beta_v}}\sin(\phi_v(s)) \\ -\left(r_1\alpha_v\sqrt{\frac{2\mathcal{J}_v}{\beta_v}} + r_3\sqrt{2\mathcal{J}_v\beta_v}\right)\cos(\phi_v(s)) - r_1\sqrt{\frac{2\mathcal{J}_v}{\beta_v}}\sin(\phi_v(s)) \\ r_0\sqrt{2\mathcal{J}_v\beta_v}\cos(\phi_v) \\ -r_0\left(\alpha_v\sqrt{\frac{2\mathcal{J}_v}{\beta v}}\cos(\phi_v(s)) + \sqrt{\frac{2\mathcal{J}_v}{\beta_v}}\sin(\phi_v(s))\right) \end{pmatrix} \tag{3.50}$$

This representation of the motion, which consists of several separate components of the transformation of the coordinates, is one of most important for the theoretical understanding of betatron coupling.

Intrinsic emittance

A 4–D symmetric beam matrix σ consists of ten parameters, four of which denote betatron coupling factors. The projected beam emittances on the BPM–coordinates ε_x and ε_y, are defined as the square root of the determinants of the on–diagonal 2×2 submatrices, the (1,1) and (2,2) components. If one or more of the components in the off–diagonal submatrices of σ have finite values and are nonzero, the orthogonal betatron oscillations of the beam are coupled. This phenomenon is called X-Y coupling. The relationship between the coordinates of the orthogonal betatron oscillations and the laboratory coordinates is a rotational transformation. Especially, in the case of the 4–D beam, the correlation matrix is represented by a diagonal betatron emittance

matrix, the 4–D beam correlation matrix σ is given by

$$\sigma = \mathcal{R}\mathcal{B}(\vec{x}\vec{x}^{\mathrm{T}})\,{}^{t}\mathcal{B}\,{}^{t}\mathcal{R} = \mathcal{R}\mathcal{B}\sigma_{\beta}\,{}^{t}\mathcal{B}\,{}^{t}\mathcal{R} = \mathcal{R}\mathcal{B}\begin{pmatrix} \varepsilon_u & 0 & 0 & 0 \\ 0 & \varepsilon_u & 0 & 0 \\ 0 & 0 & \varepsilon_v & 0 \\ 0 & 0 & 0 & \varepsilon_v \end{pmatrix}{}^{t}\mathcal{B}\,{}^{t}\mathcal{R}, \tag{3.51}$$

where σ_β is called the intrinsic betatron beam size, and ε_u and ε_v are called the intrinsic emittances of the U-mode and V-mode, respectively. The analysis and correction of X-Y coupling involves measuring the beam matrix on the laboratory coordinates in order to find the source of the errors causing the skew quadrupole effects. In the linear coupling, the skew quadrupole strength corresponds to block diagonalizing or the coordinate transformation from intrinsic to apparent emittances.

The Case in which only a Single Eigenmode is Excited

If only the U-mode oscillation is excited, it is necessary to consider the U-mode vector Eq. (3.44) as the normalized beam property. The beam motion of individual modes can then be expressed as

$$\vec{x} = \mathcal{R}\mathcal{B}\vec{u}_{\mathcal{N}} \tag{3.52}$$

which is the same as Eq. (3.49) with an eigenmode frequency $f_u = 2\pi\nu_u$. Furthermore, each component of $\vec{x}$ should be in harmonic oscillation with different amplitudes and phase-offsets because the original oscillation is also a harmonic oscillation. According to this physical logic, Eq. (3.52) becomes

$$\vec{x} = \begin{pmatrix} x \\ p_x \\ y \\ p_y \end{pmatrix} = \sum_{n=0}^{\infty} \begin{pmatrix} A_{x,n}\cos\left(2\pi n\nu_u + \phi_{x0}\right) \\ A_{px,n}\cos\left(2\pi n\nu_u + \phi_{px0}\right) \\ A_{y,n}\cos\left(2\pi n\nu_u + \phi_{y0}\right) \\ A_{py,n}\cos\left(2\pi n\nu_u + \phi_{py0}\right) \end{pmatrix} \tag{3.53}$$

with sinusoidal wave properties. The necessity of summation via the matrix equation comes from the Fourier series expansion. Equations (3.52) and (3.53) are physically equivalent, thus each coefficient is derived using Fourier amplitudes and phases. When representation of the beam motion is based on the motion of the x-axis, Eq. (3.53) is

written as

$$\vec{x} = \sum_{n=0}^{\infty} \begin{pmatrix} A_{x,n} \cos \phi_{x,n} \\ A_{px,n}\{\cos \phi_{x,n} \cos(\phi_{px0} - \phi_{x0}) - \sin \phi_{x,n} \sin(\phi_{px0} - \phi_{x0})\} \\ A_{y,n}\{\cos \phi_{x,n} \cos(\phi_{y0} - \phi_{x0}) - \sin \phi_{x,n} \sin(\phi_{y0} - \phi_{x0})\} \\ A_{py,n}\{\cos \phi_{x,n} \cos(\phi_{py0} - \phi_{x0}) - \sin \phi_{x,n} \sin(\phi_{py0} - \phi_{x0})\} \end{pmatrix}, \tag{3.54}$$

where $\phi_{x,n} = 2\pi n \nu_u + \phi_{x0}$.

By using Eq. (3.54), the analysis of the Fourier transform can be clearly understood. In later sections, this representation of particle motion is used to derive the betatron coupling parameters via harmonic analysis.

3.2.3 3rd order: Nonlinear Kick

Introduction to the nonlinear effect on beam dynamics

Nonlinear effects are calculated in the equations for motion, meaning that each electromagnetic field should be rewritten as coefficients of the Hamiltonian. The beam system within particle accelerators satisfies symplectic conditions; thus, it also satisfies Liouville's theorem and can be dealt with via the conservative system for volume in phase space. Generally, although the energy of the system is not conserved in the storage rings for the electron/positron, it can be considered as an approximate energy conservation system as the effect of RF acceleration and energy loss along the ring are automatically equivalent. The Hamiltonian canonical equation therefore can clearly be used to discuss beam motion even though beam dynamics is a many–body problem. The dynamics of charged particles obey classical relativistic electrodynamics in Minkowski space $\mathbb{M}^4 := \mathbb{E}^3 \times \mathbb{R}$. The well-known Lorentz expression for force is

$$F = qE + qu \times B \tag{3.55}$$

where $q \in \mathbb{R}$ is the electric charge of a particle, $u \in \mathbb{E}^3$ is the velocity vector of that particle, $E := -\partial \vec{A}/\partial t - \nabla \phi$ is the external electric field that comes from the electric potential of the vector $\vec{A}$ and scalar ϕ, and $B := \nabla \times \vec{A}$ is the external magnetic field. These potentials satisfy the Lorentz condition

$$\frac{\partial \phi}{\partial t} + \nabla A = 0 \tag{3.56}$$

and the Lorentz invariant wave field equation is given by

$$\frac{\partial^2\phi}{\partial t^2} - \nabla^2\phi = \rho\frac{\partial^2\phi}{\partial t^2} - \nabla^2 A = J, \tag{3.57}$$

where ρ is the charge and J is the current density of the matter, respectively. These parameters obey the charge continuity relationship:

$$\frac{\partial\rho}{\partial t} + \nabla J = 0. \tag{3.58}$$

The nonlinear effect is calculated via the integral of the electromagnetic interaction coming from the magnets, in the same manner as the beam–beam kick calculation. Hamiltonian systems are suitable for integrating the interactions as the system of the beam in the storage ring is approximately the same as conservative systems for the volume factor of the phase space and the energy of the particles. The classical Hamiltonian for a charged particle in an electromagnetic field is

$$\mathcal{H} = \frac{1}{2m}(\vec{p} - q\vec{A})^2 + q\phi. \tag{3.59}$$

The two most common issues concerning nonlinear effects in accelerators are the fringe field and the higher order multipole field error. Details of these effects are described below. The sextupole field is especially important, so it will be considered separately from the higher order multipoles.

The Error of Higher Order Multipoles

In order to discuss the multipole fields clearly, magnetic fields in general form are approximated by using an effectively finite number of terms in a Taylor series. The effective number depends on the particle conditions considered. In the case of the SuperKEKB conditions, sextupole fields are effective on the motion of particles at the IP. This effective order of fields, which is sometimes in the form of the Hamiltonian, can be evaluated by the results of the canonical equation of the Hamiltonian around the ring. Table 3.2 gives the effective early terms of the Taylor series expansion for

magnetic fields, in which

$$B_y + iB_x = \sum_{n=0}^{\infty} \frac{1}{n!} f_n (x + iy)^n, \tag{3.60}$$

$$f_n = \frac{\partial^{n+1} B_y}{\partial x^{n+1}},$$

are listed. The multipole gradient in Eq. (3.60) is usually normalized using the relationships

$$\frac{F(s)}{|\vec{v}| \cdot |\vec{p}|} = \frac{q(\vec{v} \times \vec{B})}{|\vec{v}| \cdot |\vec{p}|}, \tag{3.61}$$

$$K_n = \frac{q}{|\vec{p}|} \cdot f_n, \tag{3.62}$$

$$k_n = 0.3 \frac{f_n}{|\vec{p}|} \frac{[T/m^n]}{[GeV/c]}, \tag{3.63}$$

where the dimension of K_n is $[1/m^{n+1}]$.

Multipole	order	B_x	B_y
Dipole	0	0	B_0
Quadrupole	1	$f_1 y$	$f_1 x$
Sextupole	2	$f_2 2xy$	$f_2(x^2 - y^2)$
Octupole	3	$\frac{1}{6} f_3(3yx^2 - y^3)$	$\frac{1}{6} f_3(x^3 - 3xy^2)$

Table 3.2: Taylor Series of the magnetic fields

The procedure used to evaluate the multipole errors is discussed using sextupole field errors as an example. Let $x(s)$, L, and $\mathcal{M}$ be the position of a particle, the circumference of a ring, and the map of the circumnavigation of the ring, respectively. The relationship between the parameters can be represented by

$$x(s + L) = \mathcal{M} x(s). \tag{3.64}$$

This map, which represents one revolution, can be transformed by using short distance transfer maps with perturbations in the multipole. This transformation of the map

is given by

$$\mathcal{M} = \prod_{i=0}^{N-1} e^{-\mathcal{H}(x,s_i)} M(s_i, s_{i+1}) \tag{3.65}$$

$$= \left\{ \prod_{i=0}^{N-1} M^{-1}(s_i, s) e^{-\mathcal{H}(x,s_i)} M(s_i, s) \right\} M(s) \tag{3.66}$$

$$\tag{3.67}$$

$$= \left\{ \prod_{i=0}^{N-1} e^{-\mathcal{H}(M(s,s_i)x,s_i)} \right\} M(s) \tag{3.68}$$

$$\tag{3.69}$$

$$\approx e^{-\oint ds' \{\mathcal{H}(M(s,s')x,s')\}} M(s) \tag{3.70}$$

where M represents the transfer map without any perturbation. Therefore, only the integral of the Hamiltonian is required in order to evaluate the effect of the field errors. In the case of a sextupole field, the Hamiltonian of sextupoles corresponds to the third order Hamiltonian following $\mathcal{H}_1 + \mathcal{H}_2$:

$$\mathcal{H}_1 = \frac{K_2}{6}(x_3 - 3xy^2), \tag{3.71}$$

$$\mathcal{H}_2 = \frac{SK_2}{6}(3x^2y - y^3), \tag{3.72}$$

where $\mathcal{H}_1$ and $\mathcal{H}_2$ denotes the Hamiltonian for a normal sextupole and skew sextupole, respectively. The physical variables of Eq. (3.71) and (3.72) are those variables that are present at the location of each magnet. In order to calculate the impact on the beam motion at the IP, the variables must be transferred from the IP to each magnet during every step of the calculation.

A calculation using twenty terms is required in order to evaluate the total effect of the sextupoles. When unexpected skew sextupole fields are excited in a ring, the terms y^3, y^2p_y, yp_y^2, p_y^2, x^2y, xp_xy, p_x^2y, x^2p_y, xp_xp_y, and $p_x^2p_y$ are required to estimate the effect of the error fields. Canonical equations that are used to estimate these

effects and find the effective terms follow two pairs of Hamiltonian equations:

$$\begin{cases} \bar{X} & = X - \frac{\partial \mathcal{H}}{\partial P_X}, \\ \bar{P_X} & = P_X + \frac{\partial \mathcal{H}}{\partial X}, \end{cases} \tag{3.73}$$

$$\begin{cases} \bar{Y} & = Y - \frac{\partial \mathcal{H}}{\partial P_Y}, \\ \bar{P_Y} & = P_Y + \frac{\partial \mathcal{H}}{\partial Y}, \end{cases} \tag{3.74}$$

where $\bar{A}$ represents the gradient of A in each turn. The variables in capitals are normalized by the square root of the betatron amplitudes as follows:

$$\begin{cases} X & = \frac{x^*}{\sqrt{\beta_x^*}}, \\ P_X & = \sqrt{\beta_x^*} p_x^*, \\ Y & = \frac{y^*}{\sqrt{\beta_y^*}}, \\ P_Y & = \sqrt{\beta_y^*} p_y^*. \end{cases} . \tag{3.75}$$

According to the definition of beam size $\sigma_i = \sqrt{\varepsilon_i \beta_i}$, the envelope of the motion is expected to be approximately $\sqrt{\varepsilon_{x,y}}$. Each parameter used to calculate skew sextupole terms in the design of SuperKEKB is given in table 3.3.

parameter	LER	HER
$\sqrt{\varepsilon_x}$	5.6×10^{-5}	6.78×10^{-5}
$\sqrt{\varepsilon_y}$	2.94×10^{-6}	3.39×10^{-6}

Table 3.3: Square roots of emittances of SuperKEKB design parameters

The effect of unexpected multipole fields can be evaluated by using the integral of the Hamiltonian around the ring. Consequently, the effective term for the field error can be found by comparison with the envelope of the particle motion at approximately ε for each parameter in the canonical equation.

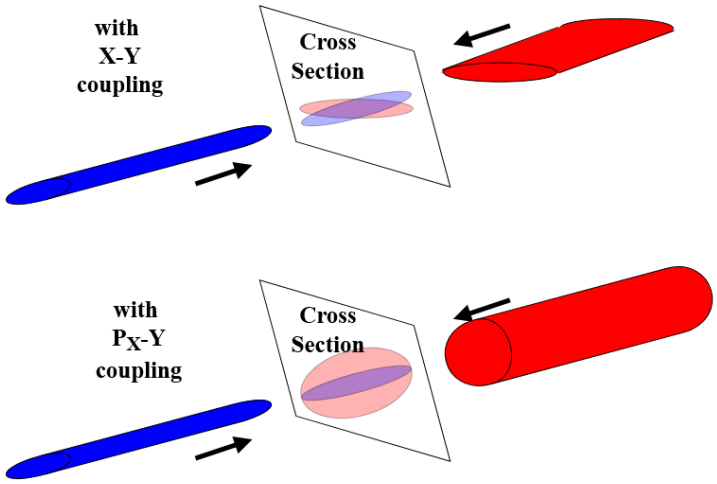

Figure 3.3: Model in which coupling parameters work as tilts for each variable in 2–D phase space.

3.3 Luminosity Formulae with Betatron Coupling

3.3.1 The IP Transverse Rotation that is due to the Linear X-Y Coupling

X–Y coupling is essentially a rotation of the coordinates of 4–D phase space. The focus of this section is the behavior of the beam at the collision point, and formulation of the luminosity in the presence of X–Y coupling is attempted.

Because SuperKEKB adopted the nano-beam scheme, beam collision is constructed on the basis of a large crossing angle with the hourglass effect. It is also assumed that the axis is rotated in transverse phase space. Two types of rotation model can therefore be considered. One is the relative coordinate rotation between the two beams, and the other considers the projected cross section for the individual rotation of the beam.

Figure 3.3 is a schematic illustration of a collision with a relative beam rotation. The important point is that the actual area of the collision is treated as a relative value.

Figure 3.4 is a schematic image of a collision in which the beam is rotated independently. In this collision model, the reduction in the collision area that is due to the rotation is redefined as an independent beam size instead of being a relative value.

Although methods in which the beam coordinates are rotated independently can provide good visibility of the geometric beam size in the form of an equation, it is

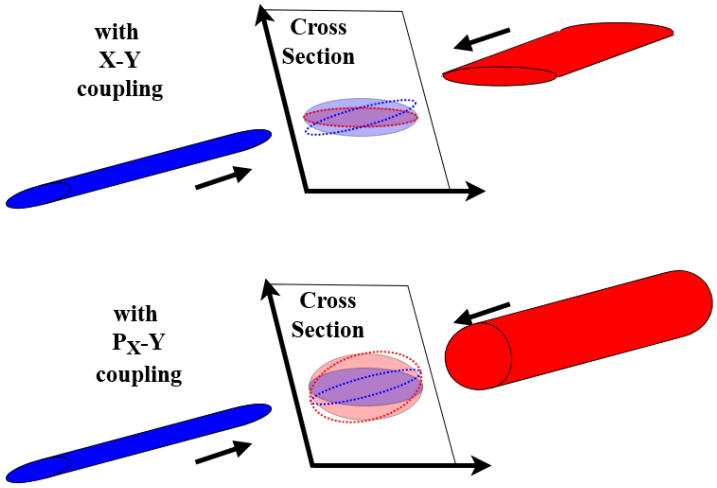

Figure 3.4: Coupling parameters as changed beam sizes in absolute coordinates.

necessary to discuss this as a relative difference in real conditions. In fact, due to the properties of rotation in 4–D phase space, any rotation that is related to momentum must be approached independently, and only the rotation of a projected plane in real space (x, y) can be considered as a relative rotation. Because the inclination of the 4–D ellipsoid in the direction of momentum appears only as a projection in real space, it is apparent that the emittance will be increased locally.

Next, the models illustrated in Fig. 3.3 and 3.4 are applied to derive the specific luminosity and beam–beam parameters.

3.3.2 Luminosity and Beam–Beam Parameters

To derive a formula for specific luminosity, a consistent model with specific coordinates and boundary conditions must be defined. First, derivation of the luminosity formula has to be performed, summarizing the situation, the coordinate system, and the boundary conditions. Second, the luminosity formula is introduced with the associated conditions. Finally, a model for the beam–beam parameter is introduced using a similar process.

The luminosity formula with linear X–Y coupling

Luminosity is a measure of the collisions that occur in an accelerator, and total luminosity is therefore a result of the repeated revolutions that occur in a circular collider. However, a simple model can be constructed in order to obtain geometric luminosity, as the luminosity formula can be used to describe only the geometric

factors without the cumulative effects of repeated beam–beam interactions. The influence of X–Y coupling should be focused only on the deviation of phase space at the collision point; thus, a vertical–horizontal rotation is applied to a horizontal–longitudinal rotation with a finite crossing angle($0 < |\phi_x| < \infty$). Although the formula appears complicated, the idea is simple.

The rotation using coupling parameters is applied to the projected plane of the cross section with the presence of a crossing angle and the hourglass effect. As the combination of the components of momentum is reflected in the geometry, it is necessary to calculate the size of the beam from σ to emittance. The collision point is therefore required to be a waist of the beta function, and $\alpha = 0$ in the Twiss parameter.

$$\begin{cases} \sigma_{1x} = \sqrt{r_{1,0}^2\beta_{1x}^*\varepsilon_{1x} + r_{1,4}^2\beta_{1y}^*\varepsilon_{1y} + r_{1,2}^2\frac{\varepsilon_{1x}}{\beta_{1x}}}, \\ \\ \sigma_{1y} = \sqrt{r_{1,0}^2\beta_{1y}^*\varepsilon_{1y} - r_{1,1}^2\beta_{1x}^*\varepsilon_{1x} + r_{1,2}^2\frac{\varepsilon_{1x}}{\beta_{1x}}}, \end{cases} \tag{3.76}$$

$$\begin{cases} \sigma_{2x} = \sqrt{r_{2,0}^2\beta_{2x}^*\varepsilon_{2x} + r_{2,4}^2\beta_{2y}^*\varepsilon_{2y} + r_{2,2}^2\frac{\varepsilon_{2x}}{\beta_{2x}}}, \\ \\ \sigma_{2y} = \sqrt{r_{2,0}^2\beta_{2y}^*\varepsilon_{2y} - r_{2,1}^2\beta_{2x}^*\varepsilon_{2x} + r_{2,2}^2\frac{\varepsilon_{2x}}{\beta_{2x}}}, \end{cases} \tag{3.77}$$

This transformation corresponds to the model in Fig. 3.4.

Using this transformation to calculate the luminosity and its geometric factor,

$$\begin{aligned} \mathcal{L} = & \frac{N_1 N_2 f N_\mathrm{b}}{2\pi\sqrt{\sum_i (r_{i,0}^2\beta_{ix}^*\varepsilon_{ix} + r_{i,4}^2\beta_{iy}^*\varepsilon_{iy} + r_{i,2}^2\frac{\varepsilon_{ix}}{\beta_{ix}})}} \\ & \times \frac{1}{\sqrt{\sum_i (r_{i,0}^2\beta_{iy}^*\varepsilon_{iy} - r_{i,1}^2\beta_{ix}^*\varepsilon_{ix} + r_{i,2}^2\frac{\varepsilon_{ix}}{\beta_{ix}})}} \cdot \mathcal{R}_{\mathrm{H}\theta\mathrm{R}}, \end{aligned} \tag{3.78}$$

and

$$\mathcal{R}_{\mathrm{H}\theta\mathrm{R}} = \frac{\cos^2\frac{\theta}{2}\prod_k\sqrt{\sum_i(r_{i,0}^2\beta_{ix}^*\varepsilon_{ix}+r_{i,4}^2\beta_{iy}^*\varepsilon_{iy}+r_{i,2}^2\frac{\varepsilon_{ix}}{\beta_{ix}})}}{\pi\sqrt{\sum_i\sigma_{is}^{*2}}} \tag{3.79}$$

$$\times\iint_{-\infty}^{\infty}dxds\left\{\frac{\exp\left(-\frac{(\sum_i s_i)^2}{2(\sum_i\sigma_{is}^2)}\right)}{\sqrt{\sum_i(r_{i,0}^2\beta_{iy}^*\varepsilon_{iy}-r_{i,1}^2\beta_{ix}^*\varepsilon_{ix}+r_{i,2}^2\frac{\varepsilon_{ix}}{\beta_{ix}})\left(1+\frac{s_i^2}{\beta_{iy}^{*2}}\right)}}\right.$$

$$\left.\times\prod_{i=\{1,2\}}\frac{\exp\left(-\frac{x_i^2}{2(r_{i,0}^2\beta_{ix}^*\varepsilon_{ix}+r_{i,4}^2\beta_{iy}^*\varepsilon_{iy}+r_{i,2}^2\frac{\varepsilon_{ix}}{\beta_{ix}})\left(1+\frac{s_i^2}{\beta_{ix}^{*2}}\right)}\right)}{(r_{i,0}^2\beta_{ix}^*\varepsilon_{ix}+r_{i,4}^2\beta_{iy}^*\varepsilon_{iy}+r_{i,2}^2\frac{\varepsilon_{ix}}{\beta_{ix}})\sqrt{1+\frac{s_i^2}{\beta_{ix}^{*2}}}}\right\}, \tag{3.80}$$

respectively. The subscript HθR in the geometric factor $\mathcal{R}_{\mathrm{H}\theta\mathrm{R}}$ therefore represents the "hourglass", "crossing angle", and "X–Y coupling". The coupling in the x direction also affects the s direction. The coupling of r_2 with p_x is effective for use with each beam size via $1/\sqrt{\beta_x}$. As the emittance in the x and y directions has an isolation of $\varepsilon_y/\varepsilon_x = 0.01$, the emittance in the y direction is 10 times higher than that of the x direction. Therefore, if $\beta_x = 0.1$ mm and $\beta_y = 0.002$, a difference of 0.014 times is apparent because the difference between x and y comes from $\sqrt{\beta_y/\beta_x}$. An emittance ratio of 2.8×10^{-4} was used in the design of SuperKEKB, and $\sqrt{\beta_y/\beta_x} = \sqrt{0.3/25} \simeq 0.11$, meaning that the r_2 term differs by a total of 1.8×10^{-3}-times in x and y. Therefore, the effect of p_x in the x direction is negligible compared to that of the y direction, and the effect of crossing angle on the s direction from the x direction is also negligibly small.

The transformation of coordinates is a very complicated expression for a geometric factor when transformation from the y direction to the s direction is considered. The"betatron coordinates" of each beam are transformed first, followed by the relative "collision coordinates" of both beams. This situation means that the coordinate system of the collision is rotated using coordinates that have been inclined by X–Y

coupling. Therefore, the relationship used for coordinate transformation is

$$\mathcal{R}_{6\times6} = \begin{pmatrix} r_0 & 0 & r_4 & -r_2 & 0 & 0 \\ 0 & r_0 & -r_3 & r_1 & 0 & 0 \\ -r_1 & -r_2 & r_0 & 0 & 0 & 0 \\ -r_3 & -r_4 & 0 & r_0 & 0 & 0 \\ 0 & 0 & 0 & 0 & 1 & 0 \\ 0 & 0 & 0 & 0 & 0 & 1 \end{pmatrix} \tag{3.81}$$

$$\Theta_{6\times6} = \begin{pmatrix} \cos\theta & 0 & 0 & 0 & \sin\theta & 0 \\ 0 & \cos\theta & 0 & 0 & 0 & \sin\theta \\ 0 & 0 & 1 & 0 & 0 & 0 \\ 0 & 0 & 0 & 1 & 0 & 0 \\ -\sin\theta & 0 & 0 & 0 & \cos\theta & 0 \\ 0 & -\sin\theta & 0 & 0 & 0 & \cos\theta \end{pmatrix} \tag{3.82}$$

and

$$\begin{pmatrix} x' \\ p'_x \\ y' \\ p'_y \\ s' \\ \delta' \end{pmatrix} = \mathcal{R}_{6\times6}\Theta_{6\times6} \begin{pmatrix} x \\ p_x \\ y \\ p_y \\ s \\ \delta \end{pmatrix} \tag{3.83}$$

$$= \begin{pmatrix} (r_0x + r_4y - p_yr_2)\cos\theta + s\sin\theta \\ (r_0p_x - r_3y + r_1p_y)\cos\theta + \delta\sin\theta \\ r_0y - r_1x - r_2p_x \\ r_0p_y - r_3x - r_4p_x \\ s\cos\theta - (r_0x + r_4y - r_2p_y)\sin\theta \\ \delta\cos\theta - (r_0p_x - r_3y + r_1p_y)\sin\theta \end{pmatrix}. \tag{3.84}$$

Because this relationship is used, the integration of y cannot be simplified. Thus,

luminosity must be calculated using the quadruple integrals of the Gaussian beams:

$$\begin{aligned}
\mathcal{L} = & \frac{2N_1N_2fN_b\cos^2\frac{\theta}{2}}{8\pi^3} \\
& \times \iiiint_{-\infty}^{\infty} dxdydsds_0 \left\{ \left[\frac{1}{\sigma_{1x}} \exp\left(-\frac{([r_0x_1 + r_4y_1 - p_{y1}r_2]\cos\theta - s_1\sin\theta)^2}{2\sigma_{1x}^2} \right) \right] \right. \\
& \times \left[\frac{1}{\sigma_{1y}} \exp\left(-\frac{(r_0y_1 - r_1x_1 - r_2p_{x1})^2}{2\sigma_{1y}^2} \right) \right] \\
& \times \left[\frac{1}{\sigma_{1s}} \exp\left(-\frac{(s_1\cos\theta + [r_0x_1 + r_4y_1 - r_2p_{y1}]\sin\theta - s_0)^2}{2\sigma_{1s}^2} \right) \right] \\
& \times \left[\frac{1}{\sigma_{2x}} \exp\left(-\frac{([r_0x_2 + r_4y_2 - r_2p_{y2}]\cos\theta + s_2\sin\theta)^2}{2\sigma_{2x}^2} \right) \right] \\
& \times \left[\frac{1}{\sigma_{2y}} \exp\left(-\frac{(r_0y_2 - r_1x_2 - r_2p_{x2})^2}{2\sigma_{2y}^2} \right) \right] \\
& \left. \times \left[\frac{1}{\sigma_{2s}} \exp\left(-\frac{(s_2\cos\theta - [r_0x_2 + r_4y_2 - r_2p_{y2}]\sin\theta - s_0)^2}{2\sigma_{2s}^2} \right) \right] \right\}, \qquad (3.85)
\end{aligned}$$

as the beam size of y depends on x.

3.3.3 Discussion of the factors that are included and excluded in IP coupling

When developing a luminosity formula, factors that require sequential calculation will be lost. For example, coordinate rotation is defined in 4–D phase space; therefore, the effect of the beam rotation on the momentum for the beam–beam kick cannot be calculated if the model used calculates only the 2–D projection. This beam–beam effect is one of reasons why simulation is essential for the calculation of luminosity.

It is therefore important to express luminosity with a single formula in simulations because the influence that the beam–beam effect has on the transverse coordinate rotation can be extracted. Of course, it should be noted that this is an incomplete formula that cannot track the effect of changes in the momentum.

Here, the means by which the rotation of the momentum coordinate at the collision point affects the beam dynamics is evaluated by comparing the luminosity calculation that was derived from the formula with the luminosity calculated using the beam–beam simulation.

First, the differences in the models will be discussed. Figure 3.5 depicts the collision conditions that are included in the Luminosity formula, which does not include rotation in a 2–D momentum space. On the other hand, Fig. 3.6 is the collision model used in the simulation, in which the coordinates rotate in both 2–D

position space and 2–D momentum space. As the position is coupled with momentum while the direction of the position and the momentum are independent, the model that is used to represent the entire rotation is constructed with rotation in 3–D space (p_x, y, p_y). As a projected component, coordinate rotation occurs in 2–D space with four combinations.

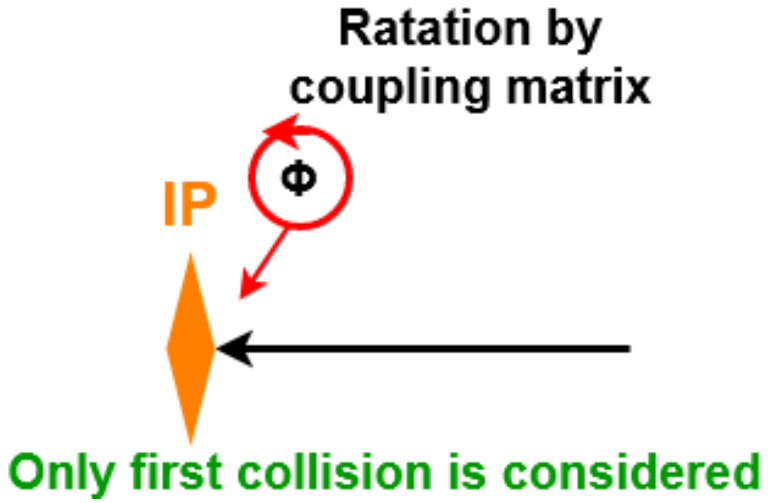

Figure 3.5: Illustration of the coupling model for the geometric factors in beam collision.

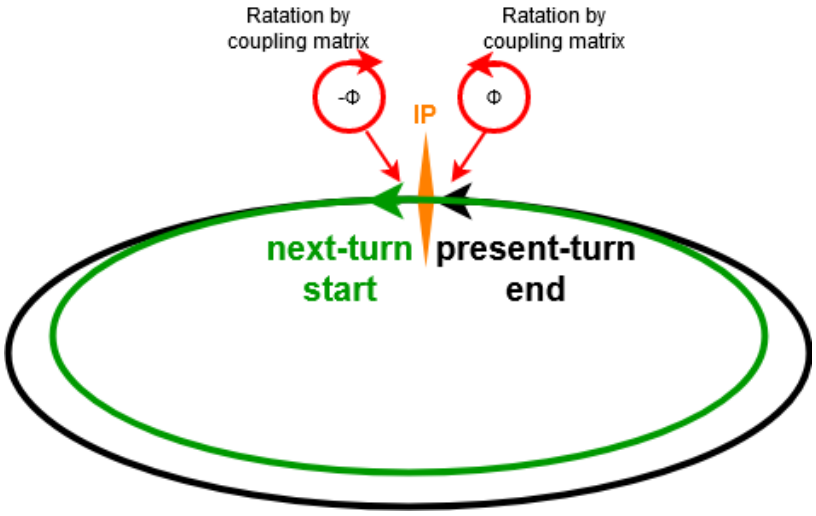

Figure 3.6: The illustration of the coupling model for the iterative factor of beam collision.

In the next subsection, the quantitative differences in X–Y coupling that are included in the model are explicitly clarified by comparing the two luminosities (calculated by formula and simulation) from the different models.

3.4 Comparison of the luminosity calculated by formula and beam–beam simulation

3.4.1 Conditions used for the calculations

A comparison of the luminosity calculated with the formula using X–Y coupling and beam–beam simulation is carried out in this section. The luminosity formula is a model that only takes the coordinate errors that occur in real space into account because of the variables that are used in the formula. As the momentum changes because of the error in the coordinates, it is applicable to assume that there may be optical aberrations over the entire ring. However, as it is necessary to perform sequential calculations in order to include each revolution, luminosity cannot be calculated precisely using a single equation. By comparing the two calculations, it is possible to determine the cumulative effect of the optical aberration at the IP with respect to the beam–beam kick.

Before actually applying the calculation, the conditions used in the calculation of luminosity must be determined. The parameters used are the conditions that developed during commissioning in Phase-2 and Phase-3 of SuperKEKB in 2019. It is clear that each β^* is gradually squeezed. To avoid the influence of spreading in a transverse direction via processes such as intra–bunch scattering and the Touschek effect, which could occur because of the large number of particles within a bunch, the calculations are performed in conditions of large emittance, regardless of the presence or absence of optical aberration at the collision point. As there is a cumulative effect at each turn in the simulation, which is affected by the operable region in the tune diagram, it is important to understand the optical aberration at the IP in order to avoid limitations that are due to beam–beam interaction[41, 42] when assuming conditions of low beam emittance.

Table 3.4 lists the conditions used in the calculation with large emittance in each β. In this situation, the results of the calculation are not affected by the upper limit of the luminosity, and it is therefore easy to determine the influence that is solely due to optical aberration. Table 3.5 shows the conditions used in the calculation when emittance is set at a realistic value. Although this condition is close to that of realistic operation, the luminosity is easily limited unless the tuning condition is selected optimally. Therefore, even if all coupling parameters are zero, the specific luminosity is decreased by an amount that depends on the current of the beam. This problem is caused by the beam–beam limit and occurs because the beam current is large compared to the luminosity, which does not increase. This problem is obviously

different from the influence of optical aberration. However, when the same conditions are used during actual operation, the value obtained is no better than that from the simulation; it is therefore apparent that this value is of significant importance in determining the upper limit of the conditions under which the accelerator can operate.

	HER	LER
ε_x	4.6×10^{-9}	3.2×10^{-9}
ε_y	4.6×10^{-11}	16.0×10^{-11}
β_x^*	0.1	0.2
β_y^*	0.003	0.003
τ_x^{-1}	1.7×10^{-4}	2.3×10^{-4}
τ_y^{-1}	1.7×10^{-4}	2.53×10^{-4}
τ_z^{-1}	3.4×10^{-4}	4.6×10^{-4}
ν_x^{-1}	45.5275	44.561
ν_y^{-1}	41.57	46.57
ν_s^{-1}	0.026	0.0225
ϕ_c	0.0413	

Table 3.4: Set parameters for Luminosity calculation #1

	HER	LER
ε_x	4.466×10^{-9}	1.64×10^{-9}
ε_y	16.2×10^{-12}	6.05×10^{-12}
β_x^*	0.1	0.2
β_y^*	0.003	0.003
τ_x^{-1}	2.5×10^{-4}	1.67×10^{-4}
τ_y^{-1}	2.5×10^{-4}	1.67×10^{-4}
τ_z^{-1}	5.0×10^{-4}	3.33×10^{-4}
ν_x^{-1}	45.5275	44.561
ν_y^{-1}	41.57	46.06
ν_s^{-1}	0.026	0.0225
ϕ_c	0.0413	

Table 3.5: Set parameters for Luminosity calculation #2

3.4.2 Application of the beam–beam simulation

Figure 3.7- 3.10 shows the results of a beam–beam simulation without any optical aberration. The beam currents used in the simulations are $\times 0.01$, $\times 0.02$, $\times 0.03$, $\times 0.04$, $\times 0.05$, $\times 0.1$, $\times 0.25$, $\times 0.5$, and $\times 1.0$ for both beams.

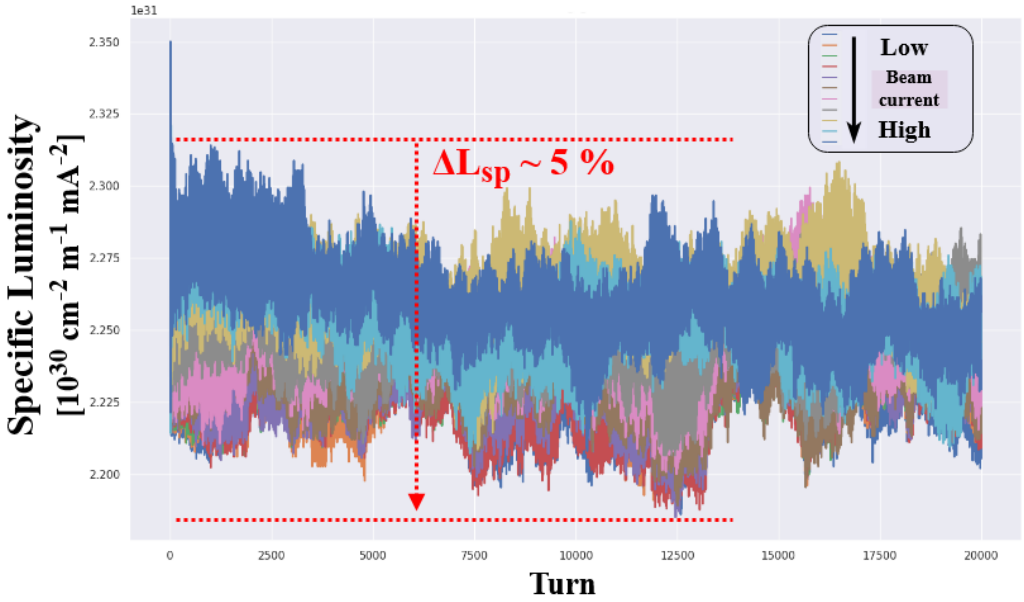

Figure 3.7: Specific luminosity from scanning the product of bunch current.

Figure 3.7 shows the specific luminosity per revolution. It seems that the disturbance increases as the beam current is increased; however, little change is seen in the calculated value of Lsp. This result correlates well with the definition of specific luminosity. Figure 3.8 shows the size of the horizontal beam in each revolution. Although there is an increase in emittance that depends on the beam current, this enhanced emittance is not reflected in the luminosity. The reason for this phenomena is theoretically that the large crossing angle at the IP has little impact on the effective horizontal beam size at the IP. The simulation therefore reproduced the phenomena observed when a large crossing angle is used with high accuracy. Figure 3.9 shows the vertical beam size in each revolution. The size of the vertical beam is not changed by collision. As this value does not depend on the beam current, this phenomena directly reflects the luminosity. Furthermore, when no optical aberration is apparent, it can be seen that collision affects no change in the corresponding emittance. In the case of this simulation, the unchanged vertical beam size comes from a head-on collision. Figure 3.10 shows the correlation between the x and y of a strong beam. This result is important for evaluating the X–Y coupling conditions when optical aberration is observed.

Figure **??** shows the results of a simulation in which the conditions surrounding the strong and weak beams have been swapped. The effect of swapping the parameters of the beams is reflected in the increase in the vertical beam size. The beam

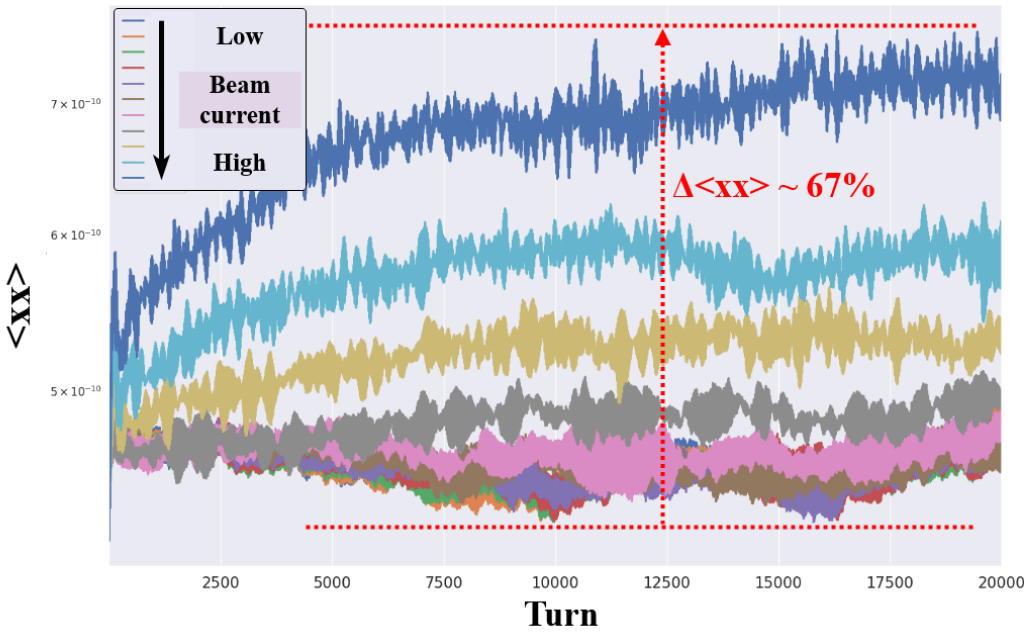

Figure 3.8: Horizontal beam size from scanning the product of bunch current .

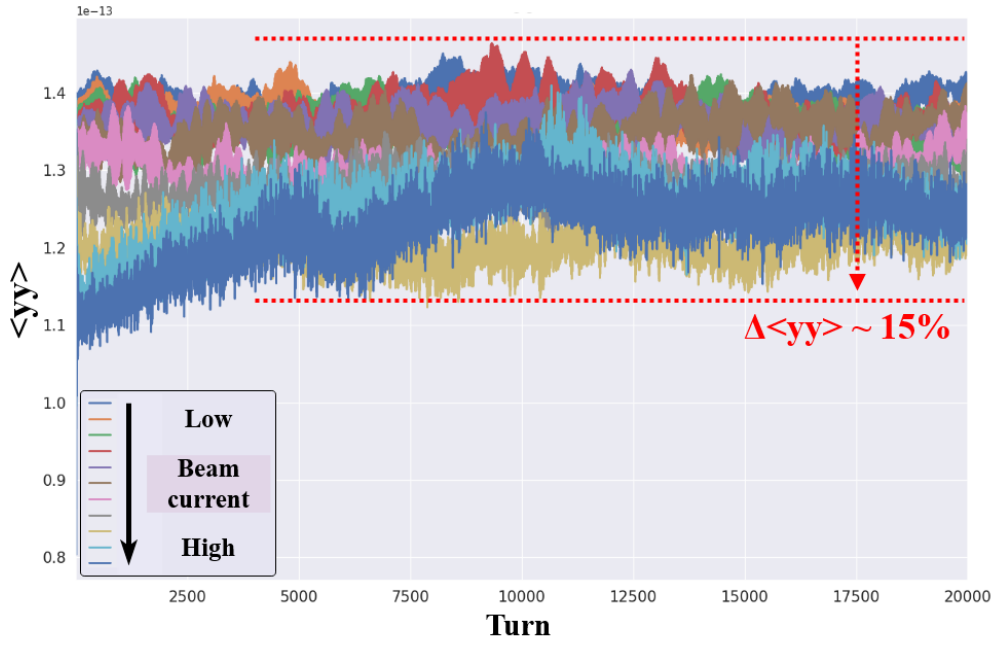

Figure 3.9: Vertical beam size from scanning the product of bunch current .

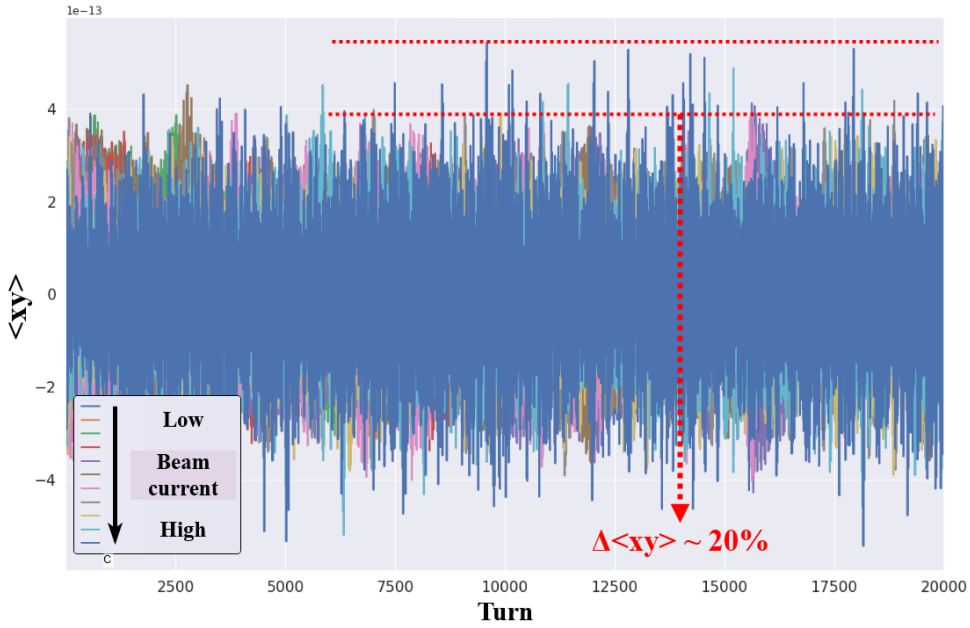

Figure 3.10: Correlation between horizontal and vertical beam size from scanning the product of bunch current .

that has been kicked has been reversed. As seen in this figure, it is necessary that the appropriate beam to be kicked is pre-selected in order to set the Weak–Strong simulations in line with reality. In other words, it is necessary to appropriately select a set of parameters that provide a state of equilibrium. Otherwise, as shown in Fig. 3.11– 3.14, each of the calculated values changes from the geometric values and shows behavior approaching the equilibrium state after repeated collisions. Conversely, it is possible to obtain the appropriate geometric values by iterating this simulation, Therefore, the beam–beam simulation is useful for evaluating both the operating parameters and the measured parameters.

Figure 3.15– 3.18 shows a simulation in which the vertical beam size is increased by $\sqrt{2}$. The specific luminosity has been reduced by nearly $1/\sqrt{2}$ times, as seen in the corresponding value $< yy >$. This is an important result that shows there is generally no change in behavior before and after beta squeezing, and that the specific luminosity directly reflects any change in the parameters.

Figure 3.19 shows the result of a simulation using the parameters given in Tab. 3.5. If a current is scanned under these conditions, the emittance increases in accordance with the beam current, and the luminosity deteriorates significantly. It can be seen that it is difficult to calculate the luminosity with any accuracy in order to simulate

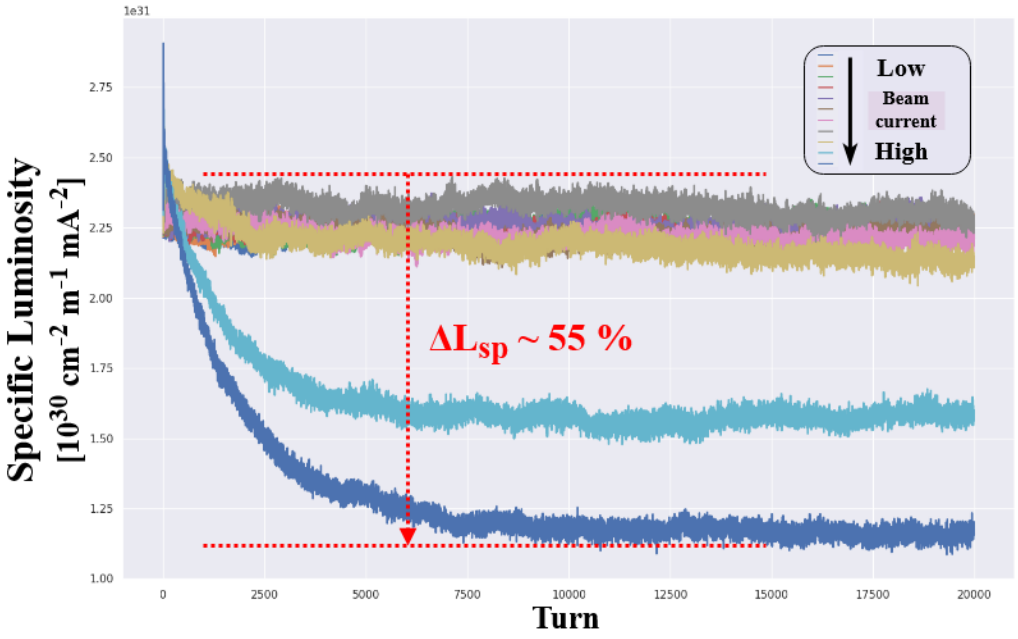

Figure 3.11: Specific luminosity with the weak and strong beams swapped.

realistic operating conditions unless each parameter is set optimally in accordance with the current value. This is because there is no guarantee that each value that is measured at low current during operation is retained when operation occurs under a high current.

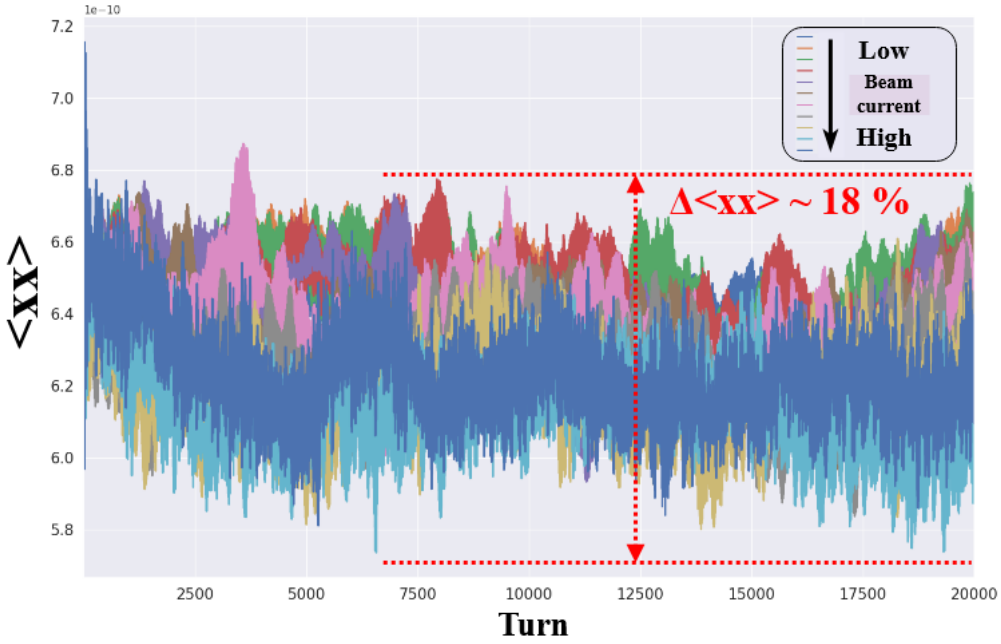

Figure 3.12: Horizontal beam size with the weak and strong beams swapped.

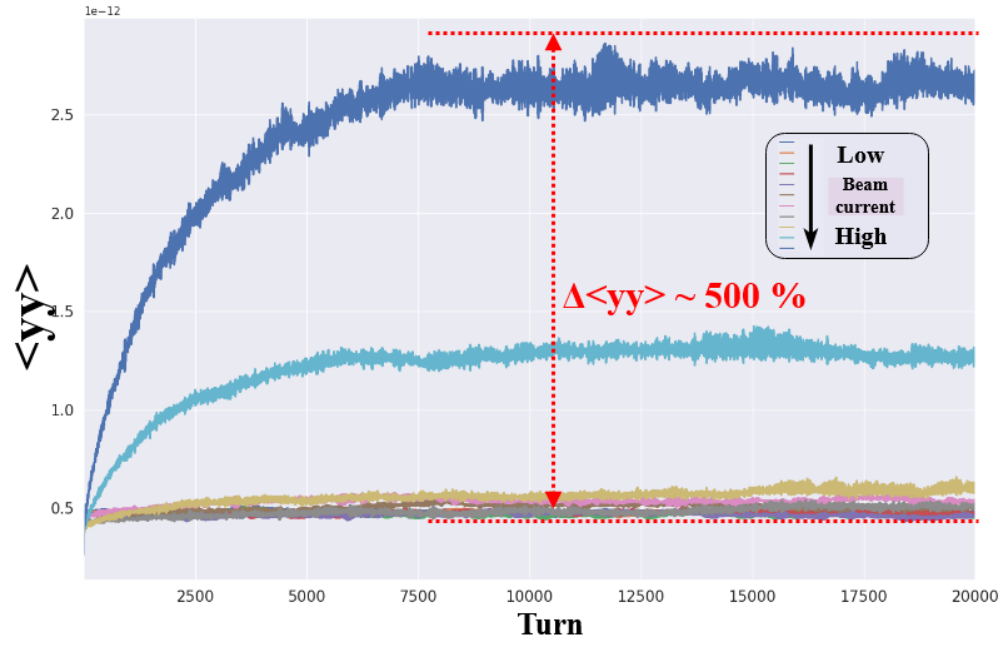

Figure 3.13: Vertical beam size with the weak and strong beams swapped.

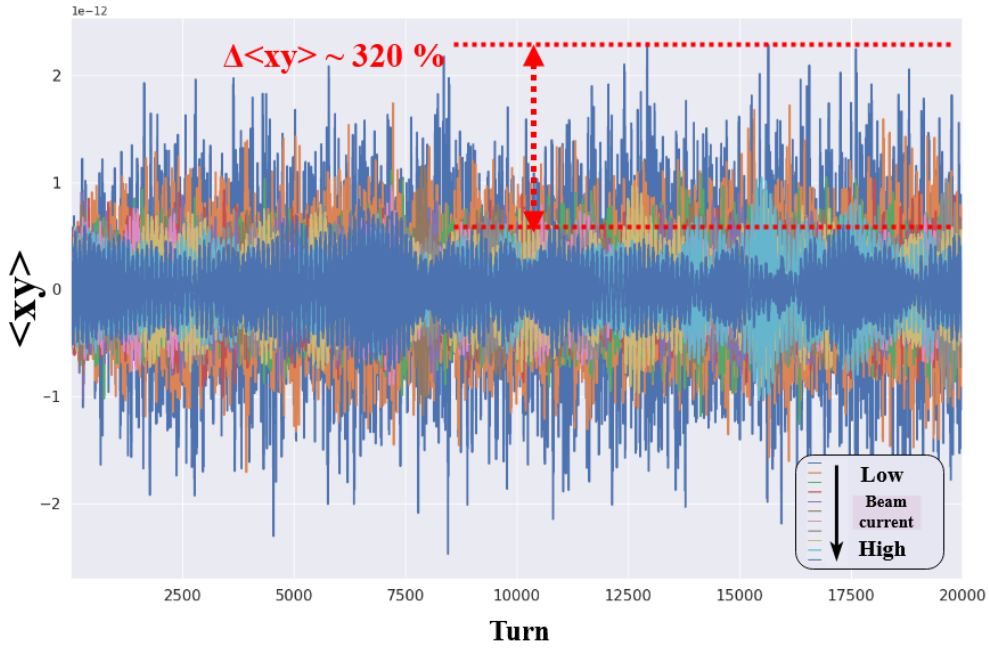

Figure 3.14: Correlation of x and y with the weak and strong beams swapped.

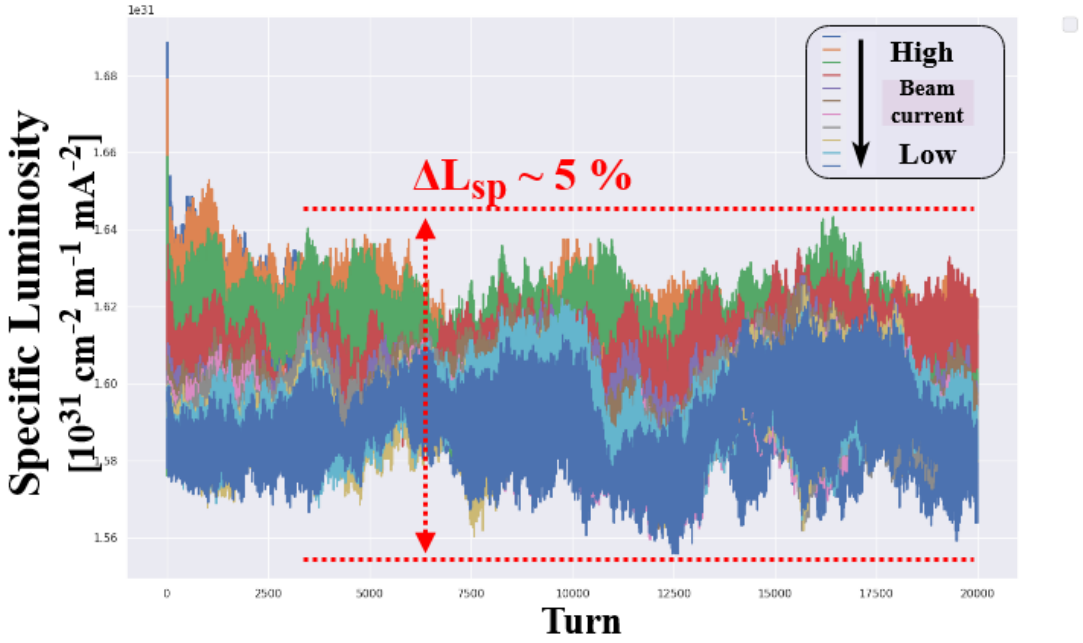

Figure 3.15: Specific luminosity depending on iteration for collision with the vertical beta doubled.

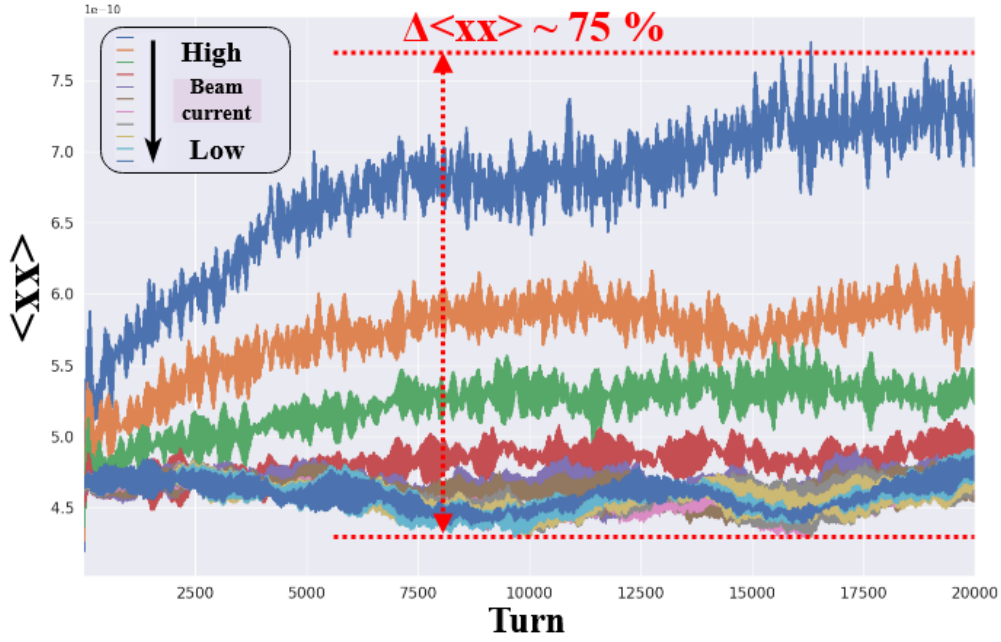

Figure 3.16: Horizontal beam size depending on iteration for collision with the vertical beta doubled.

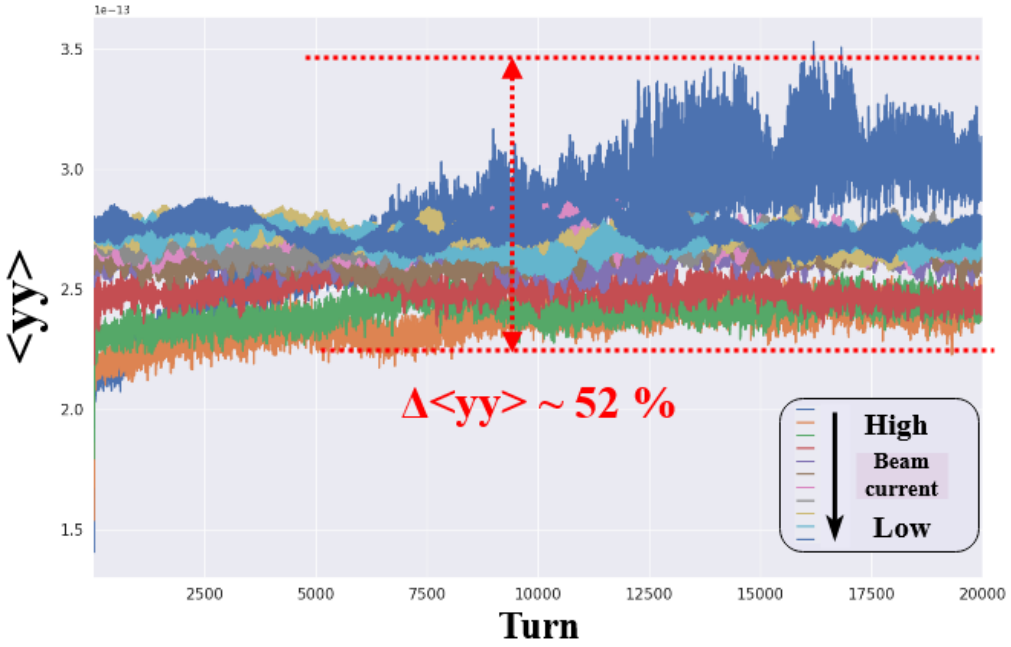

Figure 3.17: Vertical beam size depending on iteration for collision with the vertical beta doubled.

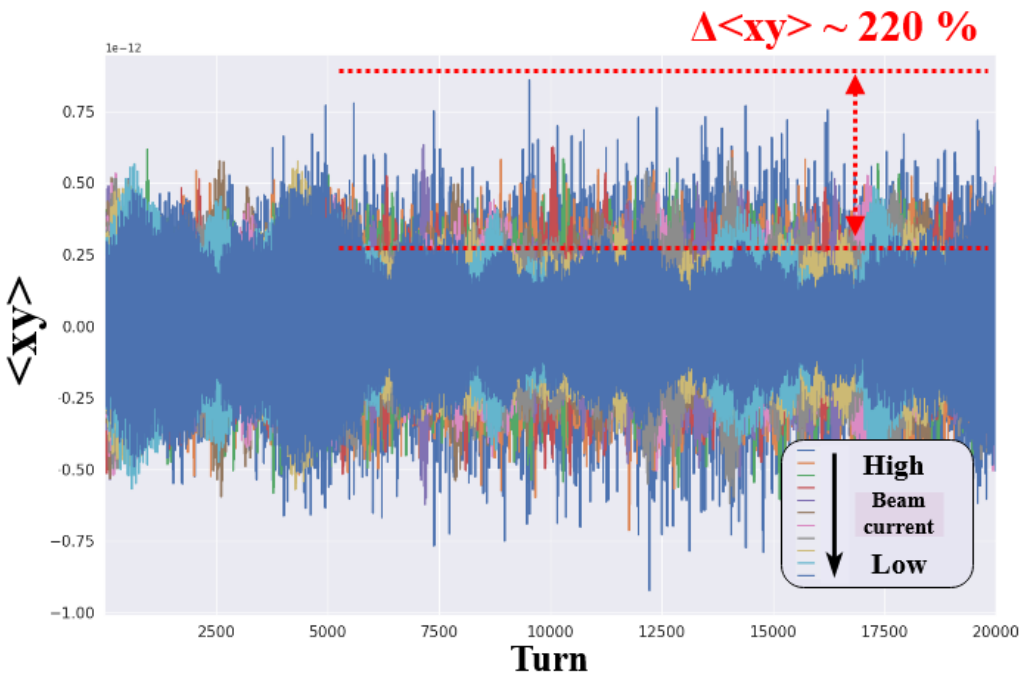

Figure 3.18: Correlation of x and y depending on iteration for collision with the vertical beta doubled.

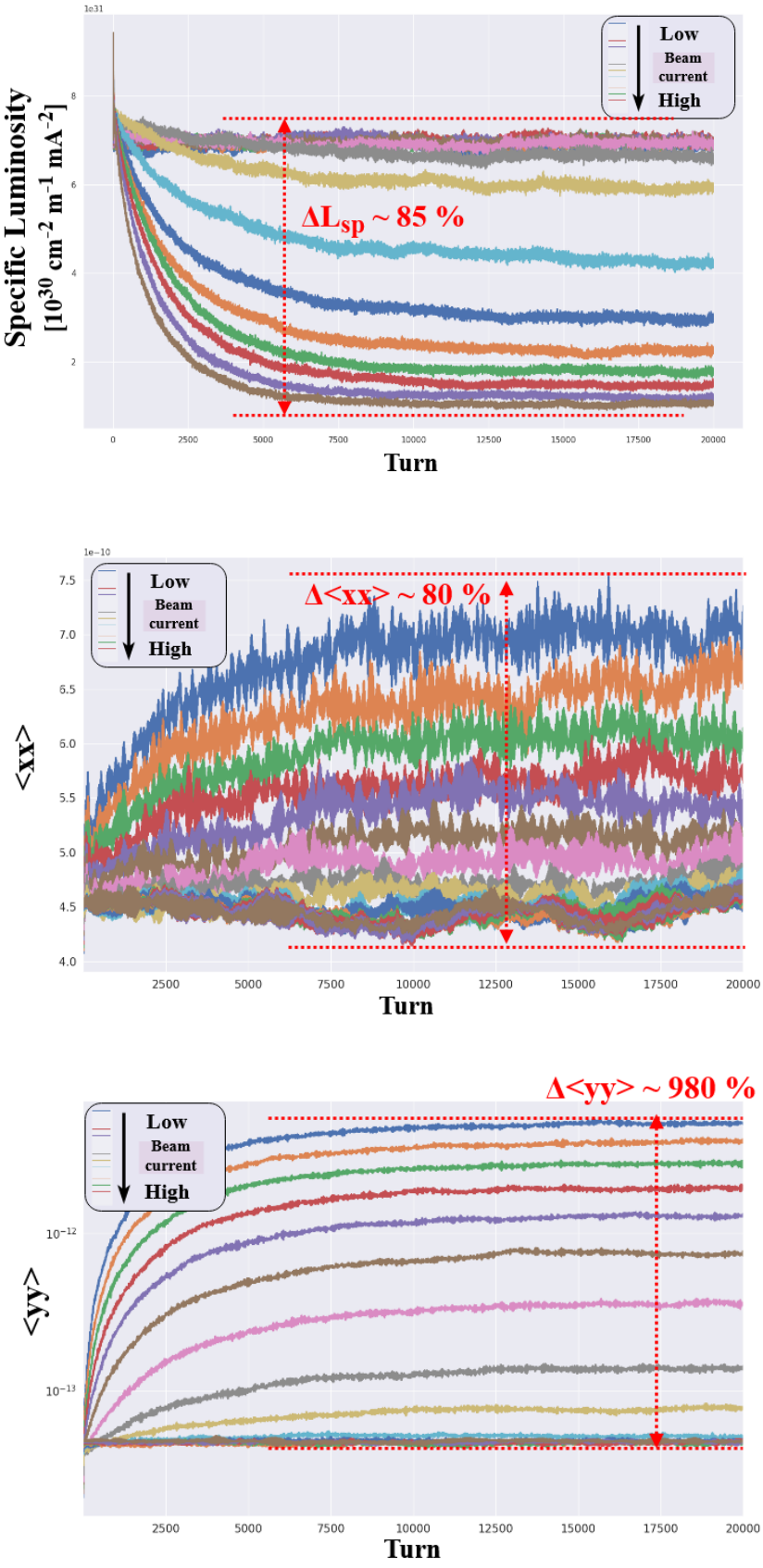

Figure 3.19: Beam–beam simulation result of condition in Tab. 3.5.

Chapter 4

Luminosity with Linear IP optics aberrations

4.1 Optical correction and the beam diagnostics system used at the IP of SuperKEKB

4.1.1 Tunable magnets to correct X–Y coupling at IP

SuperKEKB uses antechambers to counteract the electron–cloud instability that is due to horizontal synchrotron radiation, while avoiding irradiation of the beam pipe with vertical synchrotron radiation. Therefore, skew quadrupole-like corrector coils have been newly installed in the sextupole magnets of SuperKEKB instead of a vertical bump trajectory, in order to correct X–Y coupling and vertical dispersion.

The non-interleaved sextupole scheme[43] adopted in SuperKEKB can be used as a magnet for adjusting the vertical dispersion and X–Y coupling independently when a skew quadrupole magnetic field is excited. These types of sextupole magnets are operated in pairs and are placed at positions where the betatron phases differ from each other by π. By exciting the symmetrical quadrupole fields with the pair of sextupoles, the vertical dispersions cancel each other and therefore do not leak globally. On the other hand, as the X–Y coupling parameter is not canceled out, it can be used as a tuning parameter for the global X–Y coupling, by changing the strength of the skew quadrupole field. Inversely, when the skew quadrupole fields are excited antisymmetrically, the X–Y coupling parameters cancel each other and the vertical dispersion remains. In this case, it can be used as a vertical dispersion tuning parameter. Global parameter controls are therefore relatively easily made for the independent correction of X–Y coupling and vertical dispersion by determining

the function of a pair of non-interleaved sextupoles. Beam parameters at the IP require only a minimal amount of correction in order to keep the global parameters stable, while the correction of the tuning parameters is more significant because of the relationship in the betatron amplitude between the tunable magnets and the IP. Therefore, it is difficult to compensate for the X–Y coupling parameters at the IP using only global corrector magnets.

To alleviate this problem, we proposed a new local method for coupling the correction at the IP with the IR section by using skew corrector coils[44, 45, 46], which are installed in the QCS magnets. By exciting the QCS corrector coils, the skew quadrupole component SK1 of QCS magnets is changed by the pair of magnets at both sides of the IP (left and right side), and the X–Y coupling parameters are adjusted locally at the IP. The advantage of correcting the IP optical aberrations in the IR section is that the beta function is set to be significantly larger in preparation for the extremely low beta function at the IP. Since the beta function is high at the location of the QCS magnets, the effect of the magnetic field on the IP beam dynamics can be applied strongly. This means that the X–Y coupling parameters at the IP can be changed dramatically. As QCS corrector coils are not suitable for fine tuning, the skew quadrupole corrector coils of the non-interleaved pair of sextupole magnets is useful for precise tuning.

The luminosity peak is then obtained by scanning each parameter of the X–Y coupling and the vertical dispersion.

4.1.2 Diagnostics system for IP beam dynamics

Important parameters that influence beam dynamics at the IP are the components of the 6×6 beam matrix, which reveal information about a beam in 6-dimensional phase space. As they can be defined at each point on the ring, the control system of the beam over the entire ring handles a very large number of independent variables. However, we need only 21 variables for the upper triangular components of an IP beam matrix because the beam matrix is symmetrical at the IP. Diagonal components in the matrix represent the principal components of each physical variable, and the off-diagonal components represent the correlation or coupling variables. When the coordinates are completely independent over the entire ring, the off–diagonal components are zero. Generally, betatron and synchrotron oscillations are weakly coupled due to the characteristics and misalignment of the lattice components, and the off–diagonal components become non–zero. The important factor in this study is the off-diagonal components in the transverse direction, which represent the so-called X–Y betatron coupling.

The beam diagnostic system of SuperKEKB consists of beam position monitors (BPMs), which are provided for all the quadrupole magnets, and synchrotron radiation monitors [47, 48, 49, 50, 51]. Three types of synchrotron radiation monitors are used in SuperKEKB; synchrotron radiation interferometers (SRMs) [47, 52] and streak cameras for visible light, X-ray beam profile monitors (XRMs) [53, 54], and large angle beamstrahlung monitors (LABMs). LABMs are used to measure the relative offset and size ratio of the beams at the IP. XRMs are used to measure the vertical emittance. SRMs are used to measure the horizontal emittance. Streak cameras are used to measure the longitudinal bunch profile. BPMs are used to measure the beam position. The location of the synchrotron light sources for the measurement of the optics in the main ring of SuperKEKB is shown in Fig. 4.1.

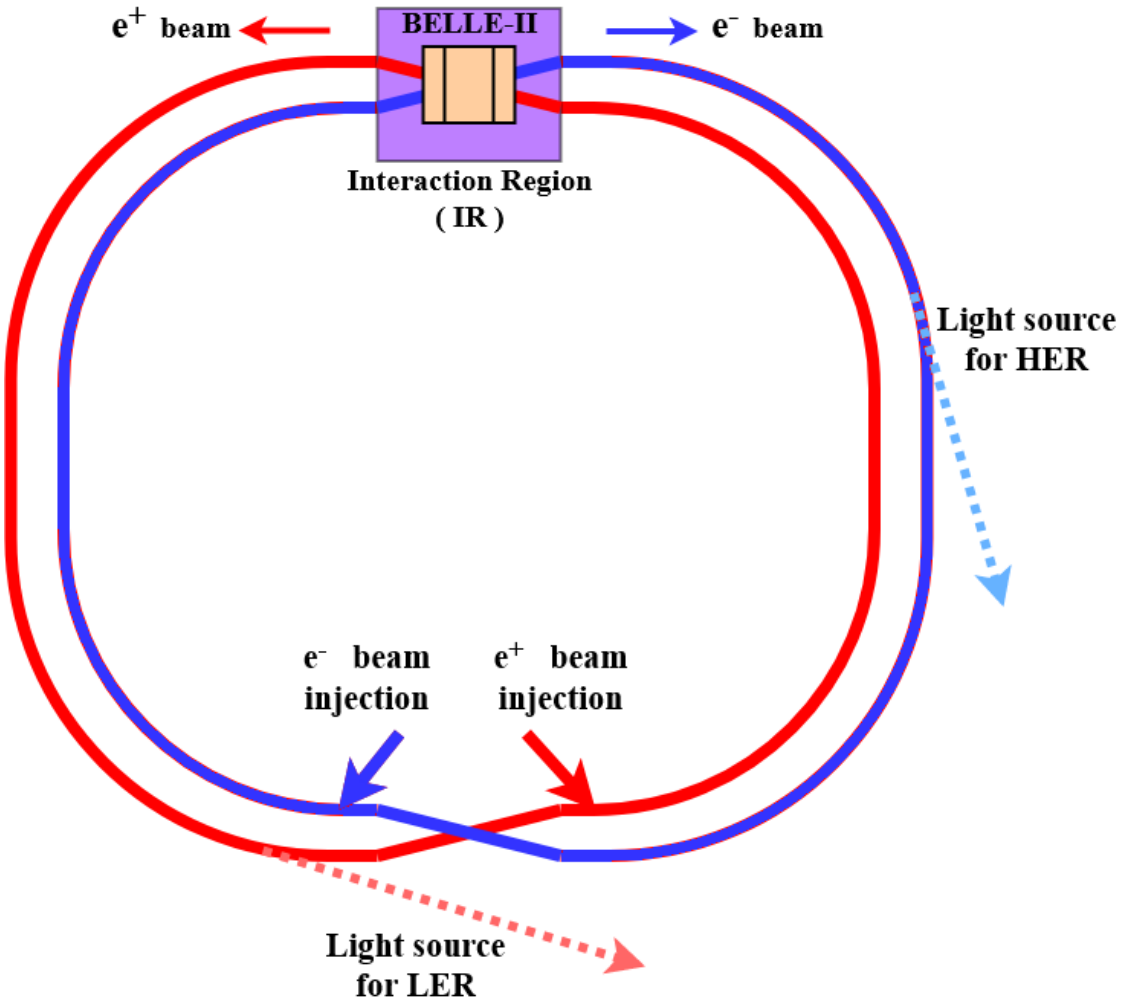

Figure 4.1: location of the synchrotron light source for beam diagnostics in SuperKEKB

LER has 438 BPMs in its BPM system, which is based on a 509 MHz narrow band detector, and there are 460 BPMs in HER, which is based on a 1 GHz narrow band detector[55]. All of the detectors are operated in an average mode. The average mode is also usually used in the measurement of optics, at 0.25 Hz. This mode can be used for the correction of the beam orbit and the alignment of a neighboring magnet. Some of the BPMs can also be performed in gated turn–by–turn (TbT) mode.

4.1.3 The difference in the effect of X–Y coupling between the positions of excitation and measurement

X–Y coupling is the difference in coordinates between the betatron oscillation and components of the lattice such as BPMs or magnets. As a result, the difference in the type of component with X–Y coupling (a measured (BPM) position and an interacted (kicker) position) affects the behavior of different parts of the beam in the measured data. The TbT measurement data is analyzed with the same sampling frequency as that of revolution, and it is usually subjected to spectrum analysis by Fourier transform. Since the eigenmodes of the betatron oscillation have individual fractional tuning, each peak of the betatron tune always appears at a different position in the Fourier spectrum. According to this property, the spectrum of the TbT data shows different behavior depending on the coupling position.

For example, if there is an X–Y coupling at the kicked location, the kicking magnet rotates slightly from the U- and V-axis of the betatron coordinates. When the dipole kick $\mathcal{F}_x$ is rotated by angle θ, the kick force is decomposed into each eigenmode:

$$\begin{cases} \mathcal{F}_u = \mathcal{F}_x \cos\theta \\ \mathcal{F}_v = \mathcal{F}_x \sin\theta \end{cases}, \tag{4.1}$$

as shown in Fig. 4.2. Thus, the leakage of the kick force that corresponds to the rotation angle occurs in the direction that should be orthogonal. As a result, the X–Y coupling at the kicker location shows the peak of each eigenmode for both directions in the spectrum. In other words, oscillations appear in two directions even though a kicker excites in only one direction. On the other hand, when there is the X–Y coupling at the measurement (monitoring) position, one eigenmode is measured on both directions of the BPM coordinates. This is the decomposition of a betatron oscillation into two directions. Fig. 4.3 shows the situation in which X–Y coupling takes place at the position of the monitor.

This phenomenon appears in the Fourier spectrum as a clear demonstration of

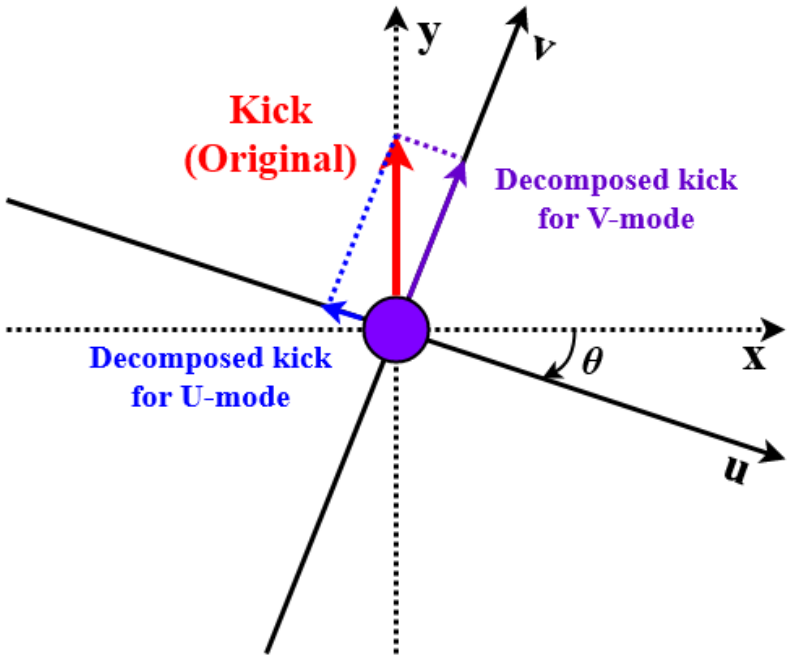

Figure 4.2: Kick force decomposition from physical coordinates to each betatron eigenmode.

harmonic analysis. Figure 4.4 shows the Fourier amplitude spectrum for the x and y direction of the BPM. The U-mode tune is colored green and the V-mode tune is colored orange. The frequency component after the Fourier transform is a fractional tune, which is the betatron or synchrotron frequency per revolution. For example, if there is kick in the x direction with a dipole field, and peaks appear at the same tune in the spectrum data of the x and y direction, there is a coupling at the monitor position as one eigenmode appears in the measurement for both directions. On the other hand, in the same situation, if a peak corresponding to the U-mode appears in the x direction and a peak corresponding to the V-mode appears in the y direction, there is a coupling at the kick position as the kick, which occurs only in one direction, is decomposed into both modes. This property works very well with the harmonic analysis that is discussed in a later section.

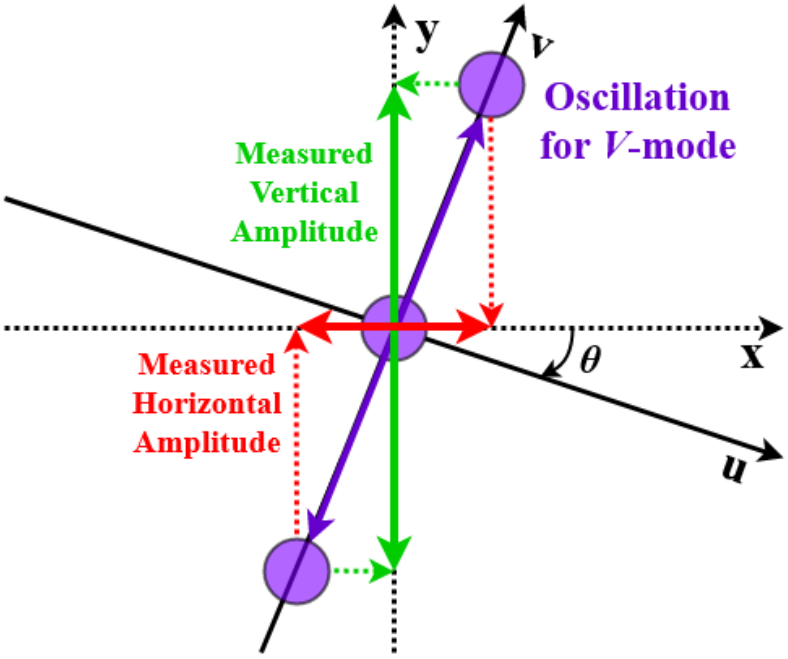

Figure 4.3: Oscillation decomposition from betatron eigenmode to the physical variables of the BPMs.

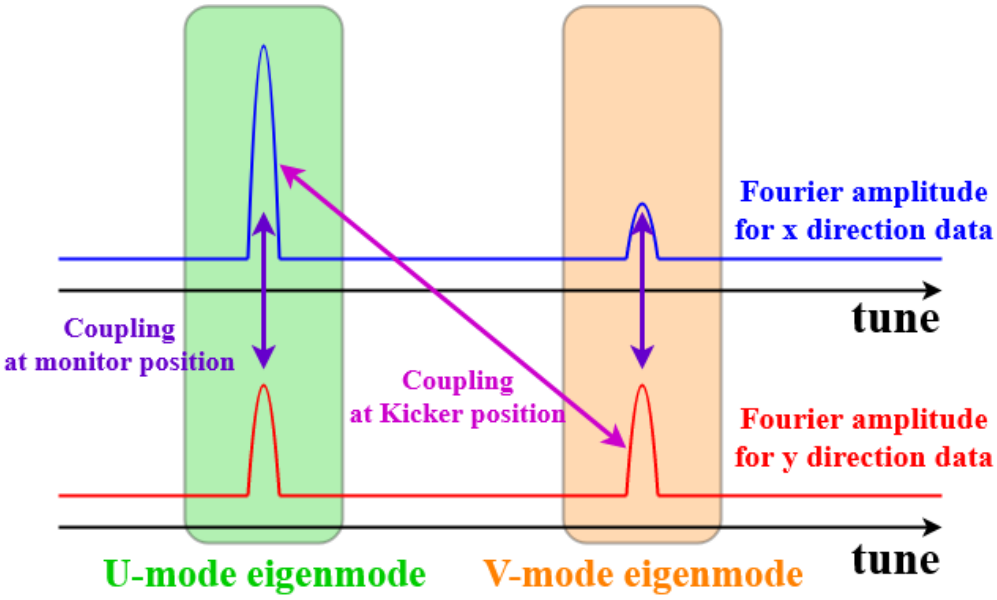

Figure 4.4: The difference in a Fourier spectrum caused by two coupling positions.

4.2 IP optical correction in Phase-2 Commissioning of SuperKEKB

4.2.1 The problem of optical aberrations at the IP in Phase-2 Commissioning

The collision method used in SuperKEKB is based on collision at a large crossing angle, which is part of the crab waist method that was proposed by P. Raimondi[19]. Thus far, analysis of the beam–beam effect and evaluation of luminosity with a finite crossing angle has been well modeled[56], and simulations of these collisions have been performed several times. In the early days of the collider, the vertical beam size was thought to be sufficiently unsqueezed because of the hourglass effect. One recent idea is pinpointing the waist of the beta function by setting a large crossing angle. Consequently, it is possible to expect a beam size that has effectively been sufficiently squeezed. In SuperKEKB, the effect of squeezing the beam size can be verified at the same time as sequential beam adjustments are made by squeezing the beta function step by step. One aim of SuperKEKB is to succeed using method of collision for the first time.

As the emittance must be preserved around the ring, the beam size at the collision point has a one-to-one correspondence with the beta function of the IP. Therefore, when the beta function is squeezed, the luminosity or specific luminosity should be smaller by $\beta_{\rm before}/\beta_{\rm after}$. However, no significant change was observed, even though the beta function was squeezed. Figure 4.5 shows the change in luminosity that is due to the change in β_y, where the vertical axis is the specific luminosity and the horizontal axis is the bunch current product. The different line colors in the plot denote the different values of β_x^* and β_y^*. Although there is a clear difference between the blue and orange plots , there are no significant differences between the $L_{\rm sp}$ of the orange, red, and green plots. As can be seen in the figure, the specific luminosity was not strong enough to squeeze the beta function at the IP for the smaller values of β_y^* at 4 mm and 3 mm. This problem remained even after collision tuning was carried out for first order aberrations.

It is thought that this occurred because the orbit was not properly adjusted at the collision point . In SuperKEKB, a method for scanning luminosity scan is used to adjust the trajectory of the collision point. Luminosity scanning is performed by making small successive changes to the trajectory in the transverse direction using steering magnets. For a shift in the longitudinal direction, the colliding position is scanned by changing the phase of the synchronized RF acceleration field (RF frequency).

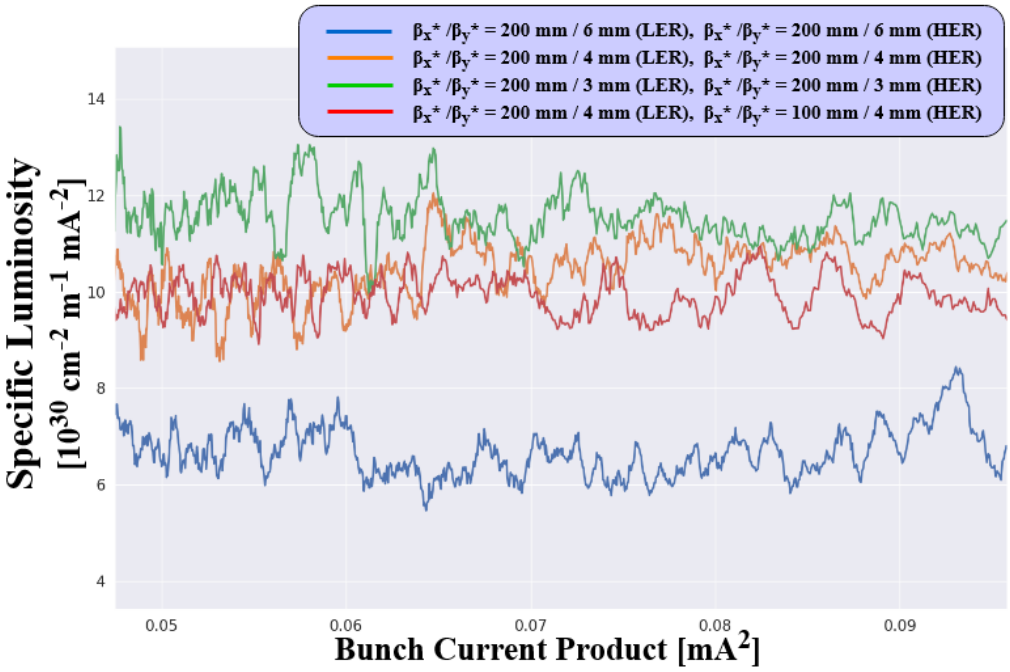

Figure 4.5: Specific luminosities for squeezing the beta function at IP

The systems used to measure Luminosity are LumiBelle2 (Luminosity Monitoring for Belle–2) and ZDLM (Zero Degree Luminosity Monitoring)[57, 58, 59].

The results of the luminosity scan of the closed orbit tuning for the vertical betatron waist function at the IP and RF phase tuning are shown in Fig. 4.6, 4.7, and 4.8, respectively. Correction of the orbit in a vertical (y) direction can be tuned by vertical offset scanning. The error in the longitudinal (z) direction can be corrected by tuning the RF phase via the synchronous phase of particles. The orbit in the horizontal (x) direction is adjusted by tuning the waist position in the betatron function. As shown in the Fig. 4.9, as the waist of the betatron function shifts, the betatron waist is adjusted in order to correct errors in the x direction. The trajectory in the x direction in real space does not dominate the projected beam size because of the effects of the large crossing angle collisions. From the result of the orbit tuning shown above, even when the first order error was adjusted sufficiently, the expected luminosity could not be obtained. Therefore, second order errors should be considered in order to correct the degradation in luminosity.

The conditions under which the problem remains unsolved, even when the adjustment for first order aberrations has been carried out, requires consideration. There are several possible causes for this problem. One potential reason is that β_y^* is not set properly. However, this can be avoided by measuring the beta function near the IP.

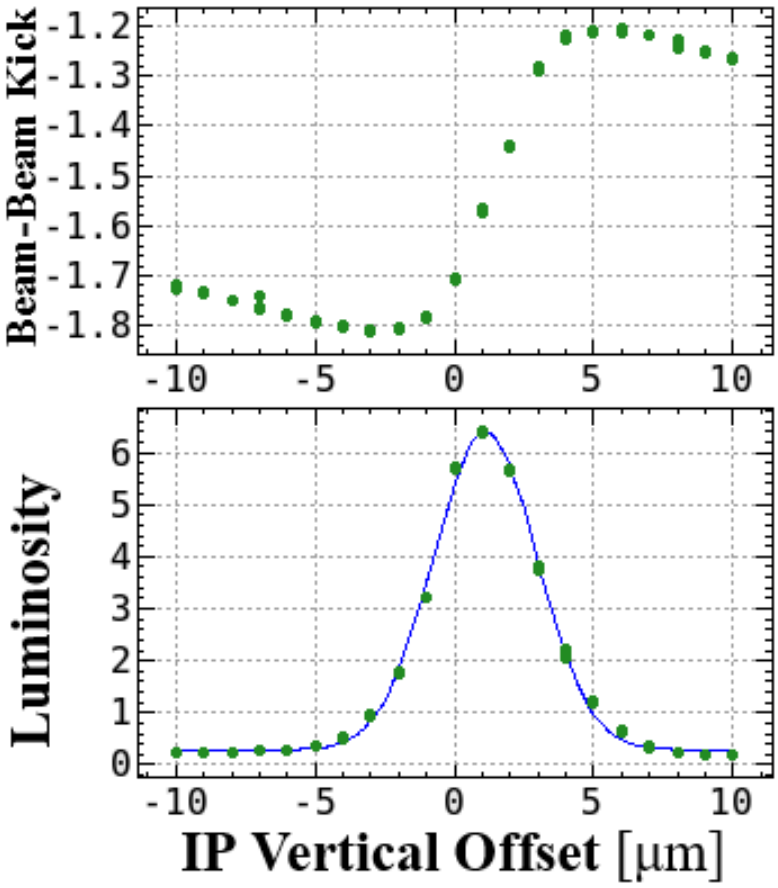

Figure 4.6: Measurement of the luminosity with a vertical offset scan.

The reason is that the pair of BPMs (MQC1) in the monitoring system are closer to the IP than the QC1, which is the final focusing quadrupole magnet that is located nearest to the IP. Figure 4.10 shows the positional relationship of QC1 and MQC1. As the interval between the IP and the MQC1 can almost be considered drift space, there is no problem if changes in the measured beam sizes correspond to a change in the betatron amplitudes before and after beta squeezing. The K–modulation method can be used to measure the β function at the collision point[60].

Another candidate for the problem is the situation under which β_y^* is not effective. This occurs when the effective beam size does not depend on β_y^*. As mentioned later, it was found that this was the actual cause of the problem. A hint for solving this problem can be found by investigating the relationship between the bunch current and the specific luminosity.

Figure 4.11 is a plot of “bunch current product vs. specific luminosity" under low luminosity. The blue and orange plots represent the specific luminosities that were

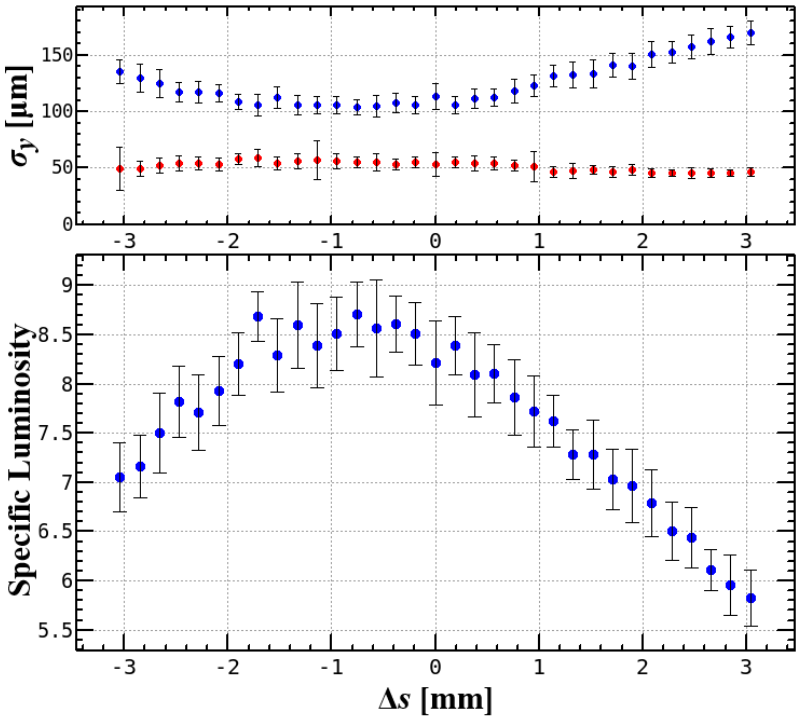

Figure 4.7: Measurement of the luminosity with a β waist scan.

calculated from the measured luminosity and the emittance measured with the XRM, respectively. This figure shows that there are two kinds of problem that can lead to luminosity degradation. One is the dependency of specific luminosity on current, even though specific luminosity is not supposed to depend on beam current, as indicated by the red line in the figure. The other problem is that the effective vertical beam size σ_y^* at the IP does not match the intrinsic beam size $\sqrt{\beta_v^* \varepsilon_v}$ at the IP. The green arrow in Fig. 4.11 indicates the presence of this issue. This problem can be seen in the discrepancy between the emittance measured by X-ray monitor and the luminosity measured using the luminosity monitor. In this study, we focused on the second problem and researched the cause of the situation at the IP in order to solve it.

4.2.2 Strategy of the IP optics correction

First, the effective beam size was calculated. As discussed in Sec. 3.2.2, the effective beam size is represented by Eq. (3.51), using the intrinsic emittance. The effective

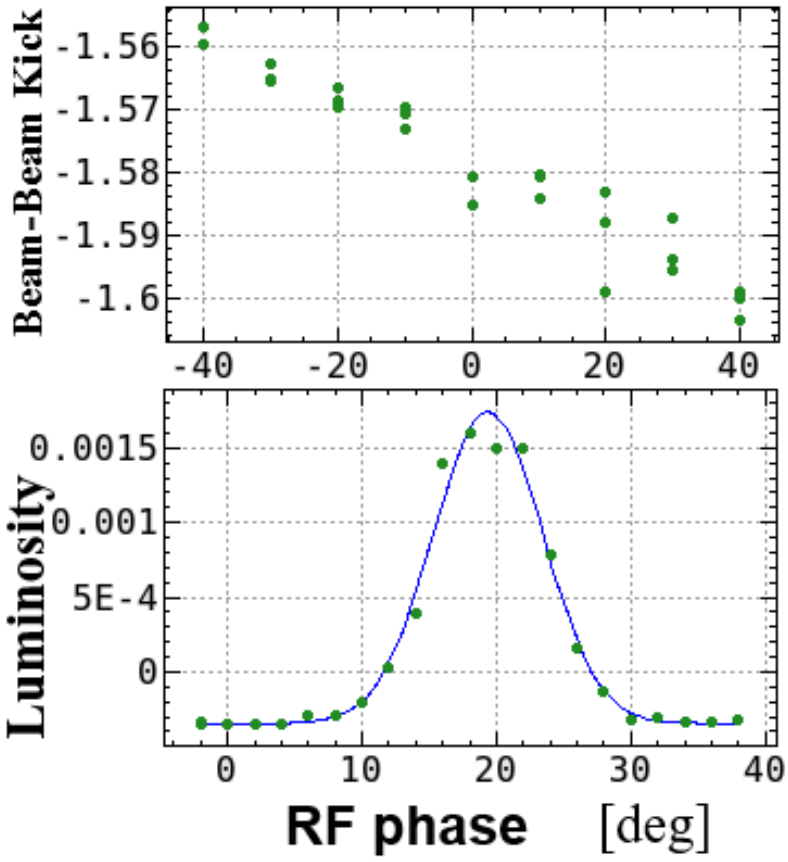

Figure 4.8: Measurement of the luminosity with a RF phase scan.

beam matrix is written as

$$\mathcal{R}.\mathcal{B}^*.\vec{x}.{}^t\vec{x}.{}^t\mathcal{B}^*.{}^t\mathcal{R} \tag{4.2}$$

$$= \begin{pmatrix} r_0^2\sigma_u^{*2} + r_4^2\sigma_v^{*2} + r_2^2\sigma_{u'}^{*2} & -r_3r_4\sigma_v^{*2} - r_1r_2\sigma_{v'}^{*2} & -r_0r_1\sigma_u^{*2} + r_0r_4\sigma_v^{*2} & -r_0r_3\sigma_u^{*2} - r_0r_2\sigma_{v'}^{*2} \\ -r_3r_4\sigma_v^{*2} - r_1r_2\sigma_{v'}^{*2} & r_0^2\sigma_{u'}^{*2} - r_3^2\sigma_v^{*2} + r_1^2\sigma_{v'}^{*2} & -r_0r_2\sigma_{u'}^{*2} - r_0r_3\sigma_v^{*2} & r_0r_1\sigma_{v'}^{*2} - r_0r_4\sigma_{u'}^{*2} \\ r_0r_4\sigma_v^{*2} - r_0r_1\sigma_u^{*2} & -r_0r_2\sigma_{u'}^{*2} - r_0r_3\sigma_v^{*2} & r_0^2\sigma_v^{*2} - r_1^2\sigma_u^{*2} - r_2^2\sigma_{u'}^{*2} & r_1r_3\sigma_u^{*2} + r_2r_4\sigma_{u'}^{*2} \\ -r_0r_3\sigma_u^{*2} - r_0r_2\sigma_{v'}^{*2} & r_0r_1\sigma_{v'}^{*2} - r_0r_4\sigma_{u'}^{*2} & r_1r_3\sigma_u^{*2} + r_2r_4\sigma_{u'}^{*2} & r_0^2\sigma_{v'}^{*2} + r_3^2\sigma_u^{*2} + r_4^2\sigma_{u'}^{*2} \end{pmatrix}, \tag{4.3}$$

with Edward-Teng parametrization, where $\sigma_u^{*2} = \beta_u^*\varepsilon_u$, $\sigma_v^{*2} = \beta_v^*\varepsilon_v$, $\sigma_{u'}^{*2} = \varepsilon_u^*/\beta_u$, and $\sigma_{v'}^{*2} = \varepsilon_v^*/\beta_v$. It is assumed that $\alpha_i = 0$ at the betatron waist of the IP. This beam matrix is the same as the beam correlation matrix at the IP. The diagonal components denote the expected beam size in each direction, and the off-diagonal components denote the correlation in two-dimensional phase space.

The vertical beam size should be used in the evaluation of the effect of X–Y coupling on the IP. The effect that this coupling has on the vertical components is

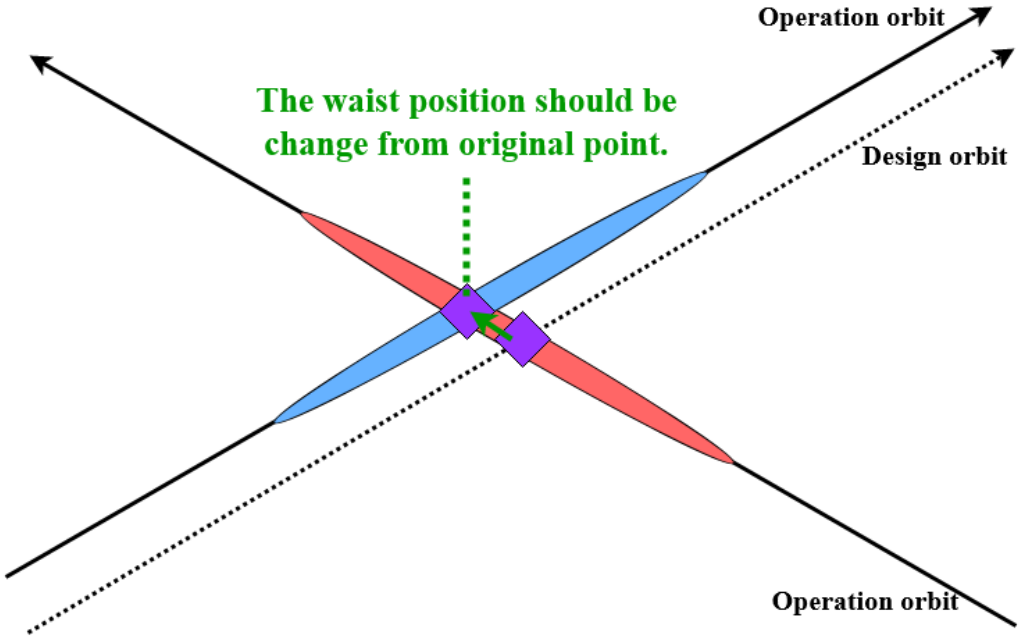

Figure 4.9: Schematic of the relationship between a horizontal orbit error and a waist in the beta function.

important to luminosity performance because the emittance ratio $\varepsilon_v/\varepsilon_u$ equals 0.01 under SuperKEKB commissioning. As the effective beam size in each direction is represented by the diagonal components, the effective vertical beam size is given by the intrinsic emittance, as follows

$$\sigma_y^{*2} = r_0^2\beta_v^*\varepsilon_v - r_1^2\beta_u^*\varepsilon_u - r_2^2\frac{\varepsilon_u}{\beta_u^*} \tag{4.4}$$

$$\sigma_{py}^{*2} = r_0^2\frac{\varepsilon_v}{\beta_v^*} + r_3^2\beta_u^*\varepsilon_u + r_4^2\frac{\varepsilon_u}{\beta_u^*}. \tag{4.5}$$

It is apparent from this equation that r_1 and r_2 cause a blow up of the vertical beam size, and r_3 and r_4 cause a blow up of the vertical momentum. Although a single collision is not effective in creating vertical momentum, the beam properties are affected by the accumulated beam–beam effects in a circular collider.

The effective vertical beam size is directly affected by r_1 and r_2 when X–Y coupling occurs. r_3 and r_4 affect the momentum, and the beam–beam effect, together with the effects from the revolution around the ring, will affect the cumulative beam blow-up in the next revolution in a circular accelerator. Each coupling parameter can be adjusted using skew quadrupole correction coils, either using sextupole magnets outside the IR or QCS skew corrector coils inside the IR. Table 4.1 and 4.2 show the name and positional relationship of each correction magnet of the non-interleaved

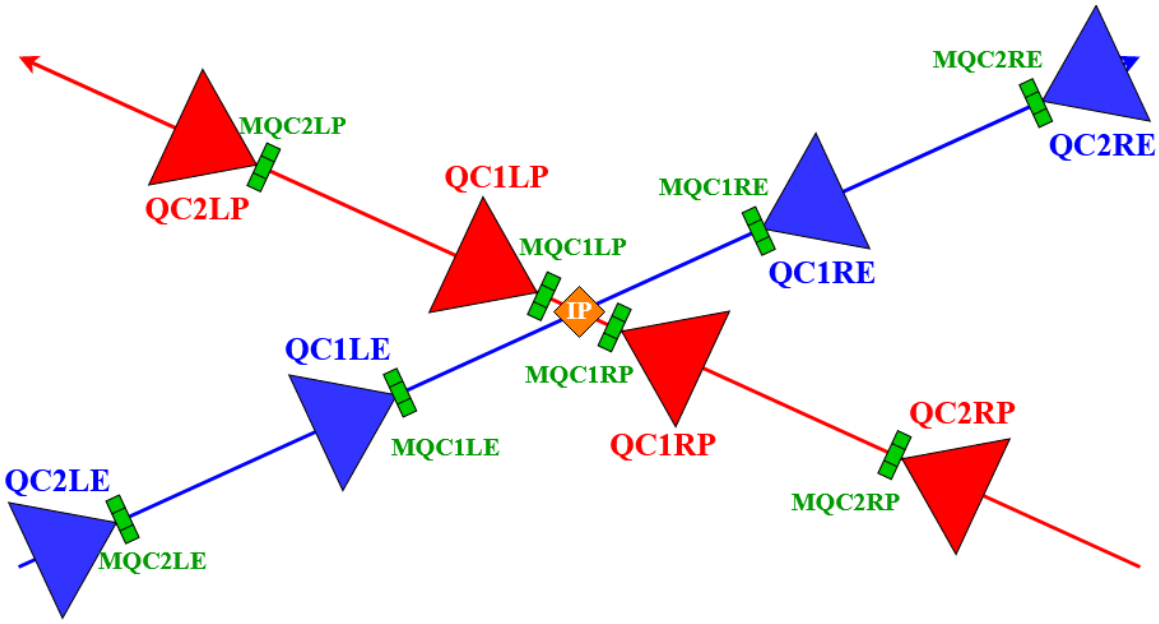

Figure 4.10: Illustration of the positional relationship between QCS magnets and their monitors.

sextupole of HER. In these tables, #1 and #2 are the index of the pair components for each skew quadrupole (installed in the sextupole). As can be seen, there is a much higher betatron amplitude at SLYTRE/LE than at other positions, so magnets that are located in this position are most effective in changing the IP beam parameters.

4.2.3 Calculations of the effect of each magnet on IP beam dynamics

The effect that the correction made by the corrector magnet at the IR and the QCS has on the IP coupling parameters is calculated in this subsection. The model used for this calculation is shown in Fig. 4.12. The optical aberration for the beam at a particular location is calculated using the revolution matrix that was designed for this purpose, which consists of the multiplied transfer matrixes for each cell on the beam line. If the transfer matrix from the source to the destination is known, the revolution matrix can be easily calculated, including the errors. It is important that the thin lens approximation model is applied as an additional error in the transfer matrix in order to calculate the revolution matrix with the associated errors included. As the length of the component is neglected in the thin lens approximation model, the same transfer matrix as that used to calculate the interval between the error source and the transfer destination can be used to calculate the inverse matrix for a round trip.

For the development of a more realistic model, the complete form of a transfer

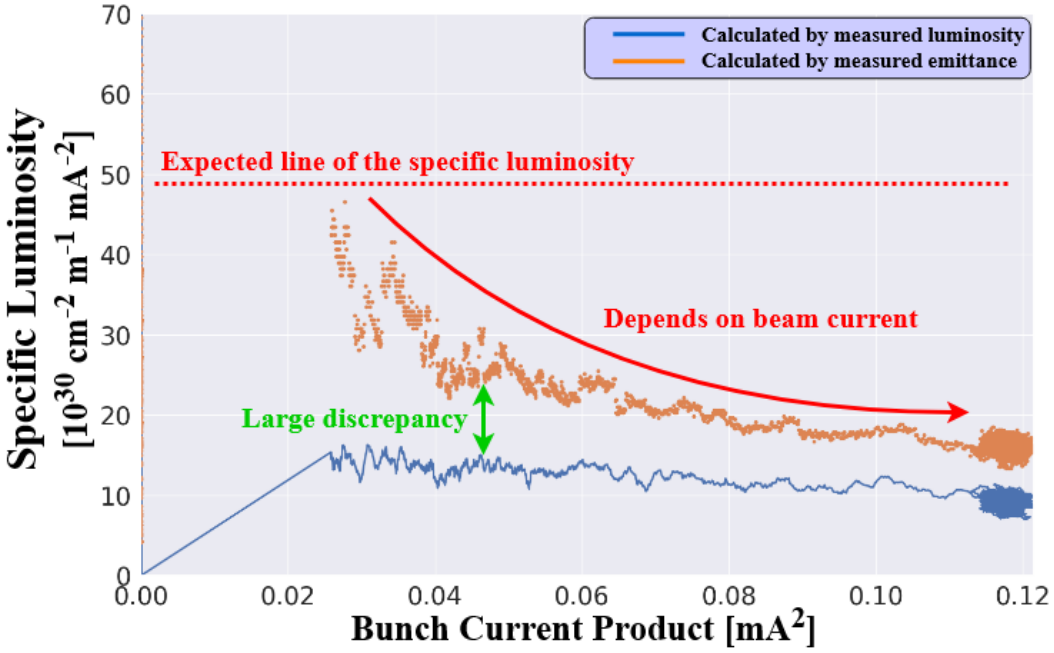

Figure 4.11: Luminosity measurements to investigate the dependence of specific luminosity on the bunch current before X–Y coupling correction is carried out at the IP.

matrix should be used, Which includes the effective length; therefore it is necessary to use a transfer matrix which depends on length. A model of an error matrix with an effective length is shown in Fig. 4.13. It is difficult to define an accurate edge position in this model, meaning that it becomes very complicated. Therefore, the thin lens approximation model is adopted in this study.

The effect of the magnet located outside the IR on the IP can be calculated using the transfer matrix of the SAD. Referring to Table 4.1 and 4.2, we find that there are two major differences in the beam properties at the positions of the skew quadrupole coils. One is the difference in the amplitudes of the beta functions. Apparently, the beta function of SLYTLE / RE differs from that of the other magnets. For example, the effects of the two magnets (#1 and #2) at SD3RE and SLYTRE on the IP are calculated and compared, as shown below. The action of the magnet is converted into a normalized beam matrix and rewritten as a Twiss parameter for evaluation. In

Name	s [m] (#1)	s [m] (#2)	β_x (#1)	β_x (#2)	β_y (#1)	β_y (#2)
SF2OLE	2385.37194	2420.93347	30.1743	32.0504	9.68394	9.20193
SF4OLE	2461.04235	2496.60387	30.1743	32.0504	9.68394	9.20193
SF6OLE	2536.71275	2572.27428	30.1743	32.0504	9.68394	9.20193
SF8OTE	2612.80954	2663.39391	25.7300	28.6248	19.9147	18.7856
SD3OLE	2426.45925	2454.82056	7.36690	7.15343	20.2939	17.0478
SD5OLE	2502.12965	2530.49097	7.36690	7.15343	20.2939	17.0478
SD7OLE	2577.80006	2606.16138	7.36690	7.15343	20.2939	17.0478
SF6TRE	2703.92917	2739.49070	30.1743	32.0504	9.6839	9.2019
SF4TRE	2779.59958	2815.16111	30.1743	32.0504	9.6839	9.2019
SD7TRE	2669.3460	2697.7073	7.3668	7.1534	20.2939	17.0478
SD5TRE	2745.0164	2773.3778	7.3668	7.1534	20.2939	17.0478
SD3TRE	2820.6868	2849.0482	7.3668	7.1534	20.2939	17.0478
SLYTRE	2961.22187	2988.31336	12.6848	14.0985	187.7451	163.7934

Table 4.1: Non-interleaved sextupoles with tunable skew quadrupole coils on the right-side of the IP for HER.

this example, the X–Y coupling parameters for each magnet are calculated using

$$\begin{cases} r_1 &= -0.297 k_{\mathrm{SD3RE}} \\ r_2 &= 1.499 k_{\mathrm{SD3RE}} \\ r_3 &= -2145.1 k_{\mathrm{SD3RE}} \\ r_4 &= -148.0 k_{\mathrm{SD3RE}} \end{cases} \begin{cases} r_1 &= -1.183 k_{\mathrm{SLYTRE}} \\ r_2 &= -5.61 k_{\mathrm{SLYTRE}} \\ r_3 &= -10019.8 k_{\mathrm{SLYTRE}} \\ r_4 &= -191.1 k_{\mathrm{SLYTRE}} \end{cases} . \tag{4.6}$$

Table 4.3 lists the values of the coupling parameters at the IP by setting $k_{\mathrm{name}} = k_{\#1,\#2} = 1$ for each component in Eq. (4.6). Although this result is trivial from the above equations, the effect of SLYTRE is 5 times greater than that of SD3RE. Many of the other components are similar to SD3RE, so tuning SLYTRE should be performed carefully in order to avoid unexpected results.

The correction by the QCS can also be calculated using the transfer matrix of SAD. The beta function at the QCS is particularly high around the ring, so the effect of optical errors on the beam in the IR section is significant. Let the skew errors of QC1 and QC2 be $k_{\mathrm{1L/R}}$ and $k_{\mathrm{2L/R}}$, respectively. In this case, the formula for

Name	s [m] (#1)	s [m] (#2)	β_x (#1)	β_x (#2)	β_y (#1)	β_y (#2)
SLYTLE	27.50208	54.39357	19.4207	18.7513	170.0203	167.5412
SD3TLE	164.75795	193.11927	7.3668	7.1534	20.2939	17.0478
SD5TLE	240.42836	268.78968	7.3668	7.1534	20.2939	17.0478
SD7TLE	316.09877	344.46008	7.3668	7.1534	20.2939	17.0478
SF4TLE	199.34105	234.90258	30.1743	32.0504	9.6839	9.2019
SF6TLE	275.01146	310.57298	30.1743	32.0504	9.6839	9.2019
SF8TNE	351.08329	400.73960	21.6101	24.5508	26.4936	24.5566
SD7NRE	406.6668	435.0281	7.3668	7.1534	20.2939	17.0478
SD5NRE	482.3372	510.6985	7.3668	7.1534	20.2939	17.0478
SD3NRE	558.0076	586.3689	7.3668	7.1534	20.2939	17.0478
SF6NRE	441.24990	476.8114	30.1743	32.0504	9.6839	9.2019
SF4NRE	516.92031	552.48184	30.1743	32.0504	9.6839	9.2019
SF2NRE	592.5907	628.1522	30.1743	32.0504	9.6839	9.2019

Table 4.2: Non-interleaved sextupoles with tunable skew quadrupole coils on the left-side of the IP for HER.

$k_{\mathrm{SD3.1/2}}$	$k_{\mathrm{SLY.1/2}}$	r_1	r_2	r_3	r_4
1	0	-0.297	1.499	-2145.1	-148
0	1	-1.183	-5.61	-10019.8	-191.1

Table 4.3: Comparison of coupling parameters at IP by setting $k_{=}1$ for SD3RE and SLYRE.

estimating the effect of each magnet is:

$$\begin{cases} r_1 &= -4.07k_{1\mathrm{L}} - 0.000719 \\ r_2 &= -0.0137k_{1\mathrm{L}} - 0.0000795 \\ r_3 &= -288k_{1\mathrm{L}} + 0.0732 \\ r_4 &= -262k_{1\mathrm{L}} - 0.0555 \end{cases} \tag{4.7}$$

$$\begin{cases} r_1 &= -32.3k_{2\mathrm{L}} - 4.0 \times 10^{-6} \\ r_2 &= -1.38k_{2\mathrm{L}} - 4.56 \times 10^{-7} \\ r_3 &= -223k_{2\mathrm{L}} + 0.000453 \\ r_4 &= -2235k_{2\mathrm{L}} - 0.000315 \end{cases} \tag{4.8}$$

Table 4.4 shows the values of the coupling parameters at the IP that are obtained by setting $k_{1\mathrm{L}} = 1$ or $k_{2\mathrm{L}} = 1$. The transfer matrix for the IR is symmetrical to that of the IP; thus, the effect at the counter side (QC1RE and QC2RE) is the same as that seen in Table 4.4.

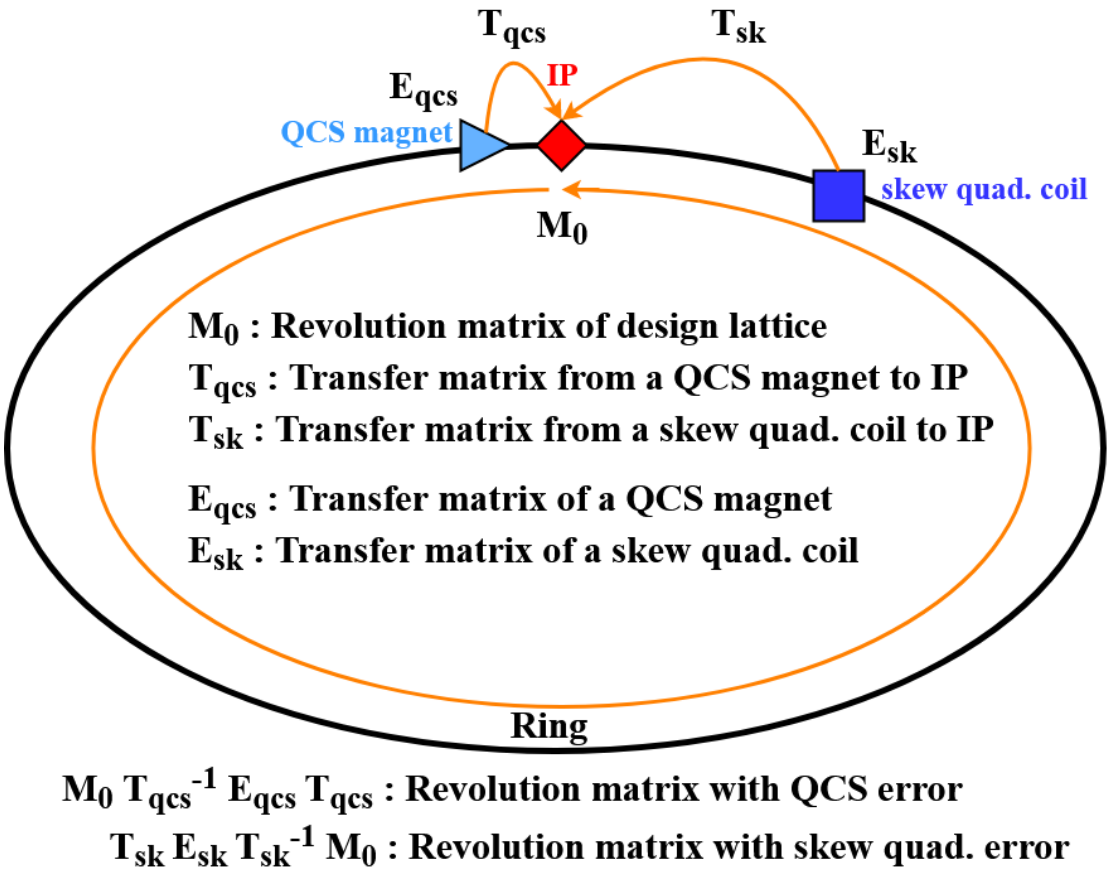

Figure 4.12: Schematic of the error transfer model for the IP beam property at each location.

4.2.4 Numerical simulation of the effect of each coupling parameter on luminosity and IP beam parameters

As the conditions under which collision takes place cannot be directly measured, beam–beam simulation is the only means by which it can be estimated by using measurable information about the beam. Simulation is one of the most important indicators used for collision tuning, as it can be used to estimate beam conditions at the IP by calculating the luminosity response obtained using scanning parameters that cannot be measured directly. By comparing between the simulated and the measured luminosity, a reasonable model of the collision conditions can be obtained.

Two levels of the simulation for detail of the collision; strong–strong and weakŮstrong, are introduced in Sec. 3.1. The strong–strong simulation, which includes the coherent phenomenon, complicates the calculation. Thus, the weak–strong beam–beam simulation is suitable for estimating the luminosity performance with several optical errors without obtaining the wrong reason for the cause of degradation. This study

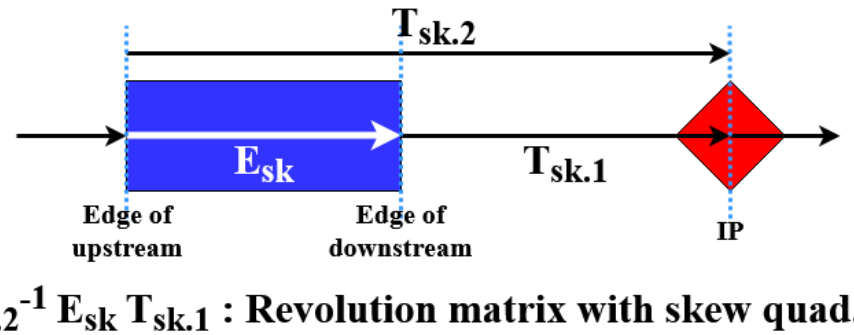

Figure 4.13: Schematic of the error transfer model with finite magnet length for an error component.

k_{1L}	k_{2L}	r_1	r_2	r_3	r_4
1	0	−4.072	−0.01378	−288.1	−262.1
0	1	−32.28	−1.378	−223.4	−2236

Table 4.4: The effect of thin skew components at QC1LE and QC2LE on the IP linear coupling parameter.

discusses only beam–beam conditions with lattice imperfections within the incoherent dynamics of the beams at the IP. In this step, several types of optical errors are assumed in the beam–beam simulations, and the results of these simulations are used as a reference to estimate the beam conditions during the operation of SuperKEKB by using data analysis from the previous section (Sec. **??**)

The important parameters in beam-beam simulations are the emittance, beta at the IP, damping rate, bunch current, crossing angle, and the optical aberrations at the IP. Table 4.5 lists these parameters for beam-beam simulations under several conditions used in the operation of SuperKEKB in Phase-2 and Phase-3 commissioning. Table 4.6 shows the list of beam-beam parameters and the tune shift for the results of the simulation at the designed current.

Phase	#2(HER)	#2(LER)	#3(HER)	#3(LER)	#3'(HER)	#3'(LER)
ε_y	20.0	8.0	16.2	6.05	40	40
ε_x	5.0	2.2	4.466	1.64	4.49	1.93
β_y^*	3	3	2	2	2	2
β_x^*	100	200	80	80	80	80
ν_y	43.57	46.57	43.5835	46.606	43.583	46.605
ν_x	45.5275	44.561	45.5345	44.542	45.53	44542
ν_s	0.02717	0.02349	0.02717	0.02349	0.02717	0.02349

Table 4.5: Beam parameters for the simulation of SuperKEKB Phase–2 and –3 commissioning.

Condition	B–B param. of e^- x/y	B–B param. of e^+ x/y	tune shift of e^- x/y
#2	0.4506/0.4936	1.599/1.3847	0.0048/0.0517
#3	0.4457/0.6905	1.5878/1.9446	0.0048/0.0727
#3'	0.8967/3.6162	1.6582/2.3843	0.0049/0.2661

Table 4.6: beam-beam parameters and tune shift for the conditions used in each beam–beam simulation at the designed current.

The simulations of several parameters are shown in Fig. 4.14 - 4.16, using scanning coupling parameters (r_1, r_2, r_3, r_4). These figures suggest the impact of the coupling parameters on the IP beam dynamics. Figure 4.14 shows the dependence of the beam collision on these coupling parameters during Phase 2 commissioning.

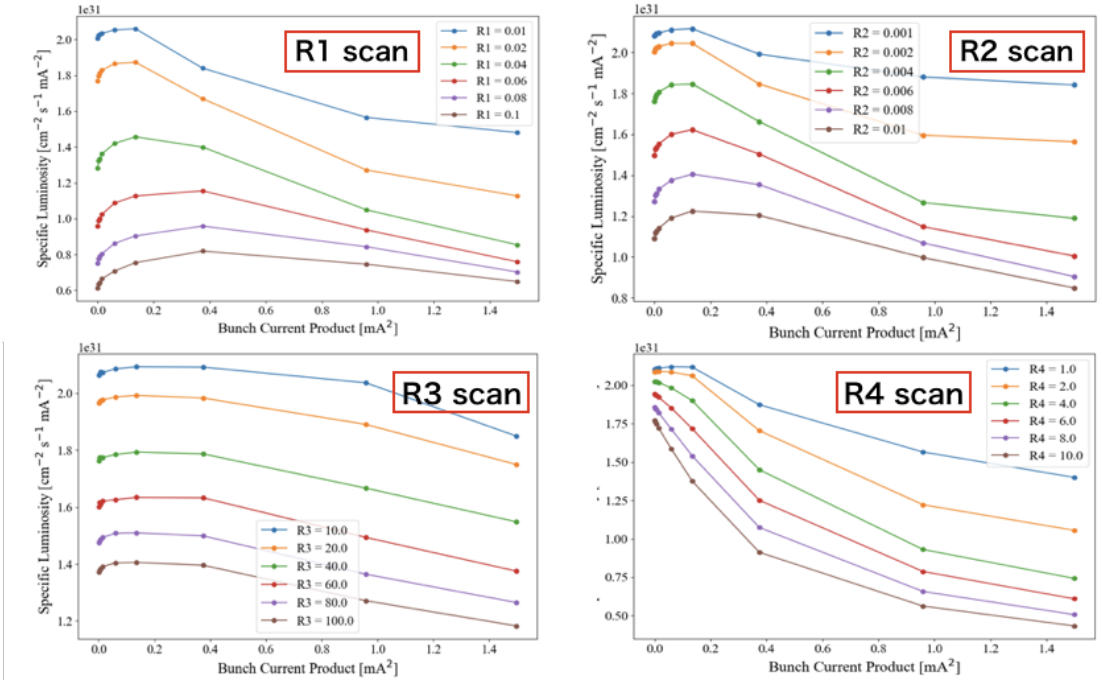

Figure 4.14: Luminosity degradation for scanning coupling parameters of SuperKEKB Phase-2 commissioning.

Figure 4.15 shows the response of luminosity to the scanning coupling parameters. In Phase-3 commissioning, the beta function of the IP was $(\beta_x^*, \beta_y^*) = (100, 2)$ for LER and $(200, 4)$ for HER. This value is same as Phase-2.2 commissioning but the luminosity degradation is a little different from that obtained using the Phase-2.2 condition, because the other parameters were changed.

Scanning is carried out in steps in order to investigate the luminosity degradation on a linear scale. The effective scale used for each coupling parameter r_1, r_2, r_3, and r_4 is in the order 0.01, 0.001, 1000, and 1000, respectively. In geometric terms, r_1

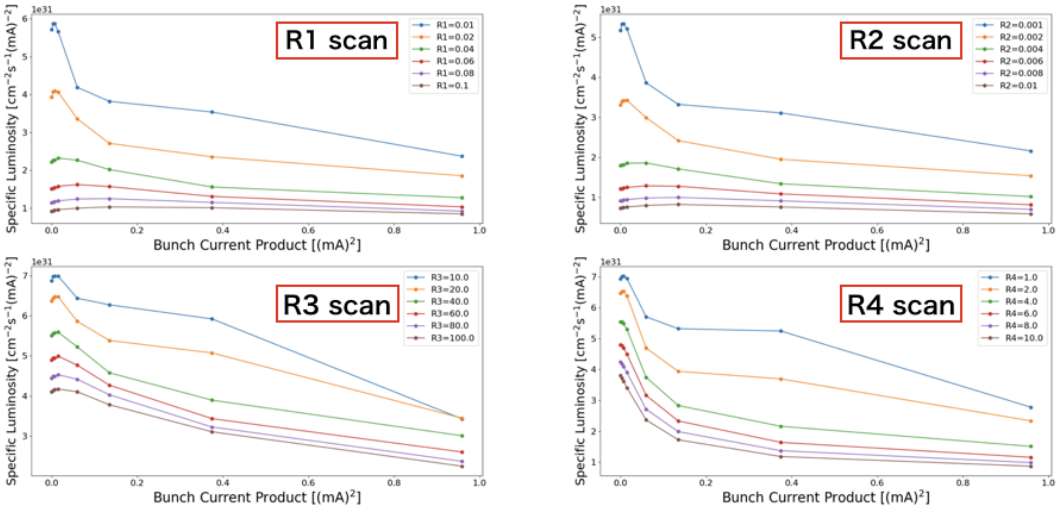

Figure 4.15: Luminosity degradation with the scanning coupling parameters of SuperKEKB Phase-3 commissioning version 1 (Phase-3.1 in Table 4.6).

and r_2 directly enlarge the projected beam size of y. r_3 and r_4 enlarge the vertical momentum, which is coupled with the horizontal beam size. The horizontal beam size is coupled with the vertical beam size via the parameter r_1. The physical meaning of these scales is the transverse tilt of the bunches, affecting the beam size as follows:

	r_1	r_2	r_3	r_4
$\Delta\sigma_y^*$	0	0	0	0

Table 4.7: Optical aberrations of the beam size corresponding to coupling parameters.

4.2.5 The result of the correction of IP X-Y coupling and comparison with simulations

The coupling error at the IP was adjusted using r1 and r2 for the main adjustment. The coupling parameters were adjusted to obtain the peak value of the scanned luminosity using skew quadrupole corrector coils and luminosity monitors. The parameters r_1, r_3, and r_4 could only be scanned sufficiently and on a global basis by using the corrector magnets located outside the IR. Figure 4.17- 4.20 shows examples of the scanned parameters. In the scan results of r_1, r_3, and r_4, it is apparent that the scanning covered a sufficient range in order to find the peak in luminosity. On the other hand, regarding the r_2 scan, it is thought that the peak in luminosity was located outside the range of the scan. Thus, a means of changing the parameter r_2 by a large amount is required.

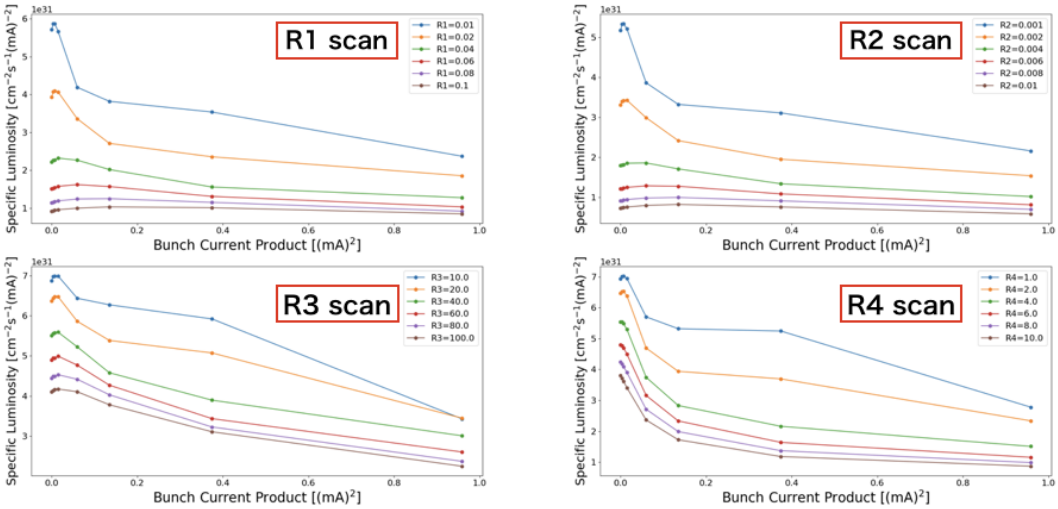

Figure 4.16: Luminosity degradation with the scanning coupling parameters of SuperKEKB Phase-3 commissioning version 2 (Phase-3.2 in Table 4.6).

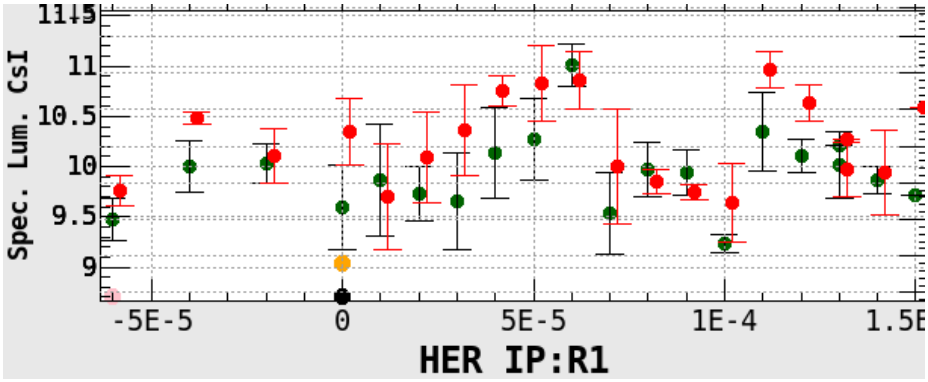

Figure 4.17: Specific Luminosity measurements for scanning linear coupling parameters.

The adjustment of r_2 at the IP was corrected by using the skew collector coil at QC1. A good collision can only be achieved if the optical errors are compensated for, at least at the local point of the collision. In addition, the effect of the coupling correction cannot be allowed to leak globally, in order to avoid complicating the effect that other components have on the beams. Thus, coupling parameters must be compensated for locally, in the immediate vicinity of the IP.

The effect of QC1 coupling parameters can be modeled as illustrated in Fig. 4.21. This model is actually the same as the calculation of the error sources around the IP that are shown in Fig. 4.50. The difference between the models in Fig. 4.21 and Fig. 4.50 is that the former model is only assumed to calculate the relationship between the coupling parameters at the IP and the skew components at the QC1

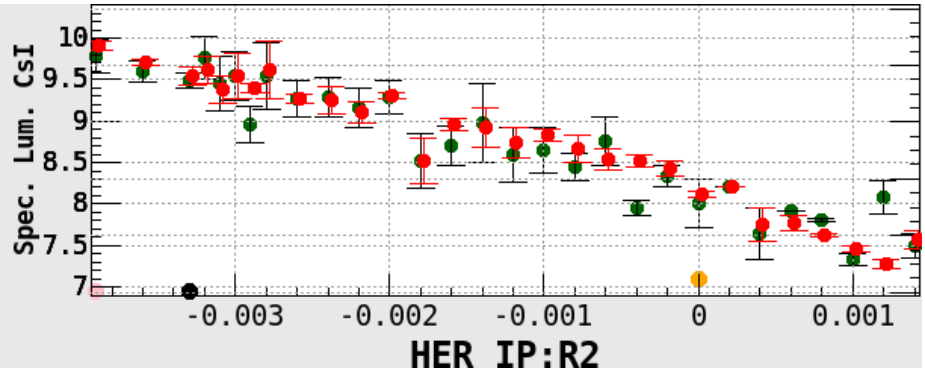

Figure 4.18: Specific Luminosity measurements for scanning linear coupling parameters.

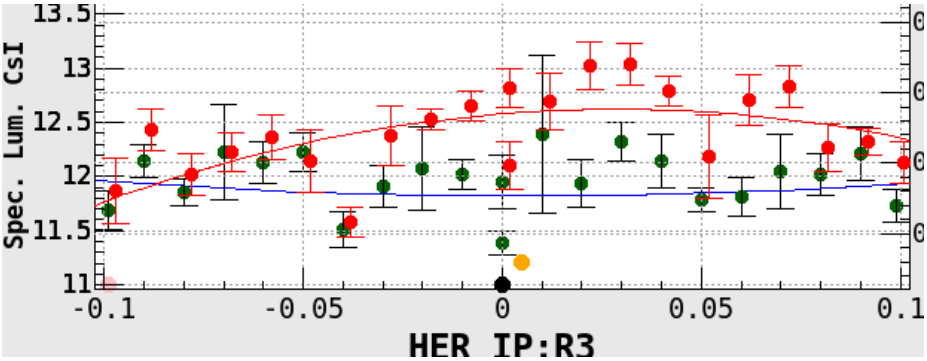

Figure 4.19: Specific Luminosity measurements for scanning linear coupling parameters.

magnets. If QC1 is represented by a skewed thin quadrupole lens, the relationship between its components k_{1l}, k_{1r} and the coupling parameters can be written

$$r_1 = -14.9k_{1l} - 14.9k_{1r} \tag{4.9}$$
$$r_2 = 0.716k_{1l} - 0.716k_{1r} \tag{4.10}$$
$$r_3 = 487k_{1l} - 487k_{1r} \tag{4.11}$$
$$r_4 = -1156k_{1l} - 1156k_{1r}, \tag{4.12}$$

and

$$r_1 = -6.52k_{1l} - 6.52k_{1r} \tag{4.13}$$
$$r_2 = -0.136k_{1l} + 0.136k_{1r} \tag{4.14}$$
$$r_3 = -533k_{1l} + 533k_{1r} \tag{4.15}$$
$$r_4 = -483.9k_{1l} - 483.9k_{1r}, \tag{4.16}$$

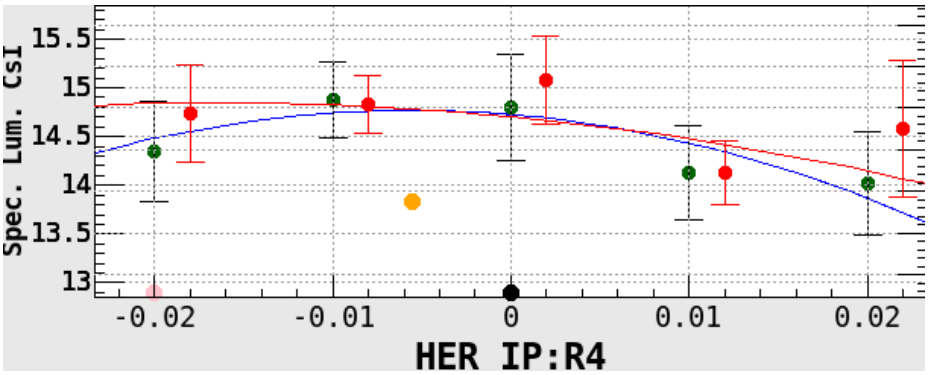

Figure 4.20: Specific Luminosity measurements for scanning linear coupling parameters.

for HER and LER, respectively. In the same manner as that used for calculating the QC1 skew error, the combination of the QC1 and QC2 errors can be obtained via

$$\begin{pmatrix} r_1 \\ r_2 \\ r_3 \\ r_4 \end{pmatrix} = \begin{pmatrix} -14.9 & -38.6 & -14.9 & -38.6 \\ 0.716 & 2.05 & -0.716 & -2.05 \\ 487 & 843 & -487 & -843 \\ -1156 & -3030 & -1156 & -3030 \end{pmatrix} \begin{pmatrix} k_{\mathrm{l1}} \\ k_{\mathrm{l2}} \\ k_{\mathrm{r1}} \\ k_{\mathrm{r2}} \end{pmatrix} \tag{4.17}$$

and

$$\begin{pmatrix} r_1 \\ r_2 \\ r_3 \\ r_4 \end{pmatrix} = \begin{pmatrix} -6.52 & -13.6 & -6.52 & -13.6 \\ -0.136 & -0.421 & -0.136 & 0.421 \\ -533 & -825 & 533 & 825 \\ -483.9 & -1034 & -483.9 & -1034 \end{pmatrix} \begin{pmatrix} k_{\mathrm{l1}} \\ k_{\mathrm{l2}} \\ k_{\mathrm{r1}} \\ k_{\mathrm{r2}} \end{pmatrix} \tag{4.18}$$

for HER and LER, respectively. If the cause of the error comes only from QC1 (in fact, large global X–Y couplings are not observed in the practical operation of SuperKEKB), the skew component must be symmetrical as $k_{\mathrm{1r}} = -k_{\mathrm{1l}}$, because the error does not leak outside the IR. In this case, $r_1 = r_4 = 0$ is obtained by Eq. (4.9). Thus, it seems that the coupling parameters r_1 and r_4 cannot be used effectively to explain IP aberration. The parameters r_3 and r_4 affect the blow up of σ_x, as the phase–space ellipse is tilted on a $x - y(p_y)$ plane. Hence, r_2 has the most effect on IP coupling.

Figure 4.17- 4.20 shows the results of both the r2 parameter scan and the other parameter settings. The scans of r_1 and r_2 were carried out on 15/June/2018, the scanning of r_3 was conducted on 17/June/2018, and the scanning of r_4 was performed on 18/June/2018. Beam–beam simulations of the scanned coupling parameters were

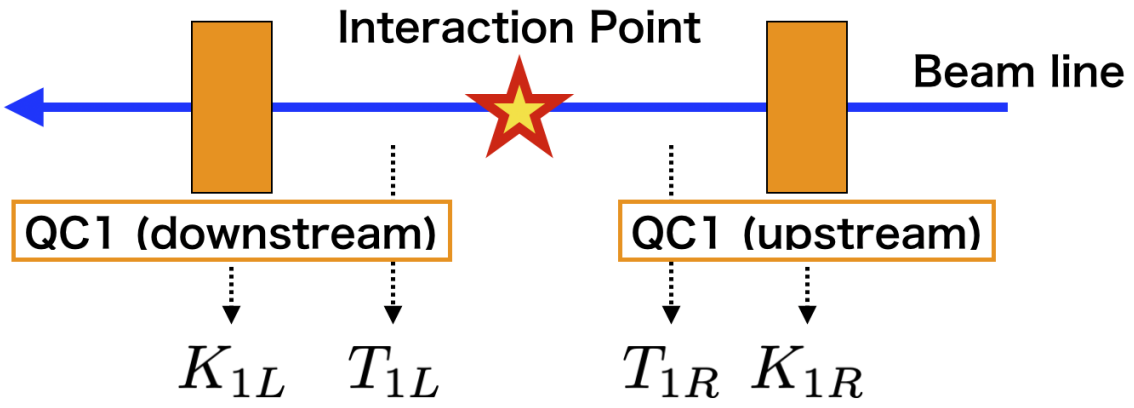

Figure 4.21: The skewed error model of the QC1 magnet.

referred to in the process of scanning. The results of the luminosity scan indicate that the parameter r_2 had the largest effect on tuning. The results of the simulation also indicated that r_2 is the most sensitive. When $k_{1\mathrm{r}} = -k_{1\mathrm{l}} = 0.0049$, $r_1 = r_4 = 0$, $r_2 = -0.007$, and $r_3 = 4.76$, the effective value of r_3 is greater than 10.0.

Figures 4.22 and 4.23 show the specific luminosity before and after optimization of the coupling parameters, respectively. Before tuning of the coupling parameters was carried out, the specific luminosity was very low, and the beam size measured by the luminosity monitor disagreed with that obtained as measured emittances by the X-ray monitors. After the coupling parameters were tuned, specific luminosities gathered by the two methods were found to agree. Consequently, the measured specific luminosity in the high current operation is two times higher than that before correction, and the luminosity tuning of linear X-Y coupling has been well established using this method.

4.3 Comparative investigation of the coupling analysis at the IP

4.3.1 The type of measurement and the data generated

The measurement of the X–Y coupling at the collision point is an interesting topic in the field of particle colliders, and the method used for the derivation of accurate coupling factors was adequately discussed in KEKB[61, 62]. The method of deriving X–Y coupling by measurement is equivalent to obtaining four-dimensional phase space coordinates at a specified position. The X–Y coupling, which describes the coupling

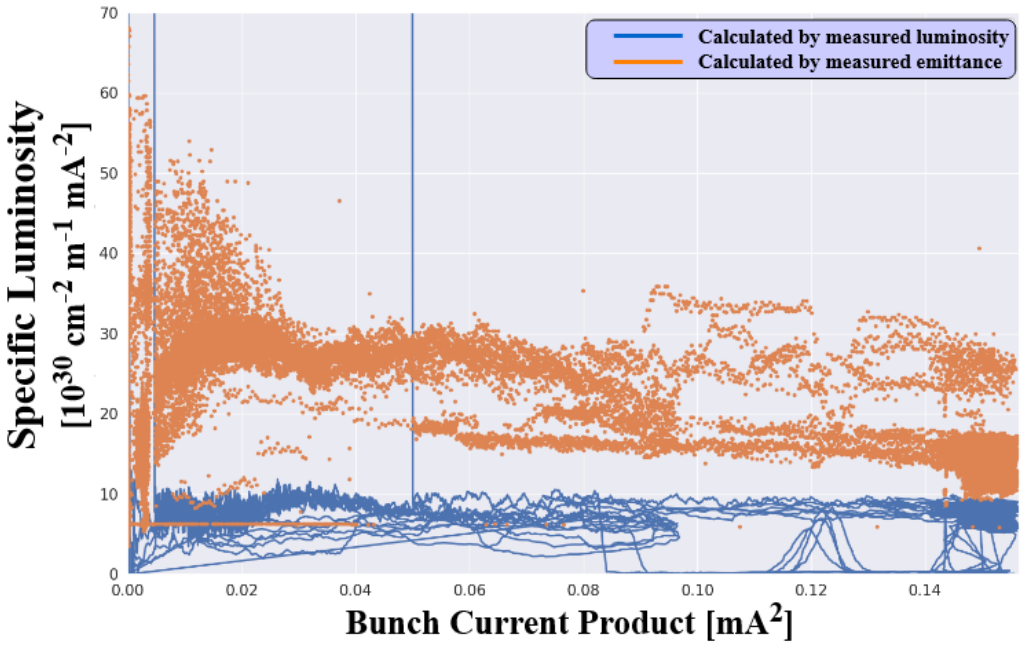

Figure 4.22: The Specific luminosity calculated by measured luminosity (blue) and by measured beam emittance using the X-ray monitor (orange) before the coupling parameter optimized.

of betatron eigenmodes, can be analyzed via the behavior of the beam at a certain point, because the beam can be considered a circle or ellipse with respect to the oscillation of the betatron eigenmodes, in the manner proposed by E. D. Courant and H. S. Snyder[22]. In other words, X-Y coupling is defined as the deviation of the BPM coordinate system from the betatron coordinate system. Therefore, two methods can be used to derive the coupling parameter: drawing an ellipse for each mode of the betatron oscillation, or separating and analyzing the mode of betatron oscillation via harmonic analysis. In this thesis, the former method is named the ellipsoid fitting method or the orbit response analysis method, and the latter is the harmonic analysis method.

In order to perform the ellipsoid fitting method, it is necessary to measure an exact elliptic orbit without any perturbation. From the definition of betatron oscillation, the motion of accelerated particles in the phase space at any position is characterized by an ellipse in four-dimensional phase space with a conservation system for the emittance. It is therefore necessary to initiate a kick in the direction of the eigenmode of the betatron oscillation. The betatron phase at the point measured depends on the kick position. An accurate ellipse can be drawn if the beam is kicked at different posi-

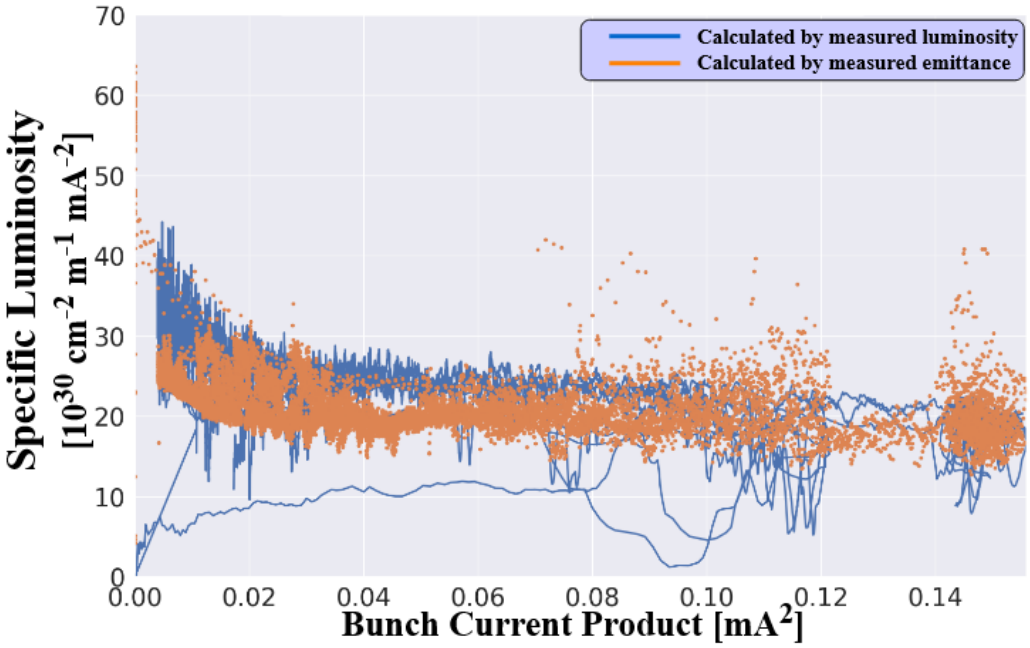

Figure 4.23: Specific luminosity calculated from the measured luminosity (blue) and the measured beam emittance using an X-ray monitor (orange) after the coupling parameter is optimized.

tions with different betatron phase shifts between the IP and each of these positions. This method is the same as the single kick COD measurement used in the measurement and fitting of the beta function. The method utilizes a forced oscillation in the direction of the kick using a dipole magnet (steering magnet) that is installed for use in both a vertical and a horizontal direction. The single kick COD is expressed using Eq. (3.34). In SuperKEKB, this single kick COD is measured in 6 different phases to fit the beta function. Fitting an ellipse to the phase space obtained via a single kick COD allows the evaluation of the betatron amplitude and phase advance, the tilt of the U-mode plane (α), and the X-Y coupling parameters. As the X–Y coupling to be calculated is the coupling at the point of measurement, it is necessary to consider the case in which the oscillation of one eigenmode is measured on both coordinate axes in the BPM coordinate system. Therefore, measurement of the X–Y coupling at locations that are not measurement points is not preferable for calculating coupling parameters because the kick affects the oscillation of the unexpected mode. Normally, unexpected kick forces are eliminated by correcting the global X–Y coupling, the skewed steering magnet, which is an external force of the forced oscillation, can be given a large coupled amplitude. It is therefore necessary to be more careful when

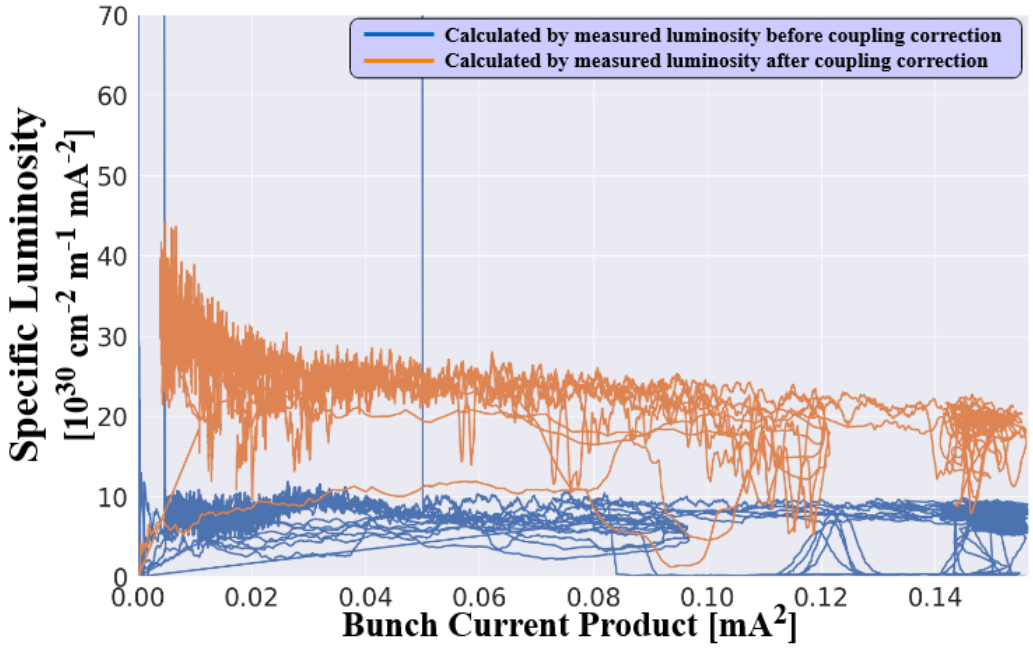

Figure 4.24: Comparison of the measured luminosity between conditions of large X–Y coupling (blue) and the same conditions under correction (orange).

correcting global optical errors in order to measure the IP coupling parameters.

In order to perform harmonic analysis, the bunch orbit in the phase space at the measurement point must be in the form of an ellipse or spiral. The bunch position is acquired by carrying out sampling at every revolution in the ring via BPM measurement in a turn–by–turn mode. In a circular accelerator, this condition is automatically satisfied because tuning is not carried out with a half-integer multiplication when creating stability conditions, so that a half-integer resonance can be avoided. The simplest method used for separation is the Fourier transform. The two eigenmodes can remain separate as they are not degenerated because of the stability of the betatron coupling. In such stable conditions, it is possible to find an operable region in the fractional tune by plotting a tune diagram. Since the object of this study is the coupled motion of the U-mode in the y direction, turn–by–turn measurement can be performed using oscillation that is initiated by an injection kicker. In addition, forced oscillation using a AC dipole magnet synchronized with the betatron phase of the bunches is a powerful tool that can be used for analyzing betatron oscillation, but it must be noted that the analysis becomes complicated because the additional kick force is joined with a beam–beam kick at the IP and the injection kicker.

4.3.2 Simulated Data from SAD

In order to prepare for analysis of the actual measured data, sample data were simulated using SAD [63]. By using the simulated data, verification of the logic used in deriving coupling parameters from the measured data and the codes used in the analysis can be demonstrated. In addition, acceptable errors in the measured data can be evaluated by scanning, using the standard deviation of the additional Gaussian noise in the simulated data. Data simulated by SAD were therefore prepared for use in a turn–by–turn mode and the averaging mode of the BPM system for the harmonic analysis and performance of the orbit response method, respectively.

SAD simulation of the BPM Data using the Turn–by–Turn mode

SAD simulations of turn–by–turn mode BPM were performed by reading the lattice model of SAD and changing the SK1 value of “QC1LE" and “QC1RE" manually. The read lattice model is used in the actual operation of SuperKEKB. In the simulation code, a particle that represents the center of a bunch is tracked. The beam positions of the tracked trajectory at each monitor are then successively transferred to an output file. The initial position is determined by a random seed that is placed inside the envelope of the betatron oscillations in the equilibrium state of a beam. If we want to match the simulations with the actual operation, the initial amplitude of the betatron oscillation is determined by the measured amplitude and the initial position of a particle is required in order to set it at the injection position of the storage ring.

SAD simulation of the BPM Data using the averaging mode

COD is simulated using the same turn–by–turn conditions in the simulation. For COD, as the positional difference from the ideal orbit has to be obtained, the values of “dx” and “dy” of the particle trajectory are calculated for a state of equilibrium . The deviations of “dx” and “dy” in the SAD script can be derived using the “Twiss” command. The results of the COD simulation can then be output collectively.

4.3.3 Ellipsoid fitting method

The method of fitting the measured phase space variables with an ellipse can be used to derive the Courant–Snyder Twiss parameters[22] and the X–Y coupling parameters in the Edwards-Teng parameterization[64] for the eigenmode of betatron oscillation. The evaluation is performed by ordered fitting from the low–dimensional to the high–dimensional relationships. To draw an ellipse (or circle) in normalized phase space,

the derivation of the betatron amplitude and its phase advance are required, and the Courant–Snyder invariant can then be obtained by two-dimensional fitting. Subsequently, the parameters α and r are obtained by three-dimensional fitting. To perform fitting in three dimensions, no correlation can occur between y and p_y, so it can be fitted only if the U-mode, which is the eigenmode in the x direction, is excited. In the single kick COD measurement the dipole kicks in the direction of the eigenmode which is to be measured; therefore, only a single mode can be excited if the coupling at the steering magnet is negligible.

There are two possible means by which r parameters can be obtained from the fitting. One is fitting the sample points onto the phase space by the least squares method. The other is deriving a normal vector of the ellipse. The normal vector can be obtained by arbitrarily selecting two vectors at the sample points. The normal vectors are then averaged in order to reduce the errors in the measured data.

Cosine fitting for the Courant–Snyder invariant

When deriving the beta function from a single kick COD Eq. (3.34), the practical betatron amplitude, the phase advance, and the Courant–Snyder invariant for the whole ring are evaluated from the measured data. The derivation of the Courant–Snyder invariant is determined by the horizontal and vertical position and the betatron phase advances of the BPMs along the ring. For example, the relationship between the horizontal betatron motion and the Courant-Snyder invariant can usually be represented by

$$x(s) = \sqrt{2J_u\beta_u(s)}\cos\left(\phi_u + \phi_{u0}\right) \tag{4.19}$$

where (J_u, ϕ_{u0}) are the action-angle variables with the relationship $\mathcal{W} = \sqrt{2J_u}$, which is the Courant-Snyder Invariant. As Eq. (4.19) produces a simple sinusoidal wave, it is easy to fit the data. The procedure to obtain Twiss parameters also includes the least square method. It can be seen that the fitting function agrees with the measured positional data well from Fig. 4.25. As the betatron phase is reset at the steering magnet, there are two different fitting curves in the COD data.

The analyzed data for COD that has been kicked at different positions by the steering magnets already includes x, β_u, and ϕ_u is evaluated by finding the envelope of the betatron oscillations. Thus $x/\sqrt{\beta}$ has purely cosine behavior with an amplitude of $= \sqrt{2J_u}$ and it can be fitted via the least square method in the form

$$\frac{x}{\sqrt{\beta}} = A\cos\left(\phi + B\right) \tag{4.20}$$

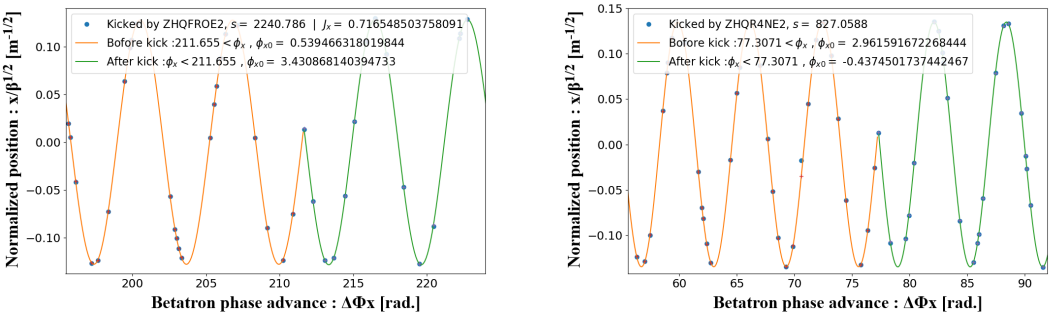

Figure 4.25: Detailed behavior of the motion from fitting curves at the position of steering magnets.

where $A = \sqrt{2J_u}$ and $B = \phi_{u0}$ which is the phase jump that is due to the steering kick. This method can be used to obtain a precise value for the Courant-Snyder invariant.

Least square fitting for a phase space ellipsoid

By finding the Courant–Snyder invariant, the area of the ellipse on the phase space was obtained. The Twiss and coupling parameters can be obtained by fitting the elliptic function with the limit cycle in the phase space. Although the parameters to be obtained are rotation angles in phase space, it should be noted that this is not an isometric transformation such as that of an axis rotation. The reason is that the off–diagonal components (r_1, r_2, r_3, r_4) in the Edwards-Teng parameterization are independent of each other in terms of the relationship between the on–diagonal and off–diagonal components.

For the U-mode oscillation, r_1 and r_2 describe the tilt in the y direction, and r_3 and r_4 represent the tilt in the p_y direction. Thus, the fittings for $r_1/2$ and $r_3/4$ are performed independently. When α is obtained by fitting, it is important that the ellipse fitting should be performed on a plane that is inclined in the y direction or the p_y direction, instead of the fitting to the projected ellipse on the $x - p_x$ plane.

To calculate the coupling factors, parameters are obtained by fitting on the $x - y$ plane and $p_x - y$ plane. The relationship of the betatron coupling is written as

$$\begin{pmatrix} x \\ p_x \\ y \\ p_y \end{pmatrix} = \begin{pmatrix} \mu & 0 & r_4 & -r_2 \\ 0 & \mu & -r_3 & r_1 \\ -r_1 & -r_2 & \mu & 0 \\ -r_3 & -r_4 & 0 & \mu \end{pmatrix} \begin{pmatrix} x_\beta \\ p_{x\beta} \\ y_\beta \\ p_{y\beta} \end{pmatrix}. \tag{4.21}$$

The tilts of the ellipse on the $x - y$, $p_x - y$, $x - p_y$, and $p_x - p_y$ plane correspond to

r_1, r_2, r_3, and r_4, respectively.

Deriving a normal vector of the ellipse

For deriving a normal vector of the ellipse, the projections of the normal vector onto the $x-y$, p_x-y, $x-p_y$, and p_x-p_y planes correspond to the inverse of the tilt of the ellipse on each plane. Consequently, the coupling parameters can be obtained from the inverse of the tilts. The sample point on the Courant-Snyder ellipse in the phase space conforms to a single-value function which corresponds to the betatron phase. The betatron phases at the positions of the individual steering magnets are relatively different from each other. Hence beam trajectories with different betatron phases can be obtained via kicks carried out with different steering magnets. Figure 4.26 illustrates the method of deriving normal vectors. In this figure, six samples of the COD data are illustrated as an example. Two arbitrary sample points are selected in order to obtain a sample vector. The normal vector describing the ellipse is derived from the cross–product of the two selected sample vectors. If there are six samples included in the COD data, then there are a total of fifteen combinations possible for the selection of the two sample vectors. The normal vector is averaged using the fifteen combinations. The absolute value of the averaged normal vector is then used to align the direction of surface of the ellipse.

Application to the measured data in Phase-2 Commissioning

As an example, Fig. 4.27 and 4.28 show the results of fitting the COD data in the Phase-2 commissioning under two different coupling conditions. Figure 4.27 is the case where $r_2 = -3$ mm is produced by tilting the IP, and Fig. 4.28 is the case where a tilt of $r_2 = -6$ mm is produced by the QC1 skew corrector. The figure shows the six cases of kicking using different steering magnets. The Curves in the figure denote fit functions, where the points marked with a red "+" indicate the values used for fitting the functions at each BPM position, and the blue dots are the measured data of $x/\sqrt{\beta}$. The orange and green curves are the results fitted before and after use of the steering kick, respectively. Important information (such as the name and the position of the steering magnets, the phase of the steering kick position, and the fitted values) is given in the legends of the following figures.

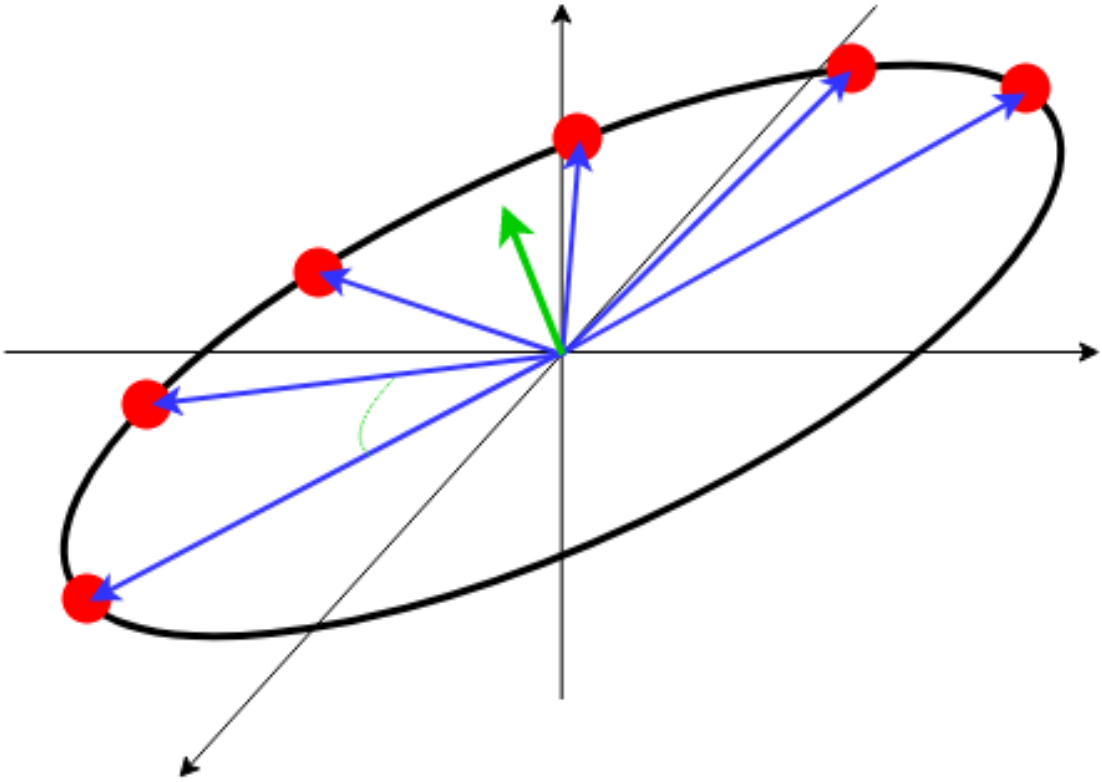

Figure 4.26: Illustration of the average of the normal vectors for calculation of the phase space ellipse.

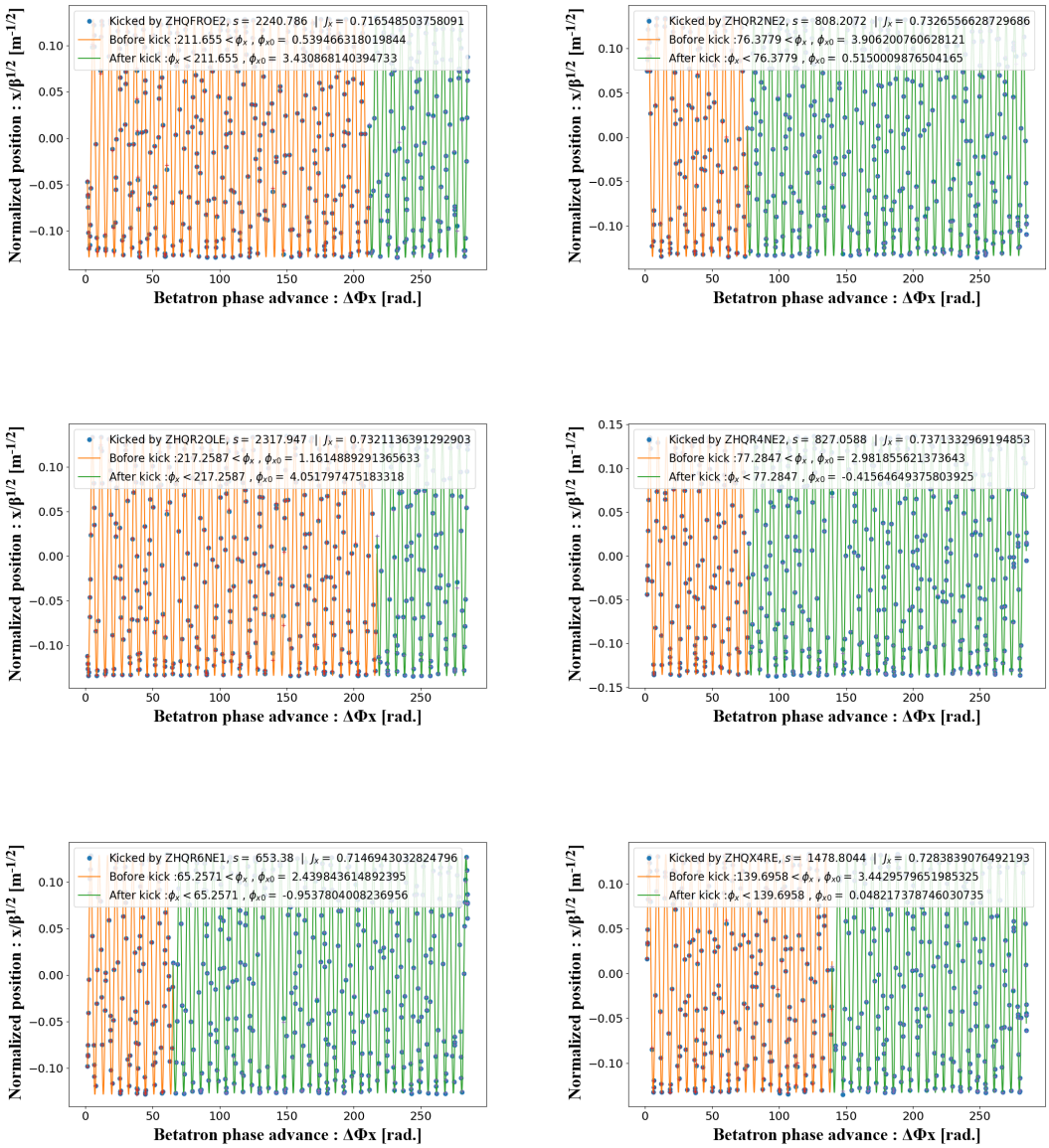

Figure 4.27: Fitting results for COD data at each BPM position (for IP Tilt $r_2 = -3m$). Vertical axis denotes $x/\sqrt{\beta}[m^{1/2}]$, and horizontal axis denotes betatron phase advance[rad]

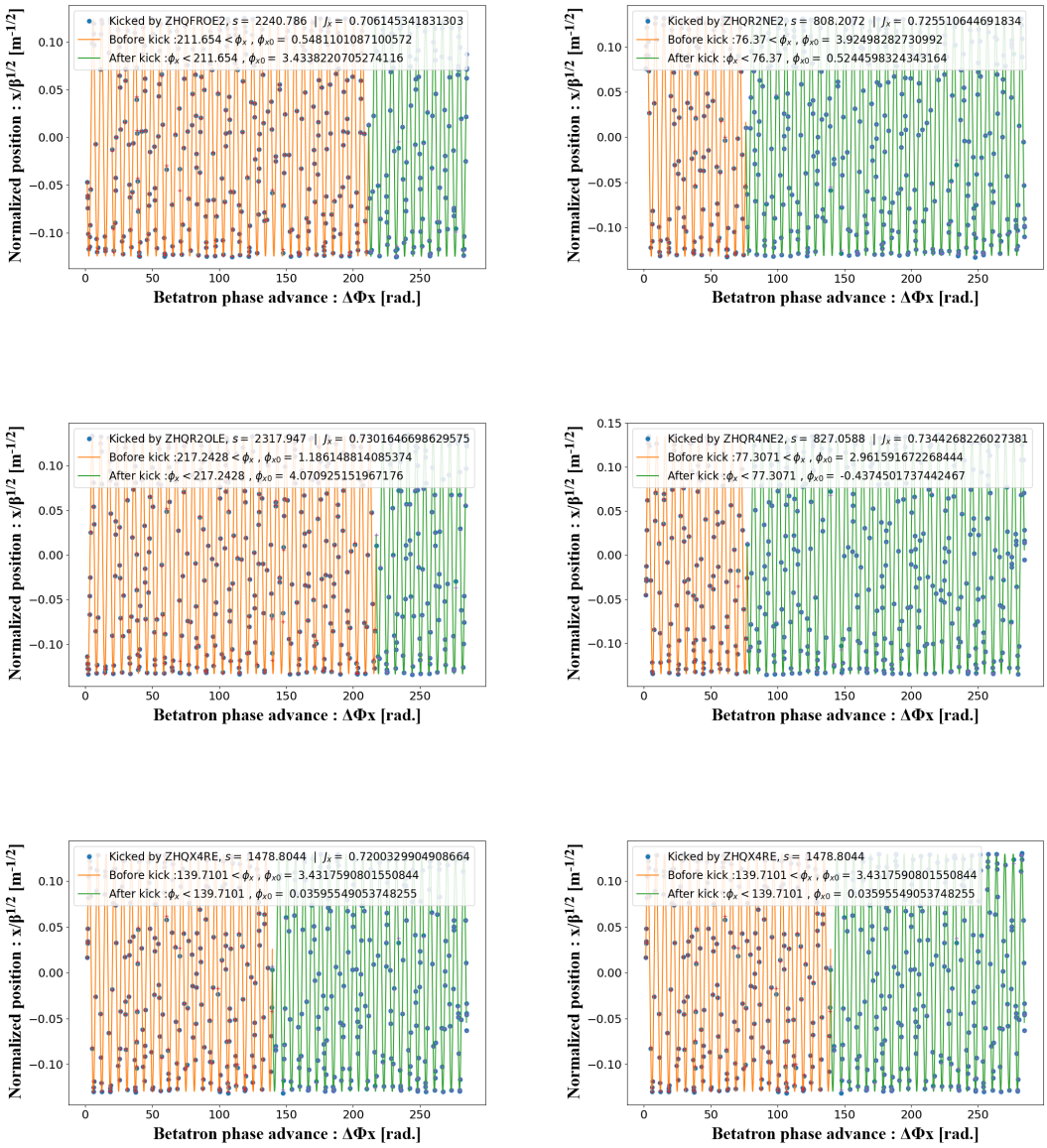

Figure 4.28: Fitting results for COD data at each BPM position (for QC1 skew corrector $r_2 = -6m$). Vertical axis denotes $x/\sqrt{\beta}$ in $m^{1/2}$, and horizontal axis denotes betatron phase advance in radian.

Figure 4.29 shows the measured sample data for x, p_x, and y at MQC1LE (left side) and the IP (right side). Each plot has six COD samples, which are obtained when $r_2 = -3m$. An ellipse like behavior can be seen in each plot of Fig. 4.29. The ellipse is tilted in the x-y and p_x-y plane, although there is no correlation between the y and (x, p_x) planes outside the IR. In order to derive the tilt in Fig .4.29, Courant–Snyder Twiss parameters are calculated from the fitted COD data with the implicit function of the phase space ellipses in each individual plot. The data therefore consists of COD data at each BPM position. Thus p_x and p_y, which are at arbitrary positions, are also transferred in the data of the nearest two BPMs. The transfer of physical variables between two points is given by

$$\begin{pmatrix} x(s_2) \\ p_x(s_2) \\ y(s_2) \\ p_y(s_2) \end{pmatrix} = \begin{pmatrix} m_{11}(s_1,s_2) & m_{12}(s_1,s_2) & m_{13}(s_1,s_2) & m_{14}(s_1,s_2) \\ m_{21}(s_1,s_2) & m_{22}(s_1,s_2) & m_{23}(s_1,s_2) & m_{24}(s_1,s_2) \\ m_{31}(s_1,s_2) & m_{32}(s_1,s_2) & m_{33}(s_1,s_2) & m_{34}(s_1,s_2) \\ m_{41}(s_1,s_2) & m_{42}(s_1,s_2) & m_{43}(s_1,s_2) & m_{44}(s_1,s_2) \end{pmatrix} \begin{pmatrix} x(s_1) \\ p_x(s_1) \\ y(s_1) \\ p_y(s_1) \end{pmatrix} \tag{4.22}$$

The momentum derivation at a target point is constructed using the relationship between the two inverse transfer matrixes:

$$\begin{pmatrix} x(s_1) \\ p_x(s_1) \\ y(s_1) \\ p_y(s_1) \end{pmatrix} = \begin{pmatrix} m_{11}(s_1,s_2) & m_{12}(s_1,s_2) & m_{13}(s_1,s_2) & m_{14}(s_1,s_2) \\ m_{31}(s_1,s_2) & m_{32}(s_1,s_2) & m_{33}(s_1,s_2) & m_{34}(s_1,s_2) \\ m_{11}(s_1,s_3) & m_{12}(s_1,s_3) & m_{13}(s_1,s_3) & m_{14}(s_1,s_3) \\ m_{31}(s_1,s_3) & m_{32}(s_1,s_3) & m_{33}(s_1,s_3) & m_{34}(s_1,s_3) \end{pmatrix}^{-1} \begin{pmatrix} x(s_2) \\ y(s_2) \\ x(s_3) \\ y(s_3) \end{pmatrix} \tag{4.23}$$

where m_{ij} $(i, j = 1, 2, 3, 4)$ are components of the transfer matrix from s_2 and s_3 to s_1 variables, respectively.

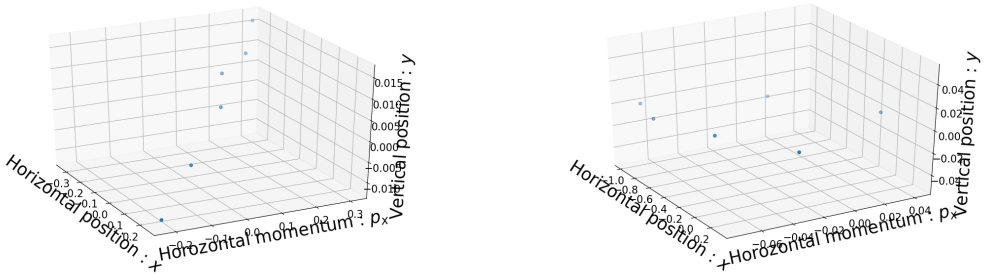

Figure 4.29: Phase space plots for (x[mm], p_x[mrad], y[mm]) plane.

The ellipse is not on the same plane as the unexcited V-mode oscillation, and it

appears in the y direction because the steering magnet providing the kick possesses the betatron coupling parameter. The inclination of the plane on which the ellipse lies indicates the coupling at the monitor position, and the deviation of the sample from the plane indicates the coupling at the kick position. By investigating this behavior, it is possible to distinguish between the coupling at the kick position and the coupling at the monitor position.

The fitting results for the coupling parameters are shown in Fig. 4.30 and Table 4.8. Two types of fitting were attempted: the least square method for the tilted ellipse and the derivation of the normal vectors at each sample point. In Fig. 4.30, as we can see, it is not possible to fit both measured datasets with an ellipse. The cause of this mis–fitting can be assumed to be the result of significant amounts of noise in the y and p_y correlations. It seems that too few data samples are available in order to reduce the noise and obtain the correct tilt in several of the phase space correlations.

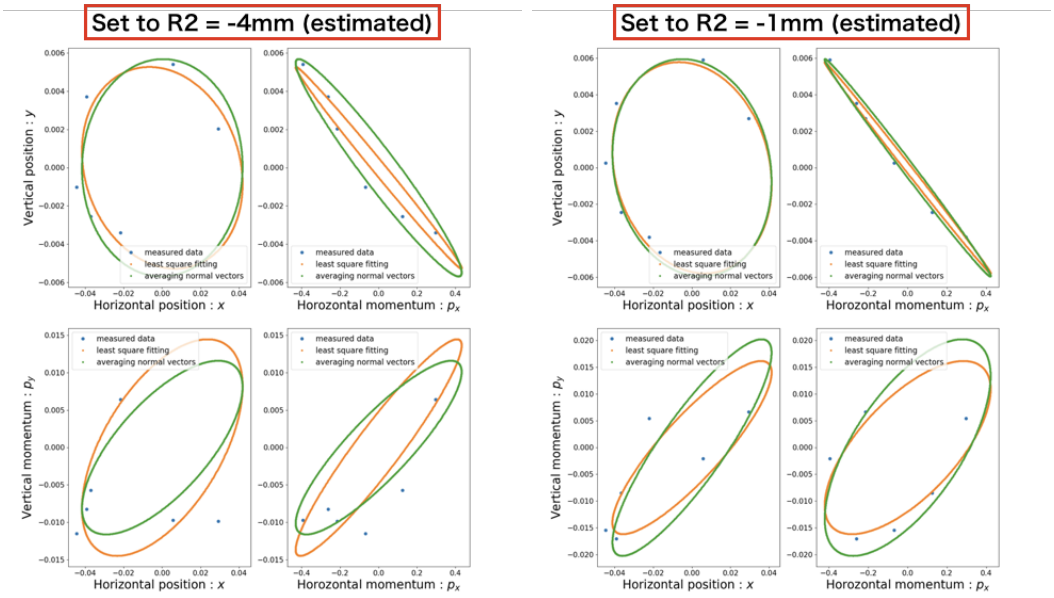

Figure 4.30: Ellipse fitting for phase space correlations of the coupling condition: $r_2 = 4$mm(left) and $r_2 = 1$mm(right). Orange ellipses are fitted by the least square method and green ellipses are fitted by the averaging the normal vectors of each measured point on the phase space. The dimensions of the axes are mm and mradian for position and momentum, respectively.

Finally, a comparison of some of the conditions that occur involving these r_2 parameters is shown in Fig. 4.31. These conditions change the r_2 parameters as given in the legends of the figure. It is apparent that coupling parameters that are close to the IP have a significant effect, and the IP parameters, which are our objectives,

	r_1[rad]	r_2[m]	r_3[1/m]	r_4[rad]
Least square for $r_2 = 4$mm	-0.0127	0.0124	-0.1194	-0.0286
Normal vector for $r_2 = 4$mm	-0.0374	0.0136	-0.1410	-0.0199
Least square for $r_2 = 1$mm	-0.0075	0.0138	-0.2976	-0.01196
Normal vector for $r_2 = 1$mm	-0.0135	0.0143	-0.3781	-0.0238

Table 4.8: Comparison between two methods and two conditions for evaluating coupling parameters. Conditions are just before and after r_2 changed

are much less than that seen in other positions. This situation makes it difficult to calculate the IP coupling parameters exactly by fitting ellipses.

4.3.4 Harmonic analysis method

Harmonic analysis is commonly used in order to derive a coupling parameter which can analyze the U-mode oscillation and V-mode oscillation separately by performing mode separation via Fourier transform. The oscillation of the U-mode is expressed by Eq. (3.49), and the V-mode is expressed by Eq. (3.50). It is important that the Fourier amplitude and phase are obtained for the eigenmodes via mode separation carried out with Fourier transform. Because data is measured in the x and y directions independently, the coupling parameters are reflected in the spectrum in a form that includes rotation errors in both the monitor and the kicker.

We are interested in IP beam dynamics, and therefore have to calculate phase space variables at the IP from measured positions at monitors near the IP, in a similar manner as the ellipsoid fitting method used for the measurement of COD. Because both the Fourier transform and the matrix calculation are linear transforms, they act commutatively in the analysis. Therefore, there are two options for the order at which the coupling parameters are calculated; calculating the transfer to the IP first, and calculating the mode separation by the Fourier transform first. Both options were carried out in order to compare the derivation accuracy.

In the harmonic analysis method, turn–by–turn data from multiple rotations at a single point is used. At least two sampling points are necessary for the turn–by–turn monitoring, because the momentum parameters, (p_x, p_y), which are transferred from the monitors near the IP, are required for the analysis. The turn–by–turn data from the two different cases are introduced as examples and comparisons. The optical conditions used for the turn–by–turn measurement are mostly the same as those used for the ellipsoid fitting analysis.

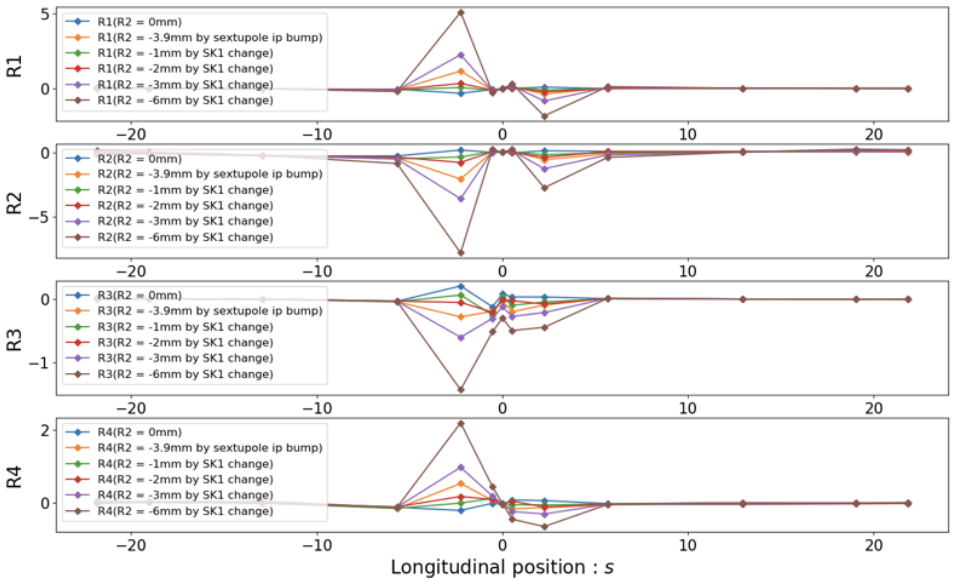

Figure 4.31: Comparison of the coupling parameters calculated by the least square method for COD data among some r_2 parameters in Phase-2 commissioning. In these measurements, r_1, r_3, and r_4 parameters are not focused for optical tuning, but these coupling parameters are also important in collision and were therefore tuned carefully following these measurements.

Validation of the Procedure used for the Analysis and Estimation of the Allowable Error

Figure 4.32 and 4.33 show the simulated BPM data from the turn-by-turn mode. In Fig. 4.32, the orange and blue plots denote the position and momentum in the x-direction, respectively. In Fig. 4.33, the orange and blue plots also denote the position and momentum in the y-direction, respectively. In order to compare between data from simulations carried out with and without the SK1 change in the QC1 magnets, optics with no aberrations (upper plots) and with SK1 $\pm 1.0 \times 10^{-3}$ difference from the referenced lattice model of SAD (lower plots) are given in each figure. As these plots are produced using initial conditions that were determined by Gaussian random seeds, the conditions of the SuperKEKB beam operation are not reflected in the results. The reason why the simulations are not adapted to include the actual conditions is that the objective of this simulation is to validate the procedure used for the evaluation of the harmonic analysis by mode separation using Fourier transformation. Thus, the simulated data has to include both the U and V modes as the arbitrary initial conditions. The plots include Gaussian noise at $\sigma = 3.0 \times 10^{-6}$, for which the Box-Muller method for producing white noise was used.

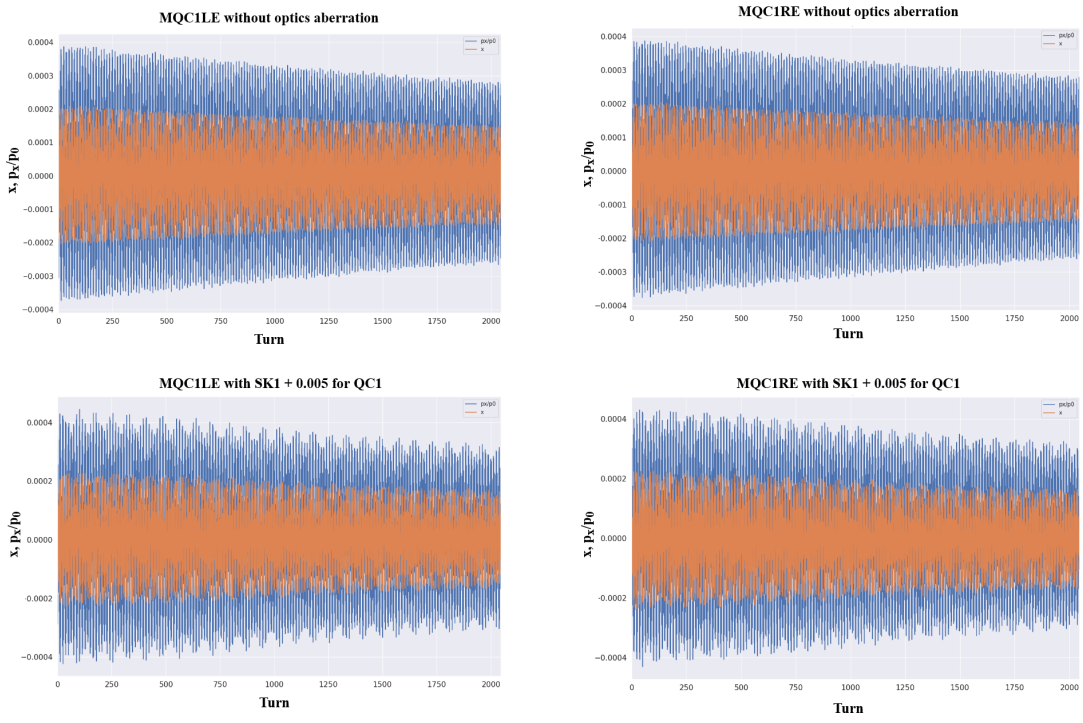

Figure 4.32: Simulated x-position and -momentum data of turn-by-turn mode BPM readings for x and y direction.

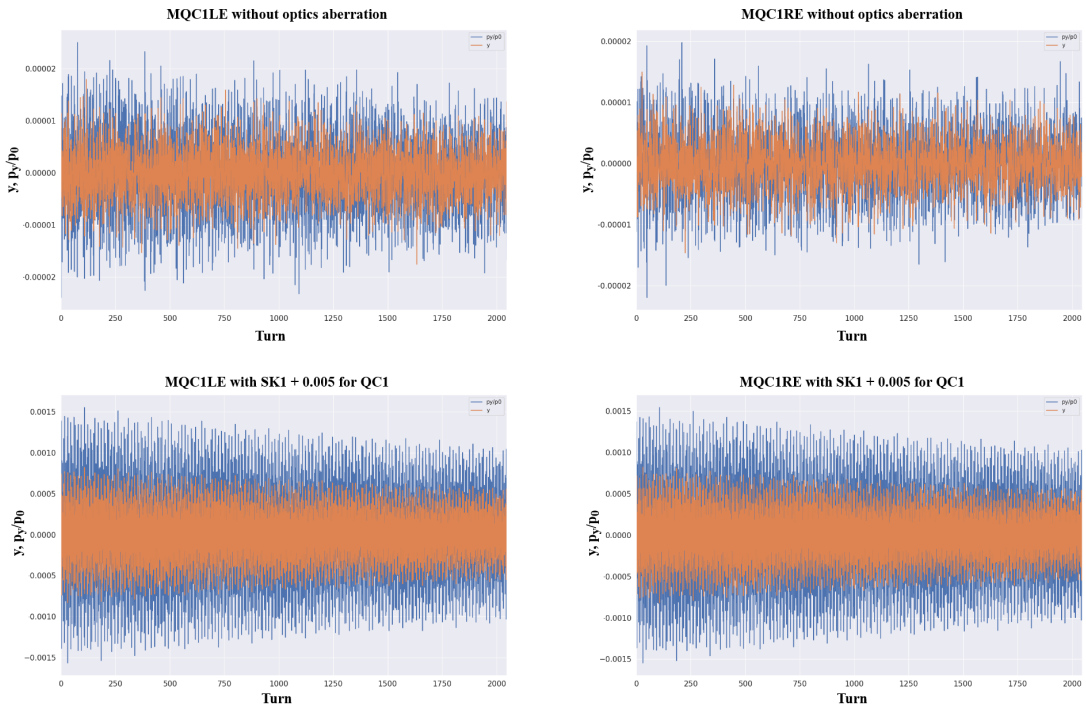

Figure 4.33: Simulated y-position and -momentum data of turn-by-turn mode BPM reading in the x and y directions.

To check the calculation of the coupling parameters at the IP, directly measured data concerning the four-dimensional physical variables at the IP are simulated artificially. Figure 4.34 and 4.35 show the results of the Fourier transformation of the directly measured simulations for the position and momentum in the x- and y-directions. Figure 4.34 shows the Fourier spectrum of the simulated data without any aberration or noise. It can be seen that the U- and V-mode oscillations measured in the x- and y-direction are excited by the Gaussian random seed when the revolving beam was in an equilibrium state. Figure 4.35 shows the Fourier spectrum of the simulated data with a SK1 change of $\pm 1.0 \times 10^{-3}$ for the QC1 from the reference optics model and without any noise. The effect of the additional skew component at the QC1 magnets on the measured coordinates of the beam at the IP can be observed in the figure as the existing peaks in the U-mode on the y-direction spectrum. The coupling parameters that were produced using the data from these figures are summarized in table4.9. The ideal coupling value at the IP that was calculated using the transfer matrix and the coupling matrix of the Edwards-Teng parametrization and the analyzed coupling parameters that were calculated using the quasi measured data at the IP in the turn-by-turn mode are compared in this table. The limit of the evaluable order for each coupling parameter can also be found as the highest

power of the parameters in the results of the analysis of this table. According to the calculation for the simulation of quasi direct measurement at the IP, it is confirmed that the analyzed results for r_2 and r_3 agree perfectly with the theoretical values. This comparison of the turn-by-turn simulation with the theoretical calculation of the coupling parameters can prove the reliability of the procedure used for analysis that is described below.

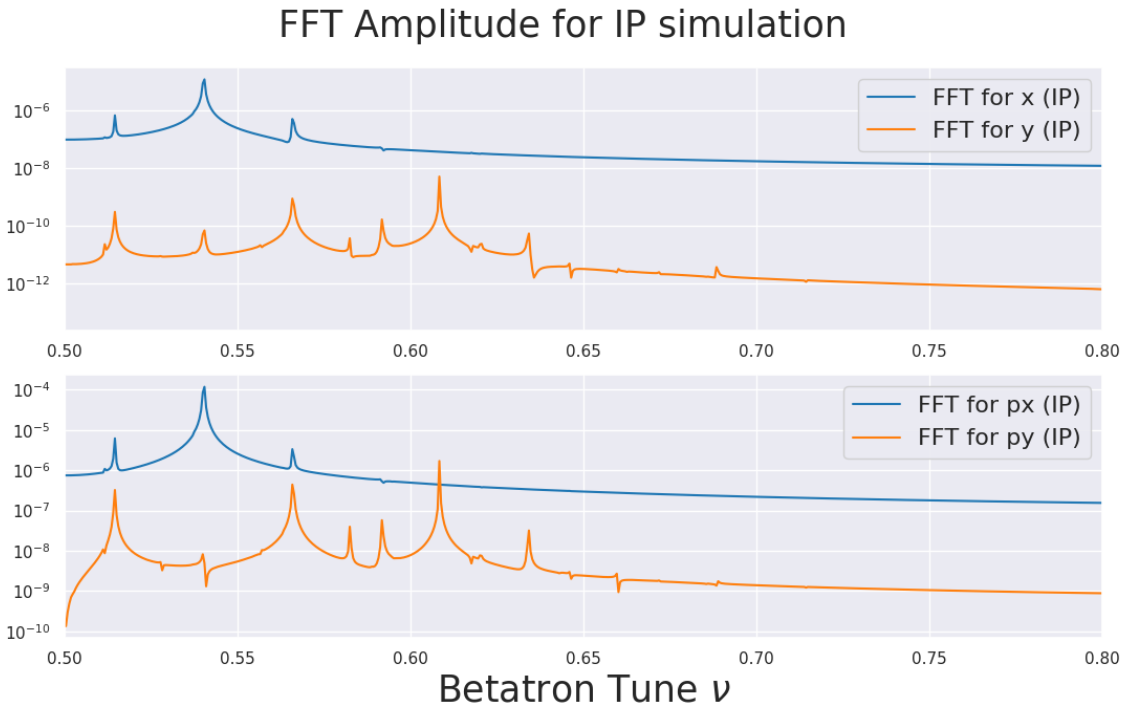

Figure 4.34: Fourier spectrum for simulated four dimensional physical variables at the IP with no change from reference lattice model.

	r_1[rad]	r_2[m]	r_3[1/m]	r_4[rad]
Before SK1 change (± 0 for QC1)				
IP(Theoretical)	-2.0×10^{-13}	-8.0×10^{-14}	2.0×10^{-11}	5.0×10^{-12}
IP(Analytical)	2.6×10^{-6}	-5.3×10^{-7}	4.0×10^{-4}	1.3×10^{-5}
After SK1 change ($\pm 1.0 \times 10^{-3}$ for QC1)				
IP(Theoretical)	6.0×10^{-6}	-1.8×10^{-3}	-1.555	6.0×10^{-4}
IP(Analytical)	-3.6×10^{-6}	-1.8×10^{-3}	-1.588	1.4×10^{-3}

Table 4.9: Coupling parameters calculated by transfer matrix theoretically (upper) and harmonic analysis of the turn-by-turn simulated data (lower).

Next, simulations of the measurement of BPMs located at both sides of the IP are performed using the analysis procedure verified by the calculation of coupling

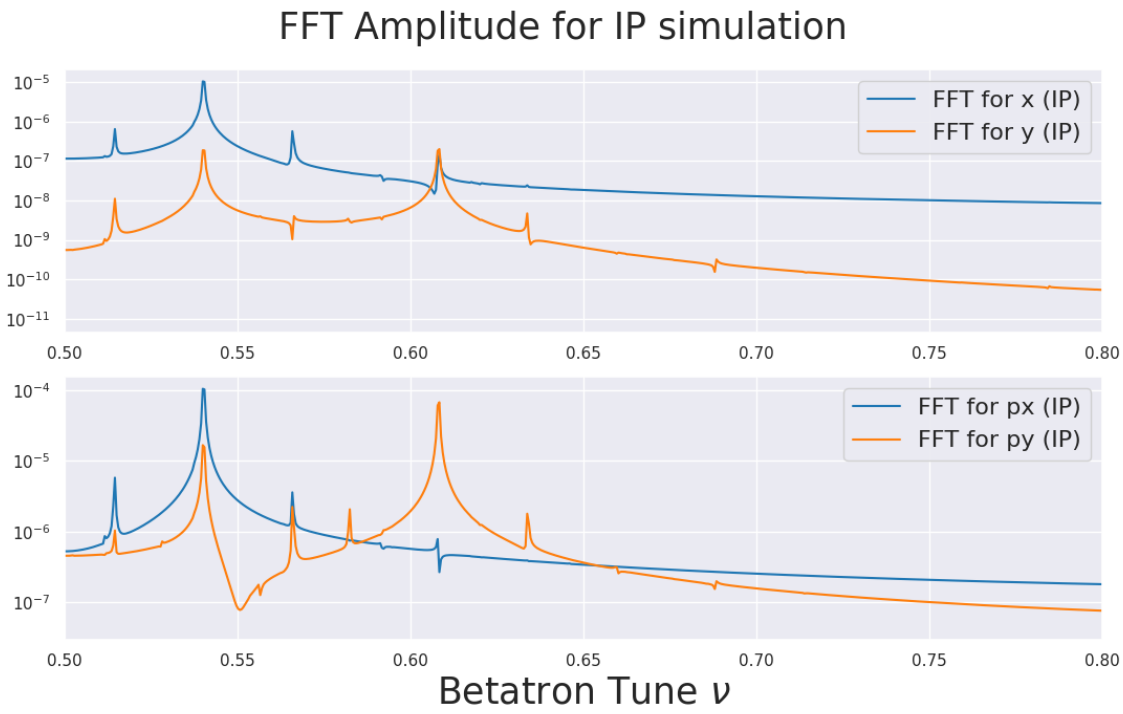

Figure 4.35: Fourier spectrum for simulated four dimensional physical variables at the IP with SK1 change of $\pm 1.0 \times 10^{-3}$ from the reference lattice model.

parameters from the quasi direct measured data at the IP that was described in the last paragraph. The conditions used in the simulation assume the following:

- The data is measured at MQC1LE and MQC1RE, which are the nearest BPMs to the IP.
- The measured data consists of x and y displacements ± 0.53 m away from the IP.
- The 2048 samples are recorded in the analyzed data.
- A Gaussian noise of $\sigma = 3.0 \times 10^{-6}$ is added to each measured position as the measured error.

The Fourier spectrum of the BPM data simulated using the previous conditions is given in Fig. 4.36 and 4.37. As reference data for comparison with Fig. 4.36 and 4.37, the noiseless data describing the individual figures are given in Fig. 4.38 and 4.39. In Fig. 4.38, the U-mode peaks can be seen clearly as the oscillation in the x-direction; however, the V-mode peaks are difficult to see because of the noise. On the other hand, in Fig. 4.39, the U-mode oscillation becomes visible as peaks in the

y-direction. These U-mode peaks in the y-direction are affected by the additional coupling at the QC1 magnets. The coupling parameters that were calculated using the Fourier spectrum in Fig. 4.36 and 4.39 are summarized in Table 4.10. In this table, the upper results were calculated from the simulated results with noiseless data given in Fig. 4.38 and 4.39. The middle results are calculated from the simulated results of the data with the measurement errors shown in Fig. 4.36 and 4.37. The upper results agree completely with the results of the analysis (lower result in the table) of the quasi-direct measurement at the IP. The individual parameters in the middle results are slightly deflected.

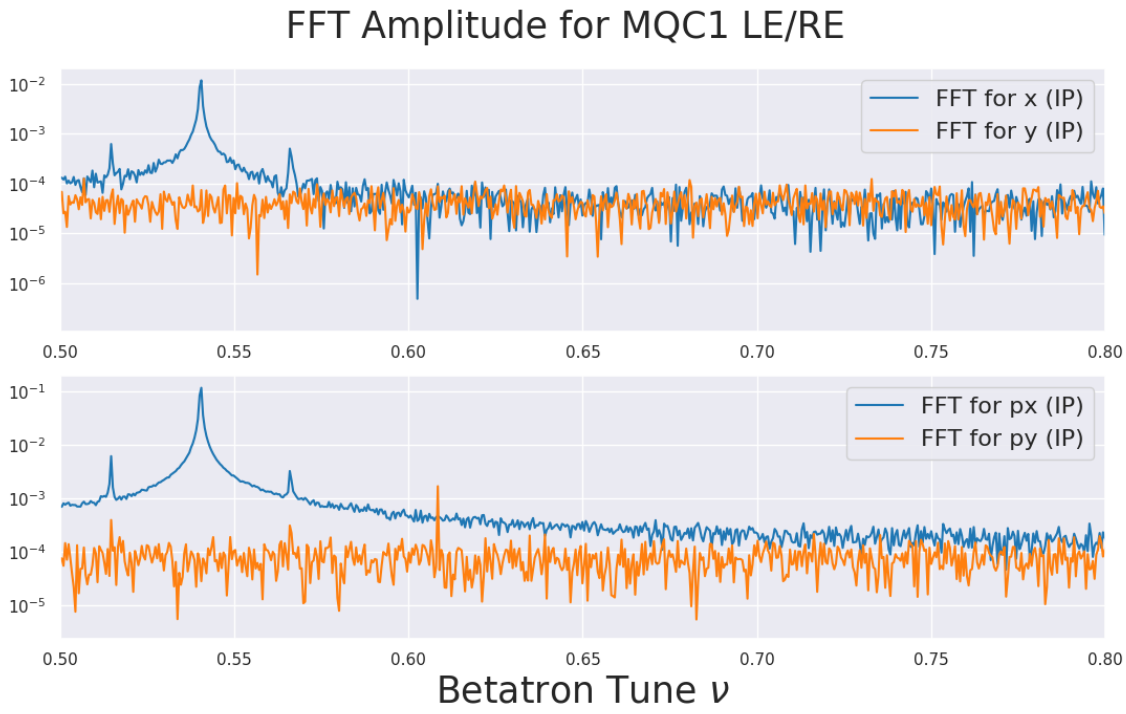

Figure 4.36: Fourier spectrum for transferred physical variables at the IP from MQC1 BPMs with measurement errors, which is simulated using the unchanged lattice of the original SAD model used for beam operation.

To evaluate the effect of the measurement error in Table 4.10, coupling parameters with scanning dispersion values from the Gaussian noise are calculated. Figures 4.40 - 4.43 show the results of calculating the scanning dispersion. The statistical number of trials is 1.0×10^4 for the individual data. Figures 4.40, 4.41, 4.42, and 4.43 describes the calculation results for r_1, r_2, r_3, and r_4, respectively. The scanned values of the dispersion are $\sigma = 3.0 \times 10^{-7}$, $\sigma = 3.0 \times 10^{-6}$, $\sigma = 3.0 \times 10^{-5}$, and $\sigma = 3.0 \times 10^{-4}$. The histogram entries are estimated using individual simulations of the same simulation data with different Gaussian dispersions. The orange curves show the fitted results

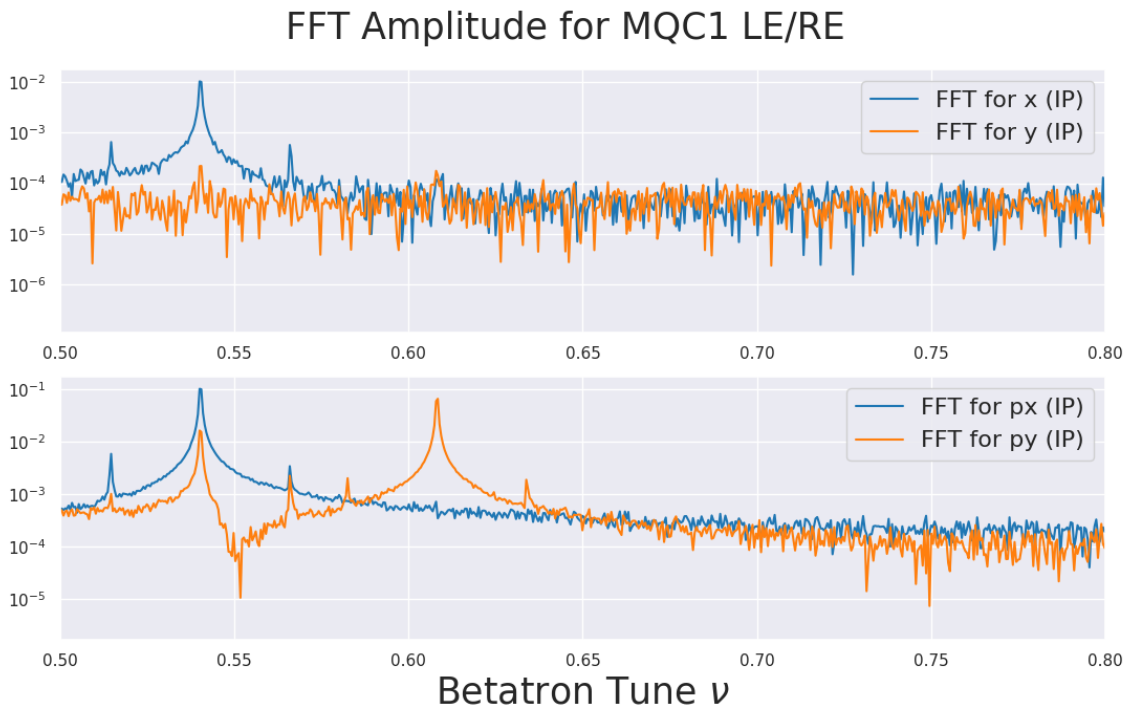

Figure 4.37: Fourier spectrum for transferred physical variables at the IP from MQC1 BPMs with measurement errors, which is simulated using the lattice model of SK1 changed for QC1 magnets $\pm 1.0 \times 10^{-3}$ from the original SAD model used for beam operation.

from the envelope of the histogram entries. According to the results of the error evaluations for r_1 and r_2, the allowable threshold for error in the measurement is in the order of 1.0 μm.

Analysis of the Practically Measured Data

In the last subsection, the analysis procedure is verified. In this subsection, the coupling parameters from the practical measured data of the Phase-2 commissioning under similar conditions to the simulation are analyzed, by changing the SK1 value of the QC1 magnets. Figures 4.44 and 4.45 show plots of the raw data for the turn–by–turn measurement at MQC1/2 and LE/RE. In Fig. 4.44 and Fig. 4.45, the measured data for the x–direction and the y–direction are plotted, respectively. The upper two plots of each figure are the data measured when $r_2 = 4$mm, and the lower two plots are the data measured when $r_2 = 1$mm. The blue and orange lines in the figures denote the data measured at MQC2 and MQC1, respectively.

From the above figures, it is verified that the measured data are suitable for analysis by confirming the ratio of the betatron amplitudes between the two BPMs sets.

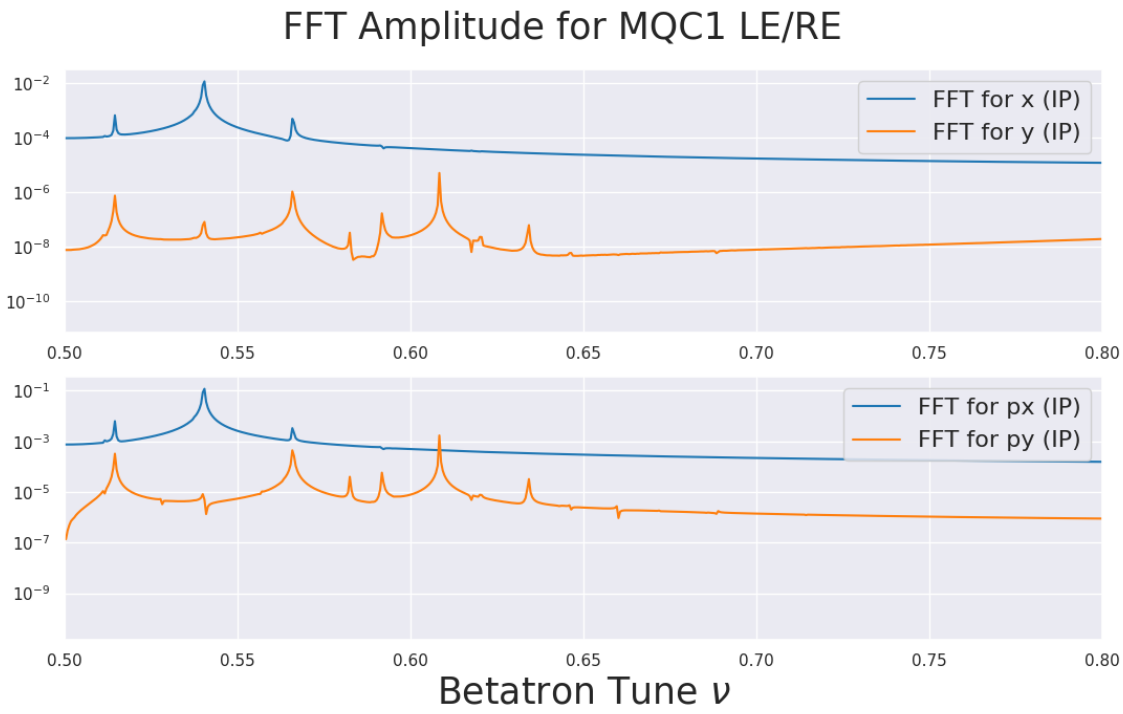

Figure 4.38: Fourier spectrum for transferred physical variables at the IP from MQC1 BPMs, which is simulated using the unchanged lattice of the original SAD model used for the beam operation.

The betatron amplitudes at each of the monitors are summarized in Table 4.11. The ratio of the amplitudes in the orange and blue plots of Fig. 4.44 and 4.45 match Table 4.11 well. These results indicate that the BPMs measured the betatron oscillation accurately in both directions.

The calculation order: Transfer -> mode separation

The detailed calculation follows the theoretical approaches in Sec. 3.2.2. The relationships on the x–p_x plane can be expressed using

$$\begin{pmatrix} x(s) \\ \\ p_x(s) \end{pmatrix} = \begin{pmatrix} r_0\sqrt{2J_u\beta_u(s)}\cos\left(\phi_u+\phi_{u0}\right) \\ \\ -r_0\sqrt{2J_u}\frac{\alpha_u(s)}{\sqrt{\beta_u(s)}}\cos\left(\phi_u+\phi_{u0}\right) - r_0\sqrt{\frac{2J_u}{\beta_u(s)}}\sin\left(\phi_u+\phi_{u0}\right) \end{pmatrix} \tag{4.24}$$

where the coefficients of the trigonometric functions correspond to the Fourier amplitude, and the phases correspond to the Fourier phase. The relationships of the y and p_y with U-mode oscillation is a little different from that produced by Eq. (4.24). According to the previous section, when only U–mode oscillation is initiated, the y

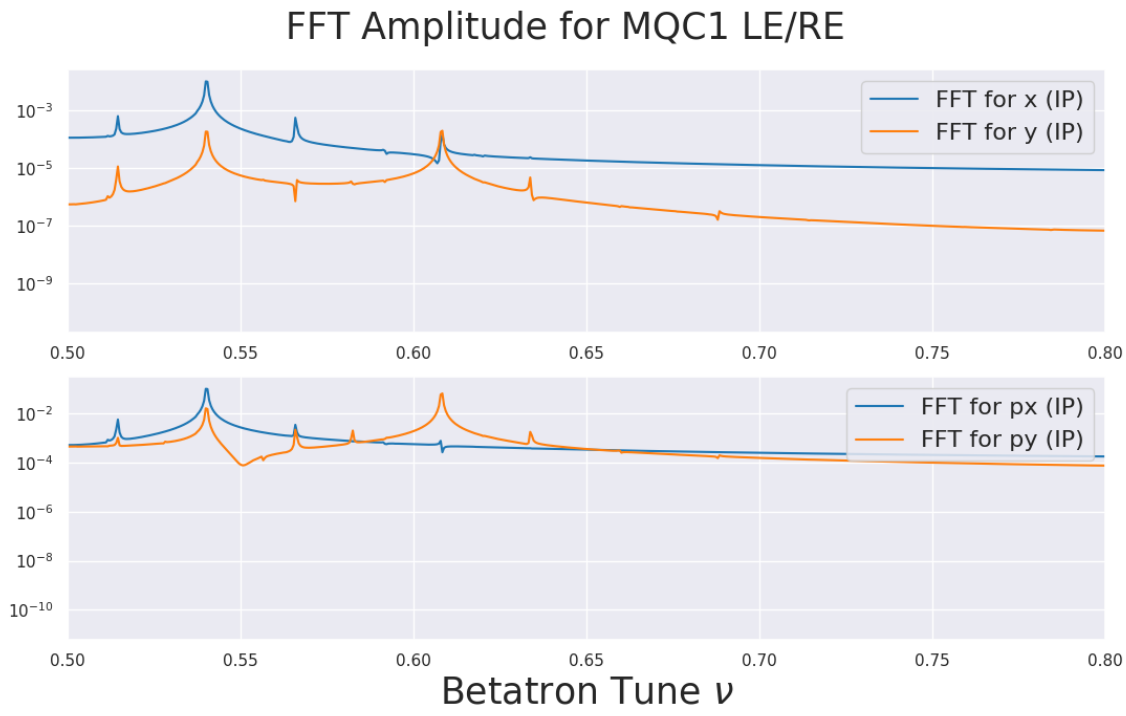

Figure 4.39: Fourier spectrum for transferred physical variables at the IP from MQC1 BPMs, which is simulated using the lattice model of SK1 changed for QC1 magnets $\pm 1.0 \times 10^{-3}$ from the original SAD model used for beam operation.

direction is given by

$$\begin{pmatrix} y(s) \\ \\ p_y(s) \end{pmatrix} = \begin{pmatrix} (-r_1\sqrt{2J_u\beta_u(s)} + r_2\sqrt{2J_u}\frac{\alpha_u(s)}{\sqrt{\beta_u(s)}})\cos(\phi_u + \phi_{u0}) - r_2\sqrt{\frac{2J_u}{\beta_u(s)}}\sin(\phi_u + \phi_{u0}) \\ \\ (-r_3\sqrt{2J_u\beta_u(s)} + r_4\sqrt{2J_u}\frac{\alpha_u(s)}{\sqrt{\beta_u(s)}})\cos(\phi_u + \phi_{u0}) - r_4\sqrt{\frac{2J_u}{\beta_u(s)}}\sin(\phi_u + \phi_{u0}) \end{pmatrix} \tag{4.25}$$

To apply this equation, the variables ($x \in \mathbb{C}$) of the Fourier transform will be changed to the form of an absolute and an argument. As an example, we consider the case where there is a definite betatron coupling factor and only U–mode oscillation is initiated. By conducting the Fourier transformation and applying the transfer functions $\mathcal{M} : \vec{x} \mapsto \vec{x^*}$ where $\vec{x} = (x_1, y_1, x_2, y_2)^T$ are independent, it is apparent that both are

	r_1[rad]	r_2[m]	r_3[1/m]	r_4[rad]
Before SK1 change (± 0 for QC1)				
MQC1(without noise)	2.6×10^{-6}	-6.3×10^{-7}	3.9×10^{-4}	1.4×10^{-5}
MQC1(with noise)	5.8×10^{-5}	-1.3×10^{-4}	-8.0×10^{-4}	7.1×10^{-4}
IP(Analytical)	2.6×10^{-6}	-5.3×10^{-7}	4.0×10^{-4}	1.3×10^{-5}
After SK1 change ($\pm 1.0 \times 10^{-3}$ for QC1)				
MQC1(without noise)	-5.3×10^{-6}	-1.8×10^{-3}	-1.588	1.4×10^{-3}
MQC1(with noise)	1.6×10^{-3}	-2.1×10^{-3}	-1.586	6.9×10^{-4}
IP(Analytical)	-3.6×10^{-6}	-1.8×10^{-3}	-1.588	1.4×10^{-3}

Table 4.10: Coupling parameters calculated from harmonic analysis of the turn-by-turn simulated data (upper two data). As the reference, analyzed values from noiseless data of quasi-direct measurement at the IP (lower).

Position	$\lvert\beta_x\rvert$ $[m^{1/2}]$	ν_x	$\lvert\beta_y\rvert$ $[m^{1/2}]$	ν_y
IP(start)	0.1	0.0	0.003	0.0
IP(end)	0.1	45.5399	0.003	43.608
MQC1LE	2.90874	0.22032	93.6286	0.24910
MQC1RE	2.90873	45.3196	93.6284	43.3589
MQC2LE	142.968	0.24102	291.140	0.24998
MQC2RE	190.713	45.2986	263.746	43.3579
MQLC3LE	26.9933	0.26170	7.67744	0.29538
MQLC3RE	34.9614	45.2833	25.6036	43.3323

Table 4.11: Betatron amplitude and phase advance from IP at each BPM in the IR

linear transformations. Thus, these transformations are commutative as follows:

$$\vec{x^*}(\omega) = \int_{\infty}^{\infty} dt\{\mathcal{M}\vec{x}(t)e^{-i\omega t}\} \tag{4.26}$$

$$= \mathcal{M}\int_{\infty}^{\infty} dt\{\vec{x}(t)e^{-i\omega t}\}. \tag{4.27}$$

However, the order used to conduct these transformations for an ideal data set is mathematically the same; the Fourier transformation should be applied first because the actual data includes noise in the measurement. The theoretical preference for calculation order in order to reduce the noise is easier to see in the signal processing theory of transfer functions.

According to Eq. (4.26), the process for the estimation of the coupling factor is carried out in the following steps.

1. Apply the composed transfer function to the measured variables

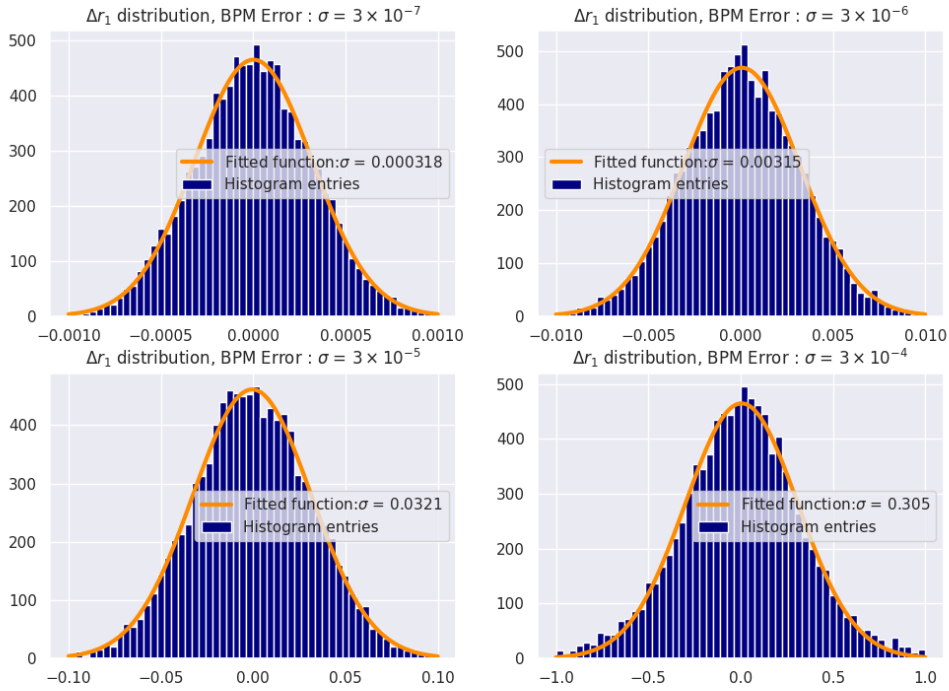

Figure 4.40: Evaluation of the effect of error on r_1 parameter the dispersion of Gaussian which is scanned from $\sigma = 3.0 \times 10^{-7}$ to $\sigma = 3.0 \times 10^{-4}$ in order.

2. Calculate the Fourier transform for the transferred variables

3. Search for the peaks associated with Fourier amplitude

4. Calculate the coupling parameters (r_1, r_2) and (r_3, r_4) from the formulae for the y and p_y components of the U-mode.

The important point in this method is to search for the exact frequency of the betatron mode.

The physical variables at the IP are calculated using the transfer matrix. Figure 4.46 shows an example of the correlations among each of the variables in the phase space. The diagonal histogram denotes the position–frequency plots. These plots are the results of the calculation of step #1 in the above list for the measured data in Fig. 4.44 and 4.45. If these correlations have obvious features indicating tilting of the four–dimension ellipsoid, the coupling parameters can be determined.

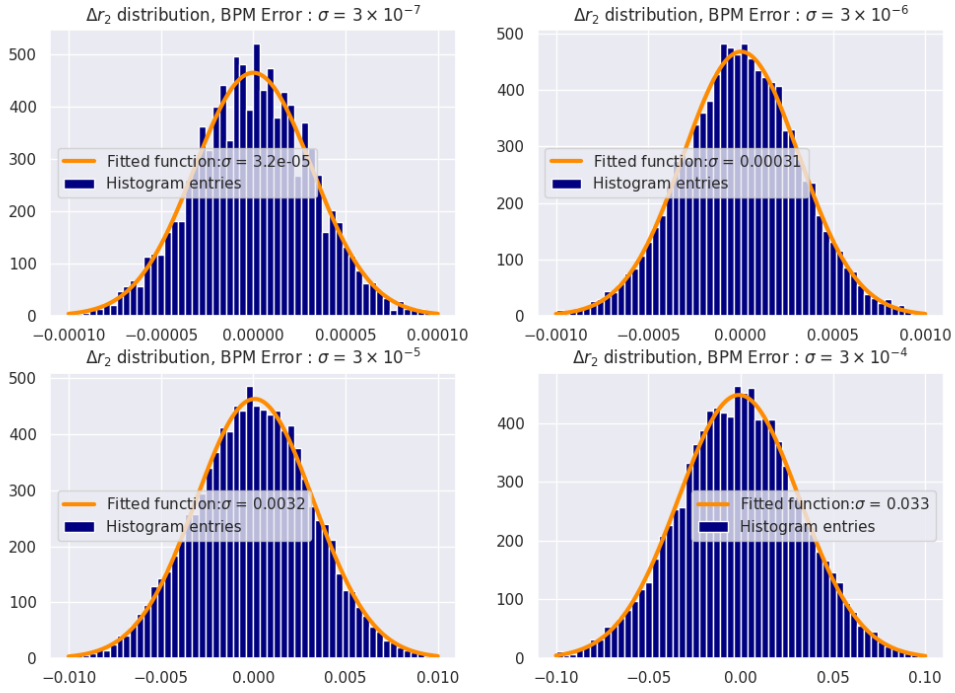

Figure 4.41: Evaluation of the effect of error on r_2 parameter the dispersion of Gaussian which is scanned from $\sigma = 3.0 \times 10^{-7}$ to $\sigma = 3.0 \times 10^{-4}$ in order.

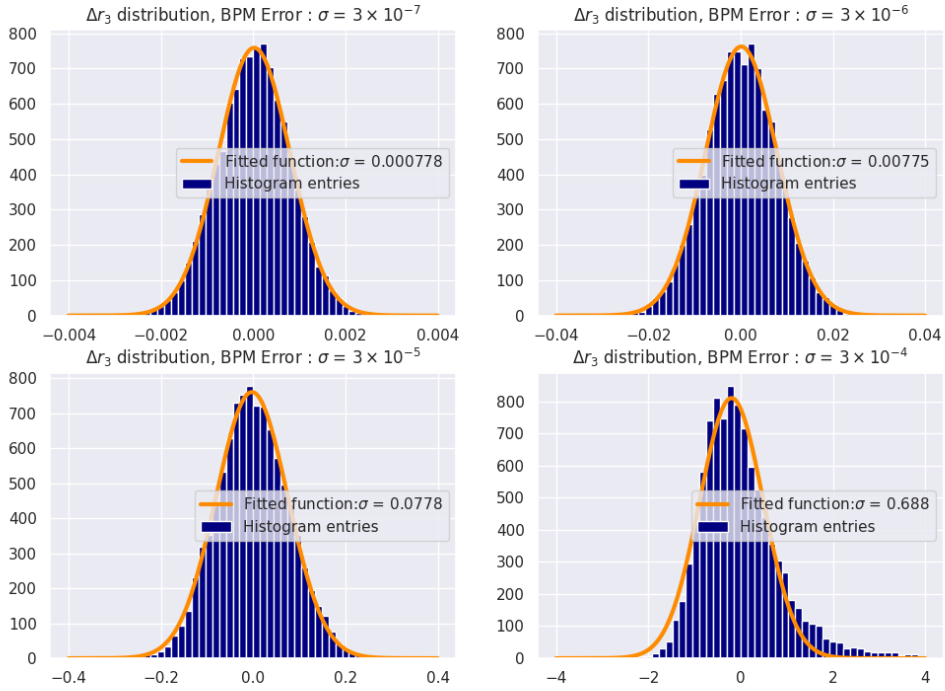

Figure 4.42: Evaluation of the effect of error on r_3 parameter the dispersion of Gaussian which is scanned from $\sigma = 3.0 \times 10^{-7}$ to $\sigma = 3.0 \times 10^{-4}$ in order.

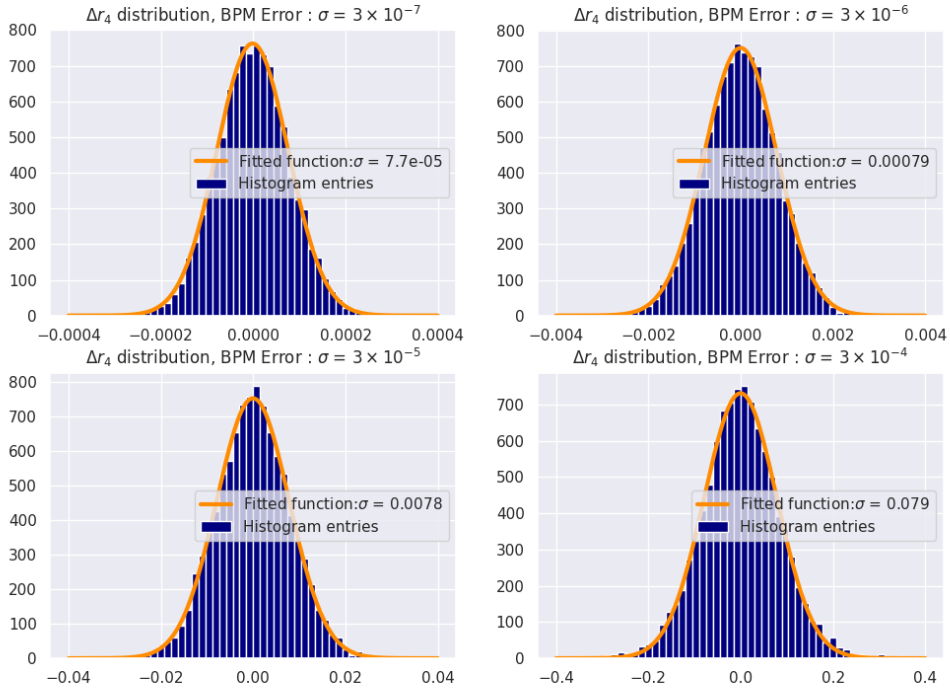

Figure 4.43: Evaluation of the effect of error on r_4 parameter the dispersion of Gaussian which is scanned from $\sigma = 3.0 \times 10^{-7}$ to $\sigma = 3.0 \times 10^{-4}$ in order.

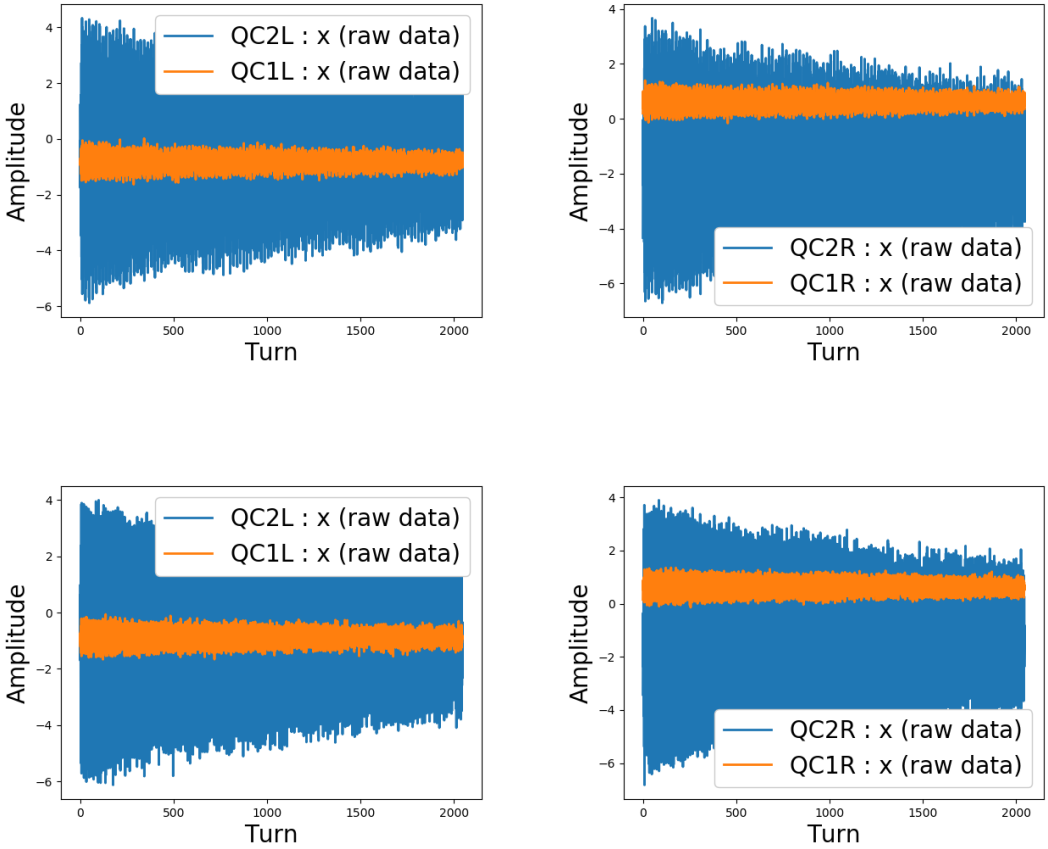

Figure 4.44: Raw data from the turn–by–turn measurement and comparison of the amplitude for x-axis at QC1LE and QC2LE or QC1RE and QC2RE. The upper and lower two plots denote $r_2 = 4$mm and $r_2 = 4$mm, respectively. The unit of the vertical axis of each plot is μm.

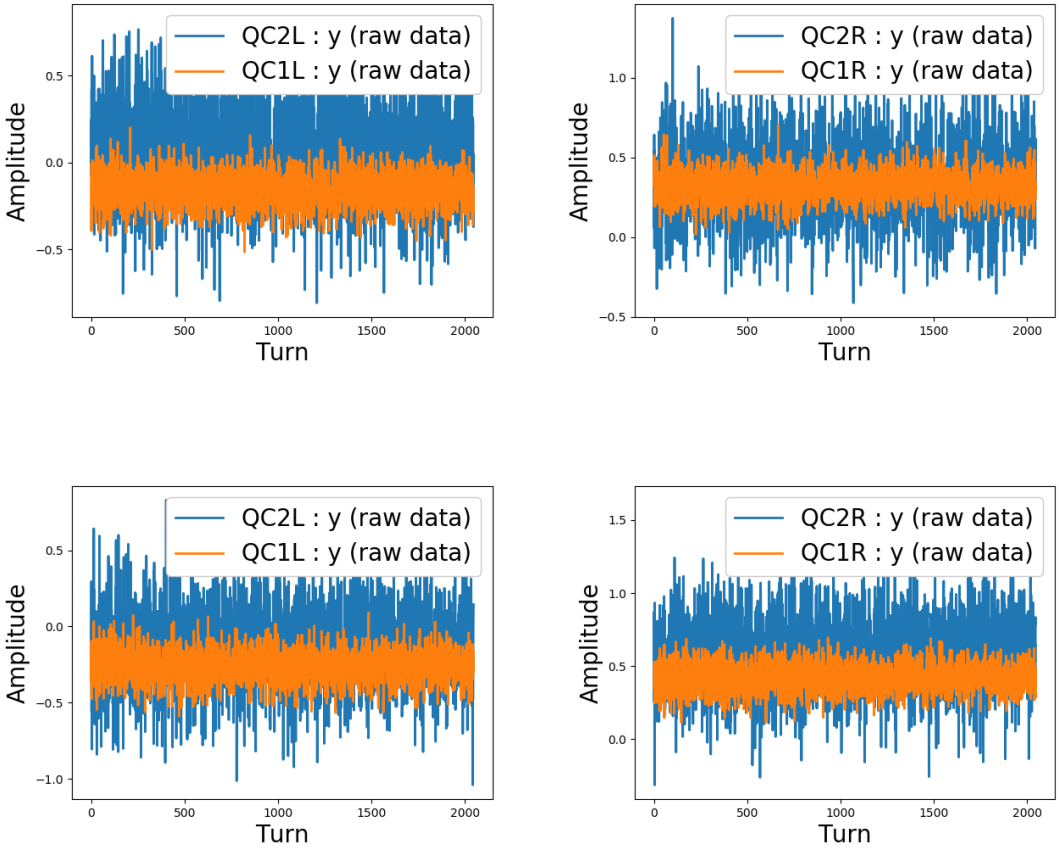

Figure 4.45: Raw data of turn–by–turn measurement and comparison of amplitude for y-axis at QC1LE and QC2LE or QC1RE and QC2RE. The upper and lower two plots denote $r_2 = 4$mm and $r_2 = 4$mm, respectively. The unit of the vertical axis of each plot is μm.

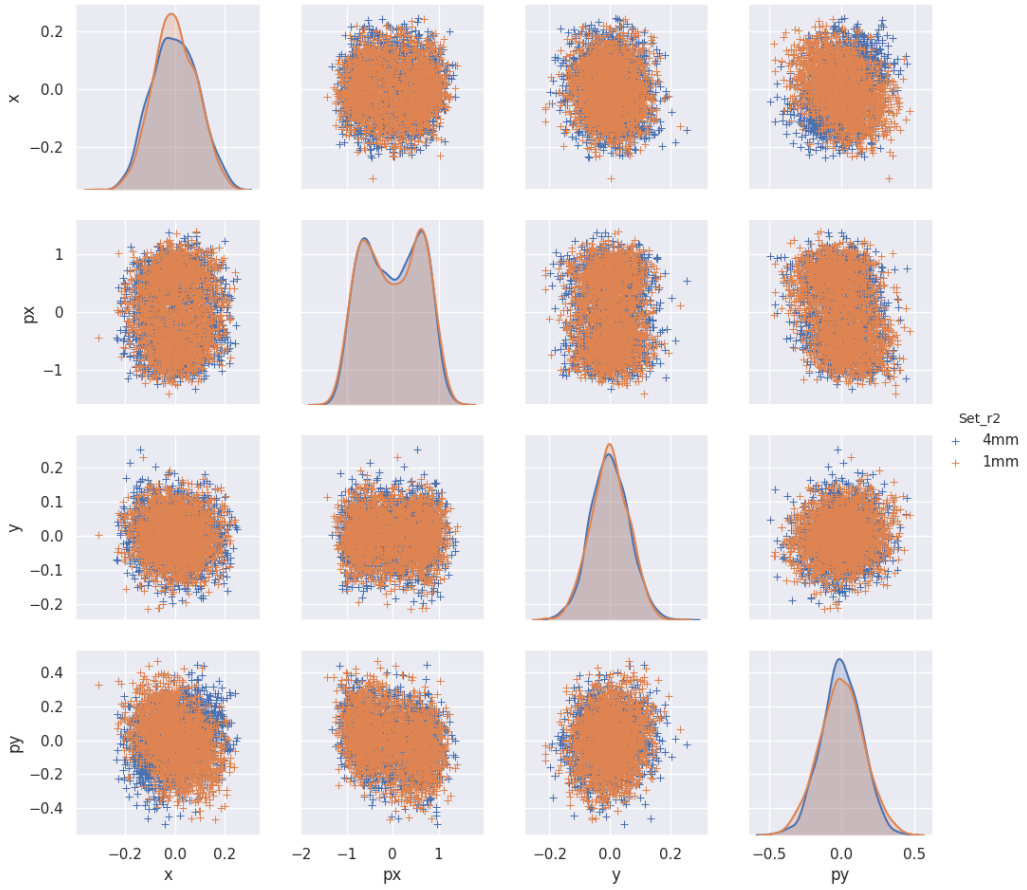

Figure 4.46: Example of scatter plots of the correlation matrix formed for the physical variables at the IP.

Because four physical variables exist for the IP, the Fourier spectrum must be calculated for each variable. The mode separation is the process by which each peak of the corresponding eigenmode in the Fourier spectrum is detected. The Fourier amplitudes and phases correspond to the relationship between the coupling parameters and the oscillations of the excited eigenmodes. Coupling parameters that are obtained via the above process with the measured data in Phase-2 commissioning are shown in Table 4.12

Setting	r_1 [rad]	r_2 [m]	r_3 [1/m]	r_4 [rad]
$r_2 = 4$mm (before SK1 change)	0.0512	−0.0043	−0.519	0.039
$r_2 = 1$mm (after SK1 change)	0.0405	−0.0075	0.8123	0.0678

Table 4.12: Coupling parameters at the IP calculated by the method of applying transfer matrix $\mathcal{M}$ first as Eq. (4.26).

The calculation order: Mode separation -> transfer

Next, the case Eq. (4.27), where the eigenmode separation is carried out first, is discussed. The positions of each monitor near the IP are listed in Table 4.13. The raw measured data at the individual BPMs and their Fourier spectra are shown in Fig. 4.47 and 4.48. Figure 4.47 illustrates the plots where $r_2 = 4$mm, and Fig. 4.48 are plots when $r_2 = 1$mm. In the figures, the left and right side correspond to the measured data in the time domain and frequency domain, respectively. The blue lines denote the data in the x-direction, and the orange lines denote the data in the y-direction. From the Fourier spectra plots, the U-mode peaks in the y-direction cannot be seen in the MQLC3 data. Therefore, it can be assumed that the betatron coupling is completely eliminated at MQLC3. The data measured at MQLC3 means that the optical aberration coming from the IR can be estimated by using the BPMs of MQLC3 as the coordinates of the BPMs are calibrated correctly with the coordinates of the beam oscillation. If the rotation errors for the monitors at the reference coordinates are negligible, we can focus on finding optical errors in the IR section for beam aberrations at the IP. In addition, coupling at the kicker position, which is the injection kicker in this case, is not observed in Fig. 4.47 and 4.48, so these conditions were excellent for analyzing the effect of a horizontal oscillation on a vertical plane.

HER	Position [m] (Left)	Position [m] (Right)
IP	0	3016.314
MQC1	0.53	3015.784
QC1L/RE inside edge	0.89	3015.404
QC1L/RE outside edge	1.9	3014.404
MQC2	2.25	3013.814
QC2L/RE inside edge	2.12	3014.074
QC2L/RE outside edge	3.2	3012.874
MQLC3	12.935	3003.380
MQLC7	27.272	2989.143

Table 4.13: The list of BPM positions near the IP. The values are distances from IP in counterclockwise direction.

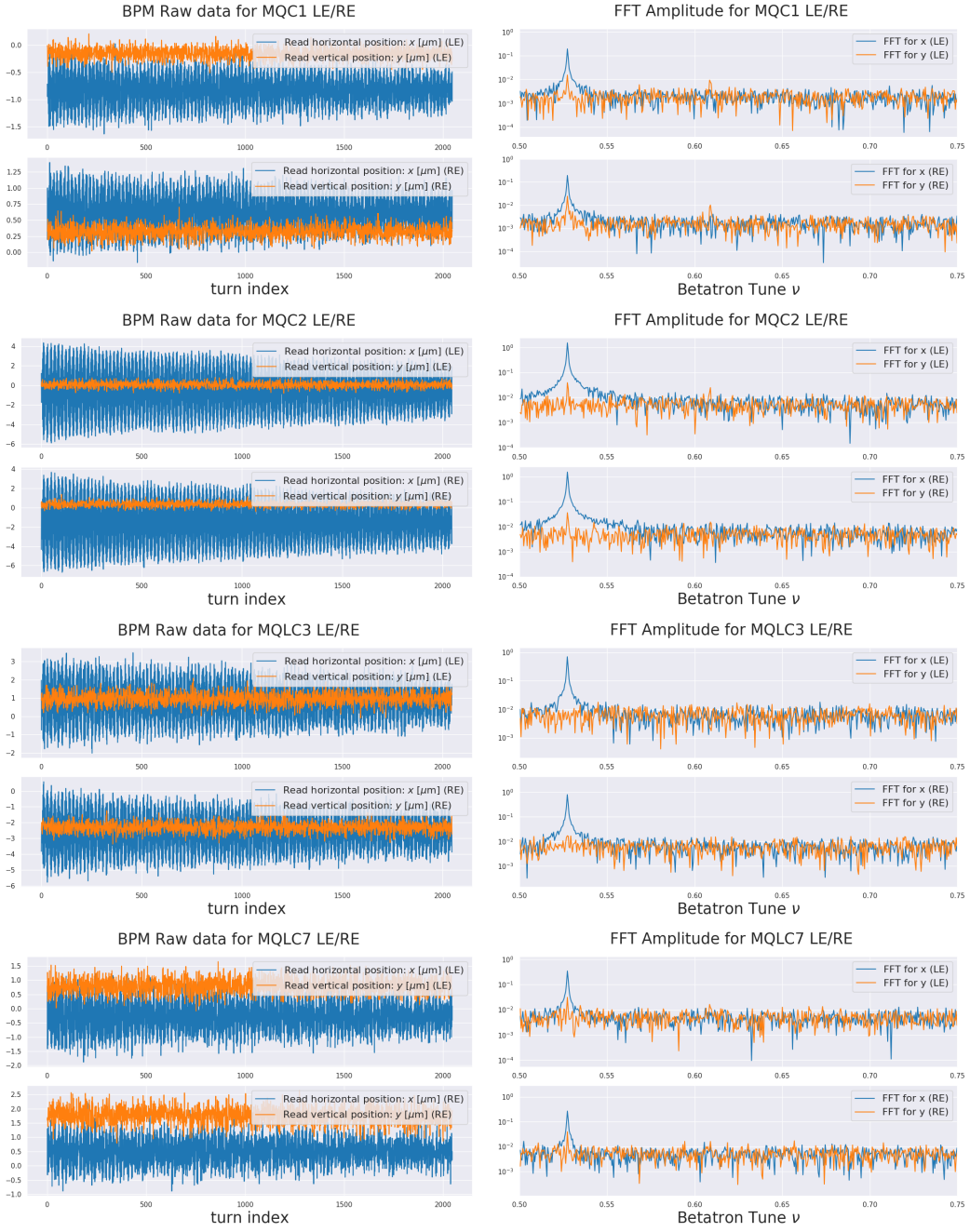

Figure 4.47: Raw of BPM signals and their FFT amplitude in and near IR section for $r_2 = -4mm$ set.

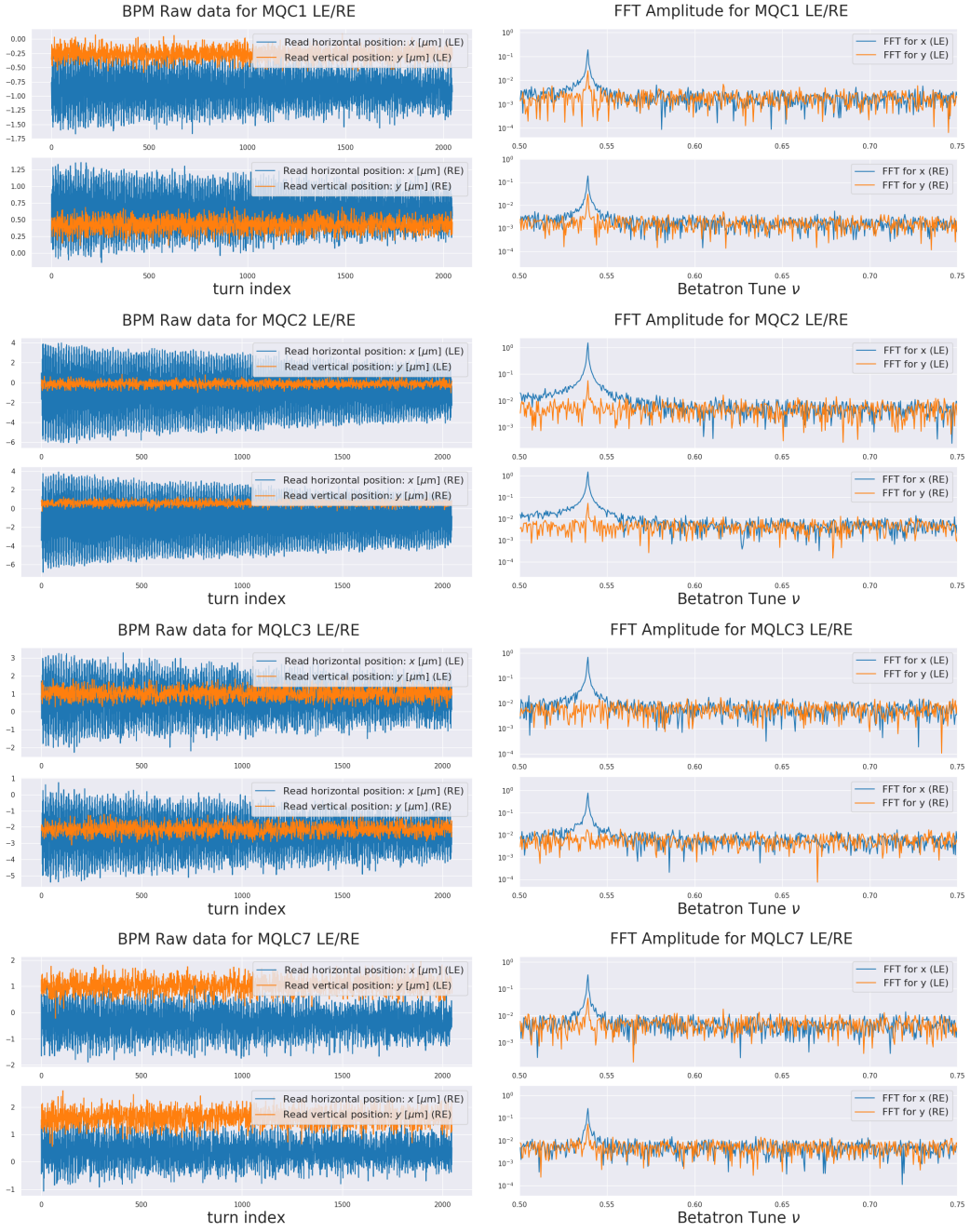

Figure 4.48: Raw of BPM signals and their FFT amplitude in and near IR section for $r_2 = -1mm$ set.

The peaks obtained in the Fourier spectrum for each measured BPM are transferred to the IP from the positions of each BPM using the transfer matrix from the SAD lattice model for $\mathcal{M}$. In order to obtain four variables describing the phase space at the IP, two data sets measured at both sides of the IP are used. The physical variables of the separated modes are calculated as complex variables. The complex physical variables in complex form are then transformed to polar coordinates after the transfer to the IP with the matrix $\mathcal{M}$, and the coupling parameters are thus derived. The coupling parameters obtained via Eq. (4.27) with the measured data in Phase-2 commissioning are listed in Table 4.14

Setting	r_1 [rad]	r_2 [m]	r_3 [1/m]	r_4 [rad]
$r_2 = 4$mm (before SK1 change)	0.34	0.0038	-0.48	-0.023
$r_2 = 1$mm (after SK1 change)	0.0069	0.0015	0.45	-0.042

Table 4.14: Coupling parameters at the IP calculated by the method of mode separation first as Eq. (4.27).

4.3.5 Ellipsoid fitting vs. harmonic analysis

To compare the methods used to calculate the coupling parameter derivation mentioned above, the results of the analysis of the coupling parameters are summarized in Table 4.15 for the data measured in the practical beam test. Comparison of the method used for ellipsoid fitting and the harmonic analysis are shown in this table. For the ellipsoid fitting method, #1 and #2 correspond to the least square method and the derivation of the normal vector for fitting the Courant–Snyder ellipse onto four–dimensional phase space, respectively. For the harmonic analysis method, #1 and #2 correspond to the initial application of the transfer matrix and the mode separation, respectively. From this table, it is found that only harmonic analysis #2 reproduces the practical values of r_2 of $r_2 = 4$mm and $r_2 = 1$mm. In this study, it is therefore apparent that the harmonic analysis with mode separation carried out first (Eq. (4.27)) has better reliability for obtaining coupling parameters from the calculation by using turn–by–turn BPM data in SuperKEKB.

Method	r_1 [rad]	r_2 [m]	r_3 [1/m]	r_4 [rad]
$r_2 = 4$mm (before SK1 change)				
Ellipsoid fitting #1	0.0127	−0.0124	−0.1194	0.0286
Ellipsoid fitting #2	0.0374	−0.0136	0.141	0.0199
Harmonic analysis #1	0.0512	−0.0043	−0.519	0.039
Harmonic analysis #2	0.34	0.0038	−0.48	−0.023
$r_2 = 1$mm (after SK1 change)				
Ellipsoid fitting #1	0.0075	−0.0138	0.2976	0.0196
Ellipsoid fitting #2	0.0135	−0.0143	0.3781	0.0238
Harmonic analysis #1	0.0405	−0.0075	0.8123	0.0678
Harmonic analysis #2	0.0069	0.0015	0.45	−0.042

Table 4.15: Summary of the deriving the coupling parameters by different methods for the case of $r_2 = 4$mm and $r_2 = 1$mm optics setting.

4.4 Discovering the source of errors via the use of a transfer matrix

4.4.1 Types of errors included in the data describing each measurement

From the FFT plots of the raw BPM data, BPMs with small deviations were found between the beam coordinates and the laboratory coordinates. As the calculation of physical variables using the transfer matrix from the BPM with small deviations is particularly suitable for evaluating the model, the reliable BPM data is used for the calculation of the coupling at each point near the IP. If the real system and the model system are different, the difference between the beam matrices transferred from the two sets directly represents the error that is included in the interval. Two possible models can lead to errors, as seen in Fig. 4.49.

4.4.2 Modelling thin skew quadrupoles to investigate additional errors

Illustration of the model

As error derivation is performed using two different sets of FFT data, BPM calibration between combinations must be calculated. However, the issues surrounding BPM errors are not discussed in this paper. Considering a model such as that illustrated at the bottom of Fig. 4.49, it is necessary to compare the two means of finding the source of the error by using two sets of BPMs with an error source in the interval.

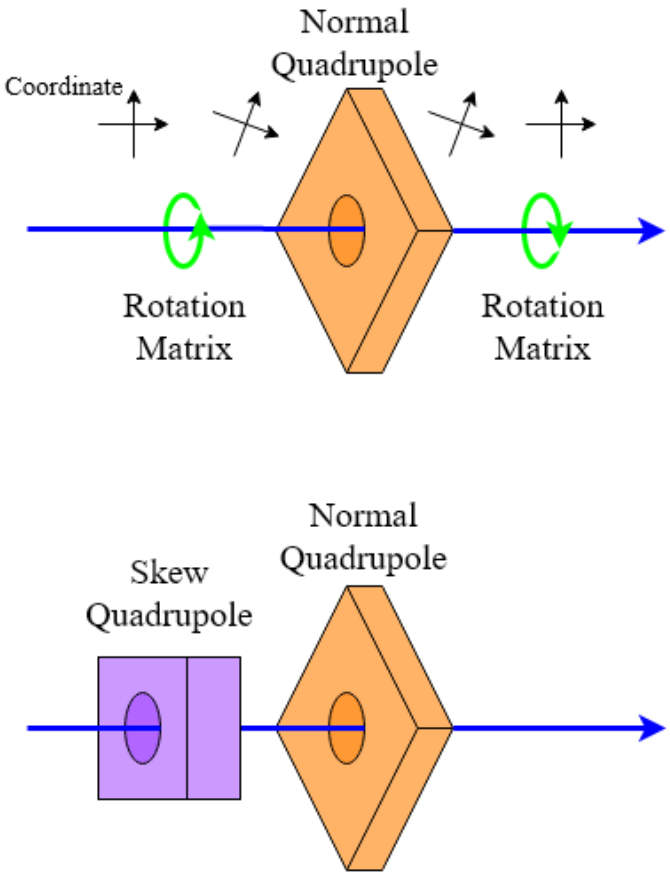

Figure 4.49: Illustration of two different models with errors leading to IP aberrations

As an example, consider that there is an error in the QC1 pair of the QCS system. Assuming an additional error source inside the QC1 (IP side), information concerning the two BPMs that are sandwiched between MQC1 and MQC2 is given in Table 4.13. Figure 4.50 is similar to the bottom of Fig. 4.49, which is a model of this situation.

Using this model, several of the parameters of transfer matrices and skew components are illustrated in Fig. 4.51. In this situation, there are two ways that coupling parameters can be calculated, as follows:

1. To calculate coupling parameters (r_1, r_2, r_3, r_4) at IP, the relationship between the revolution matrix and the error $\mathcal{M}_{\rm k}$, the coupling matrix $\mathcal{R}$, and matrices for several components are given in Fig. 4.51.

2. To calculate the true transfer matrix, the measured data at MQC1 and MQC2 are compared.

The relationship between the coupling matrix and the revolution matrix is de-

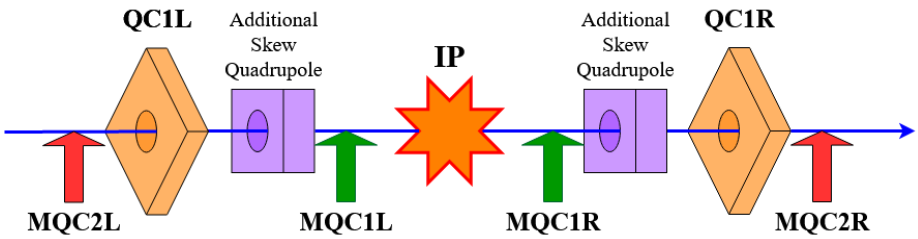

Figure 4.50: The model of the method used for calculating IP beam parameters using additional skew quadrupole errors.

scribed by

$$\mathcal{M}_{\rm k} = \mathcal{R}\mathcal{M}_0\mathcal{R}^{-1} \tag{4.28}$$

. On the other hand, $\mathcal{M}_{\rm k}$ can be calculated by using the additional skew error matrix as follow:

$$\mathcal{M}_{\rm k} = \mathcal{T}_{\rm kRIP}\mathcal{K}_{\rm 1R}\mathcal{T}^{-1}_{\rm kRIP}\mathcal{M}_0\mathcal{T}_{\rm kLIP}\mathcal{K}_{\rm 1L}\mathcal{T}^{-1}_{\rm kLIP} \tag{4.29}$$

.

Transferring the values of$(x,\ y)$ that are measured by the MQC2 monitors to the IP while including the effects of the additional skew components $K_{1R/L}$, and the transferred physical variables with additional skew errors can be written using

$$\begin{pmatrix} x^* \\ p_x^* \\ y^* \\ p_y^* \end{pmatrix}_{\rm wE} = \mathcal{T}_{\rm kR/LIP}\mathcal{K}_{\rm 1R/L}\mathcal{T}_{\rm 2kR/LIP} \begin{pmatrix} x_{\rm BM2R} \\ y_{\rm BM2R} \\ x_{\rm BM2L} \\ y_{\rm BM2L} \end{pmatrix} \tag{4.30}$$

$$= \mathcal{T}_{\rm 1R/LIP} \begin{pmatrix} x_{\rm BM1R} \\ y_{\rm BM1R} \\ x_{\rm BM1L} \\ y_{\rm BM1L} \end{pmatrix} \tag{4.31}$$

where subscript wE is a physical variable with additional skew errors, BM2R and BM2L are beam positions measured by the right and left BM2 monitoring set, and BM1R and BM1L are beam positions measured by the right and left BM1 monitor set, respectively. $\mathcal{T}_{\rm kR/LIP}$ is a composed transfer matrix of $\mathcal{T}_{\rm kRIP}$ and $\mathcal{T}_{\rm kLIP}$, $\mathcal{K}_{\rm 1R/L}$ is a composed transfer matrix of $\mathcal{K}_{\rm 1R}$ and $\mathcal{K}_{\rm 1L}$, $\mathcal{T}_{\rm 2kR/LIP}$ is a composed transfer matrix of

$\mathcal{T}_{\rm 2kLIP}$ and $\mathcal{T}_{\rm 2kRIP}$, and $\mathcal{T}_{\rm 1R/LIP}$ is a composed transfer matrix of $\mathcal{T}_{\rm 1kLIP}$ and $\mathcal{T}_{\rm 1kRIP}$.

On the other hand, if the real situation is almost same as the lattice model, the additional skew components $\mathcal{K}_{\rm 1R}$ and $\mathcal{K}_{\rm 1L}$ become identity matrices. Since transferred physical variables without additional skew errors can be written as

$$\begin{pmatrix} x^* \\ p_x^* \\ y^* \\ p_y^* \end{pmatrix}_{\rm woE} = \mathcal{T}_{\rm kR/LIP}\mathcal{T}_{\rm 2R/LkR/L} \begin{pmatrix} x_{\rm BM2R} \\ y_{\rm BM2R} \\ x_{\rm BM2L} \\ y_{\rm BM2L} \end{pmatrix} \tag{4.32}$$

where subscription woE means physical variable without additional skew errors , then the difference between the matrices with skew errors and without skew errors is

$$\begin{pmatrix} \Delta x^* \\ \Delta p_x^* \\ \Delta y^* \\ \Delta p_y^* \end{pmatrix} = \begin{pmatrix} x^* \\ p_x^* \\ y^* \\ p_y^* \end{pmatrix}_{\rm wE} - \begin{pmatrix} x^* \\ p_x^* \\ y^* \\ p_y^* \end{pmatrix}_{\rm woE} \tag{4.33}$$

$$= \left(\mathcal{T}_{\rm kR/LIP}\mathcal{K}_{\rm 1R/L}\mathcal{T}_{\rm 2kR/LIP} - \mathcal{T}_{\rm kR/LIP}\mathcal{T}_{\rm 2R/LkR/L}\right) \begin{pmatrix} x_{\rm BM2R} \\ y_{\rm BM2R} \\ x_{\rm BM2L} \\ y_{\rm BM2L} \end{pmatrix} \tag{4.34}$$

$$\equiv \mathcal{M}_\Delta \begin{pmatrix} x_{\rm BM2R} \\ y_{\rm BM2R} \\ x_{\rm BM2L} \\ y_{\rm BM2L} \end{pmatrix} \tag{4.35}$$

where $\mathcal{M}_\Delta$ is defined as the pseudo transfer matrix for the physical variables of the BM2 monitor set. In another representation, the same value can be obtained from

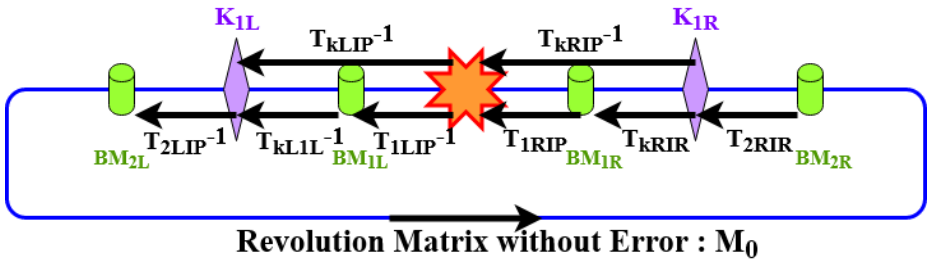

Figure 4.51: several components used in this approach and the corresponding matrices.

measured data:

$$\begin{pmatrix} \Delta x^* \\ \Delta p_x^* \\ \Delta y^* \\ \Delta p_y^* \end{pmatrix} = \begin{pmatrix} x^* \\ p_x^* \\ y^* \\ p_y^* \end{pmatrix}_{\mathrm{wE}} - \begin{pmatrix} x^* \\ p_x^* \\ y^* \\ p_y^* \end{pmatrix}_{\mathrm{woE}} \tag{4.36}$$

$$= \left(\mathcal{T}_{\mathrm{kR/LIP}}\mathcal{K}_{\mathrm{1R/L}}\mathcal{T}_{\mathrm{2kR/LIP}} - \mathcal{T}_{\mathrm{kR/LIP}}\mathcal{T}_{\mathrm{2R/LkR/L}}\right) \begin{pmatrix} x_{\mathrm{BM2R}} \\ y_{\mathrm{BM2R}} \\ x_{\mathrm{BM2L}} \\ y_{\mathrm{BM2L}} \end{pmatrix} \tag{4.37}$$

This representation does not include the factors of the assumed additional skew errors; thus, the value $\Delta\vec{x}^*$ can be calculated exactly. From Eq. (4.34) and (4.37), the realistic value of the additional skew factors k_R and k_L, and the combination of these with Eq. (4.28) can be used to derive realistic coupling parameters in the interval.

To calculate the coupling parameters and the corresponding additional skew errors, the measured data from the Phase-2 commissioning is used. Here, the skew error of the QC1 magnets is considered as the target; therefore, BPM sets of the MQC1 and MQC2 monitors are required. As seen in the discussion in the previous section concerning harmonic analysis, the measured data is formed by the FFT and adopted as Eq. (4.34), (4.37) and (4.28). As the matrix and Fourier transform ($\mathcal{F}$) are commutative, the relationship between the measured data and the quasi transfer

matrix is written as:

$$\Delta\vec{x}^* = \mathcal{M}_\Delta \vec{x}_{\mathrm{BM2R/L}} \tag{4.38}$$

$$\mathcal{F}(\Delta\vec{x}^*) = \vec{A}^*_{MQC1}(\nu_u) - \vec{A}^*_{MQC2}(\nu_u) \tag{4.39}$$

$$= \mathcal{M}_\Delta \vec{A}_{MQC2}(\nu_u) \tag{4.40}$$

where $\vec{A}(\nu)$ is the variable on the frequency domain of the peak value which is at $f = \nu$, and the others are same notations used in previous equations. Therefore, the complete form of $\vec{A}(\nu)$ is

$$\vec{A}^*_{BM}(\nu) = \begin{pmatrix} A^*_x(\nu)\cos\phi^*_x(\nu) \\ A^*_{px}(\nu)\cos\phi^*_{px}(\nu) \\ A^*_y(\nu)\cos\phi^*_y(\nu) \\ A^*_{py}(\nu)\cos\phi^*_{py}(\nu) \end{pmatrix}_{BM} = \mathcal{T}_{\mathrm{BMIP}}\vec{A}_{BM}(\nu) \tag{4.41}$$

$$\vec{A}_{BM}(\nu) = \begin{pmatrix} A_x(\nu)\cos\phi_x(\nu) \\ A_y(\nu)\cos\phi_y(\nu) \\ A_x(\nu)\cos\phi_x(\nu) \\ A_y(\nu)\cos\phi_y(\nu) \end{pmatrix} \tag{4.42}$$

where A is the Fourier amplitude, ϕ is the Fourier phase, and $\mathcal{T}_{\mathrm{BMIP}}$ is the pseudo transfer matrix that consists of two transfer matrixes from both sides of the BPM, from the BM to the IP.

Application for simulated BPM data of SAD simulation

Before applying the measured data from SuperKEKB commissioning, the method used to discover these errors is applied to the simulation data of SAD, which is the same data that was used in the previous section for verification of the method used for coupling analysis. To check the procedure of this idea for discovering error sources, the simulated turn-by-turn data without additional errors are used. Analyzed data are prepared for the ideal lattice and the modulated lattice with the SK1 parameters of the QC1 magnets $\pm 1.0 \times 10^{-3}$. In this test analysis, the analyzed result of the differences in the r_2 and r_3 parameters in the SAD simulations should be the same as the theoretical result calculated as the product of the transfer matrices. Analysis

is carried out using the equation:

$$\vec{A}^{*}_{qc1}(\nu_u) - \vec{A}^{*}_{qc2}(\nu_u) = (M_{\rm error} - M_{\rm model})\vec{A}_{qc2}(\nu_u), \tag{4.43}$$

where the subscript error denotes the matrix with the additional error and the subscript model denotes the matrix from the SAD model without any added errors. The $\vec{A}^{*}_{qc1}(\nu_u)$ and $\vec{A}^{*}_{qc2}(\nu_u)$ are the U–mode value of the Fourier transform for measured data at the MQC1 monitors and MQC2 monitors, respectively. The results of the Fourier spectrum of $\vec{A}_{qc1}(\nu_u)$ and $\vec{A}_{qc2}(\nu_u)$ are shown in Fig. 4.52. The value of $\vec{A}^{*}_{qc1}(\nu_u) - \vec{A}^{*}_{qc2}(\nu_u)$ is calculated in Fig. 4.52. Figure 4.53 shows the Fourier transforms of the simulated physical values at the IP. This figure represents the transferred values at the IP that were calculated using the transfer matrix from the SAD model. The additional error as the thin lens skew component is not included in this transfer matrix in the manual.

The quasi transfer matrix of $(M_{\rm error} - M_{\rm model})$ is applied to the U–mode peak in the lower plots of Fig. 4.52. In order to solve Eq. (4.43), an algebraic equation of at least the eighth degree is required. In this study, the Durand–Kerner method (Weierstrass method) with Aberth's initial condition is adopted as the numerical solution. The calculation used to derive additional skew value iterates the following equation for the k–th step:

$$z_i^{(k+1)} = z_i^{(k)} - \frac{q_n(z_i^{(k)})}{\prod_{j=1,j\neq i}^{n}(z_i^{(k)} - z_j^{(k)})}. \tag{4.44}$$

The analyzed results are shown in Table **??**. According to this table, similar values are obtained from the analyzed result for r_2 and r_3, as a theoretical result. The minimal difference between the two results of r_2 and r_3 comes from the difference in the error source. Because the additional error source is set to the edge of the quadrupole magnet, the position of the error has a finite distance from the practical position. In order to improve this method, a means of detecting the most likely position of errors should be developed in the future.

Application for SuperKEKB Phase-2

The case of applying the measured data in Phase-2 commissioning is discussed in this paragraph. The analyzed data in the frequency domain is shown in Fig. 4.54. Blue circles denote the U-mode and red circles denote the V-mode in each plot. The important difference between the two conditions is the existence of the V-mode peaks. Before changing r_2, the V-mode peaks are visible, but these peaks cannot be

	r_1[rad]	r_2[m]	r_3[1/m]	r_4[rad]
Before SK1 change (± 0 for QC1)				
IP (theoretical)	-2.0×10^{-13}	-8.0×10^{-14}	2.0×10^{-11}	5.0×10^{-12}
IP (analytical)	-1.3×10^{-5}	-2.0×10^{-7}	-1.2×10^{-3}	-9.8×10^{-4}
After SK1 change ($\pm 1.0 \times 10^{-3}$ for QC1)				
IP (theoretical)	6.0×10^{-6}	-1.8×10^{-3}	-1.555	6.0×10^{-4}
IP (analytical)	-1.8×10^{-2}	-1.6×10^{-3}	-2.9	1.4×10^{-3}

Table 4.16: The analytical value is reproduced by the method of additional error. The theoretical value is calculated by SAD code.

seen after changing r_2. When only the U-mode is analyzed, the difference between the two conditions was difficult to see, but V-mode analysis can provide some hints for identifying the origin of the errors. In the following sections, these behaviors are discussed in detail.

4.4.3 A Model of partial rotation instead of misalignment

Illustration of the model

A rotation error is expressed in the relationship with an error angle θ and a transfer matrix sandwiched by rotation matrices with the θ. In general, rotation errors of the quadrupoles are shown in Fig. 4.55. The corresponding relationships between the

six-dimensional physics variables for the situations seen in Fig. 4.55 are

$$\tilde{\mathcal{M}} = \begin{pmatrix} \cos\theta & \sin\theta & 0 & 0 & 0 & 0 \\ -\sin\theta & \cos\theta & 0 & 0 & 0 & 0 \\ 0 & 0 & 0 & \cos\theta & \sin\theta & 0 \\ 0 & 0 & 0 & -\sin\theta & \cos\theta & 0 \end{pmatrix} \mathcal{M} \begin{pmatrix} \cos\theta & -\sin\theta & 0 & 0 & 0 & 0 \\ \sin\theta & \cos\theta & 0 & 0 & 0 & 0 \\ 0 & 0 & 0 & \cos\theta & -\sin\theta & 0 \\ 0 & 0 & 0 & \sin\theta & \cos\theta & 0 \end{pmatrix} \tag{4.45}$$

$$\tilde{\mathcal{M}} = \begin{pmatrix} \cos\theta & 0 & \sin\theta & 0 & 0 & 0 \\ -\sin\theta & 0 & \cos\theta & 0 & 0 & 0 \\ 0 & 0 & 0 & \cos\theta & 0 & \sin\theta \\ 0 & 0 & 0 & -\sin\theta & 0 & \cos\theta \end{pmatrix} \mathcal{M} \begin{pmatrix} \cos\theta & 0 & -\sin\theta & 0 & 0 & 0 \\ \sin\theta & 0 & \cos\theta & 0 & 0 & 0 \\ 0 & 0 & 0 & \cos\theta & 0 & -\sin\theta \\ 0 & 0 & 0 & \sin\theta & 0 & \cos\theta \end{pmatrix} \tag{4.46}$$

$$\tilde{\mathcal{M}} = \begin{pmatrix} 0 & \cos\theta & \sin\theta & 0 & 0 & 0 \\ 0 & -\sin\theta & \cos\theta & 0 & 0 & 0 \\ 0 & 0 & 0 & 0 & \cos\theta & \sin\theta \\ 0 & 0 & 0 & 0 & -\sin\theta & \cos\theta \end{pmatrix} \mathcal{M} \begin{pmatrix} 0 & \cos\theta & -\sin\theta & 0 & 0 & 0 \\ 0 & \sin\theta & \cos\theta & 0 & 0 & 0 \\ 0 & 0 & 0 & 0 & \cos\theta & -\sin\theta \\ 0 & 0 & 0 & 0 & \sin\theta & \cos\theta \end{pmatrix} \tag{4.47}$$

for the left, center, and right figures, respectively, and where z is equal to s in the previous notation.

When the magnetic field is symmetrical around the reference axis, the rotation in the x-z and y-z planes can be ignored, and only the rotation in the x-y direction needs to be considered. Fig. 4.56 shows the measured quadrupole magnetic field distribution of QC1 and QC2 in SuperKEKB. Here, A_2 and B_2 are coefficients of the quadrupole term and their equation is defined as

$$Re[V(x,y)] = -\frac{cp}{e}\sum_{m=0}^{n/2}(-1)^m(A_n + B_n)\frac{x^{n-2m}}{(n-2m)!}\frac{y^{2m+1}}{(2m+1)!} \tag{4.48}$$

$$Im[V(x,y)] = -\frac{cp}{e}\sum_{m=0}^{(n-1)/2}(-1)^m(A_n - B_n)\frac{x^{n-2m-1}}{(n-2m-1)!}\frac{y^{2m+1}}{(2m+1)!} \tag{4.49}$$

where A_n and B_n are the coefficients of the scalar potential, and V is the scalar potential of the electromagnetic interaction $B = -\nabla V(x,y)$. The imaginary part is

called the normal components and the real part is called the skew component of the magnetic field. From the figure, it can be seen that the quadrupole magnetic field component A_2 and B_2, which is the subject of this discussion, has good symmetry, so that only rotation of the x-y plane needs to be considered for "x-y coupling".

The calculation sequence is exactly the same as that used previously (in the model of additional skew components). Figure 4.57 shows the model for this situation. The equation of this model is represented by

$$\mathcal{M}_{\mathrm{r}} = \mathcal{T}_{\mathrm{kRIP}}\mathcal{R}_{-\theta_{\mathrm{R}}}\mathcal{M}_{\mathrm{QC1R}}\mathcal{R}_{\theta_{\mathrm{R}}}\mathcal{T}^{-1}_{\mathrm{kRIP}}\mathcal{M}_0\mathcal{T}_{\mathrm{kLIP}}\mathcal{R}_{-\theta_{\mathrm{L}}}\mathcal{K}_{\mathrm{1L}}\mathcal{R}_{\theta_{\mathrm{L}}}\mathcal{T}^{-1}_{\mathrm{kLIP}} \tag{4.50}$$

where $\mathcal{M}_{\mathrm{r}}$ is the one-turn transfer matrix with rotation error, and $\mathcal{R}$ is the matrix of the rotation around the z direction. This equation is essentially the same as Eq (4.29), while replacing $\mathcal{K}$ with $\mathcal{R}_{-\theta}\mathcal{M}\mathcal{R}_{\theta}$. The following calculations are same as those in the additional skew model.

The important point is that the results of the two models should be identical, as the error parameters have the same dimension and the analyzed data is the same. However, the boundary conditions of the error matrices are different, so comparing the two methods is very useful for checking the accuracy of the result.

This model does not perform well at present. Thus, an improvement of this rotation model should be developed in the future.

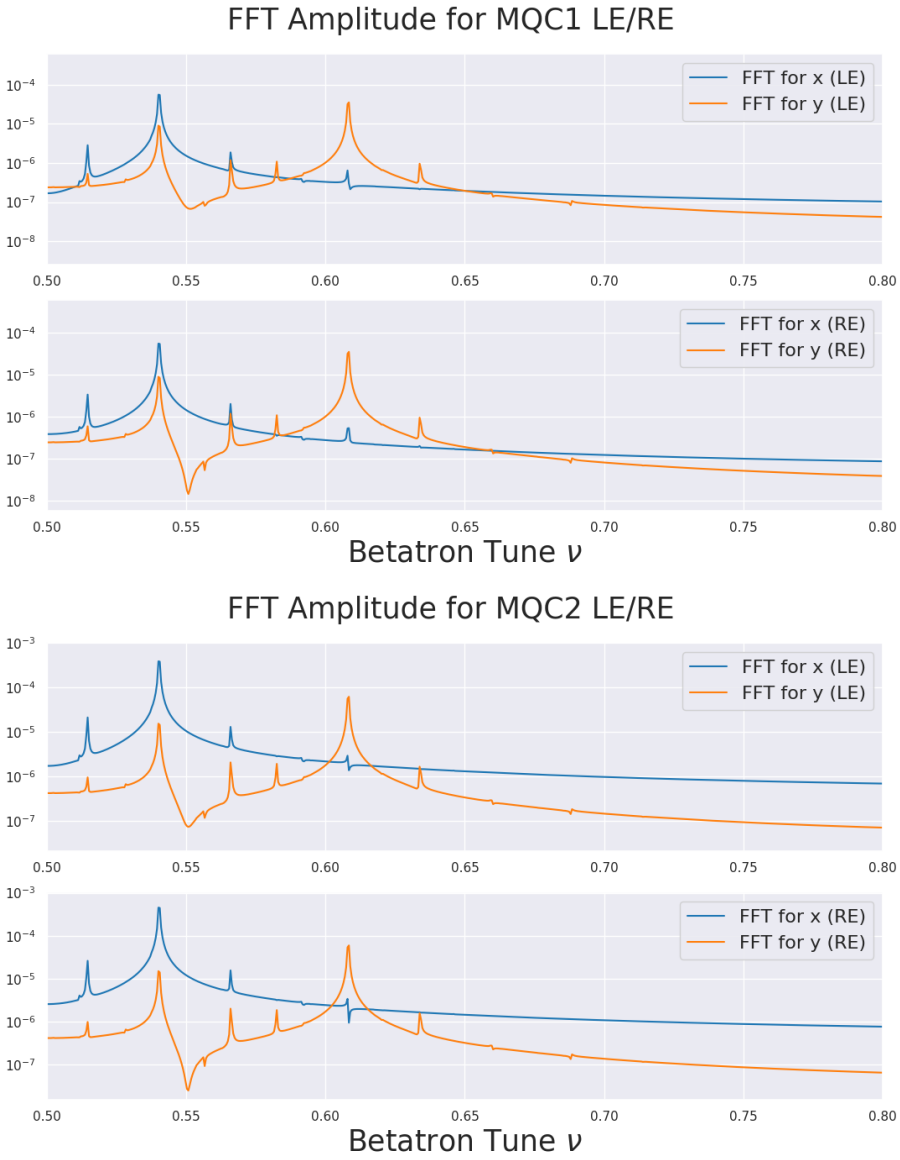

Figure 4.52: Fourier spectrum of the simulated result for the case $SK1 \pm 1.0 \times 10^{-3}$ in the SAD lattice model. The upper plots show the Fourier spectrum of $\vec{x}_{qc1}$, and the lower plots show the Fourier spectrum of $\vec{x}_{qc2}$.

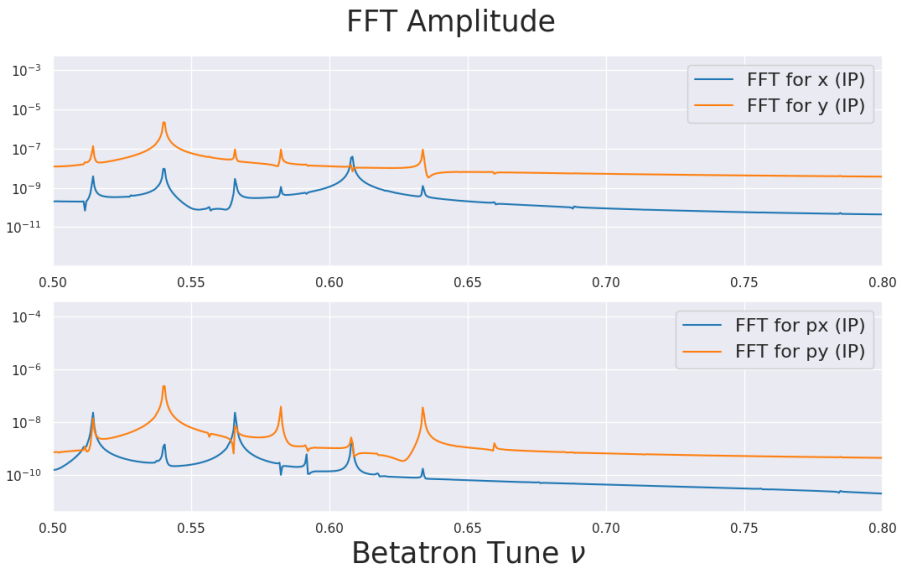

Figure 4.53: Fourier spectrum of the simulated data at the IP.

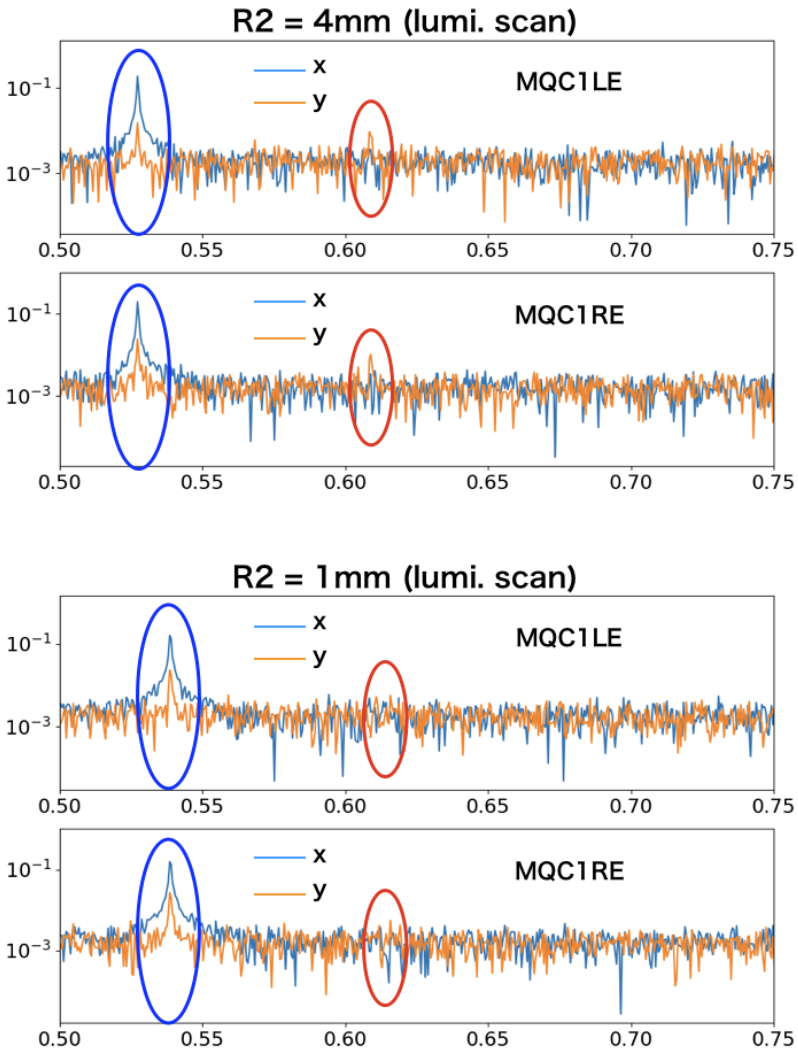

Figure 4.54: Comparison of the two conditions on the frequency domain in the additional skew model

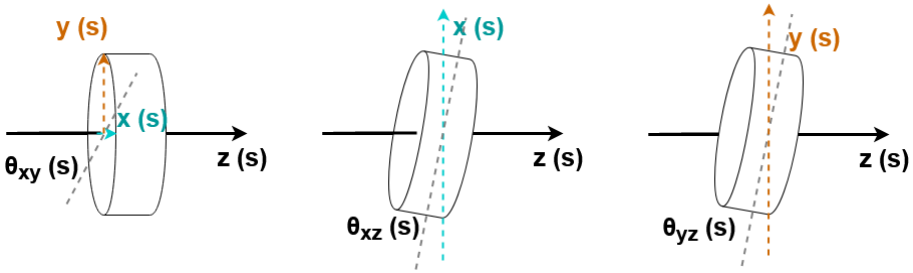

Figure 4.55: Illustration of several types of rotation errors

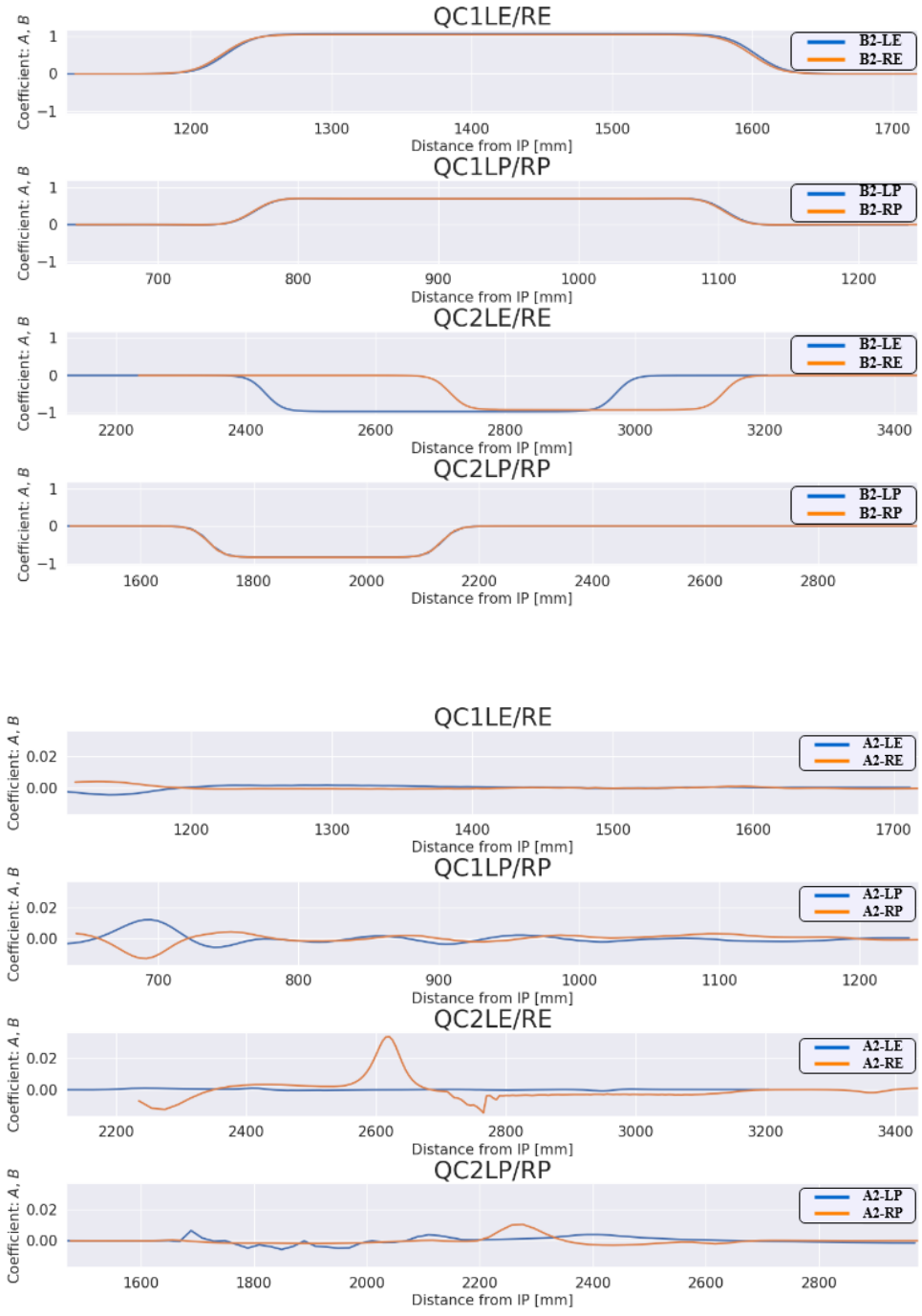

Figure 4.56: A_2 and B_2 distributions of QC1 and QC2 longitudinal magnetic field.

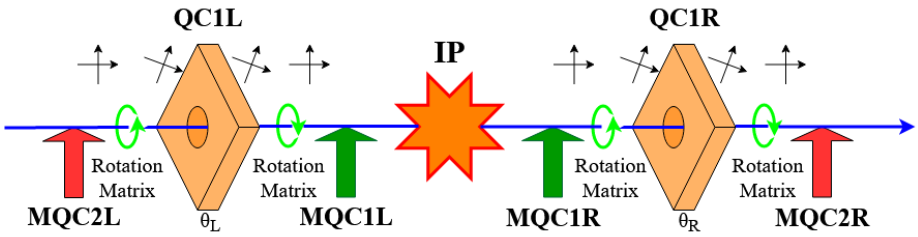

Figure 4.57: The model of the method used for calculating the IP beam parameters with additional rotation error in the QC1 magnets.

Chapter 5

Summary

The IP beam dynamics of SuperKEKB requires careful adjustment as it is the first machine that has adopted the nano-beam scheme. In this study, the X-Y betatron coupling at the IP is investigated, which is a second-order error at the collision point, and the local X-Y betatron coupling at the IP is corrected, which was a significant problem in Phase-2 of SuperKEKB.

In the analysis of the X-Y coupling, the behavior of the coupling at the collision point was investigated in detail from adjustments made to each magnetic field using the C.O.D. measurement method and the Harmonic method of Turn-by-Turn BPM data.

The QC1 skew corrector coil was used for the correction of errors, mainly in r_2 at the collision point, and a method was established for adjusting Linear X-Y coupling after Phase-2. To investigate the cause of these errors, measurement-based error models were used and research was carried out to establish a method in order to identify the individual errors that were a result of the devised model.

In this study, luminosity of the SuperKEKB operation was compensated via tuning betatron coupling parameters at the IP and evaluating the luminosity behavior, which is performed by the beam–beam simulation, in the case of the linear optics aberration existed. First, it is proved that the r_1 and r_2 of the betatron coupling parameter remarkably affect the impact of the degradation on the geometric luminosity of the nano–beam scheme, which is calculated by the effect of optics aberration on the beam dynamics at the IP in the model of Edward–Teng parametrization. Because the iterative beam–beam effect is affected by r_3 and r_4 paraemters of the IP coupling, evaluation of the collision simulation is required to find effective coupling paraemters on the luminosity. For the SuperKEKB operation, we figured that the weak–strong simulation is enough performed to simulate actual collision situation, since it was observed that one side of colliding beam is scattered by the counter side of beam.

To study about the behavior of the collision condition, bunch current dependency of the specific luminosity was calculated by simulating the coupling parameter scanned weak–strong beam–beam model. According to the simulation result, the degradation of the equilibrium luminosity mainly depends on the degradation of the geometric luminosity. It could be proved that the luminosity degradation caused by the cumulative effect of beam–beam interaction was also effective. Regarding the betatron coupling parameter, the r_2 was the most sensitive parameter, and the r_1 was the second most sentsitive parameter. As the model of the collision with betatron coupling error, r_2 and r_1 correspond to the tilt between y and p_x direction, and the tilt between y and x direction, respectively. This illustration is much apodictic, since the beam size of real space is extremely squeezed at the IP, and p_x and p_y is enlarged in response to squeezed x and y. By using this result of evaluated coupling parameters, actual IP optics tuning was performed in the SuperKEKB commissioning. As it is considered that the r_1 and the r_2 are effective on the luminosity degradation in keeping with the result of beam–beam simulations, the r_1 and the r_2 are selectively adjusted to compensate the coupling parameter errors by using the non-interleaved sextupole system. However, the problem that the tuning range for r_2 is not sufficient to scan optimum value to produce the best luminosity was occurred. The reason of this problem is that the global coupling paraemters can not be modified such a large amount. In order to solve this problem, it is proposed that the QCS skew corrector coils, which are installed to correct the misalignment and characteristics of each magnet, is used to compensate the IP X–Y coupling paraemters. The coupling parameter at the IP is too large in case that the error source was located at the global component, and the such a large coupling parameter is observed at only visinity of the IP locally are the reason why skew corrector coils are used. Before skew corrector coils were used to compensate the IP copupling parameters, the possibility and the estimated value of skew components have been calculated in the system of transfer matrix of SAD model. The parameters calculated by the transfer matrix was set to the optics condition of actual operation. The manually offset of r_2 value equals to -6 mm to establish the linear optics tuning method by using the non-interleaved sextpole system. The establishment of the optics tuning method for compensating the IP X–Y coupling by adding the manually tuned skew corrector coils to non-interleaved sextupole system for correction of the global X–Y coupling is the main conclusion of this study.

As the next topic, the analysing method of the X–Y coupling parameters by using the BPM system is studied to accurately correct the IP X–Y coupling errors. In the preceding study, the harmonic analysis and the correlation matrix method is powerful to calculate the IP coupling parameters. However, in the case of the

SuperKEKB operation, the method of using correlation matrix is much difficult to analyse IP parameters because the beam size at the IP is too small to calculate the coupling parameters remaining in the real space. In the case of the harmonic analysis method, the beam size in the real space is unrelated to analysing each parameter since this method is analysing the data of betatron oscillations in the frequency space. Nevertheless, it is important to calculate the effect of measurement noise on the result of analysing the X–Y coupling parameters because the noise of monitors affects the amplitude in the reciprocal space. In order to estimate the allowable noise level, the simulated data with the noise by adding the Gaussian noise produsedby the BoxMuller's method to TbT mode BPM data produced by SAD simulations was evaluated. And then, the actual measured data was analysed and the accuracy for analysing the IP X–Y coupling was evaluated in reference to estimated value by using changed amount of magnetic fields. Consequently, it is proved that the method of mode separation first give better result to analysing the IP coupling parameters. Furthermore, the new analysing method which uses the single kick COD trajectory of the beam with scanning the betatron phase at the IP. This method is performed by deriving the tilt of the Courant–Snyder ellipsoid in the 4–D phase space. However, this analysing method much depends on measured noises. When plural eigenmodes are included in the COD data, the derivation of the ellipsoid tilts becomes too hard. This method is still under development by using the principle component analysis.

Finally, in order to specify the error source of actual optics in SuperKEKB, the model to calculate the effect of the IP coupling parameters provided by the magnetic field in the section delimited by the BPM is considered. The subject of this study is the derivation of the true transfer matrix of the actual SuperKEKB operation, which transfers the beam along the ring. To calculate the true transfer matrix, the actual BPM data and the transfer matrix provided by the lattice model of SAD are used. Since it is difficult to assume the small error matrix for every thin slices in the delimited section, one error matrix of the thin lens approximation is installed at the center of target component. By using the SAD simulation of TbT BPM discussed above, the possibility of the analysis was evaluated. As the result, the similar value to the theoretically calculated value of the SAD could be obtained. Nevertheless, analysed values are not completely agreed with theoretical value. In order to improve this model, it is inferred that the reproducibility becomes better by adjusting the separation point of the transfer matrix to insert the additional error matrix. The result of applications for the measured data shows the significant noise dependency of the analysed error matrix. Therefore, the noise reduction is the most important before applying the proposed model to obtain the true transfer matrix.

Appendix A

Methods for Data Analysis

A.1 Singular Value Decomposition

Singular Value Decomposition (SVD) is a fundamental method that uses linear algebra to separate a matrix. The SVD is used in the processes PCA and ICA, so it is a crucial technique for use in this study. The fundamental mechanism is explained by

$$\mathcal{X} = \mathcal{U}\Sigma\mathcal{V}^T \tag{A.1}$$

Figure A.1 is an illustration of the effects of each of the matrices in the SVD, and several matrices are the same as those used in Eq.A.1. This process is therefore very similar to transformation of the beam matrix.

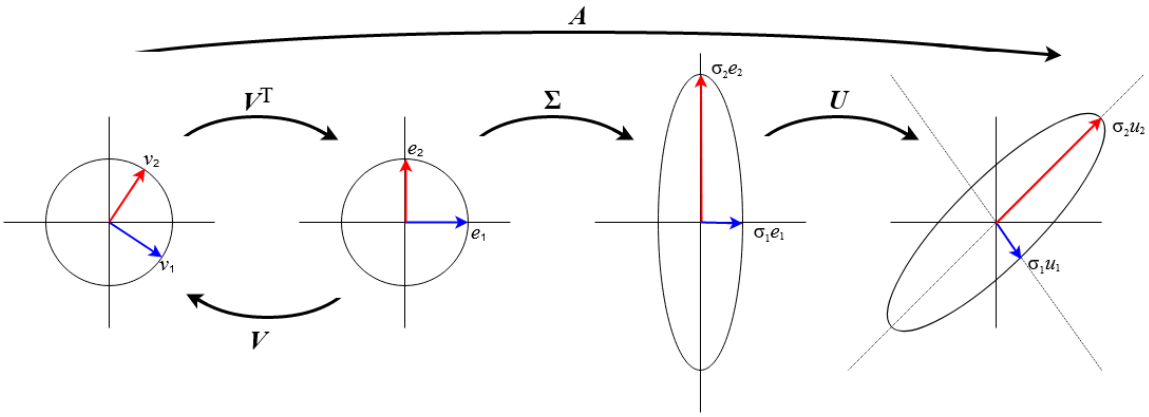

Figure A.1: The effects of each matrix in the SVD method.

A.2 Principal Component Analysis

An essential notation in principal component analysis is the linear combination of variables.

$$y = \sum_{i=1}^{v} c_i x_i == \vec{c}^T \vec{x} \tag{A.2}$$

where y is the new variable defined by the linear combination of the original variables, and the vectors $\vec{x} = (x_1, \ldots, x_v)^T$ and $\vec{c} = (c_1, \ldots, c_v)$ are the variables and coefficients of the analyzed system, respectively. Principal component analysis seeks a linear combination of the original variables such that the usual sample variance in the resulting values is at a maximum. The eigenvectors $\vec{u}_1$ provide the coefficients that define the linear combination, while the resulting values are the projected points y_{im}. The sample variance of the projected points $y_{1\mathrm{m}}$ gives the first eigenvalue e_1. The usual eigenvalue adopted is $\sum u_{11} = \vec{u}_1^T \vec{u} = 1$. Maximization of the variance of the y_{1m} subject to the given constraint leads to the eigenequation

$$(\vec{V} - e\vec{I})\vec{u} = \vec{o} \tag{A.3}$$

where V denotes the within-group co-variance matrix. Let

$$\vec{U} = (\vec{u}_1, \ldots, \vec{u}_{\mathrm{v}}) \tag{A.4}$$

denotes the matrix of eigenvectors, and the diagonal matrix

$$\vec{E} = diag(e_1, \ldots, e_{\mathrm{v}}) \tag{A.5}$$

denotes the matrix of the eigenvectors. The eigenequation thus becomes

$$\vec{V} = \vec{U}\vec{E}\vec{U}^T = \sum_{i=1}^{v} e_1 \vec{u}_{\mathrm{i}} \vec{u}_{\mathrm{i}}^T \tag{A.6}$$

. These eigenvectors satisfy $\vec{U}^T\vec{U} = \vec{1}$. Since each successive principal component accounts for a maximum amount of the variation, subject to being uncorrelated with the previous components $e_1 > e_2 > \ldots > e_v$.

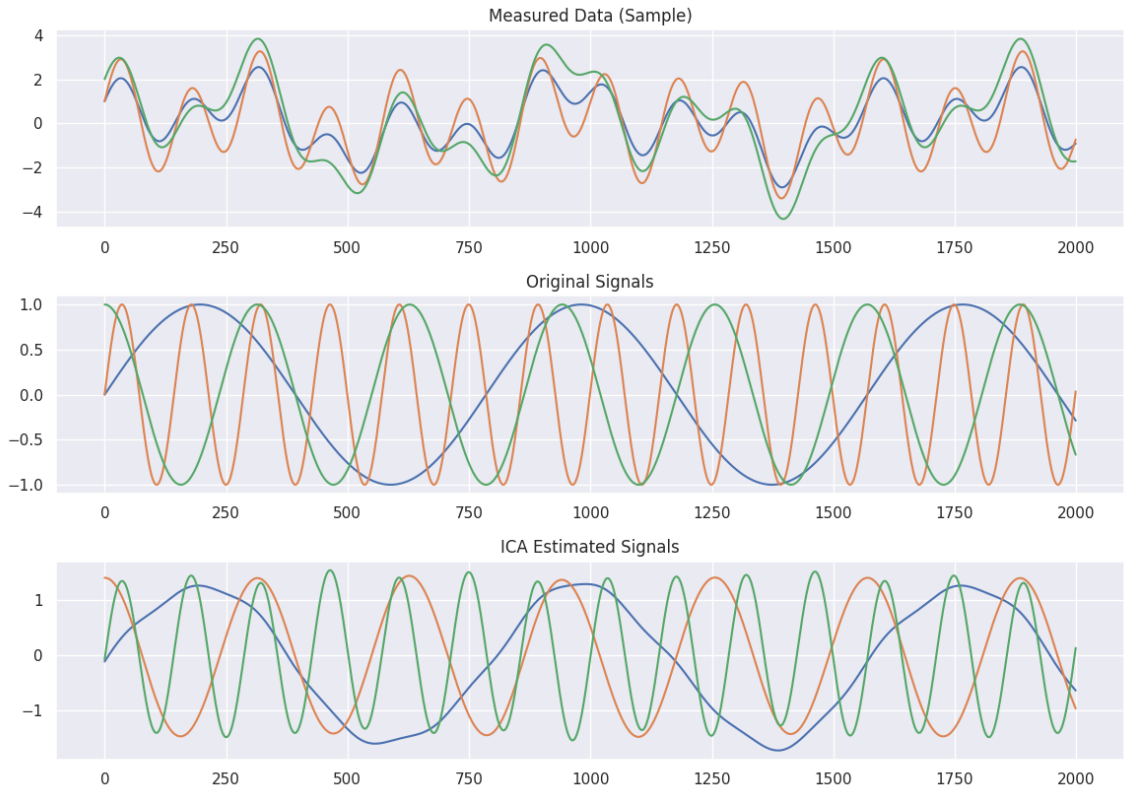

Figure A.2: An example of ICA signal separation. The top figure shows the mixed signals with random coupling coefficients, the middle figure shows the original signals, and the bottom figure shows the estimated signals which are reproduced from the original signals by the ICA using the mixed signals

A.3 Independent Component Analysis

A.3.1 Theoretical overview of the ICA

The aim of the Independent Component Analysis (ICA) is to verify the original signals and the law of the mixing signals from the measured data. As an example of signal separation, Fig. A.2 shows that original signals are predicted by the ICA as test mixed signals with arbitrary signal coupling factors. According to theory, the dimension predicted is equal to the number of test mixed signals.

The linear relationship between the m-dimensional observation vector $\vec{x}(t)$ and the n-dimensional original signal vector $\vec{s}(t)$ is represented by

$$\vec{x}(t) = \mathcal{A}\vec{s}(t) + \vec{N}(t) \tag{A.7}$$

where $\mathcal{A} \in \mathbb{R}^{m \times n}$ is the mixing matrix with $m \geq n$, and $\vec{N}(t)$ is the noise vector,

which is statistically independent of the original signal $\vec{s}(t)$.

Physical processes are generally assumed to consist of sufficient independent source signals and to be correlated temporally. The law of temporal correlation is the most important factor in analyzing measured data for the accurate explanation of several phenomena or events. The methods used for separating the important original signal from noise and physically meaningless signals has been well discussed so far by many researchers. The ICA is one of the strongest tools and it is very well–known approach in machine leaning and statistics.

Initially, the data sampled by the BPMs around the ring can be composed into a matrix such as

$$\mathcal{X} = \begin{pmatrix} x_1(1) & x_1(2) & \cdots & x_1(N) \\ x_2(1) & x_2(2) & \cdots & x_2(N) \\ \vdots & \vdots & \ddots & \vdots \\ x_m(1) & x_m(2) & \cdots & x_m(N) \end{pmatrix} \tag{A.8}$$

where N is the total number of turns, and the subscript of each component represents the number of BPMs in order. The arbitrary component $x_i(j)$ therefore denotes the ith BPM on the jth turn.

The ICA algorithm can extract the mixing matrix $\mathcal{A}$ and the original signal $\vec{s}$ from the composed matrix $\mathcal{X}$. Because the original signals are independent of each other, each signal $\vec{s}_i$ and its spatial distribution $\mathcal{A}_i$ is called a mode.

The signal that represents betatron oscillation in this study, which has a different phase at each BPM, will appear as two modes. In the frequency spectrum, an important property of betatron oscillation is the tune. When betatron oscillation is written as

$$\vec{u}(t) = \mathcal{A}_u \vec{s}_u(t) + \mathcal{A}_v \vec{s}_v(t) \tag{A.9}$$

where $\vec{s}_u(t)$ and $\vec{s}_v(t)$ are the U- and V-modes, which are assumed to be sine like and cosine like modes, the betatron amplitude and its phase advance can be derived using

$$\beta_i = a^2(\mathcal{A}_{u,i}^2 + \mathcal{A}_{v,i}^2) \tag{A.10}$$

$$\psi_i = tan^{-1}\left(\frac{\mathcal{A}_{u,i}}{\mathcal{A}_{v,i}}\right) \tag{A.11}$$

where a is a constant depending on the initial conditions. The fractional tune of the betatron oscillation can be obtained via Fourier transformation.

Bibliography

[1] M. S. Livingston. “particle accelerators a brief history". *Harvard University Press*, 1969. URL: https://www.hup.harvard.edu/catalog.php?isbn=9780674424340.

[2] S. Y. Lee. Accelerator physics. *world Scientific*, 2011. URL: https://www.worldscientific.com/worldscibooks/10.1142/8335.

[3] H. Wiedemann. Particle accelerator physics i -basic principles and linear beam dynamics-. *Springer*, 1999. URL: https://link.springer.com/book/10.1007%2F978-3-662-03827-7.

[4] H. Wiedemann. Particle accelerator physics ii -nonlinear and higher-order beam dynamics-. *Springer*, 1999. URL: https://link.springer.com/book/10.1007%2F978-3-642-59908-8.

[5] Hideki Miyake. Belle ii experiment: Status and physics prospects. *Nuclear and Particle Physics Proceedings*, 303-305:20 – 24, 2018. Seventh Workshop on Theory, Phenomenology and Experiments in Flavour Physics. The future of BSM physics FPCapri2018. URL: http://www.sciencedirect.com/science/article/pii/S2405601419300495, doi:https://doi.org/10.1016/j.nuclphysbps.2019.03.005.

[6] K. Akai, K. Furukawa, H. Koiso, and on behalf of the SuperKEKB accelerator team. “SuperKEKB collider". *Nucl. Instrum. Methods Phys. Res. A*, 907:188–199, 2018. URL: https://doi.org/10.1016/j.nima.2018.08.017.

[7] Yukiyoshi Ohnishi, Tetsuo Abe, Toshikazu Adachi, Kazunori Akai, Yasushi Arimoto, Kiyokazu Ebihara, Kazumi Egawa, John Flanagan, Hitoshi Fukuma, Yoshihiro Funakoshi, Kazuro Furukawa, Takaaki Furuya, Naoko Iida, Hiromi Iinuma, Hoitomi Ikeda, Takuya Ishibashi, Masako Iwasaki, Tatsuya Kageyama, Susumu Kamada, Takuya Kamitani, Ken-ichi Kanazawa, Mitsuo Kikuchi, Haruyo Koiso, Mika Masuzawa, Toshihiro Mimashi, Takako

Miura, Takashi Mori, Akio Morita, Tatsuro Nakamura, Kota Nakanishi, Hiroyuki Nakayama, Michiru Nishiwaki, Yujiro Ogawa, Kazuhito Ohmi, Norihito Ohuchi, Katsunobu Oide, Toshiyuki Oki, Masaaki Ono, Masanori Satoh, Kyo Shibata, Masaaki Suetake, Yusuke Suetsugu, Ryuhei Sugahara, Hiroshi Sugimoto, Tsuyoshi Suwada, Masafumi Tawada, Makoto Tobiyama, Noboru Tokuda, Kiyosumi Tsuchiya, Hiroshi Yamaoka, Yoshiharu Yano, Mitsuhiro Yoshida, Shin-ichi Yoshimoto, Demin Zhou, and Zhanguo Zong. Accelerator design at SuperKEKB. *Progress of Theoretical and Experimental Physics*, 2013(3), 03 2013. 03A011. URL: https://doi.org/10.1093/ptep/pts083, arXiv:https://academic.oup.com/ptep/article-pdf/2013/3/03A011/4439973/pts083.pdf, doi:10.1093/ptep/pts083.

[8] M. Kikuchi, T. Abe, K Egawa, H. Fukuma, K. Furukawa, N. Iida, H. Ikeda, T. Kamitani, K. Kanazawa, K. Ohmi, K. Oide, K. Shibata, M. Tawada, M. Tobiyama, and D. Zhou. "Design of Positron Damping Ring for SuperKEKB". *Proc. of the 1st International Particle Accelerator Conference*, pages 1641–1643, 2010. URL: http://accelconf.web.cern.ch/AccelConf/IPAC10/papers/tupeb054.pdf.

[9] N. Iida, Y. Funakoshi, H. Ikeda, T. Ishibashi, H. Kaji, T. Kamitani, M. Kikuchi, T. Kobayashi, H. Koiso, F. Miyahara, T. Mori, Y. Ohnishi, Y. Seimiya, H. Sugimoto, H. Sugimura, R. Ueki, Y. Yano, and D. Zhou. "COMMISSIONING OF POSITRON DAMPING RING AND THE BEAM TRANSPORT FOR SuperKEKB". *Proc. of the 62th ICFA Advanced Beam Dynamics Workshop on High Luminosity Circular e^+ e Colliders*, pages 152–156, 2018. URL: https://doi.org/10.18429/JACoW-eeFACT2018-TUPAB07.

[10] T. Natsui, D. Satoh, M. Yoshida, R. Zhang, and X. Zhou. "Injector Linac Upgrade and New RF Gun Development for SuperKEKB". *Proc. of the 58th ICFA Advanced Beam Dynamics Workshop on High Luminosity Circular e^+ e Colliders*, pages 74–78, 2016. URL: https://doi.org/10.18429/JACoW-eeFACT2016-TUT2H2.

[11] H. Koiso, A. Morita, Y. Ohnishi, K. Oide, and K Satoh. "Lattice of the KEKB colliding rings". *Prog. Theor. Exp. Phys.*, 2013:03A009 (11 pages), 2013. URL: https://doi.org/10.1093/ptep/pts086.

[12] Y. Ohnishi, H. Koiso, A. Morita, H. Sugimoto, and K. Oide. "lattice design of low emittance and low beta function at collision point for superkekb". *Proc of the 2nd International Particle Accelerator Coference*, pages pp. 3693–3695,

2011. URL: https://accelconf.web.cern.ch/accelconf/IPAC2011/papers/thpz007.pdf.

[13] T. Oki, N. Tokuda, T. Adachi, N. Ohuchi, and S. Nakamura. "Full-Scale Prototype Power Supply for SuperKEKB Final Focus Superconducting Magnets". *IEEE Trans. Applied Superconductivity*, 26:0601404 (4 pages), 2016. URL: https://doi.org/10.1109/TASC.2016.2523058.

[14] S. Nakamura, T. Oki, T. Adachi, and N. Tokuda. "SuperKEKB main ring power supply system". *Proceedings of IPAC2016*, pages 3531–3533, 2016. URL: https://doi.org/10.18429/JACoW-IPAC2016-THPMW001.

[15] Y. Suetsugu, K. Kanazawa, K. Shibata, T. Ishibashi, H. Hisamatsu, M. Shirai, and S. Terui. "Construction status of the SuperKEKB vacuum system". *Vacuum*, 121:238–244, 2015. URL: https://doi.org/10.1016/j.vacuum.2014.12.010.

[16] M. Shirai Y. Suetsugu, , and M. Ohtsuka. "Application of a Matsumoto-Ohtsuka-type vacuum flange to beam ducts for futureaccelerators". *J. Vac. Sci. Technol. A*, 23:1721–1727, 2005. URL: https://doi.org/10.1116/1.2101808.

[17] T. Kobayashi, K. Akai, K. Ebihara, A. Kabe, K. Nakanishi, M. Nishiwaki, J. Odagiri, H. Deguchi, K. Hayashi, T. Iwaki, and M. Ryoshi. "Development and Construction Status of New LLRF Control System for SuperKEKB". *Proc. of the 5th International Particle Accelerator Conference*, pages 2444–2446, 2014. URL: https://doi.org/10.18429/JACoW-IPAC2014-WEPME071.

[18] K. Oide, T. Abe, K. Akai, Y. Funakoshi, T.Kageyama, H. Koiso, K. Ohmi, Y. Ohnishi, K. Shibata, Y. Suetsugu, and M. Tobiyama. "a few issues on the upgrade of kekb bfactory". *Proc. of the 23rd Particle Accelerator Conf. (PAC09)*, pages pp. 23–27, 2009. URL: http://research.kek.jp/people/dmzhou/BeamPhysics/overview/Oide_PAC2009.pdf.

[19] P. Raimondi. Status on superb effort. *Presentation slide of 2nd Workshop on Super B-Factory*, pages pp. 1–52, 2006. URL: http://www.lnf.infn.it/conference/superb06/prog.html.

[20] K. Ohmi and D. Zhou. "crab crossing in kekb and nano-beam scheme in super-kekb". *Proc. of the International Workshop on Accelerator Science and Technology for Electron-Ion Collider (EIC14)*, page pp. 35, 2014. URL: http://research.kek.jp/people/dmzhou/BeamPhysics/overview/WECAUD4_talk.pdf.

[21] M. Bassetti and G. A. Erskine. Closed expression for the electrical field of a two-dimensional gaussian charge. *CERN-ISR-TH-80-06*, page 5 pages, 1980. URL: https://cds.cern.ch/record/122227.

[22] E. D. Courant and H. S. Snyder. "Theory of the alternating-gradient synchrotron". *Annals of Physics*, 3:1–48, 1958. URL: https://doi.org/10.1016/0003-4916(58)90012-5.

[23] M. Syphers. "Some Notes on Luminosity Calculations". *Beam-doc*, 1348, 2007. URL: http://home.fnal.gov/~syphers/Accelerators/tevPapers/LumiCalc.pdf.

[24] W. Herr and B. Muratori. "Concept of luminosity". *Proc. of the CERN Accelerator School: Intermediate Course on Accelerator Physics of Advanced Accelerator Physics*, pages 361–377, 2003. URL: https://doi.org/10.5170/CERN-2006-002.361.

[25] E. Keil. "Luminosity optimisation for storage rings with low- sections and small crossing angles". *Nucl. Inst. Meth.*, 113:333–339, 1973. URL: https://doi.org/10.1016/0029-554X(73)90498-9.

[26] W. Herr. Particle colliders and concept of luminosity. *CERN Accelerator School*, 2012. URL: https://cas.web.cern.ch/sites/cas.web.cern.ch/files/lectures/granada-2012/herr.pdf.

[27] T. Chen. "Crossing Angle Collision and Lifetime: Simulations, Analysis, Measurements and More Simulations". *SLAC-PUB*, 95-6954, 1995. URL: https://www.semanticscholar.org/paper/Crossing-Angle-Collision-and-Lifetime%3A-Simulations%2C-Chen/eb64c621656fdffc450997cd3404cbc81e61b8dc.

[28] T. Pieloni. Beam-beam effect in collider. *CERN Accelerator School*, 2013. URL: https://cas.web.cern.ch/sites/cas.web.cern.ch/files/lectures/trondheim-2013/pieloni.pdf.

[29] W. Herr and T. Pieloni. Beam-beam effect. *Proceedings of the CAS-CERN Accelerator School*, 2013. URL: https://doi.org/10.5170/CERN-2014-009.431.

[30] Kazuhito Ohmi. Simulation of beam-beam effects in a circular e^+e^- collider. *Phys. Rev. E*, 62:7287–7294, Nov 2000. URL: https://link.aps.org/doi/10.1103/PhysRevE.62.7287, doi:10.1103/PhysRevE.62.7287.

[31] H.J. Kim and T. Sen. Beambeam simulation code bbsim for particle accelerators. *Nuclear Instruments and Methods in Physics Research Section A: Accelerators, Spectrometers, Detectors and Associated Equipment*, 642(1):25 – 35, 2011. URL: http://www.sciencedirect.com/science/article/pii/S0168900211007017, doi:https://doi.org/10.1016/j.nima.2011.03.059.

[32] K. Ohmi, M. Tawada, Y. Cai, S. Kamada, K. Oide, and J. Qiang. Beam-beam limit in e^+e^- circular colliders. *Phys. Rev. Lett.*, 92:214801, May 2004. URL: https://link.aps.org/doi/10.1103/PhysRevLett.92.214801, doi:10.1103/PhysRevLett.92.214801.

[33] Miguel A. Furman, Alexander A. Zholents, Tong Chen, and Dmitri Shatilov. Comparisons of beam-beam simulations. 1995.

[34] Richard Talman. A proposed möbius accelerator. *Phys. Rev. Lett.*, 74:1590–1593, Feb 1995. URL: https://link.aps.org/doi/10.1103/PhysRevLett.74.1590, doi:10.1103/PhysRevLett.74.1590.

[35] K. L. Brown. "a first- and seceond-order matrix theory for the design of beam transport systems and charged particle spectrometers". *SLAC Report*, 75, 1967. URL: https://doi.org/10.2172/4742148.

[36] H. Qin and R. C. Davidson. "A physical parametrization of coupled transverse dynamics based on generalized courantsnyder theory and its applications". *Phys. Plasmas*, 16:050705 (4pages), 2009. URL: https://doi.org/10.1063/1.3142472.

[37] H. Qin and R. C. Davidson. "Generalized Courant-Snyder theory for coupled transverse dynamics of charged particlesin electromagnetic focusing lattices". *Phys. Rev. ST Accel. Beams*, 12:064001 (13pages), 2009. URL: https://doi.org/10.1103/PhysRevSTAB.12.064001.

[38] Andrea Franchi. "Studies and Measurements of Linear Coupling and Nonlinearities in Hadron Circular Accelerators". *Doctoral Thesis (Johann Wolfgang Goethe-Universität)*, page (166 pages), 2006. URL: http://publikationen.ub.uni-frankfurt.de/frontdoor/index/index/docId/2270.

[39] E. H. Maclean, R. Tomás, M. Giovannozzi, and T. H. B. Persson. First measurement and correction of nonlinear errors in the experimental insertions of the cern large hadron collider. *Phys. Rev. ST Accel. Beams*, 18:121002, Dec 2015. URL: https://doi.org/10.1103/PhysRevSTAB.18.121002.

[40] Andrzej Wolski. *"Beam Dynamics in High Energy Particle Accelerators"*. Imperial College Press, 2014. URL: https://doi.org/10.1142/p899.

[41] K. Ohmi, M. Tawada, and K. Oide. Study of the mechanism of the beam-beam limit. *KEK Report*, 2003-111, 2004. URL: https://lib-extopc.kek.jp/preprints/PDF/2003/0327/0327111.pdf.

[42] K. Ohmi, M. Tawada, Y. Cai, S. Kamada, K. Oide, and J. Qiang. Luminosity limit due to the beam-beam interactions with or without crossing angle. *Phys. Rev. ST Accel. Beams*, 7:104401, Oct 2004. URL: https://link.aps.org/doi/10.1103/PhysRevSTAB.7.104401, doi:10.1103/PhysRevSTAB.7.104401.

[43] Katsunobu Oide and Haruyo Koiso. Dynamic aperture of electron storage rings with noninterleaved sextupoles. *Phys. Rev. E*, 47:2010–2018, Mar 1993. URL: https://link.aps.org/doi/10.1103/PhysRevE.47.2010, doi:10.1103/PhysRevE.47.2010.

[44] N. Ohuchi, Y. Arimoto, K. Aoki, M. Kawai, T. Kawamoto, H. Koiso, Y. Kondo, M. Masuzawa, A. Morita, S. Nakamura, Y. Ohnishi, T. Oki, Y. Ohsawa, H. Sugimoto, K. Tsuchiya, R. Ueki, X. Wang, H. Yamaoka, Z. Zong, P. Wanderer, B. Parker, M. Anerella, J. Escallier, A. Marone, A. Jain, G. Velev, J. DiMarco, J. Nogiec, M. Tartaglia, T. Gardner, and T. Kim. Final–focus superconducting magnets for superkekb. *Proc. of the IPAC18*, pages pp. 1215–1219, 2018. URL: http://accelconf.web.cern.ch/AccelConf/ipac2018/papers/tuzgbe2.pdf.

[45] B. Parker, M. Anerella, J. Escallier, A. Ghosh, H. Hocker, A. Jain, A. Marone, P. Wanderer, Y. Arimotoand M. Iwasaki, N. Ohuchi, M. Tawada, K. Tsuchiya, H. Yamaoka, and Z. Zong. Superconducting corrector ir magnet production cor superkekb. *Proc. of the NA–PAC2013*, pages pp. 1241–1243, 2013. URL: http://accelconf.web.cern.ch/AccelConf/PAC2013/papers/thpba07.pdf.

[46] B. Parker, M. Anerella, J. Escallier, A. Ghosh, A. Jain, A. Marone, P. Wanderer, Y. Arimoto, M. Iwasaki, N. Ohuchi, N. Higashi, K. Tsuchiya, H. Yamaoka, X. Wang, and Z. Zong. The superkekb interaction region corrector magnets. *Proc. of the IPAC2016*, pages pp. 1193–1195, 2016. URL: https://www.bnl.gov/magnets/SuperKEKB_Correctors/docs/pdf/SuperKEKB_IPAC2016.pdf.

[47] M Arinaga, J Flanagan, S Hiramatsu, T Ieiri, H Ikeda, H Ishii, E Kikutani, T Mimashi, T Mitsuhashi, H Mizuno, K Mori, M Tejima, and M Tobiyama. Kekb

beam instrumentation systems. *Nuclear Instruments and Methods in Physics Research Section A: Accelerators, Spectrometers, Detectors and Associated Equipment*, 499(1):100 – 137, 2003. KEK-B: The KEK B-factory. URL: http://www.sciencedirect.com/science/article/pii/S0168900202017837, doi:https://doi.org/10.1016/S0168-9002(02)01783-7.

[48] Mitsuhiro Arinaga, John W. Flanagan, Hitoshi Fukuma, Takaaki Furuya, Shigenori Hiramatsu, Hitomi Ikeda, Hitoshi Ishii, Eiji Kikutani, Toshiyuki Mitsuhashi, Kenji Mori, Masaki Tejima, and Makoto Tobiyama. Progress in KEKB beam instrumentation systems. *Progress of Theoretical and Experimental Physics*, 2013(3), 03 2013. 03A007. URL: https://doi.org/10.1093/ptep/pts095, arXiv:http://oup.prod.sis.lan/ptep/article-pdf/2013/3/03A007/4440180/pts095.pdf, doi:10.1093/ptep/pts095.

[49] M. Arinaga, J. W. Flanagan, H. Fukuma, H. Ikeda, H. Ishii, S. Kanaeda, K. Mori, M. Tejima, M. Tobiyama, R. Gillard G. Bonvicini, H. Farhat, and G.S. Varner. Beam instrumentation for the superkekb rings. *Proc. of the 1st Int. Beam Instrumentation Conf. (IBIC2012)*, pages pp. 6–10, 2012. URL: http://accelconf.web.cern.ch/AccelConf/IBIC2012/papers/mocb01.pdf.

[50] H. Fukuma. Beam instrumentation in superkekb. *Proc. of the 60th ICFA ABDW on High Luminosity Circular e^+e^- Colliders (eeFACT2016)*, pages pp. 164–167, 2016. URL: http://accelconf.web.cern.ch/AccelConf/eefact2016/papers/wet1h3.pdf.

[51] G. Mitsuka, M. Arinaga, J. W. Flanagan, H. Fukuma, H. Ikeda, H. Ishii, S. Iwabuchi, K. Mori, E. Mulyani, M. Tejima, , M. Tobiyama, G. S. Varner, and G. Bonvicini. Beam instrumentation at superkekb. *Proc. of the 62th ICFA ABDW on High Luminosity Circular e^+e^- Colliders (eeFACT2018)*, pages pp. 169–172, 2018. URL: https://doi.org/10.18429/JACoW-eeFACT2018-TUPBB05.

[52] N. Iida, John Flanagan, Y. Funakoshi, and Katsunobu Oide. Synchrotron radiation interferometer calibration check by use of a size control bump in kekb. pages pp. 1478–1480, 2007. URL: https://doi.org/10.1109/PAC.2007.4440795.

[53] J. W. Flanagan, M. Arinaga, H. Ikeda, H. Fukuma, K. Kanazawa, T. Mitsuhashi, and G. S. Varner. Design considerations for x-ray beam profile monitor for superkekb. *Proc. of the 7th Annual Meeting of PASJ*, pages pp. 618–622,

2010. URL: http://pasj.jp/web_publish/pasj7/proceedings/P_4PM/P_EH_4PM/WEPS095.pdf.

[54] J.W. Flanagan, M. Arinaga, H. Fukuma, H. Ikeda, A. Lyndaker, D. P. Peterson, and N. Rider. High–power tests at cesrta of x-ray optics elements for superkekb. *Proc. of the 2nd Int. Beam Instrumentation Conf. (IBIC2013)*, pages pp. 844–847, 2013. URL: http://accelconf.web.cern.ch/AccelConf/IBIC2013/papers/wepf15.pdf.

[55] H. Sugimoto, Y. Ohnishi, H. Koiso, A. Morita, K. Mori, and M. Tejima. Optics measurents at superkekb using beam based calibration for bpm and bba. *Proc. of the 10th Int. Particle Accelerator Conf. (IPAC19)*, pages pp. 1198–1202, 2019. URL: https://doi.org/10.18429/JACoW-IPAC2019-TUZPLM2.

[56] Kohji Hirata. Analysis of beam-beam interactions with a large crossing angle. *Phys. Rev. Lett.*, 74:2228–2231, Mar 1995. URL: https://link.aps.org/doi/10.1103/PhysRevLett.74.2228, doi:10.1103/PhysRevLett.74.2228.

[57] Toshihisa Hirai, Sadaharu Uehara, and Yasushi Watanabe. Real-time luminosity monitor for a b-factory experiment. *Nuclear Instruments and Methods in Physics Research Section A: Accelerators, Spectrometers, Detectors and Associated Equipment*, 458(3):670 – 676, 2001. URL: http://www.sciencedirect.com/science/article/pii/S016890020000766X, doi:https://doi.org/10.1016/S0168-9002(00)00766-X.

[58] D. E. Khechen, P. Bambade, C. Rimbault, V. Kubytskyi, D. Jehanno, Y. Peinaud, A. Blin, P. Cornebise, Y. Funakoshi, Y. Ohnishi, and S. Uehara. First tests of superkekb luminosity monitor during 2016 since beam commissioning. *Proc. of the 7th International Particle Accelerator Conference*, pages pp. 81–83, 2016.

[59] C.G. Pangy, P. Bambade, S. Di Carlo, D. Jehanno, V. Kubytskyi, Y. Peinaud, C. Rimbault, Y. Funakoshi, and S. Uehara. First tests of superkekb fast luminosity monitors during 2018 phase-2 commissioning. *Proc. of the 9th International Particle Accelerator Conference*, pages pp. 2254–2257, 2018.

[60] P. Thrane. Measuring β^* in superkekb with k modulation. *CERN-THESIS*, 2018-300:pp. 1–29, 2018.

[61] Y. Ohnishi, Y. Funakoshi, K. Mori, E. Perevedentsev, M. Tanaka, M. Tejima, and M. Tobiyama. “measurement of xy coupling using turn-byturn bpm at kekb". *Proc. of the 7th European Particle Accelerator Conf. (EPAC2000)*, pages

pp. 1537–1539, 2000. URL: http://accelconf.web.cern.ch/AccelConf/e00/PAPERS/MOP3B11.pdf.

[62] K. Ohmi, T. Ieiri, Y. Ohnishi, Y. Seimiya, M. Tejima, M. Tobiyama, and D. Zhou. "optics measurement at the interaction point using nearby position monitors in kekb". *Proc. of the 1st Int. Particle Accelerator Conf. (IPAC10)*, pages pp. 1539–1541, 2010. URL: http://accelconf.web.cern.ch/AccelConf/IPAC10/papers/tupeb012.pdf.

[63] Sad (strategic accelerator design) home page. URL: http://acc-physics.kek.jp/SAD/.

[64] D. A. Edwards and L. C. Teng. "Parametrization of Linear Coupled Motion in Periodic Systems". *IEEE Trans. on Nuclear Science*, 20:3, 885–888, 1973. URL: https://doi.org/10.1109/TNS.1973.4327279.